Sequencing & Agglomeration of Cycles in Variable Amplitude Underload Spectra: Effects on Surface Crack Growth in a Near-neutral pH Environment

by

Rui Ning Li

A thesis submitted in partial fulfillment of the requirements for the degree of

Master of Science

in

Materials Engineering

Department of Chemical and Materials Engineering

University of Alberta

ABSTRACT

Stress corrosion cracking (SCC) is one of the biggest integrity threat facing pipelines. Large numbers of SCC defects are detected every year, but scheduling the repair work for these defects is an enormous challenge. Pipeline companies have limited resources to take on the repairs. Therefore the repairs for these defects are prioritized using SCC growth models. However, current SCC growth models often make inaccurate life prediction and cannot meet the needs of the pipeline operators.

One of the reasons these models perform poorly is because they do not consider the variable amplitude pressure fluctuations experienced by a pipeline. It is known throughout the pipeline industry that pressure fluctuations in the pipeline drives SCC propagation, but what is not known is how the different cycles within a pressure spectrum interact with each other and affect crack growth rate. Pipeline operators are interested in determining the relative severity of different spectra. The biggest difference between these spectra is how the individual cycles are sequenced within.

The objective of this thesis is to investigate how the sequencing and agglomeration of cycles within a spectrum can affect crack growth rates. SCC tests were conducted on surface crack samples made from X-65 pipeline steel in an anaerobic NNpH environment purged with 5% CO_2/95% N_2 gas. Traditionally, SCC studies were conducted using thru-wall crack specimens such as the compact tension (CT) specimen. Surface crack samples were used in this study because they simulate SCC more accurately. Additional sample preparation techniques were developed specifically for surface crack samples during this study since they are seldom used by other researchers. Six load spectra with different sequencing and agglomeration of cycles were

applied to the samples. The basic building blocks of all the test spectra were: minor cycles with high R ratios (minimum stress/max stress), severe underload cycles with low R ratio, and mild underload cycles with medium R ratios. The proportion of the different types of cycles remained constant for all spectra, and only the sequencing was changed for each spectrum. The spectra tested simulate underload-type spectrum experienced by an oil pipeline at pump station discharge, where most SCC's have been found.

The crack growth rates obtained from the experiments were compared to determine the relative severity of the spectra. It was found that increasing the agglomeration level in a spectrum (i.e. grouping together the same type of cycle) increased the hydrogen embrittlement effects by allowing more hydrogen to build up in front of the crack tip during the minor cycles, and this tend to increase crack growth rate. However, increasing the agglomeration level also decreased the number of interaction events (i.e. how many damage causing cycles are enhanced by hydrogen embrittlement), which tend to decrease crack growth rate. Therefore the resultant crack growth rate is determined by the competition of these two effects. The most severe spectra balance these two opposing force to optimize the crack growth enhancement.

Sequencing of damage-causing underload cycles is also important. For spectra with high agglomeration level where multiple underload cycles are grouped together, the more aggressive underload cycle should not be the first cycle in the group because the hydrogen embrittlement effect is the strongest right at the start of the underload group. Spectra that 'shielded' the more aggressive underload cycle behind other mild underload cycles experienced slower crack growth rate.

Pipeline operators could use the finding from this study to help them determine the relative severity of their pressure spectra and make improvements to their existing SCC model.

Acknowledgement

I would like to express my deepest gratitude to Dr. Weixing Chen for giving me the opportunity to work on this research project. Thank you for your support and guidance. This has been a fantastic learning opportunity, and I really appreciated being given the freedom to try new things. I would also like to acknowledge the contribution of Dr. Hao Zhang and Dr. Reg Eadie during our group discussions.

I would like to thank the Natural Science and Engineering Research Council of Canada, TransCanada Pipelines Limited, Enbridge Inc., and Pipeline Research Council International for their financial support.

Special thanks to my colleagues, whose input greatly helped me throughout my research: Devin Engel, Jerome Ang, Mengshan Yu, Jiaxi Zhao, Zhezhu Xu, Olayinka Tehinse, and others. Thank you for your efforts toward making the lab a better place.

I would also like to thank all the staff at U of A who had given me a helping hand. In particular I would like to thank James McKinnon, Walter Boddez, Nathan Gerein, Lily Laser, Jack Gibeau, and Marion Pritchard.

It goes without saying my parents were my biggest supporters. Without you I would not be where I am today. Thank you for being there every step of the way.

Table of Contents

List of Figures

List of Tables

List of Abbreviations

%WT   Crack depth unit, given in percentage of pipe wall thickness

BSE   Backscattered Electron

CA   Constant Amplitude

CEPA   Canadian Energy Pipeline Association

CP   Cathodic Protection

CSA   Canadian Standards Association

CSA Z662   Canadian Standards Association Standard - Oil and gas pipeline systems

CSE   Copper–Copper(II) Sulfate Electrode

CT   Compact Tension specimen

EAC   Environmentally Assisted Cracking

EDM   Electrical Discharge Machining

EDX/EDS   Energy-dispersive X-ray spectroscopy

EMAT   Electromagnetic Acoustic Transducer

FB   Fundamental Block

FPZ   Fracture Process Zone

FBE   Fusion Bonded Epoxy

HE   Hydrogen Embrittlement

HEAC   Hydrogen Environment Assisted Cracking

HELP   Hydrogen Enhanced Localized Plasticity

HIC   Hydrogen Induced Cracking

IHAC   Internal Hydrogen Assisted Cracking

ILI   In-line Inspection

MAOP   Max Allowable Operating Pressure

MC   Minor Cycles

NEB	National Energy Board
NNpH	Near-Neutral pH
NNpH SCC	Near-Neutral pH Stress Corrosion Cracking
OCP	Open Circuit Potential
SCC	Stress Corrosion Cracking
SCE	Saturated Calomel Electrode
SCT	Surface Crack Tensile specimen
SE	Secondary Electron
SEC	Single Edge Cracked specimen
SEM	Scanning Electron Microscope
SIF	Stress Intensity Factor
SMYS	Specified Minimum Yield Strength
SSRT	Slow Strain Rate Testing
UL	Underload cycles
VAL	Variable Amplitude Loading

1 Introduction

1.1 Research Objective

Oil and gas pipelines are an integral part of our society. They deliver energy in a safe and economical manner to fuel our daily activities. The role pipelines play in ensuring the economic stability and growth of Canada cannot be underestimated. Even with the strong interest in renewable energy in the past decade, countries around the world still rely on pipelines to meet their energy demands.

Many in the industry and government agree that pipelines are the safest way to move oil and gas [1]. The pipeline industry is heavily regulated to ensure the public and environment is protected from leaks and ruptures. Despite the best effort from both the companies and regulators, leaks and ruptures still occur. There is over 760,000 km of pipelines in Canada [2], and there are numerous integrity threats to pipelines. Despite these challenges, companies and regulators continue to strive for zero incidents in order to maintain public trust [3].

A major integrity threat facing Canadian pipelines is stress corrosion cracking (SCC). SCC is a form of environmentally assisted cracking (EAC). Most pipelines are buried under the ground, and are coated with different types of coating to protect against the corrosive groundwater. However, certain types of coating are more prone to disbondment (coating lose adhesion to the pipe surface), and a result, can expose the pipe to the groundwater in the soil. When this happens, the combination of corrosive environment and operating stress on the pipe steel can initiate SCC on the outer surface of the pipe wall. If left unchecked, these cracks can grow and eventually penetrate the pipe wall, causing leaks or ruptures.

SCC affects pipelines around the world. Two types of SCC's have been documented in the pipeline industry: high pH SCC and near neutral pH SCC (NNpH SCC). The high pH and near-neutral pH refers to the acidity of the soil environment in which these SCC were found. There are also many distinguishing features between the two types of SCC which will be discussed later in this thesis. Most SCC found in Canada is NNpH SCC, which is the focus of this study.
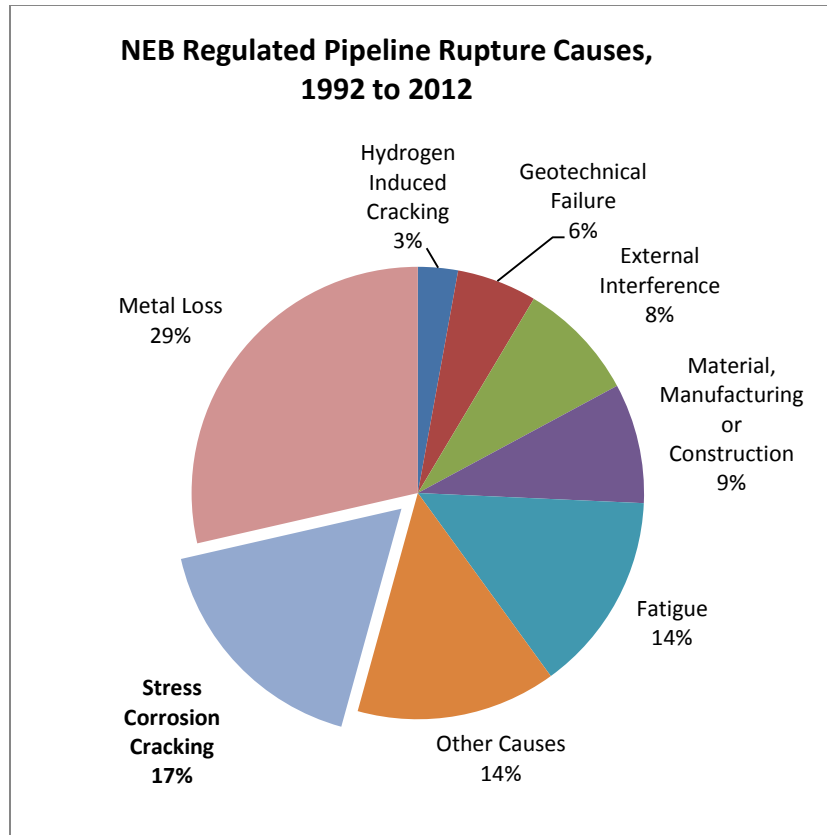
Figure 1-1 Pie chart showing the distribution of rupture causes on NEB-regulated pipelines in Canada from 1992 to 2012[1]. Data is compiled from the NEB's database of pipeline ruptures [4]

NNpH SCC is a relatively recent phenomenon. The first case in Canada was discovered in 1977. According to the 1996 National Energy Board (NEB) public inquiry [5], there were 22 failures (10 leaks and 12 ruptures) caused by SCC from 1977 to 1996 in Canada. Most failures occurred on vintage pipelines (constructed prior to the 1980's) coated with single- or double-wrapped polyethylene tape coating.

---

[1] The NEB regulates only 73,000 km out of the 760,000 km of pipelines in Canada[2]. Pipelines in Canada that do not cross provincial or international borders are regulated by their provincial energy regulators. Figure 1-1 may not paint complete picture for the extent of SCC. Most provincial regulators do not specifically keep track of SCC failures. The NEB tends to regulate larger diameter transmission pipelines that cross major borders, while provincial regulators tend to regulate smaller diameter pipelines. The NEB statistics should be representative of SCC prevalence on large diameter pipelines.

Statistics of Canadian pipeline failures have consistently listed SCC as a major integrity threat. Figure 1-1 shows that from 1992 to 2012, SCC is the second most common cause of pipeline failures on NEB-regulated pipelines.

A string of SCC failures from the late 1980's to the mid-1990's in Canada increased the public scrutiny in how pipeline companies are dealing with the threat of SCC. A formal inquiry was conducted by the NEB in 1993, and then again in 1996 [5] into the state SCC on Canadian pipelines. The 1996 inquiry made some recommendations on the mitigation of SCC threats, but it also stressed the need for more research to better understand the problem. Since then, significant progress has been made in the area of SCC prevention. As a result, SCC is rarely an issue on newly constructed pipelines. Advances in inline inspection (ILI) tools in recent years, such as the introduction of the electromagnetic acoustic transducer (EMAT), has made locating SCC cracks in a pipeline much easier. As shown in Table 1-1, the introduction of crack detection ILI has a made a huge contribution to the amount of cracks detected.

Table 1-1 Number of significant SCC reported to NEB categorized by the detection method. Reproduced from [6], with permission from ASME.

Detection Method	Significant SCC Reported
Hydrotest	12
Predictive Soils Model excavation	23
Investigative excavations	81
Crack Detection ILI	314
Total	**430**

ILI tools capable of detecting the size, orientation, and geographical location of cracks over the entire span of a pipeline. It is good that so many cracks that previously couldn't be detected could now be easily detected, but it also brought on more challenges. A huge number of SCC cracks are detected every year. Pipeline companies have limited resources to mitigate all the cracking defects, therefore repair work needs to be prioritized so that the most severe defects are repaired first.

There is currently a lot of uncertainty in prioritizing the severity of SCC defects. SCC is influenced by a large number of factors, including soil composition, CO_2 level in the groundwater, temperature, electrical resistance of the soil, seasonal variations in soil, cathodic protection level, crack dimension, pipe material, max allowable operating pressure (MAOP), pressure fluctuation cycles, the rate of pressure fluctuation, and many more. Determining how fast a crack will grow under different conditions is critical to prioritizing the severity. The current approach in pipeline integrity is to use various crack growth models to predict how long it will take for a crack to reach a critical size (i.e. in need of immediate repair). The pipeline companies can then prioritize the cracks based and how much time they have until the crack becomes critical, and schedule repairs accordingly.

One of the most important factors in determining the growth rate of SCC is the cyclic pressure fluctuations. The modern view of NNpH SCC is that it's not true SCC, and should be instead classified as a corrosion fatigue phenomenon (fatigue crack growth driven by cyclic loading in a corrosive environment). Corrosion fatigue is heavily influenced by the cyclic load spectra. Pipeline pressure fluctuates minute by minute, and thus the stress experienced by the pipe wall due to the internal pressure also fluctuates, creating a load spectrum over time. In real-world operation, the fluctuation amplitude varies widely, with small fluctuations most of the time, and occasional large fluctuations. This is called Variable-Amplitude Loading (VAL).

Data collected from the field has shown that the majority of SCC is found within a short distance (30km) downstream of a compressor/pump station [5–7]. The VAL spectra seen just downstream of compressor/pump stations are called underload-type spectra [8–10]. Typical underload-type spectra seen for gas and oil pipelines are shown in Figure 1-2. Pressure cycles in underload-type spectra can be categorized into minor cycles (MC) and underload cycles (UL). Minor cycles are small amplitude cycles fluctuating just below MAOP, and they make up the majority of cycles within a spectrum. Underload cycles have much larger amplitude than minor cycles. Underload cycles also occur less frequently, but they make the most contribution to crack growth.

(a) Oil Pipeline   **(b) Gas Pipeline**
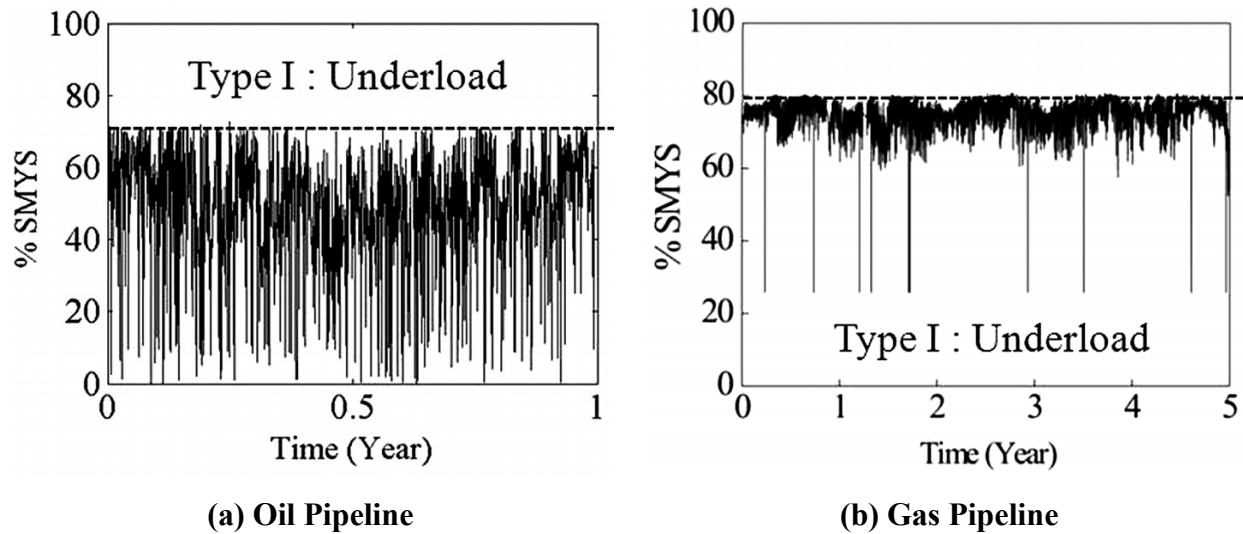
Figure 1-2 Underload-type pressure fluctuation spectrum found within 30km downstream of compressor station or pump station, and are typically associated with SCC failure: a) for an oil pipeline, b) for a gas pipeline. Reproduced from, with permission from ASCE [11]

Different pipelines experience different underload-type spectra, and that is the main cause behind the differences in SCC growth rates at different sites. The pipeline industry is interested in learning about the effects of different spectra on crack growth rate and using that knowledge to help it prioritize repairs. Current crack growth models are very simple and have yet to consider variable amplitude loading. One area which hasn't been studied is the effect of sequencing & agglomeration of cycles in an underload-type spectrum for pipeline steel. Since the basic building blocks of an underload-type spectrum are just MC's and UL's, how these cycles are arranged and sequenced has a big impact on crack growth due to load interaction effects.

The objective of this thesis is to investigate how VAL underload-type spectra affect SCC growth rates in an NNpH environment for an oil pipeline. Specifically, the effect of cycle sequence and agglomeration within a spectrum is studied. A focus is placed on simulating oil pipelines since they are more susceptible to SCC failures due to a larger number of cyclic events within its lifetime. Oil pipelines are also more difficult to repair than gas pipelines, and the consequence of ruptures are also more severe.

Corrosion fatigue experiments were carried out on surface crack samples that simulate near-neutral pH conditions on the outer surface of a pipeline. The crack growth rates from various spectrum sequences are compared. The question that this study aims to answer is: which type of

sequencing will be the most dangerous to an oil pipeline? The findings from this study will help pipeline operators better prioritize their SCC repairs.

1.2 Thesis Structure

Chapter 2 contains the literature review for this thesis. Various aspects that affect SCC will be discussed, including the role of variable amplitude corrosion fatigue and hydrogen on SCC propagation.

Chapter 3 describes the techniques that were used to precrack semi-elliptical surface crack specimen for testing. Most SCC research was conducted using thru-wall crack specimens. Surface crack specimens simulate SCC better since SCC's are also surface cracks. However, precracking surface crack specimens present many new challenges that need to be addressed.

Chapter 4 describes the experimental methods used for the corrosion fatigue tests. The corrosion fatigue tests simulate pipeline SCC growth in NNpH environment under various VAL underload-type spectra.

Chapter 5 contains the results and discussions of the corrosion fatigue experiments

Chapter 6 contains the conclusion and recommendations of this thesis.

2 Chapter 2 Literature review

2.1 Environmentally Assisted Cracking (EAC)

High pH and NNpH SCC are examples of environmentally assisted cracking (EAC). EAC is a broad term to describe several types of cracking in metals that are influenced by the surrounding environment[12]. It includes:

- Stress Corrosion Cracking (SCC)
- Hydrogen Embrittlement (HE)
- Corrosion Fatigue (CF)

The key components of EAC are shown in Figure 2-1. The metallurgy determines basic mechanical properties like strength and crack resistance. The environment provides a corrosive factor. The chemical composition of the material also plays a key role in determining how the material reacts with the environment. The environment can also generate atomic hydrogen on the metal surface which can diffuse in the metal and cause HE damage. Stress typically refers to tensile stress, which can be either static or cyclic.
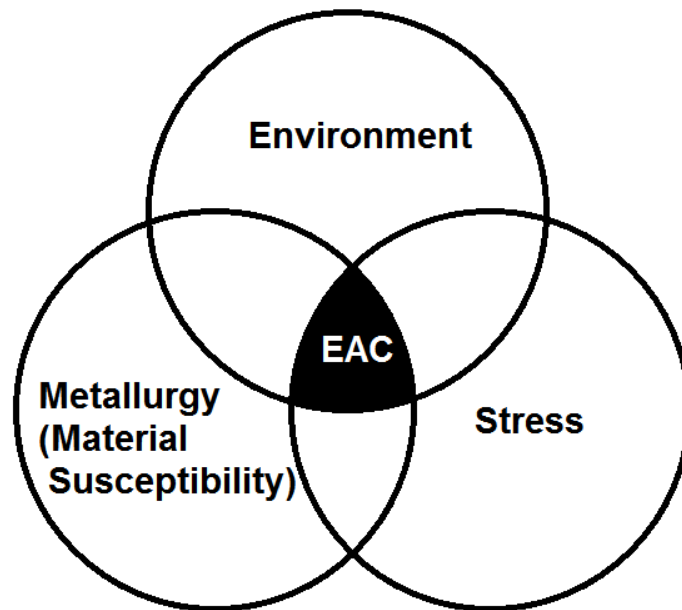
Figure 2-1 Key components of EAC.

2.2 Classical SCC and High-pH SCC

Traditionally, SCC[2] refers to cracks that propagate due to anodic process at the crack tip, and at loading below a material's tensile strength [12]. SCC is characterized by little general corrosion on the surface of the metal, because the combination of environment and metal tend to form a passive film (usually an oxide film) that protects the metal from further corrosion. The crack tip, on the other hand, is an area of high stress concentration, and can generate enough stress to break the protective film locally at the crack tip. This process is called the film rupture model, and is illustrated in Figure 2-2. Inside the crack crevice, the crack walls also form a protective passive film. Only the crack tip experiences film rupture and dissolution of metal, leading to very thin cracks with very little general corrosion.
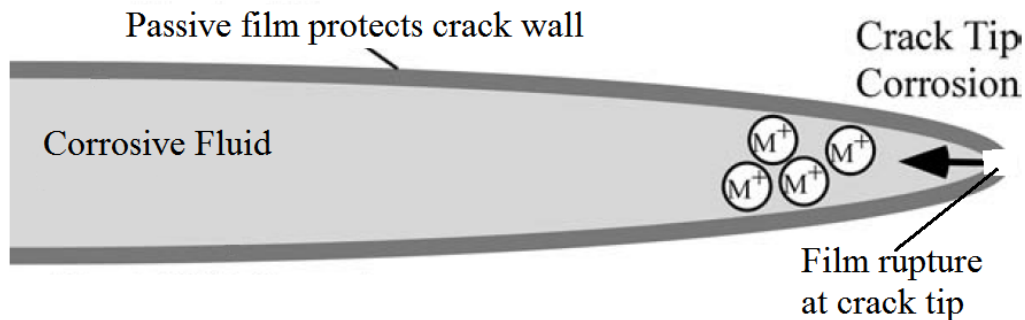
Figure 2-2 SCC propagation through anodic dissolution at the crack tip. Film rupture model is shown. The crack walls are protected with a passive film. The passive film cannot withstand the high stress at the crack tip, and ruptures, exposing the metal at the crack tip to dissolution. Adapted from [12], with permission of Taylor and Francis Group, LLC, a division of Informa plc.

Two types of SCC are found on pipelines: high pH SCC and near-neutral pH SCC (NNpH SCC). Only high-pH SCC is associated with the film rupture mechanism. In high-pH SCC, the crack tip dissolution strongly favours the grain boundaries [5,13–15], as a result, cracks have an intergranular crack morphology. High pH SCC [5,14,16] is mostly found within 20km downstream of a compressor/pump station, where the high temperature in the pipe is favourable for crack growth. It is found in soil containing concentrated carbonate-bicarbonate groundwater solution with alkaline pH greater than 9.3. It occurs in a relatively narrow potential range (-600 to -750 mV CSE).

---

[2] The use of the term "SCC" in this section refers specifically to the classical definition of SCC. For the rest of the thesis, the term "SCC" will be used to refer to near-neutral pH SCC, unless otherwise stated.

NNpH SCC is actually a misnomer that has stuck due to the industry's lack of understanding of its mechanisms when it was first discovered. Researchers now believe NNpH SCC is a combination of hydrogen embrittlement and corrosion fatigue as will be discussed later.

2.3 Near-Neutral pH SCC (NNpH SCC)[3] Contributing Factors

2.3.1 Basic Characteristics of NNpH SCC

NNpH SCC, also known as transgranular SCC, has a different mechanism than the film-rupture model described above. Some of the main characteristics of NNpH SCC are summarized in Table 2-1.

Table 2-1 Summary of Near-neutral pH SCC characteristics. Table adapted from [5] with the permission of Public Works and Government Services, 2018.

Factor	NNpH SCC Characteristics
Location	65% of SCC occur between the compressor/pump station and the 1st downstream valve (typically within 16 to 30 km of compressor/pump station) - Specific terrain conditions, alternate wet-dry soils, soils that tend to disbond or damage coatings
Temperature	- Unlike high-pH SCC, there is no apparent correlation between temperature and NNpH SCC [17,18] - Appears to occur primarily in colder climates, possibly due to higher CO_2 solubility in groundwater
Electrolyte	Dilute carbonate-bicarbonate solution (and other ions) containing dissolved CO_2 with near neutral pH (5.5 to 7.5)
Electrochemical Potential	- At free corrosion potential -760 to -790 mV (Cu/CuSO4) - No cathodic protection (CP) reaches pipe surface due to coating shielding
Crack Path and Morphology	- Primarily Transgranular - Quasi-cleavage [19] - Cracks are wider closer to the surface, due to corrosion - Crack becomes thinner and sharper if it's able to grow past dormant stage. See Figure 2-3

---

[3] From here on, the term SCC will be used to refer to NNpH SCC, unless otherwise stated.
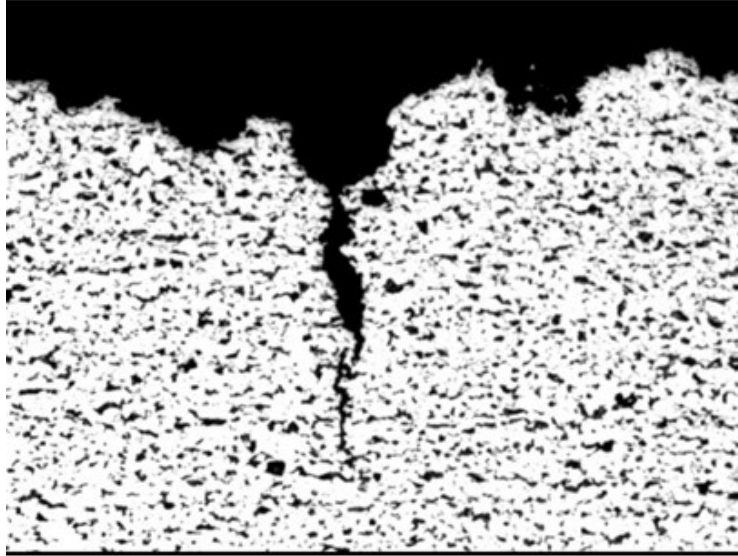
Figure 2-3: Transverse sections of NNpH SCC found in the field. The crack initiates from the base of a corrosion pit. The crack is wider at near the surface due to corrosion. The crack becomes thinner and sharper as it grows in depth direction. Reproduced from [5], with permission from R.J. Eiber.

2.3.2 Coating

Pipeline coating is the first line of defence against SCC, and is perhaps the most important factor in preventing SCC. Pipeline coatings are electrical insulators that isolate the steel pipe from the wet soil environment. Certain types of coating are more susceptible to SCC.

73% of SCC failures have occurred on pipelines with polyethylene tape coating [5]. Polyethylene tape coating contributed to the majority of SCC failures due to its propensity to disbond (lose adhesion) from the pipe surface. Disbondments can also occur, to a lesser extent, on asphalt and coal tar coatings, and have led to some cases of SCC under those coatings as well.

Some examples of tape coating failure are shown in Figure 2-4. Soil stress can cause wrinkling in the coating and create folds where water can enter. Areas where tape overlap is susceptible to groundwater penetration, especially at the pipe long seam, where the weld cap creates a "tent" when the tape is stretched over it. Figure 2-5 shows where SCC could occur on a pipe due to coating disbondments. At locations such as the long seam weld, the heat affected zone (HAZ) already has microstructure susceptible to cracking, and disbondment due to tenting will further increase SCC risk.
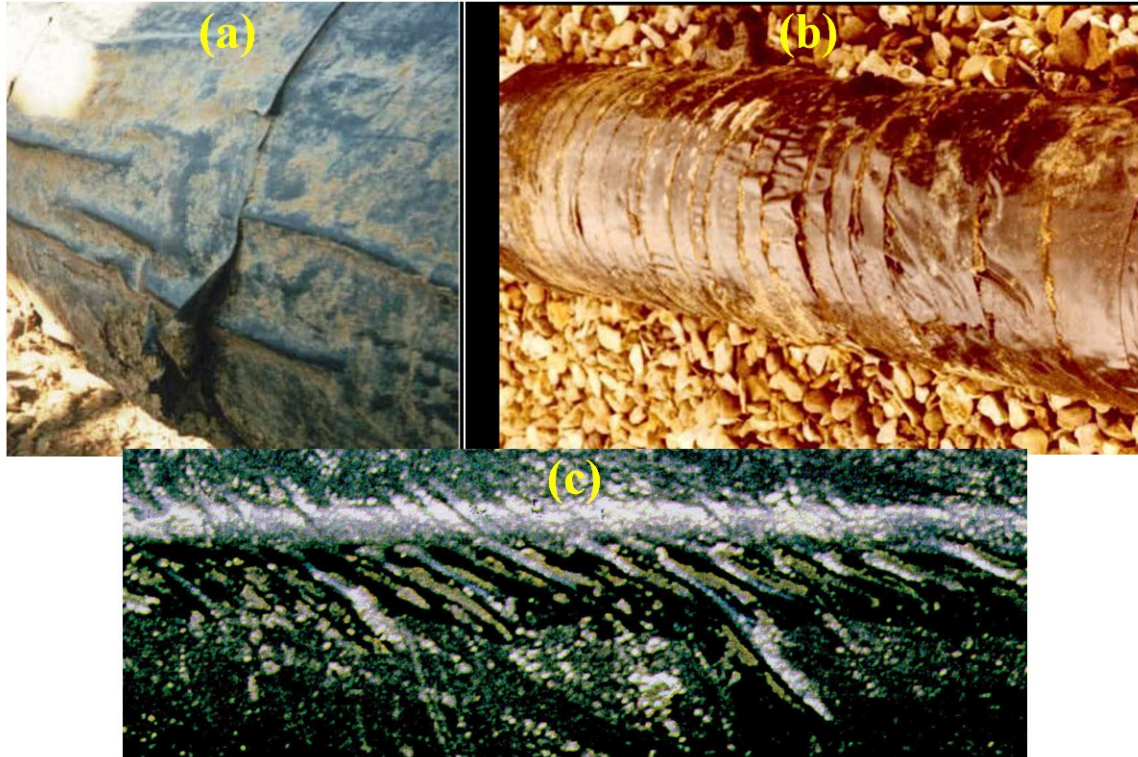
Figure 2-4 Examples of tape coating failures [20]: (a) coating wrinkling due to soil stress. (b) Adhesion loss at tape overlap. (c) Tenting at weld bead. Reprinted from *The Encyclopedia of Pipeline Defects, Third Ed.* **© 2017 ROSEN Group [x]. Used with permission.**
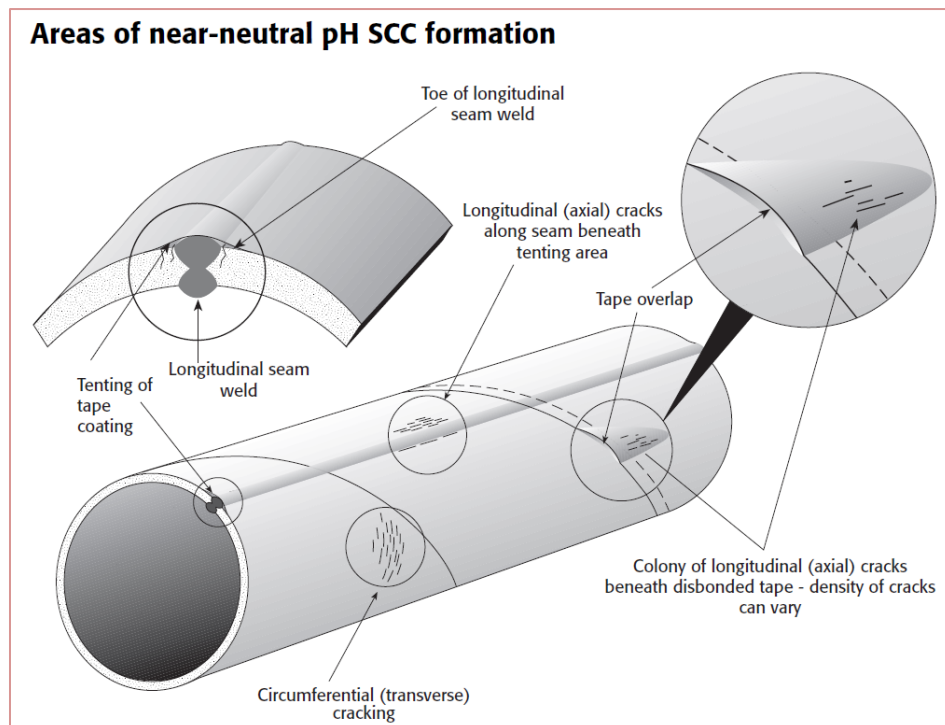
Figure 2-5 Areas of NNpH SCC formation Reproduced from [5], with the permission of Public Works and Government Services, 2018.

Mill-applied fusion bonded epoxy (FBE) coatings were introduced in the 1970's, and is the predominant coating used in new pipeline construction today. Based on field observations, modern FBE coatings appear to be effective in preventing SCC [5,14,21,22]. No SCC has been found under FBE and other similar coatings such as liquid epoxy and urethane [5,14]. The excellent performance of FBE can be largely attributed to its excellent adhesion to the pipe surface [21]. The rigorous surface preparation techniques used today (e.g. sandblasting) have also dramatically reduced disbondment occurrence [21].

2.3.3 Cathodic Protection

The evidence for the lack of CP reaching the pipe surface comes from the field measurements of the pH under disbonded coatings where SCC has been found. Researchers have found that the pH of the undercoating electrolyte at these locations are slightly acidic, ranging from 5.5 to 7.5 (see Figure 2-6) [7,18,23,24]. These near-neutral readings are inconsistent with the high pH readings expected for a pipe protected with CP. The cathodic reaction under CP would produce large amounts of hydroxide ions which can easily raise the pH above 10.

CP systems on pipelines typically apply a potential of -0.85 V_{SCE} [25], which is sufficient to polarize the pipe away from the SCC-susceptible potential range. However, inside a disbondment, the CP protection decreases sharply, and has little to no effect. This is illustrated in Figure 2-7. Pipe-to-soil potential surveys at sites where SCC failures had occurred indicated that the CP systems were all working properly, and proper amount CP was applied [26–30], but corrosion and SCC were still found under the disbondments. These were strong evidence that suggested disbonded coating is shielding the CP current from reach the bare pipe surface.
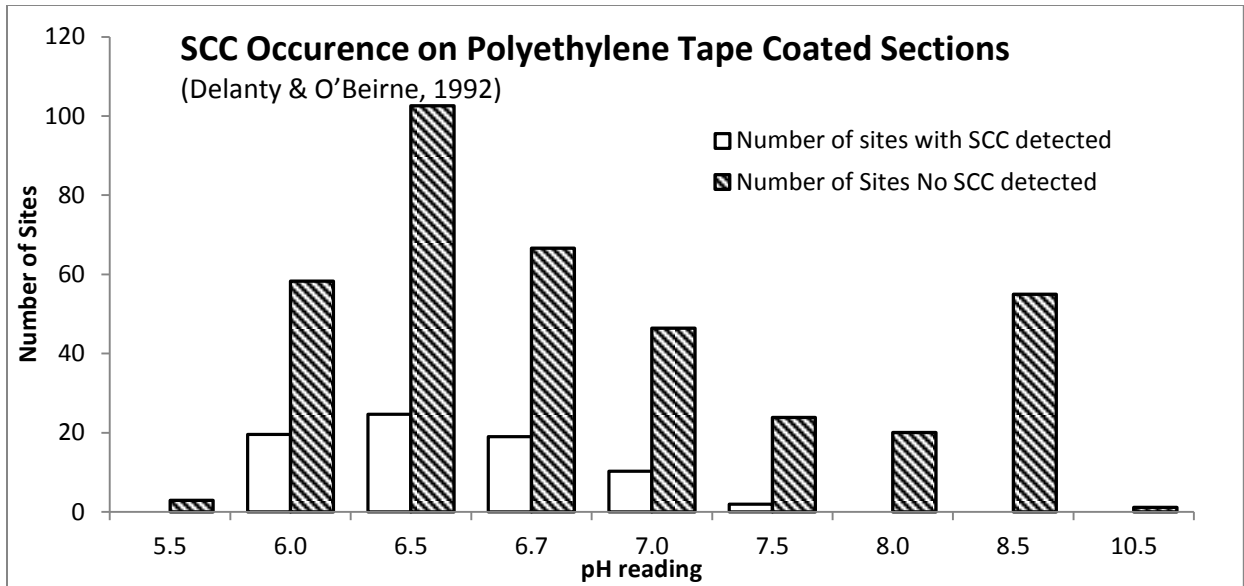
Figure 2-6 SCC occurrence on polyethylene tape coated sections on TransCanada systems for different undercoating pH. Reproduced from [7], with the permission of Oil & Gas Journal.
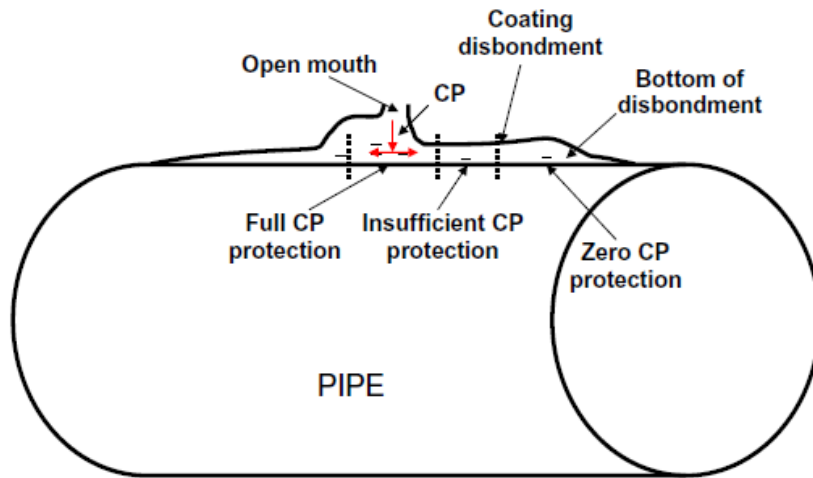
Figure 2-7 Diagram illustrating the decrease in cathodic protection from the open mouth of the coating disbondment. Reproduced from [31], with permission from Elsevier.

2.3.4 Material Susceptibility

Pipe steel of all grades has been found to be susceptible to SCC [5,14]. SCC failures have occurred on pipe grades ranging from 241 MPa (35 ksi) to 448 MPa (65 ksi)[5]. It is difficult to

judge pipe grade susceptibility from field data, because the data is skewed due to the wider use of some specific grades.

The heat affected zones (HAZ) adjacent to the seam welds are known to be susceptible to SCC due to their microstructure[22,32]. Harle et al. [32] have found that the coarse grain heat affected zone (CGHAZ) is significantly more susceptible to SCC than the base material. Electrical resistance welded (ERW) pipes have also been found to be particularly susceptible to SCC through field experience [5,14] and research studies[22,32]. Eadie et al [33] also found that the geometry of the weld cap for double submerged arc welded (DSAW) seam on a pipe creates a large stress concentration at the weld toe, which helps explain why so many SCC is found at the toe of seam welds as shown in Table 2-2.

Table 2-2 Comparison of occurrence of SCC on pipe body vs. toe of seam weld. Data from NEB's significant SCC database. Data from [6]

Location on Pipe	No. of Significant SCC Reported
Pipe Body	78
Toe of Seam Weld	296
Total	**374**

The surface condition of the pipe also plays a big role in SCC initiation. The general consensus is millscale increases the risk of SCC initiation. Experimental studies on NNpH SCC initiation have compared polished steel samples and steel samples with millscales. Those studies have shown samples with millscales consistently initiated more cracks under the same load and environment than polished samples[17,34,35]. The reason for this is the millscale and underlying metal form a micro-scale galvanic couple [36,37]. The millscales are cathodic to the steel, causing micro pits to form on the steel surface. Microcracks could initiate from the small pits and eventually lead to a larger crack.

2.3.5 Residual Stress

Residual stresses in the pipeline that resulted from manufacturing and construction process could also affect SCC initiation and growth. Beavers et al. [38] used the hole drilling technique to measure the residual stresses in SCC-affected steel pipelines. Their study showed that the

residual stress is a function of depth and varied from pipe to pipe as shown in Figure 2-8. The residual stress near the free surface was generally compressive or neutral, and increased (became more tensile) with depth. A strong correlation was found between high tensile residual stress and presence of NNpH SCC. Areas with high tensile residual stress were more likely to contain SCC than low residual stress areas.
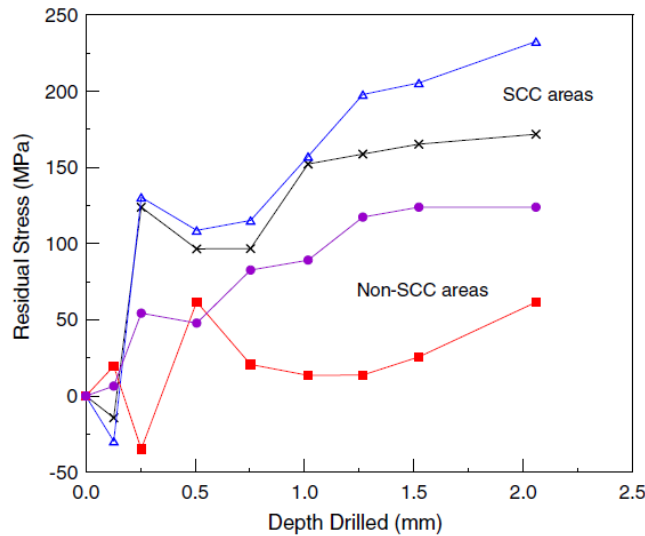
Figure 2-8 Residual stress distribution in depth direction determined using hole-drilling technique. Original data from [38]. Figure reproduced from [39], with permission from Elsevier.

Van Boven et al [40,41] also studied the effect of residual stress by artificially introducing residual stress into steel samples through three-point bending (cold working). The residual stress distribution in the thickness direction was measured using neutron diffraction technique. Cyclic loading were then applied to steel samples in an NNpH environment in order to initiate cracks. Although no sharp cracks were initiated, the study did find that high tensile residual stress at the near the surface (150 – 200 MPa) produced significantly more crack-like micro-pits. The author suggested that tensile residual stress regions were anodic to compressive stress regions, and galvanic couples formed on the pipe surface, resulting in preferential pitting in tensile regions.

Chen et al. [39] analyzed Van Boven et al.'s data further, and suggested compressive residual stress could be beneficial to the pipeline by slowing down crack growth. An interesting observation of SCC in the field is that an initially active crack may become dormant, often at a depth of less than 1 mm [39]. Chen suggested the reason for this is due to the residual stress distribution in the pipeline. Since the net residual stress in a body must be zero, a surface with

15

high tensile residual stress would decrease and become compressive going into the wall thickness. The compressive residual stress deeper in the pipe wall could reduce the mechanical driving force and cause dormancy. The validity of this claim still needs to be verified since it was based on samples with artificially created residual stress profiles that are were representative of the real residual stress distribution in a pipe. To artificially introduce residual stress, Van Boven et al. [40,41] started out with a chevron shaped steel sample, and flattened it using three-point bending. The samples were then milled on both the top and bottom to remove the peaks and valleys left over after the bending operation. The aggressive cold work during the three-point bending generated residual stress profile far more aggressive than those typically seen in a pipe. From Chen et al.'s calculation, for a linear crack to become dormant at 1 mm depth, assuming a surface residual stress of 150 MPa, it would require a residual stress gradient of -400 MPa/mm, which is a highly unrealistic result.

Based on the above arguments, a large negative residual stress gradient is not the cause of SCC dormancy. Previous research does agree however, that high tensile residual stress near the surface is more susceptible to SCC initiation. The cause may be due to the galvanic coupling effect between tensile residual regions and compressive residual regions, leading to preferential pitting in the tensile region. Residual stress may have a minor contribution in crack dormancy, but the main cause behind dormancy still need more research.

2.3.6 Soil

SCC has been found in wide range of soil conditions. There have been many attempts trying to correlate SCC severity with various soil parameters such as drainage, pH, dissolved gases, bacteria, temperature, chemistry, etc.[5,7,14,23,42–44] However this has been difficult because there doesn't seem to be a consistent indicator for SCC [23,43]. This is to be expected since SCC also depends on material susceptibility and amount of stress applied, therefore it is difficult to isolate individual environmental effects.

Despite these challenges, some general observations have been made on SCC-susceptible environments:

- SCC is associated with wet anaerobic environments [5,7,14,42,43]

16

- SCC typically found in the pH range of 5.5 to 7.5 [5,7,14]
- Dissolved carbon dioxide plays important role in maintaining the near-neutral pH environment [7,17]. CO_2 also plays important role in the initiation and growth of SCC, and will be discussed in more detail in later sections
- Since CP does not penetrate coating disbondment and reach the SCC, the undercoating environment is at open circuit potential (OCP) (around -760 to -790 mV(Cu/CuSO$_4$)) [5]
- Passivation does not occur in NNpH environment [17,45–47]

2.3.7 The Role of Carbon Dioxide

2.3.7.1 CO_2's Role in NNpH SCC

CO_2 is produced in the soil from microbial activities. Field studies have found that dissolved CO_2 concentration in groundwater adjacent to SCC locations ranged from 4% in winter to 23% in spring [7]. The increased CO_2 level has been associated increased corrosion rates, due to the increased production of carbonic acid.

Early attempts at generating NNpH SCC in a laboratory environment were met with little success. That was until Parkins discovered that the addition of carbon dioxide to the simulated soil solution could initiate transgranular cracks in slow strain rate tests (SSRT) [48].

In one of the first comprehensive experimental studies of NNpH SCC [17], Parkins made the following findings on the role of CO_2:

- Increased CO_2 levels reduced pH
- A steady supply of CO_2 is necessary to maintain near-neutral pH environment
- Increased CO_2 level decreased the ductility of pipeline steel at open circuit potential (OCP)
- The combined action of corrosion and reduction in ductility resulted in transgranular crack initiation and growth

A portion of dissolved CO_2 reacts with water to form carbonic acid, providing the corrosive agent. Parkins [17] theorized at the time that the reduction of hydrogen ions (from the carbonic

17

acid) in the anaerobic environment is generating atomic hydrogen which could diffuse into the metal and reduce ductility. It is widely accepted today that hydrogen plays important role in SCC.

2.3.7.2 CO₂ Reactions

In an anaerobic environment, the following reactions will take places due to dissolved CO_2 [49,50].

CO_2 gas dissolves in water:

$$CO_{2(g)} \leftrightarrow CO_{2(aq)} \tag{2.1}$$

Hydration of CO_2 to form carbonic acid:

$$CO_{2(aq)} + H_2O_{(l)} \leftrightarrow H_2CO_{3(aq)} \tag{2.2}$$
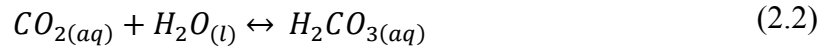
Carbonic acid is a weak diprotic acid that partially dissociates to produce bicarbonate and carbonate ions:

$$H_2CO_{3(aq)} \leftrightarrow H^+_{(aq)} + HCO_3^-_{(aq)} \tag{2.3}$$

$$HCO_3^-_{(aq)} \leftrightarrow H^+_{(aq)} + CO_3^-_{(aq)} \tag{2.4}$$

Oxidation of iron:

$$Fe_{(s)} \rightarrow Fe^{2+}_{(aq)} + 2e^- \tag{2.5}$$
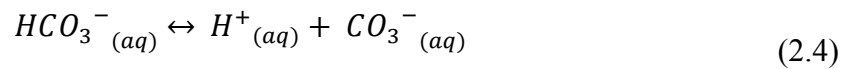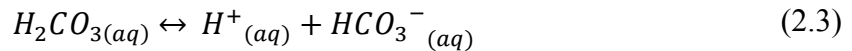
Reduction of hydrogen ions at the steel surface to form hydrogen gas (note: atomic hydrogen could be generated as well and diffuse into steel):

$$2H^+_{(aq)} + 2e^- \rightarrow H_{2(aq)} \tag{2.6}$$

Reduction of carbonic acid molecule:

$$2H_2CO_{3(aq)} + 2e^- \rightarrow H_{2(aq)} + 2HCO_3^-{}_{(aq)} \qquad (2.7)$$
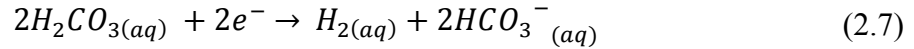
Reduction of bicarbonate ion:

$$2HCO_3^-{}_{(aq)} + 2e^- \rightarrow H_{2(aq)} + 2CO_3{}^{2-}{}_{(aq)} \qquad (2.8)$$
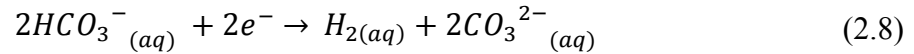
Under certain conditions, iron carbonate corrosion deposit can also form:

$$Fe^{2+}{}_{(aq)} + CO_3{}^{2-} \leftrightarrow FeCO_{3(s)} \qquad (2.9)$$
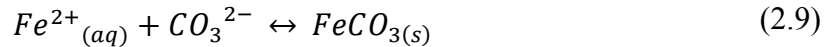
Figure 2-9 is a diagram showing the reactions (2.1) thru (2.9). Of the above cathodic reaction, Tran et al. found that the reduction of hydrogen ions is the dominant cathodic reaction [49]. Because the environment is anaerobic, all of the cathodic reactions produce hydrogen. Some of the hydrogen will stay in the atomic form and diffuse into the metal, causing hydrogen embrittlement, which will be discussed in later sections. CO_2 has two effects. First, it produces carbonic acid which can create pits from which SCC can initiate from. Second, the hydrogen produced during the cathodic reaction will accelerate crack growth through hydrogen embrittlement. Parkins has conducted studies in which the hydrogen entry into the steel is measured as the CO_2 level in the soil solution is increased. He found that the increased CO_2 level had also increased hydrogen entry into the steel [51]. This is direct evidence that CO_2 contributes to hydrogen diffusion in steel through the reduction reactions (2.6) to (2.8).
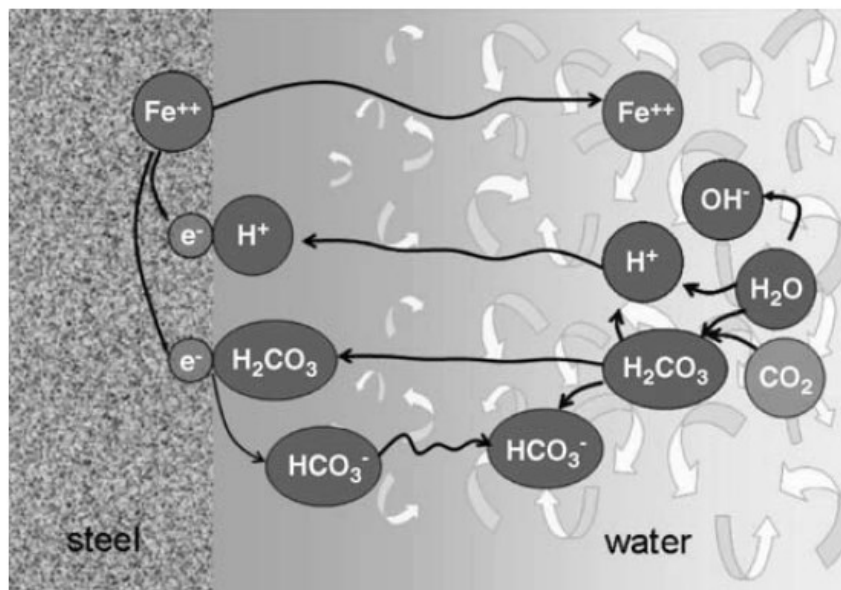
Figure 2-9 Schematic showing the possible reactions during CO_2 corrosion of mild steel in an anaerobic aqueous environment. Reproduced from [50], with permission.

One result of the consumption of hydrogen ions during the cathodic reaction is that the pH of a closed system of electrolyte will slowly increase in pH due to the increased concentration of carbonate and bicarbonate ions. As more and more CO_2 is being consumed, a closed system could move out of the NNpH susceptible region. Fang et al (2008) found that continuous CO_2 bubbling into a soil solution is necessary to keep the electrolyte in NNpH range. Once CO_2 purging was stopped, the solution slowly increased in pH, and moved out of the susceptible pH range [52].

Field pH measurements of undercoating electrolyte at SCC sites show that the pH stays within NNpH range (5.5 to 7.5) all year round [5,7,14]. These measurements imply that CO_2 level is maintained throughout the year to acidify the electrolyte regularly to keep it in the susceptible range. Field measurements of CO_2 level confirms this notion [7]. The electrolyte under a coating disbondment is not a closed system. Fluid exchange with the bulk soil could take place easily during spring and summer. Thawing soil and rain provides "fresh" water with high dissolved CO_2 content that could enter disbondments to replace the "stale" water. The warmer weather in spring/summer also promotes microbial activity which increases CO_2 production. During winter these exchange reduces significantly due to soil freezing and decreased bacterial activities. Therefore CO_2 is being consumed at a faster rate than it is being replenished during the winter.

pH should be expected to increase slightly over the winter. The seasonal cycle repeats year after year.

2.3.8 Stress

Major stresses in pipelines are illustrated in Figure 2-10. The biggest stress component is the circumferential stress (also called hoop stress), which results from the internal pressure of the pipe. This is the reason why most SCC's are aligned longitudinally on the pipe.

Buried pipelines are constrained along the axial direction; therefore longitudinal stresses can also result. Internal operating pressure can create longitudinal stresses one-third to one-half [5] of the circumferential stress. Other sources of longitudinal stress include soil settlement and thermal expansion. High levels of longitudinal stress could lead to circumferential SCC, however the occurrence of circumferential SCC is far rarer than longitudinal SCC due to the longitudinal stress being significantly smaller than the circumferential stress for most pipeline segments [5,14].
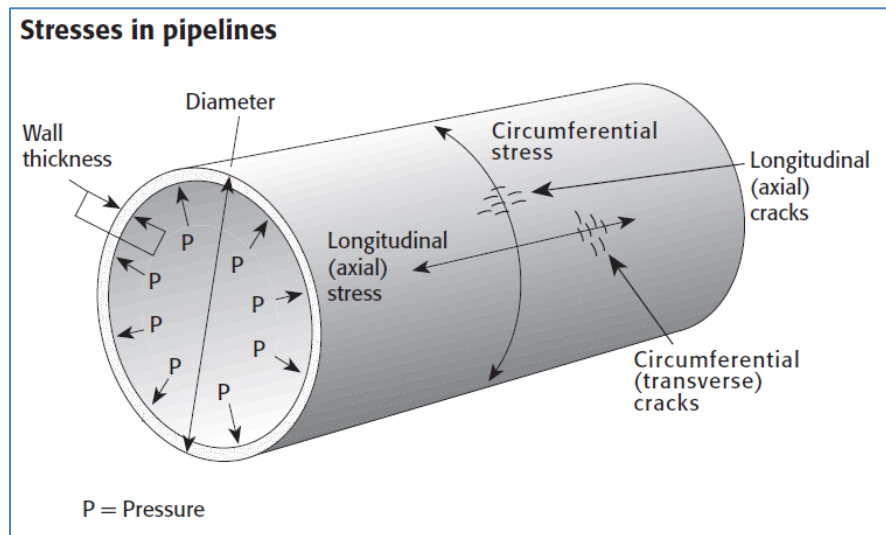
Figure 2-10 Stresses in a pipeline. Reproduced from [5], with the permission of Public Works and Government Services, 2018.

The max allowable stress, and consequently the max allowable operating pressure (MAOP), of a pipeline are determined by its class location, as shown in Table 2-3. A higher class location means a more densely populated location. Most SCC occur in class 1 locations, where the max allowable hoop stress is 80% SMYS.

Table 2-3 Class location and corresponding max hoop stress [53]

Class Location	Max allowable hoop stress (% SMYS)
Class 1	80%
Class 2	72%
Class 3	56%
Class 4	44%

Significant SCC is rarely found on class 2 pipes and above [5,14]. This could be due to the lower max stress experienced by class 2 pipes, which significantly reduces the max stress intensity factor (K_{max}) of any cracks on the pipes. Based on this observation, some in the industry asserted there could be a threshold K_{max} or stress, under which, SCC would not propagate [5]. There is some evidence to support this claim. Field data of NNpH SCC have found that majority of SCC occur within 20 to 30 km downstream of a compressor/pump station, where the pressures are higher [5–7,14,19,54].

As shown in Figure 2-11, sections close to the pump station have higher max stress, which resulted in the increased occurrence of SCC. At the wall thickness transition from 7.14 mm to 5.16 mm at the absolute distance of 87.5 km, the heavy wall section did not have any SCC, even though it had the same stress levels as the thinner walled pipe just downstream of it. This piece of information suggests that there exists a threshold max stress intensity factor K_{max}, rather than a threshold max stress σ_{max}. A simple stress intensity factor calculation for a surface crack would show that cracks of identical initial size would experience a higher K in a thinner pipe even if it has the same stress as a thicker pipe. This is an important reminder to use the fracture mechanics concept of similitude (i.e. comparing stress intensity factor K) rather than comparing stresses.
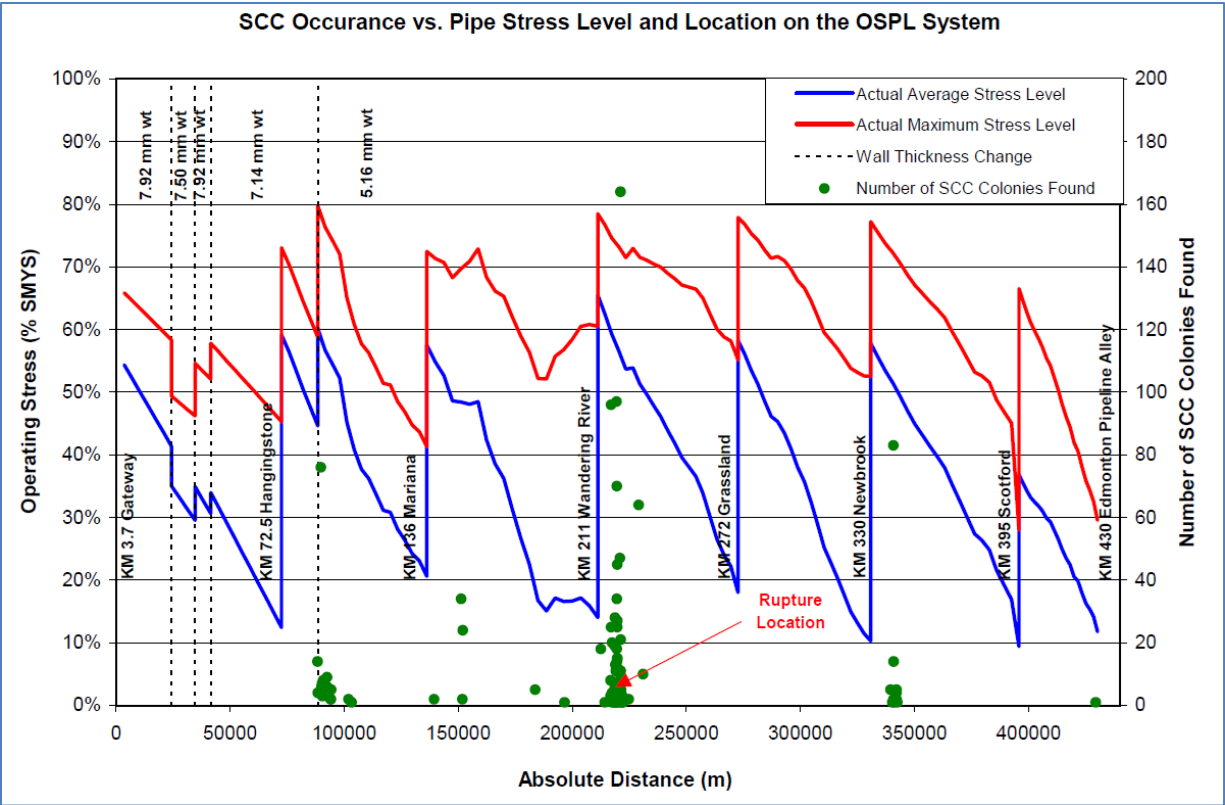
Figure 2-11 SCC occurrence and operating stress on a 426 km segment of Suncor Energy's pipeline. Reproduced from [54], with permission from ASME.

Even though there seems to be evidence to support the existence of a threshold K_{max} from the above explanations, no conclusive proof has been found. An often overlooked observation is SCC's have also been found in class 2 and 3 locations [45,46]. This is contradictory to the claim of the existence of threshold K mentioned above. The reality is SCC can initiate at stresses well below 60% SMYS. From an operations perspective, it is unfeasible to operate every pipeline at stresses that low. What's more, there is no guarantee that the low stress could prevent SCC initiation. Higher stress does increase the probability of crack initiation, but when analyzing actual field data, one has to keep in mind that class 2 pipes and above account for only a very small portion of total pipeline length, therefore it is not of a sufficiently large sample population size to draw conclusions from.

The data shown in Figure 2-11 also does not paint a complete picture of the SCC severity on that specific pipeline. The lack of data points in certain areas can be misleading. Suncor first performed ILI inspection on this line using ultrasonic (UT) tools to find possible locations with cracks. However, the crack tool had a threshold detection limit of 12.5% WT, i.e. any cracks less

than 12.5% is considered noise. This has major implications because there could be many cracks throughout the system, even on the heavy wall sections, with depth less than 12.5%. The crack length and depth reading from ILI is at best an estimate, actual crack dimension could still deviate significantly. At the end of ILI inspection, a total of 773 features were reported. It was not feasible to verify all of the ILI features. Therefore only 444 features out of the 773 were excavated and inspected. The green points plotted on Figure 2-11 is based on the field measurements of excavated defects only, it is not a plot of all SCC found on that line. Despite these limitations, the plot accurately pinpoints the locations on the pipeline with the worst SCC problems. The areas without green points should not be assumed to be free of SCC, but instead should be assumed to have cracks that were too shallow to be detected by ILI tool, or have cracks that were considered not to be an integrity threat in the near future.

2.4 Near-Neutral pH SCC – Corrosion Fatigue and Hydrogen Embrittlement Behaviour

2.4.1 Monotonic Loading

A key question for NNpH SCC is: does monotonic loading cause crack propagation? High pH SCC is known to propagate under monotonic loading, because the crack propagation is controlled by anodic dissolution process.

SCC initiation has been widely studied with monotonic loading using slow strain rate testing (SSRT). SSRT was able to initiate cracks [17,55–65]. However, the experimental conditions in those SSRT were extremely aggressive and not representative of real pipeline operating conditions. In many SSRT studies, the stress applied was near or over the SMYS of the material, while in the field the max stress allowed is only 80% SMYS. Also SSRTs could not simulate the variable amplitude pressure fluctuations experienced in the field which can affect the growth rates in many different ways. One of the reasons cracks on different pipelines grow at different rates is due to the different pressure fluctuation spectra experienced. SSRT typically produced growth rates well above those found in the field [8]. This has led some authors to wrongly conclude that hydrogen embrittlement (which is heavily influenced by stress) and dissolution play equally important roles in the initiation of SCC.

The value of SSRT could not be totally dismissed, however. SSRT was used to prove that hydrogen plays an important role in NNpH SCC. In the classic paper by Parkins in 1994 [17], the ductility of pipeline steels in soil solutions of different pH and at various potentials were measured through SSRT. Parkins found there is a local minimum in ductility of pipeline steel around the open circuit potential in NNpH environment. The decrease in ductility around OCP was caused by hydrogen embrittlement (HE). The source of atomic hydrogen in the steel comes from to the reduction of hydrogen ions in the electrolyte at the steel surface, which was discussed in section 2.3.7. Atomic hydrogen adsorbed at the surface could diffuse and segregate to areas with stress concentration, leading to HE and reduced ductility [9,31,66–68]. As the potential is made more negative, the ductility starts to improve, demonstrating a peak where CP protection is effective in reducing the HE effects. With a further decrease in potential, the ductility drops sharply due to hydrogen induced cracking (HIC) caused by excessive CP.

Parkins also noted for samples with low ductility, the fracture surface demonstrated transgranular quasi-cleavage fracture surface. SCC found in the field also demonstrates quasi-cleavage [17,19]. This meant that SCC was strongly influenced by hydrogen embrittlement in order to produce the quasi-cleavage features.

What about monotonic loading's effect on a well-developed crack? Could monotonic loading on well-developed cracks cause them to propagate? Experimental results all agree that monotonic loading does not cause crack growth in near-neutral pH environment [17,31,36–38,41,45,58,60,69–75]. A good example is demonstrated in Figure 2-12. In the figure, it is evident when the load was held constant at max stress ($\Delta K = 0$), the crack showed no growth. It is only when cyclic loading was resumed that the crack was able to grow.
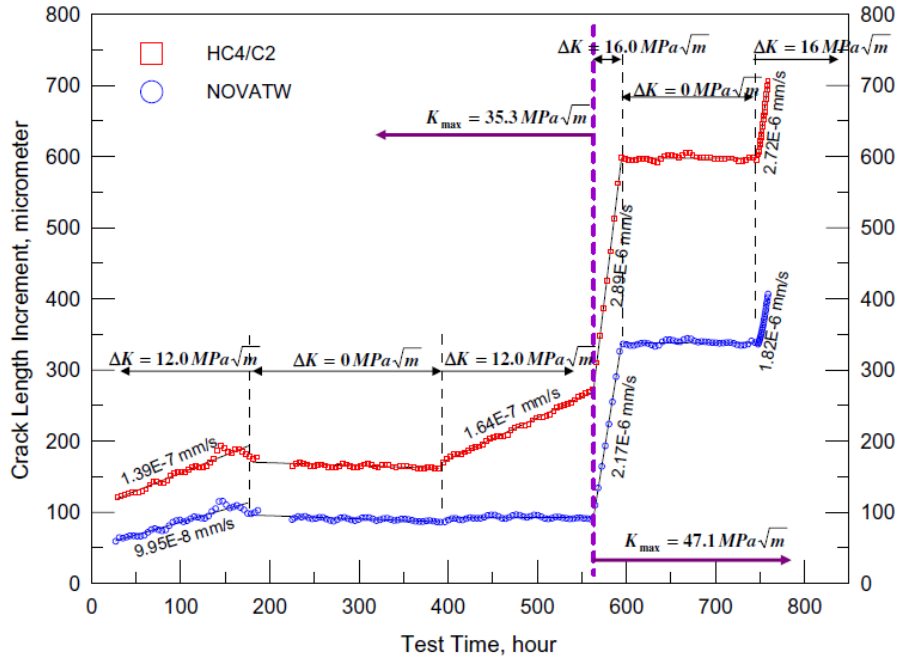
Figure 2-12 Crack growth continuously tracked by potential drop systems during different tests in two different soil solutions. Reproduced from [31], with permission from Elsevier

2.4.2 Cyclic Loading

As discussed in section 2.4.1, NNpH SCC studies should be conducted using cyclic loading instead of monotonic loading because monotonic loading cannot cause cracks to propagate. Monotonic loading does not replicate in-service operating conditions of pipelines either since pipelines undergo pressure fluctuations regularly.

Beavers et al. [76–79] have shown that large underloads (unloading and reloading) cycles stimulated crack growth, and growth only occurred on the loading part of the cycle. Their work also showed that ΔK has more effect on crack growth than K_{max}. Studies by Been et al. [80] and Chen et al. [81] have also shown that ΔK has a much bigger influence on crack propagation than K_{max}. The aforementioned studies found that small amplitude cycles (R ratio typically > 0.8) at high K_{max} often had trouble propagating cracks. Beavers et al [76–79] found crack growth rate decelerated with continued application of high R ratio & high K_{max} cycles, approaching dormancy-like behaviour. The studies by Been et al. and Chen et al. found that intermediate K_{max} values with low R ratios could propagate cracks.

These findings show that fatigue is a big contributor to SCC propagation. Larger amplitude load cycles result in faster growth. Steels also exhibit fatigue limits in which small amplitude loading could not cause further damage. Since the fatigue is also enhanced by the interaction of the metal with an aqueous environment, corrosion fatigue should be the main mechanism behind SCC propagation.

2.4.3 Corrosion Fatigue Mechanisms

Corrosion fatigue is defined as "the acceleration of fatigue crack growth due to interaction with the environment" [12]. Section 2.4.1 discussed in detail why monotonic loading should not be used for NNpH SCC experiments. Section 2.4.2 discussed how fatigue plays a major role in crack propagation. It is natural to discuss corrosion fatigue next since NNpH SCC is essentially accelerated fatigue growth in an NNpH environment.

Recent studies from multiple authors have shown that corrosion fatigue is the mechanism behind the late-stage growth of SCC [77,80–84]. It was observed that the frequency and amplitude of the loading were important in determining crack growth rate. Figure 2-13 compares the results of corrosion fatigue tests conducted in NNpH environment to the results of fatigue tests done in air. It is clear that the crack growth rate is enhanced in the NNpH environment, and could be several orders of magnitude higher than in air. This explains why some SCC cracks have grown so quickly to failure in the field even though the pipeline has only experienced a relatively small number of underload cycles in its lifetime.
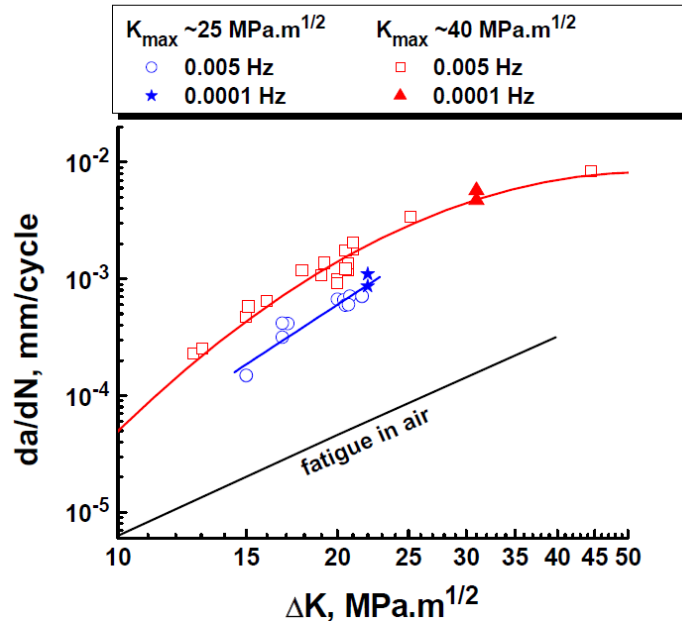
Figure 2-13 Comparison of fatigue tests conducted in NNpH environment (red and blue lines) and fatigue test conducted in air. Reproduced from [80], with permission from ASME.

(a)	(b)	(c)
Time-dependent CF	Cycle-dependent CF	Cyle-time-dependent CF
	(True CF)	(general CF)
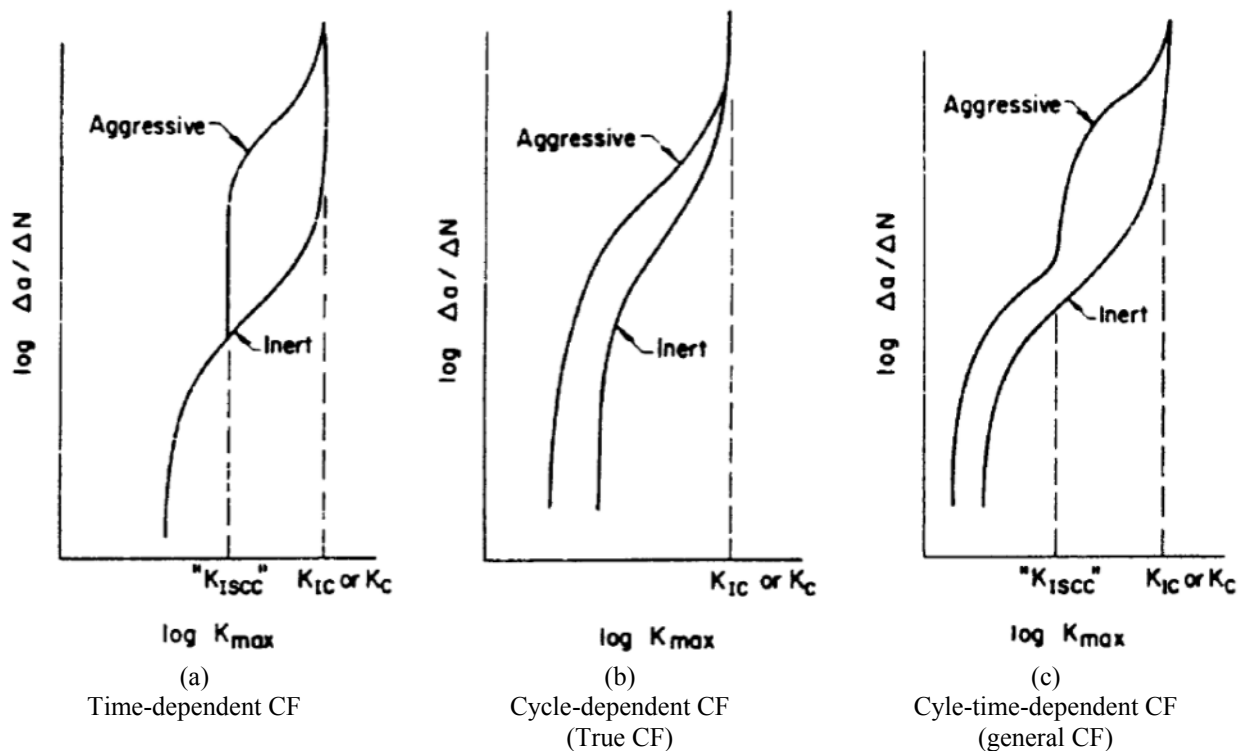
Figure 2-14 Three forms of corrosion fatigue (CF) defined by Gangloff [85]. Reproduced from [85], courtesy of NASA.

There are three types of corrosion fatigue illustrated in Figure 2-14. A brief description of each type of corrosion fatigue is listed below. A more detailed description can be found in [12,85].

1)   <u>Time-dependent corrosion fatigue:</u>

$$\left(\frac{da}{dN}\right)_{total} = \left(\frac{da}{dN}\right)_{inert} + \frac{1}{f}\left(\frac{da}{dt}\right)_{SCC} \tag{2.10}$$

Time-dependent CF is a superposition of inert fatigue crack growth and environmental cracking under static load. The second term encompasses growth due to classical SCC mechanism. f is frequency.

2)   <u>Cycle-dependent corrosion fatigue (true corrosion fatigue)</u>

$$\left(\frac{da}{dN}\right)_{total} = \Phi \left(\frac{da}{dN}\right)_{inert} \tag{2.11}$$

The crack growth in the environment is enhanced for the entire range of SIF. Φ is an acceleration factor, which can be a function of driving force parameters such as K_{max} or ΔK. The entire *(da/dN)$_{total}$* term could also be just a simple Paris law equation with more aggressive Paris law constants. There is very little growth under static loading, so the time-dependent SCC term is not needed.

3)   <u>Cycle-time-dependent corrosion fatigue (general corrosion fatigue)</u>

$$\left(\frac{da}{dN}\right)_{total} = \Phi \left(\frac{da}{dN}\right)_{inert} + \frac{1}{f}\left(\frac{da}{dt}\right)_{SCC} \tag{2.12}$$

The contribution of inert fatigue, growth under static loading, and enhanced growth due to acceleration are all considered. This is the most general form of CF equation.

Given the above description, **NNpH SCC should be classified as cycle-dependent or true corrosion fatigue**. The reasons are:

- In section 2.4.1 it was shown that monotonic loading had no effect on growth, therefore the time-dependent portion of the CF equation can be discarded.
- The crack growth in the aggressive environment is accelerated compared to that of the inert environment as shown in Figure 2-13.

The complexity of SCC growth models increases significantly if a true corrosion fatigue mechanism is used. Real world load spectra vary from cycle to cycle, and many variables need to be considered, such as R ratio, K_{max}, frequency, and the sequence of different cycles. The soil environment also varies from site to site, with different chemistry and pH that could affect growth rates. Pipe materials also demonstrate a range of fatigue resistance. Researchers face many challenges with all these variables to consider. Therefore they try to replicate the field conditions as closely as possible in order to reduce the number of variables that can be studied at one time.

2.4.4 Corrosion Fatigue Models

2.4.4.1 Paris Law

The Paris law is the simplest empirical equation used to model fatigue crack growth. It is expressed as:

$$\frac{da}{dN} = C\,(\Delta K)^m \tag{2.13}$$
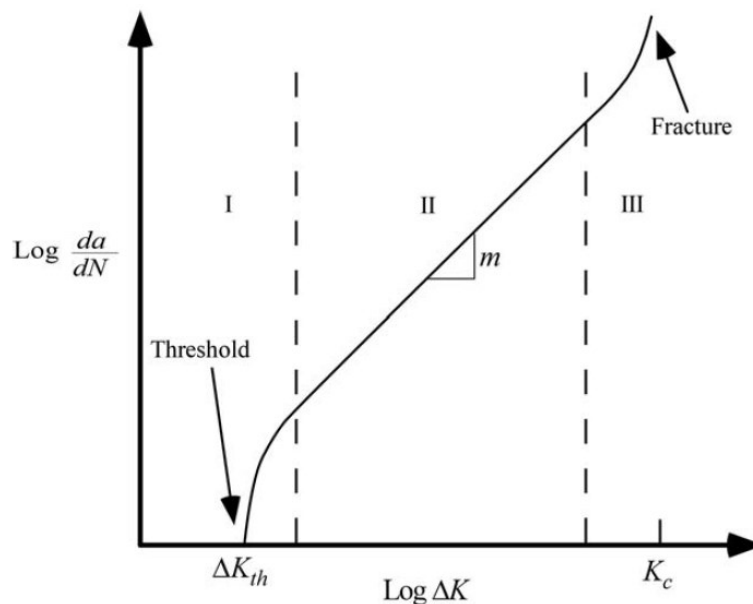
Figure 2-15 Typical fatigue crack growth behaviour in metals, modelled using Paris law. Reproduced from [86], with permission from Taylor and Francis Group, LLC, a division of Informa plc.

da/dN is the fatigue crack growth rate. ΔK is the SIF range, and can also be expressed as $\Delta K = (1 - R)K_{max}$. C and m are materials constants that are determined experimentally. Equation (2.13) is only applicable to region II in Figure 2-15.

The biggest drawback of Paris law is it's very limited in scope. Different R ratios, K_{max}, frequency, or environment, would all produce unique trends with many different C and m values. This makes it difficult to compare fatigue results since C and m are supposed to be material constants. Figure 2-13 shows an example of the Paris Law not being able to take into account different K_{max} values used even though ΔK is the same. An ideal model would have the red and blue lines overlapping each other.

Paris law can be used effectively if the user is aware of its limitations, and can be a great method to compare relative corrosion fatigue resistance in different solutions or for different materials. For actual crack growth rate modelling, a more sophisticated model should be used.

2.4.4.2 Crack tip strain rate model

The crack tip strain rate model was originally used for modelling classical SCC with a film rupture mechanism and has been successfully applied to systems under monotonic loading. It has also been used to model early crack growth behaviour [80]. Shoji et al. developed a crack tip strain rate equation for cyclic loading [87]. However, it's complex and requires many inputs on the mechanical and microstructural property of the material. Scott & Truswell developed a simpler model that could give similar results as Shoji et al.'s equation [88]. Beavers et al. have also developed a simple crack tip strain rate model specifically for NNpH environments [89]. Specific details on each crack tip strain rate model can be found within their respective sources.

Correlation between crack tip strain rate and crack growth under cyclic loading has generally been poor [81], with scatter up to several orders of magnitude [89]. Therefore the crack tip strain rate model is not widely adopted in the industry. The poor correlation is to be expected since monotonic loading could not cause SCC propagation (see section 2.4.1), and cyclic loading driving factors have been shown to be the driving force behind SCC propagation (see section 2.4.2 and 2.4.3).

2.4.4.3 Superposition Model

The superposition model uses the time-dependent corrosion fatigue model, equation (2.10). This model assumes NNpH SCC is a combination of inert of fatigue and classical SCC mechanism. Equation (2.10) can thus be written as:

$$\left(\frac{da}{dN}\right)_{total} = C\,(\Delta K)^m + \frac{1}{f}\left(\frac{da}{dt}\right)_{SCC} \tag{2.14}$$

The superposition model has been used in various studies to model NNpH SCC [77,84,90–92]. In some studies, it is able to provide a good fit to experimental data, but the cyclic loading had very low frequencies and amplitude. From a strictly empirical perspective, the superposition model may numerically fit the data, but the mechanism behind the model is wrong for NNpH SCC, since NNpH SCC does not have a monotonic load component. In cases where the superposition model has worked well, it is due to the *1/f* term making up for the unforeseen contribution of other driving force parameters. Unrealistic values for *da/dt* have often been assumed.

2.4.4.4 Combined Factor Model

A major challenge associated with Paris Law is ΔK could not be consistently used as a driving force parameter when R ratios or frequency changes. This is demonstrated in Figure 2-16 a), where different frequencies and R ratios were applied to constant amplitude cyclic loading on X-65 pipeline steel in an NNpH soil solution. Each set of frequency and R ratio would have its own unique Paris law constants (*C* and *m*), but these constants are supposed to be material constants that are independent of loading conditions.

Many different empirical fatigue crack growth equations have been proposed to overcome this shortcoming [86], but most equations only had limited success in normalizing the fatigue growth trends. The goal is to normalize all the data points on a fatigue growth plot so that points from different test conditions can be consolidated into a single scatter band and could be fitted with a single curve (e.g. Figure 2-16 (b)). The driving force parameter (independent variable) should take into account different R ratios and frequency so that normalization can be achieved.

Chen & Sutherby (2007) introduced a new driving force parameter to normalize fatigue crack growth data [81], called the combined factor: $\Delta K^2 K_{max}/f^{0.1}$. A frequency term is included in the combined factor [31,81] to account for the loading frequency effect on corrosion fatigue. Chen used the combined factor to normalize constant-amplitude corrosion fatigue growth data in NNpH environments (See Figure 2-16) and produced good correlation. Chen also found there is a combined factor threshold, similar to the fatigue threshold ΔK_{th} for Paris law. The combined factor threshold appeared to be environmentally sensitive, and had different values in different soil solutions. In C2 solution, which is a commonly used soil solution, the combined factor threshold was determined to be around 8500 $(MPa\sqrt{m})^3/Hz^{0.1}$. Chen also created a map of crack growth behaviour, shown in Figure 2-17, showing the regions of active growth and dormancy based on the threshold value of 8500 $(MPa\sqrt{m})^3/Hz^{0.1}$. The demarcation line shown in the figure also considers the effects of K_{max}, ΔK, and frequency on threshold.

(a) (b)
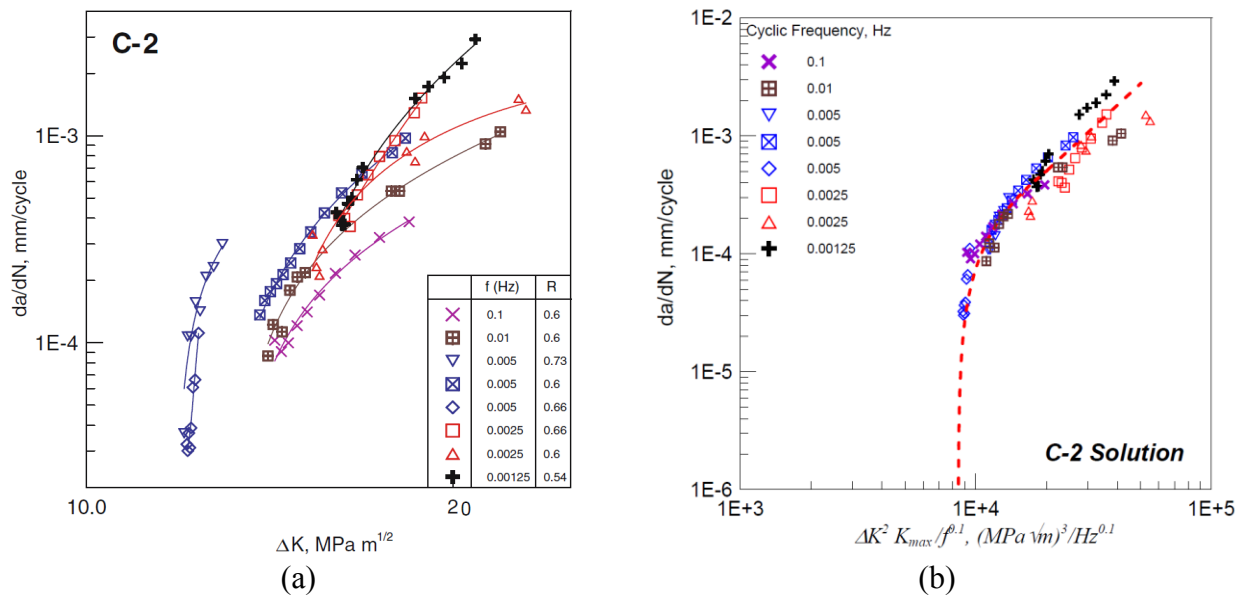
Figure 2-16 Crack growth rate da/dN in C2 solution as a function of (a) ΔK and (b) $\Delta K^2 K_{max}/f^{0.1}$. Reproduced from [81], with permission from Springer.
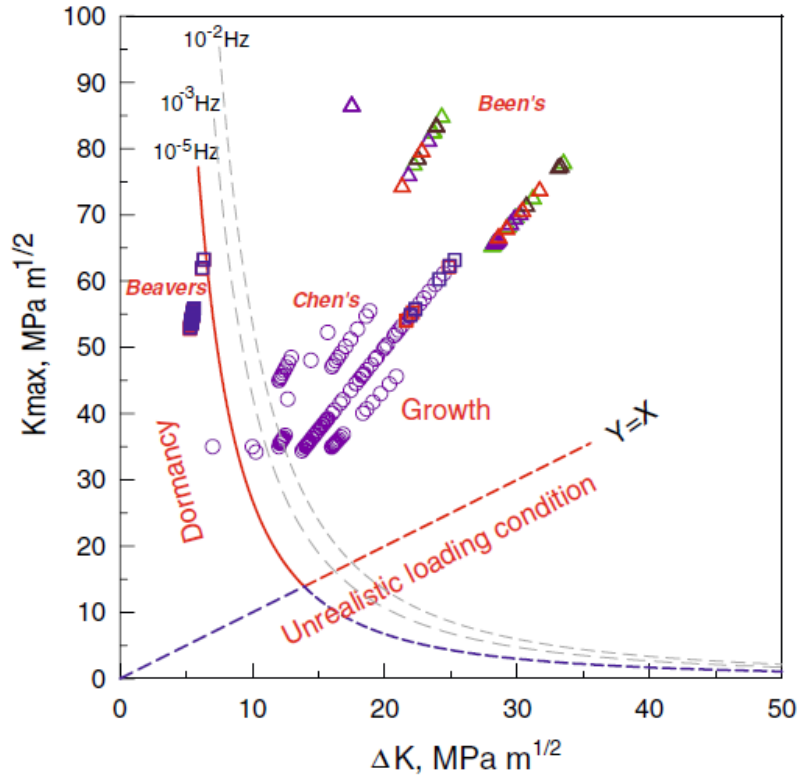
Fig. 11—Map of crack growth behaviors as affected by ΔK, K_{max}, and f.

Figure 2-17 Map of crack growth behaviour as affected by *Kmax*, *ΔK*, and frequency. Reproduced from [81], with permission from Springer.

The combined factor model was later revised to take on the form [8,9] seen below.

$$\frac{da}{dN} = A \left[\frac{\Delta K^\alpha K_{\text{max}}{}^\beta}{f^\gamma} \right]^n + h \tag{2.15}$$

- *A* and *n* are constants analogous to *C* and *m* in Paris law
- α is a material constant (=0.67 for pipeline steel), and $\beta = 1 - \alpha = 0.33$
- $\gamma = 0.033$, and is related to the influence of corrosion environment. In C2 solution, the value is 0.033, in other solutions the value may differ.
- *h* is the crack growth rate due to dissolution. The value of *h* can be determined experimentally, however, it is very low compared to the growth rate due to corrosion fatigue mechanism [31,47,81], and is usually an order of magnitude lower [9,10,93,94] than field growth rates. For simplification, the *h* term may be neglected.

The constant A in equation (2.15) also has a physical significance as it is related to the hydrogen diffusion in the material as seen in the equation below [8]:

$$A = \left[\frac{4 \sqrt{2.476}(1 + v)\Omega}{3\pi \, k_B T \sqrt{2\pi} \, \ln(1/c_o)} \right]^{1.11n} \tag{2.16}$$

Where k_B is the Boltzmann constant, T is the temperature, v is the Poisson's ratio, c_o is the atomic ratio of hydrogen to iron away from the crack tip, Ω is the partial volume of a hydrogen atom, and *n* is the same *n* found in equation (2.15).

2.4.5 Variable Amplitude Loading

The corrosion fatigue models described so far are all for constant amplitude (CA) loading. In actual pipeline operations, variable amplitude loading (VAL) is observed due to pressure fluctuations. VAL is a complex subject matter and has been studied in other industries such as in aerospace. The most difficult aspects of VAL to model are the load interaction & sequence effects. Given a fixed set of VAL cycles, different fatigue life will result just by changing the sequence of cycles. The growth rate of a cycle depends on the prior history of cycles that have occurred before it. How a series of VAL cycles are arranged is called a spectrum, and each cycle in a spectrum cannot be treated a single independent unit, their interaction effects must be considered.

The simplest way and most widely used way to predict fatigue life for VAL is to use the linear cumulative damage model (aka Palmgren-Miner Rule), where a spectrum is divided up into individual cycles (using methods such as the rainflow counting method), and the crack growth of each cycle is considered independently and added together linearly at the end. The crack growth rates were obtained from simple constant amplitude tests. This model has been used for cracks in pipelines [90,95] with questionable accuracy since it ignores all load interaction and sequence effects.

Corrosion fatigue issues on pipelines are unique in that the cyclic frequencies are much slower than those seen in other industries (in the range of 10^{-1} to 10^{-6} Hz), therefore conducting multiple

experiments to capture the effects of all the variables in a VAL spectrum would be expensive and impractical. For these reasons, constant amplitude tests have been widely used for SCC research.
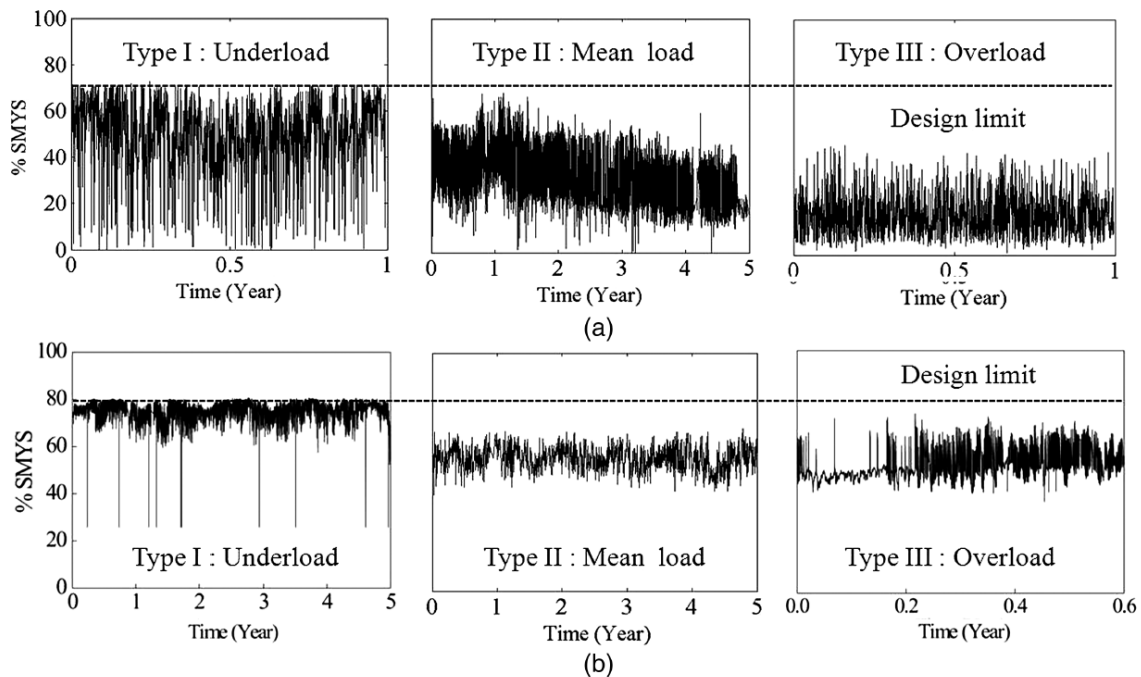
Figure 2-18 Classification of pressure fluctuation spectra: (a) oil pipeline spectra; (b) gas pipeline spectra. Reproduced from [11], with permission from ASCE.

The types of VAL spectra found on a pipeline are illustrated in Figure 2-18. Oil pipelines undergo more cyclic loading events than gas pipelines due to the incompressibility of a liquid. Gas pipelines have fewer aggressive cyclic events, and the pressure is relatively constant. From a pure inert fatigue perspective, oil pipelines would have a shorter crack life due to the high number of aggressive cycles, and gas pipelines spectra in comparison would be much milder. Most gas pipeline operators do not view pressure fluctuations to be a significant threat due to the low number of underload cycles encountered during the lifetime of service. Estimates of fatigue life based on typical gas pipeline spectra have concluded that the fatigue life would be well beyond the service life of most gas pipelines [95,96]. Actual experience with SCC failures contradict these findings, because gas pipelines can fail in 20-30 years [4,5] due to SCC, and oil pipelines also have the same SCC lifetime. This suggests that the load interaction and sequencing in a gas spectrum must have a synergistic effect to accelerate crack growth rate above crack growth rate predicted through linear summation. Therefore more studies should be done using VAL loading.

The types of pipeline spectrum in Figure 2-18 is categorized as [11]:

Type I: Underload Spectra

- Found within 30 km downstream of a compressor/pump station, where most SCC have been found.
- The maximum pressure is near or at the MAOP design limit
- Pressure can only fluctuate below the design limit
- Small fluctuations with high R-ratios are classified as minor cycles
- Large fluctuations with low R ratios are classified with underload cycles
- The underload cycles cause most of the crack propagation. The minor cycles by themselves are insufficient to propagate the crack [76–79]
- The minor cycles preceding an underload cycle can enhance the propagation that occur during the underload [9,10,94]
- This thesis is focused how the sequencing of minor cycles and underload cycles in an underload spectrum can affect crack growth rate

Type II: Mean-Load Spectrum

- Found further down the pipeline
- Mean pressure is lower than Type I spectrum. Pressure rarely reaches MAOP
- Pressures fluctuate both up and down about a mean stress
- Underload cycles can still occur, though with less severity than in Type I

Type III: Overload Spectrum

- Found near the suction side of a compressor/pump station
- The base level pressure in the pipe is low
- Frequent pressure spikes occur in the spectrum, called overload cycles
- Underload occurrence is rare
- lease susceptible region to SCC
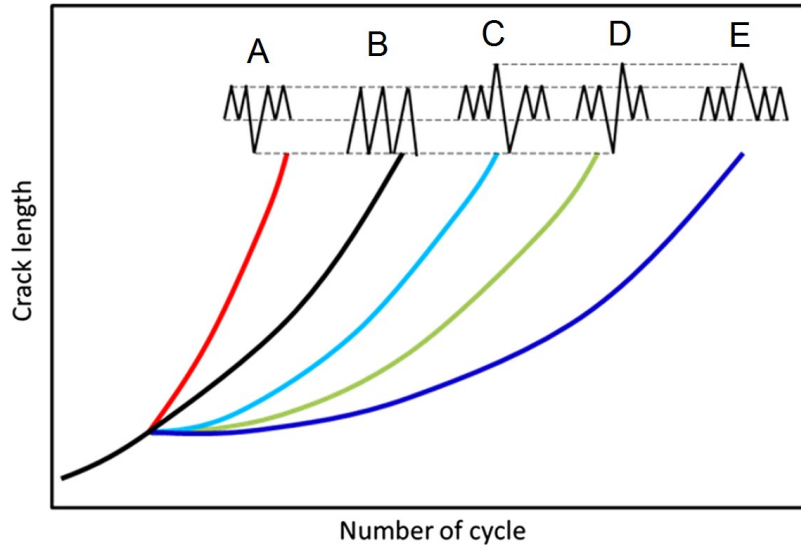
Figure 2-19 Ranking simple VAL spectra according to their crack propagation rate. Reproduced from [11], with permission from ASCE.

Figure 2-19 compares the relative severity of different types of spectra for corrosion fatigue. Spectrum A is an underload spectrum containing minor cycles and underload cycles, representative of the Type I spectrum in Figure 2-18. Spectrum B is a constant amplitude spectrum containing only underload cycles. It is interesting to note that spectrum A is more damaging than spectrum B for corrosion fatigue. In inert fatigue, spectrum B would be more damaging than A. The interaction between the minor cycles and underload cycle in A accelerates the crack growth rate during corrosion fatigue. Spectrum C and D are typical mean load spectra. Spectrum E is an overload spectrum, which has the slowest crack growth rate due to the retardation effect following an overload cycle.

The overload retardation effect is well studied. An overload cycle creates a large plastic zone ahead of the crack tip, and subsequent cycles will be retarded by the large existing plastic zone. The crack growth rate will continue to be suppressed until the crack is able to propagate past the plastic zone established by the previous overload cycle. Overload retardation is often observed in pipelines after a hydrotest. A hydrotest increases the pressure of a pipeline to 110% SMYS [53] for a period of time in order to remove near critical flaws. Since the pressure during hydrotest is above the MAOP of the pipeline, it acts as a prolonged overload cycle. Multiple studies have shown that hydrotest can retard subsequent crack growth in pipeline steel [76,97,98].

2.4.6 Underload Spectra

As mentioned in the previous section, SCC occurrence is strongly correlated with underload spectra just downstream of compressor/pump stations. Underload spectra have been studied for other materials and applications as well [99,100], and most studies show that underload spectra are more detrimental to structures than other types of loading due to the accelerated crack growth rate.

The acceleration factor (γ) has been used by many researchers to quantify the relative enhancement in crack growth rate under a certain spectrum due to load interaction effects. The formula for acceleration factor is given below.

$$\gamma = \frac{\text{measured growth rate per block}}{\substack{\text{predicted growth rate per block by a} \\ \text{linear summation of the constant} \\ \text{amplitude crack growth response}}} \tag{2.17}$$

A "block" is composed of a sequence of variable amplitude cycles that is repeated throughout a spectrum. Cycles make up a block. Blocks make up a spectrum. The acceleration factor is able to capture the interaction effects without having to understand the full mechanism behind the acceleration. The denominator in eqn (2.17) is the predicted growth rate of a block calculated from the linear summation of the constant amplitude crack growth response of all the cycles within the block. The denominator does not consider interaction effects.

Underload spectrum for pipeline steel in NNpH environment was first studied by Williams et al. [101] In that study, Williams et al. composed a spectrum using minor cycles (MC) with R ratio of 0.5 and underload cycles (UL) with R ratio of 0. The ratio of UL to MC was ranged from 1 in 40 to 1 in 160. K_{max} was in the range 20.6 to 31.4 MPa$\sqrt{m}$, however, the tests were conducted at 110% SMYS to achieve those SIF values. The results of that study showed that the spectrum used had accelerated growth when compared to the constant amplitude data. Unfortunately, the loading conditions used in the study were not realistic. MC with R ratio of 0.5 is highly aggressive when compared to actual pipeline spectrum. In the field, pipelines experience underload spectrum with minor cycle R ratio of as high as 0.9, and R ratio of 0.5 is considered an underload cycle. So the spectrum that Williams studied is actually composed of intermediate

underload cycles and aggressive underload cycles. Also, the high stress used during the experiment (110% SMYS) is significantly above the 80% SMYS design limit.

Yu et al. have conducted studies on corrosion fatigue in NNpH environments using realistic underload spectra [9,10,93,94]. Yu et al. used X60 compact tension (CT) specimens machined from a cut-out section of pipe that had experienced SCC in the field. The samples were submerged in an NNpH environment purged with 5% CO_2/95% N_2 gas mixture (pH = 6.3). Tensile testers were used to apply underload spectra and crack growths were measured after each test. The effects of the number of minor cycles [10], frequency [9], and R ratio [94] were all studied, and the findings are summarized below:

2.4.6.1 Effect of Number of Minor Cycles

The effect of the number of minor cycles in an underload spectrum was studied by Yu et al. [10]. The waveform used is illustrated in Figure 2-20, and it accurately simulated actual field pressure fluctuations. The waveform consisted of repeating blocks. Each block consisted of 'n' number of minor cycles with R ratio of 0.9 (R_{MC} = 0.9), followed by an underload cycle with R ratio of 0.5 (R_{UL} = 0.5). The starting K_{max} applied was 33 MPa√m, which is a realistic value that can be achieved by an in-service crack. The frequencies used also accurately reflected in-service frequencies: the frequency of the underload cycle (f_{UL}) is 0.00104 Hz, and the frequency of minor cycles (f_{MC}) is 0.0054 Hz.
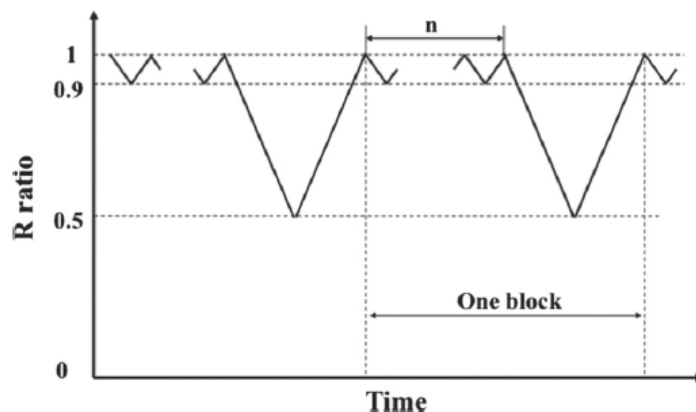
Figure 2-20 Schematic of test waveform used by Yu et al. in [10]. Reproduced from [10], with permission.

In this study, the numbers of minor cycles 'n' in between two underload cycles ranged from 0 to 1000, and the resultant crack growth rates and acceleration factors were compared. The crack

40

growth rate was given per block, so the load interaction effects can be captured. A block is defined in Figure 2-20, consisting of 'n' number of minor cycles and one underload cycle.

The effect of 'n' on crack growth rate and acceleration factor is shown in Figure 2-21. In (a), the environmental contribution of the NNpH environment (C2 solution) to corrosion fatigue is clearly demonstrated, with the crack growth rates in C2 solution being higher than the growth rate in air for the same underload spectrum. In (b), the acceleration factor was greater than 1 for all values of n, but for C2 the acceleration factor started below 1, and quickly increases with larger values of n. The acceleration factor behaviour for air agrees with previous literature, but the behaviour observed in C2 demonstrates some peculiarities. For the data points at n =1 and n = 10, the acceleration factor in C2 is around 0.8, and increases over 1 when n is around 35. It is surprising that for low values of n, the underload spectrum has decelerated block growth in C2 compared to constant amplitude loading. The reason behind this behaviour is not well understood and should be an area of further research. For n > 100 in C2, the acceleration factor increases significantly, and is close to a 500% increase for n = 1000.

For the acceleration factor calculations, Yu et al. assumed that the minor cycles in a block made no contributions in the linear summation portion (the denominator in equation (2.15)). This is a valid assumption since the crack growth due to constant amplitude minor cycles is well below the threshold determined in [81]. However, in a VAL underload spectrum (MC&UL), the minor cycles can interact with the underload cycles to contribute significantly to crack growth. This is demonstrated in Figure 2-22, where the crack growth rate for a single minor cycles in a MC&UL block shows a sharp rise from n = 15 to n = 55, and then gradually decreases from n = 55 to 960. Figure 2-23 shows an interesting comparison of growth rates for one block of MC&UL with 697 MC, one UL cycle in a CA waveform, and one UL & hold block with the hold duration equivalent to 697 MCs' duration. Some may argue that hydrogen segregation is important for crack propagation in an NNpH environment, and that holding the load at maximum stress should encourage hydrogen segregation. Thus it would be intuitive to predict that the hold would enhance the crack growth rate. However, Figure 2-23 shows this is not the case. In fact, the lowest crack growth rate resulted from the hold spectrum. There is likely also a blunting process that was competing with the HE process, and the prolonged hold is blunting the crack tip through a number of possible mechanisms such as corrosion [31,94], room temperature creep

41

[31,39,102–104], and hydrogen enhanced local plasticity (HELP) [8,105]. The minor cycles are likely able to provide enough driving force to overcome these blunting effects, and since the minor cycles maintain the stress at a high level, the effect of hydrogen segregation is preserved as well, thus leading to the high crack growth rate.
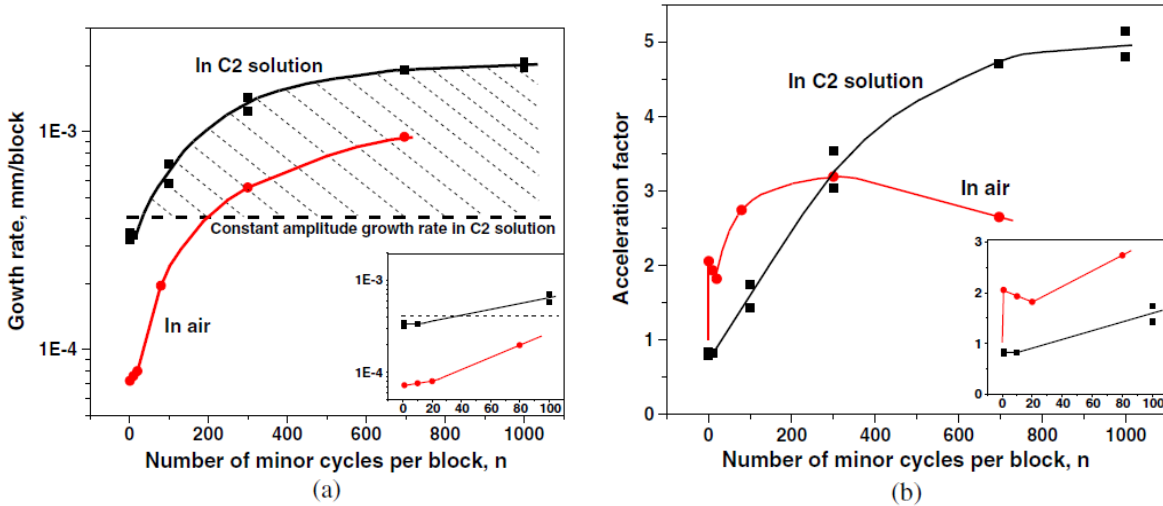
Figure 2-21 Results of the periodic underload tests in C2 solution (NNpH environment): (a) Variation in the measured crack growth rate with the number of minor cycles per block and (b) variation in acceleration factor with the number of minor cycles per block. Reproduced from [10], with permission.
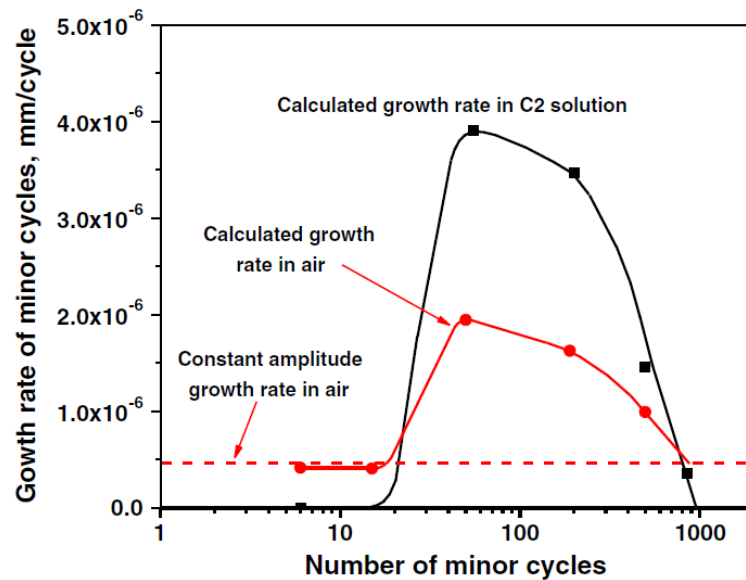
Figure 2-22 Growth rate of minor cycles varies with 'n' for underload spectrum in both air and NNpH environment. The contribution of minor cycles to crack growth is calculated using the method developed by Fleck [99]. Reproduced from [10], with permission.

42
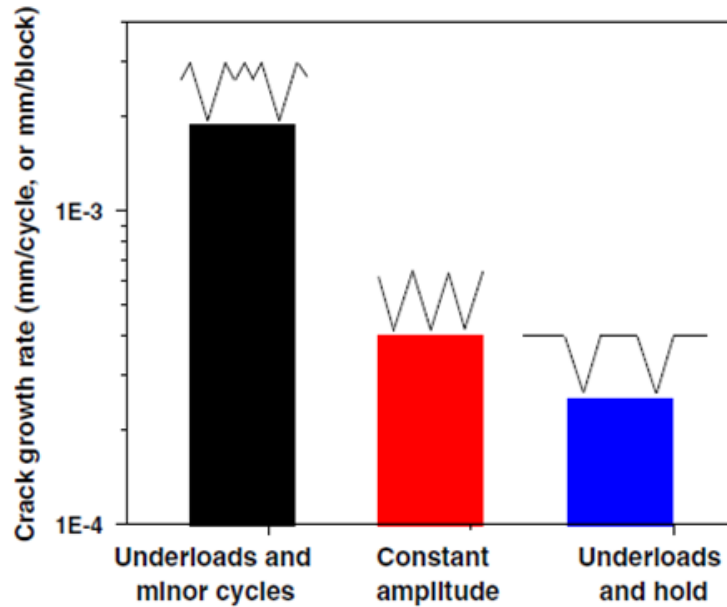
Figure 2-23 Comparison of crack growth rate under different waveforms demonstrating the effect of the number of minor cycles. All tests were done in NNpH soil solution. For all of the waveforms: K_{max} = 33 MPa, R_{UL} = 0.5, R_{MC} = 0.9, f_{UL} = 1.04×10^{-3} Hz, f_{MC} = 5.38×10^{-3} Hz. The UL+MC waveform had 697 minor cycles in between underloads. The Constant amplitude load growth rate is given in mm/cycle instead of mm/block, and consists of only underload cycles. Underload and hold spectrum has a constant hold period of 36 hours which is the same duration as 697 minor cycles. Reproduced from [10], with permission.

2.4.6.2 Effect of Frequency

In another study, Yu et al. [9] investigated the effects of frequency on MC&UL spectra. Realistic underload frequencies in pipeline operation (10^{-5} to 10^{-1} Hz) were applied to X60 CT specimens in an NNpH environment. The other loading conditions were the same as those described at the beginning of section 2.4.6.1.
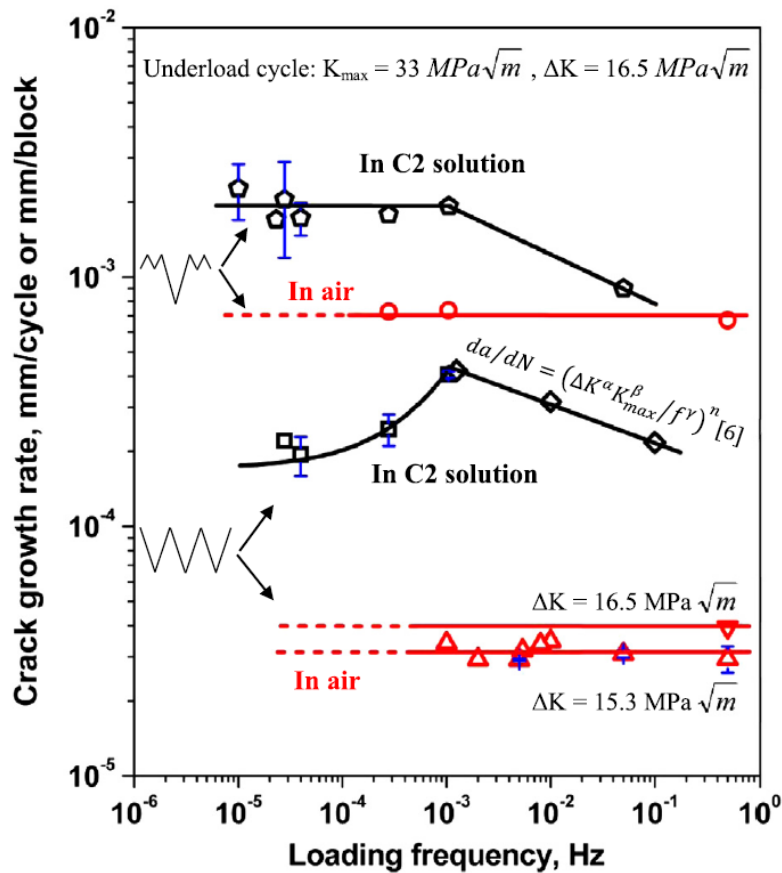
Figure 2-24 Crack growth rate vs. typical loading frequencies on a pipeline for constant amplitude and underload type spectra in air and in NNpH environment (C2 solution). K_{max} = 33 MPa√m for all tests. ΔK of underloads are indicated within the figure. Number of minor cycles = 697 for the underload type spectrum. $f_{minor\ cycles}$ = 5.4×10-3 Hz in C2 solution, and 5×10-1 Hz in air. Constant amplitude waveform growth rate was measured per cycle. VAL growth rate was measured per block. Reproduced from [9], with permission from Elsevier.

The results of this study are illustrated in Figure 2-24. The MC&UL spectrum produced faster growth rates as expected, again demonstrating the acceleration effect of the spectrum. Crack growth in air was also shown to be insensitive to frequency. But in C2 solution, the crack growth is sensitive to frequency, demonstrating the frequency dependence of a true corrosion fatigue process. A critical frequency was found at 10^{-3} Hz for both types of spectrum.

For the constant amplitude spectrum, the crack growth rates increased from 10^{-1} to 10^{-3} Hz, then the growth rates decreased for frequencies lower 10^{-3} Hz. The region from 10^{-1} to 10^{-3} Hz can be described using the combined factor relation defined by Chen & Sutherby in [81]

The frequency response for VAL MC&UL spectrum is much different. The crack growth rates still increased from 10^{-1} to 10^{-3} Hz, but then they remained constant for frequencies less than 10^{-3}

44

Hz. The reason for the different behaviour of the two spectra at frequencies below 10^{-3} Hz is not known and requires further investigation.

The transition behaviour at 10^{-3} Hz was modelled by Yu et al. using a mechanistic model based on hydrogen assisted cracking from [67,106]. Yu et al. showed through his calculations that the critical time required for hydrogen diffusion into the fracture process zone in front of the crack tip corresponds to the critical frequency of 10^{-3} Hz. Since the hydrogen diffusion and segregation process is dependent on the lattice parameter of the steel, the critical frequency is also material-dependent.

2.4.6.3 Effect of R-ratios

Yu et al. also studied the effects of R ratio on underload-type spectra [94]. Two sets of tests were conducted. The first set of test modified the R ratio of underload cycles in the underload-type spectrum. The second set of test modified the R ratio of minor cycles in the underload-type spectrum. The acceleration factor results are illustrated in Figure 2-25. The acceleration factors in air demonstrated a peak for both the UL and MC tests. In C2 solutions, however, the results formed a more linear trend, suggesting the acceleration effect is environment-dependent. It is also interesting to point out that in Figure 2-25 (c), for $R_{UL} < 0.25$, the crack growth is actually retarded. This is counterintuitive because for aggressive underload cycles, the expected behaviour is enhanced growth. The reason for this behaviour is not well understood and requires further investigation.

One important finding from this study is the threshold R ratio above which a minor cycle can be treated as static hold. The threshold R ratio was found to be 0.982, which is illustrated in Figure 2-25 (d). This is a very high R ratio, and it means that many small cyclic events that pipeline operators would typically ignore could also contribute to crack growth.
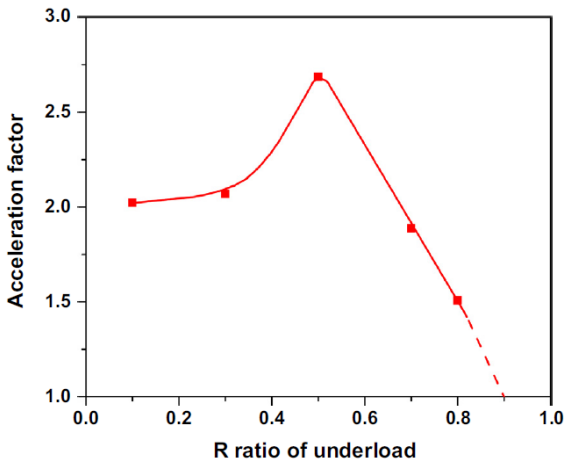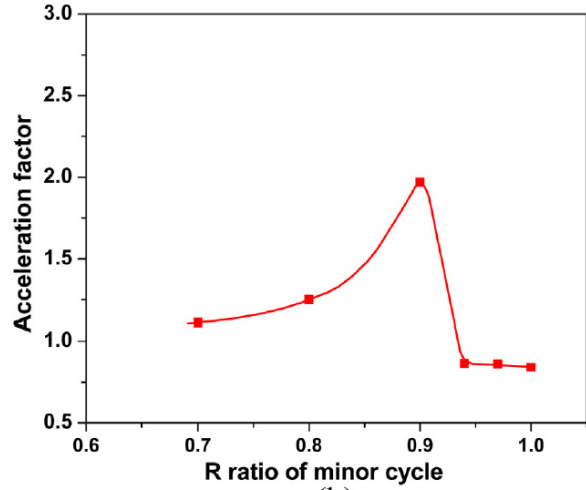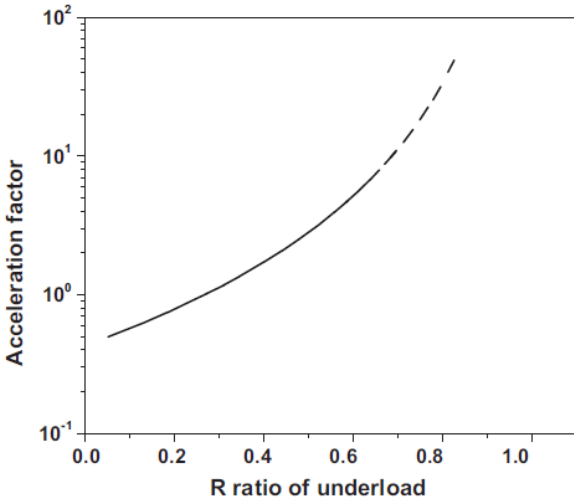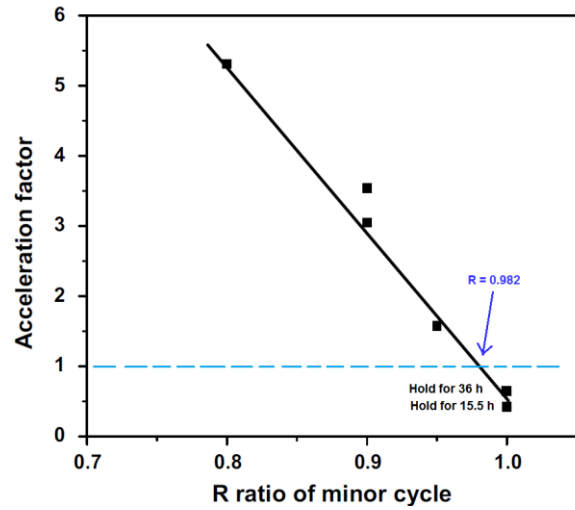
Figure 2-25 Acceleration factor behaviour: (a) Air, the effect of modifying R ratio of UL (b) Air, the effect of modifying R ratio of MC (c) C2 solution, the effect of modifying R ratio of UL (d) C2 solution, the effect of modifying R ratio of MC. Reproduced from [94], with permission from Elsevier.

2.4.7 Hydrogen Effects

As was discussed in section 2.3.7, hydrogen is produced as a result of the reduction of hydrogen ions in the NNpH environment. Some atomic hydrogen is able to diffuse into the steel and cause hydrogen embrittlement (HE). Most researchers agree that hydrogen plays a role in SCC propagation [16], and has these general observations :

- Steel exhibits decreased ductility with an increased CO_2 concentration in the solution (due to increased hydrogen levels from the carbonic acid formation) [17,51,107,108]
- During anodic dissolution in the NNpH environment, hydrogen is reduced at the exposed surface of the pipe. [72,109]
- Continuous exposure to NNpH solution is needed for brittle behaviour [57]
- Quasi-cleavage fracture surface and lack of corrosion near crack tip is indicative of hydrogen effects [17,72,110]
- Dissolution rate alone cannot account for the actual field growth rates of cracks [17,57,105,111]
- Crack growth rate is faster in an NNpH solution with lower pH, despite the prediction that the lower pH would increase dissolution and blunt the crack tips [72]

The following subsections will discuss some relevant hydrogen effects seen for NNpH SCC.

2.4.7.1 Hydrogen Assisted Cracking Modes

Before going forward with discussion of hydrogen assisted cracking (HAC), a distinction has to be made between the atomistic mechanisms behind hydrogen embrittlement and the macro mechanism of hydrogen embrittlement. The atomistic mechanisms behind hydrogen embrittlement describe on the atomic scale, how hydrogen weakens and breaks bonds in the metal lattice. The atomistic mechanisms have been heavily debated, and three major mechanisms have gained traction [112]: Hydrogen Enhanced Decohesion (HEDE), Hydrogen Enhanced Localized Plasticity (HELP), and Adsorption Induced Dislocation Emission (AIDE). The discussion of the atomistic mechanisms is not in the scope of this thesis, since hydrogen embrittlement is viewed from a macro perspective.

Gangloff classified the macro modes hydrogen embrittlement according to where the hydrogen in the fracture process zone (FPZ) comes from [112]. Understanding where the hydrogen is coming from is more important for NNpH SCC than knowing the exact micro-mechanism.

Gangloff suggested two categories of "hydrogen degradation of the crack propagation resistance" (or hydrogen assisted cracking): Hydrogen-Environment-Assisted Cracking (HEAC) and Internal-hydrogen-assisted cracking (IHAC). The two modes are shown in Figure 2-26. In both modes, hydrogen segregates to the fracture process zone near the crack tip, and as a result, the FPZ contains a higher concentration of hydrogen which can lead to more damage. The difference between these two processes is: in HEAC, the hydrogen enters the FPZ through the crack tip, but in IHAC, dissolved hydrogen in the bulk material diffuses into the FPZ.
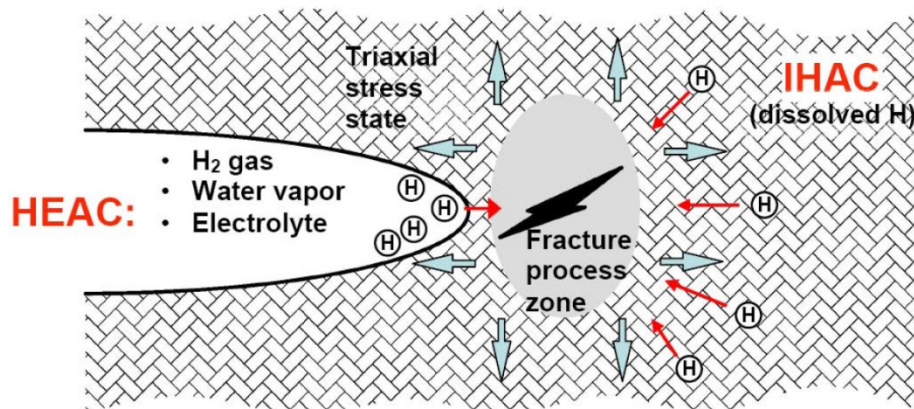
Figure 2-26 Diagram showing HEAC and IHAC modes of HAC. Reproduced from [113], with permission from Elsevier.

For NNpH SCC, both IHAC and HEAC are driven by the corrosion reaction. For HEAC, electrolyte could enter the crack crevice, and the cathodic reaction occurring within the crack crevice could produce diffusible hydrogen. Even though only small quantity of hydrogen can be produced from this small volume of fluid within the crevice, the hydrogen only has as short distance to diffuse into the FPZ. For IHAC, the dissolved hydrogen in the bulk material comes from the corrosion reaction on the outer surface of the pipe. There is a much larger area of exposed metal on the outer surface in regular contact with electrolytes that can generate large amounts of diffusible hydrogen, but the hydrogen has to diffuse into the steel. Hydrogen produced at the outer surface has to travel longer to get to the FPZ, and the diffusion process also takes times, therefore IHAC can only occur if the steel is exposed to the NNpH environment for

a prolonged period of time. The continued exposure to a corrosive environment ensures the bulk material stays charged with hydrogen.

Chen et al. [31] investigated whether HEAC or IHAC process is the dominant mode of HE for NNpH SCC propagation. A corrosion fatigue experiment was conducted using CT specimens with different coating configurations as shown in Figure 2-27: no hydrogen & no corrosion; HEAC + corrosion; HEAC + IHAC + corrosion.

Entire surface coated
No H, No Corrosion
(a)

Partially coated
HEAC + Corrosion
(b)

Bare (no coating)
HEAC + IHAC + Corrosion
(c)
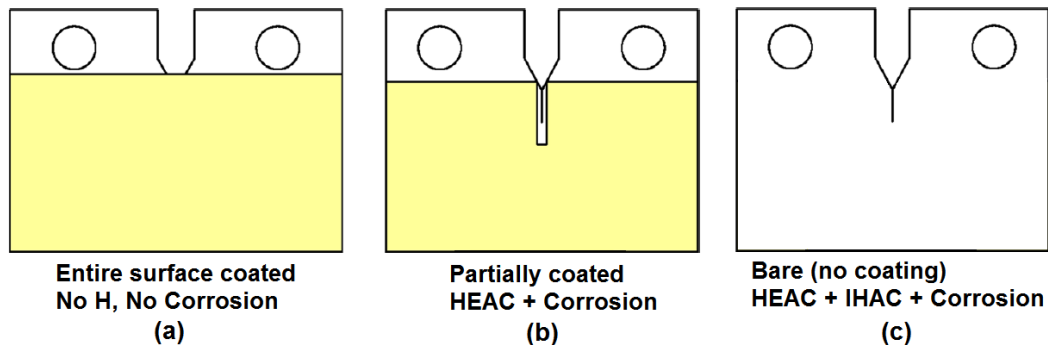
Figure 2-27 The three types of coating on CT specimen used by Chen et al. [31] to simulate different hydrogen and corrosion processes in NNpH solution. (a) Entire surface coated, solution does not make direct contact with any part of sample surface, simulates no hydrogen diffusion and no corrosion. (b) Partially coated sample with the region around the crack exposed. The partial coating blocks corrosion reaction on the bulk surface, preventing IHAC processes. The exposed region allows only HEAC and corrosion. (c) Bare sample, no coating. HEAC, IHAC, and corrosion can all occur simultaneously. Adapted from [31], with permission from Elsevier.

The results of the experiment are shown in Figure 2-28. The 'no hydrogen & no corrosion' and 'HEAC + corrosion' conditions produced similar crack growth rates, with the 'HEAC + corrosion' configuration having a slightly higher crack growth rate, suggesting a small amount of contribution from the HEAC process. However, the contribution from HEAC is insignificant when compared to the crack growth rates for the 'HEAC + IHAC + corrosion' condition, which had crack growth rates an order of magnitude higher than the other two conditions. The increased crack growth rate can be attributed to IHAC. The bare sample has more surface area to generate diffusible hydrogen which could segregate into the FPZ. The 'HEAC + IHAC + corrosion' configuration is also closest to the field SCC conditions, providing strong evidence that IHAC is the main contributor to HE/HAC in SCC.
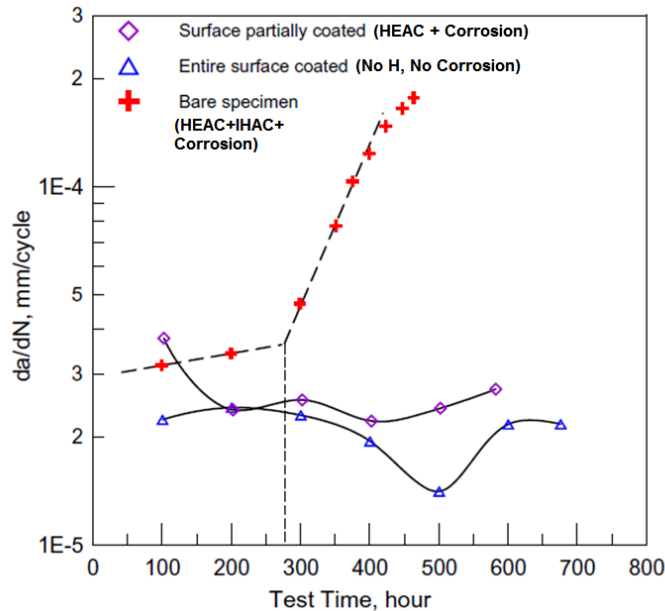
Figure 2-28 Crack growth rate as a function of test time for three specimens with different coating methods shown in Figure 2-27. Corrosion fatigue test carried out in NNpH environment. All tests were performed at same starting conditions: K_{max} = 35.3 MPa$\sqrt{}$m, ΔK = 12.0 MPa$\sqrt{}$m, and f = 0.005 Hz. Reproduced from [31], with permission of Elsevier.

2.4.7.2 Hydrogen Segregation

For a semi-elliptical surface crack like SCC, hydrogen prefers to segregate to the depth tip rather than the surface tip due to the different stress states. The surface tip resembles the plane stress condition (biaxial loading), while the depth tip resembles the plane strain condition (triaxial loading). The high degree of triaxiality at the depth tip FPZ expands the crystal lattice more, making it easier for hydrogen to enter, thus increasing the hydrogen solubility locally. Hydrogen in the bulk material segregates into the triaxial FPZ due to the favourable conditions (see IHAC process discussed above) [12,66–68,106].

Under cyclic loading, a slower loading frequency will allow more time for segregation and enhance its effects. This is demonstrated in [9] when Yu et al. found a critical frequency of 10^{-3} Hz for pipeline steel where crack growth rate is maximized (see section 2.4.6.2). The enhanced growth rate in underload type spectrum can also be partially explained with hydrogen segregation. During minor cycles, which can last for hundreds of cycles in actual operation, the pipe is held near the MAOP, and this encourages hydrogen segregation. More minor cycles mean more segregation, and this could significantly enhance the crack growth during the underload cycle (see Figure 2-21).

2.4.7.3 Discontinuous Crack Growth Mechanism

Chen et al. [8,31] recently proposed a discontinuous crack growth mechanism for NNpH SCC, in which crack growth alternated between dormancy and active growth. This implies crack growth could also be viewed as a competition between blunting and resharpening processes. Evidence of discontinuous crack growth in NNpH environment can be found in [10,31,114]. Figure 2-29 shows blunting can occur during static hold due to room temperature creep (RTC) and corrosion. Cyclic loading (underloads) can re-initiate sharp cracks and cause crack propagation. Figure 2-30 shows the striations on the fracture surface produced from underload type spectrum (MC&UL) described in section 2.4.6.1. The striations suggest successive blunting and re-sharpening of the crack tip. Figure 2-32 (c) shows the outline of a crack that has undergone multiple blunting and resharpening cycles in an NNpH environment.

Blunting in a NNpH environment is commonly attributed to corrosion and room temperature creep (RTC) [8,31,41,72,114,115]. Recently, hydrogen enhanced local plasticity (HELP) has been proposed as a crack blunting mechanism as well [8,105]. For cracks in an extended period of hold at max pressure or minor cycle near max pressure, the blunting can put the crack in a dormant state. Theoretically, a blunt crack shouldn't have enough mechanical driving force to propagate [116], so a key question that needs to be answered is how a crack is able to re-sharpen and grow again?

(a)   (b)
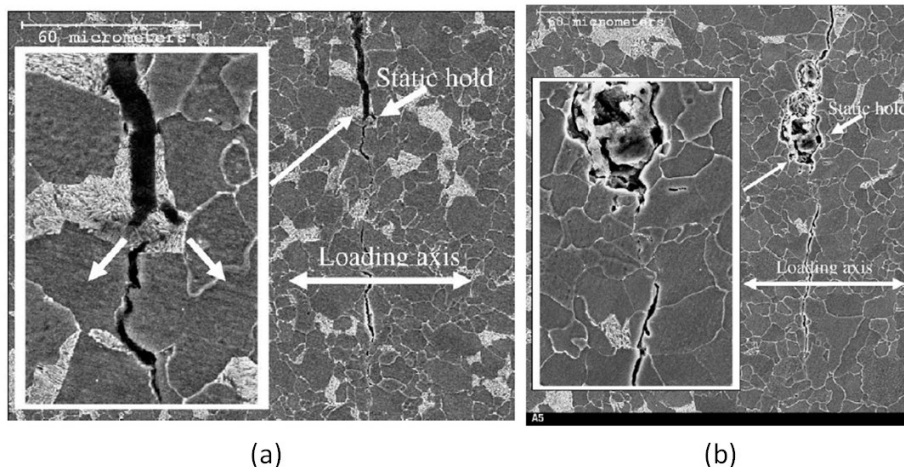
Figure 2-29 Crack tip morphology of CT specimen which had undergone static hold for 7 days before resuming cyclic loading. An insert of the magnified view of the crack tip at where the static hold ended is included for each image. The crack tip is visibly blunted during static hold and the crack stopped propagating. Resumption of cyclic loading produced sharp cracks that were able to propagate. (a) Test done in NOVATW solution which showed blunting due to creep (b) Test done in the more corrosive C2 solution, which showed blunting due to corrosion. Reproduced from [31], with permission of Elsevier.

51

Constant amplitude (n=0)   n=1   n=10
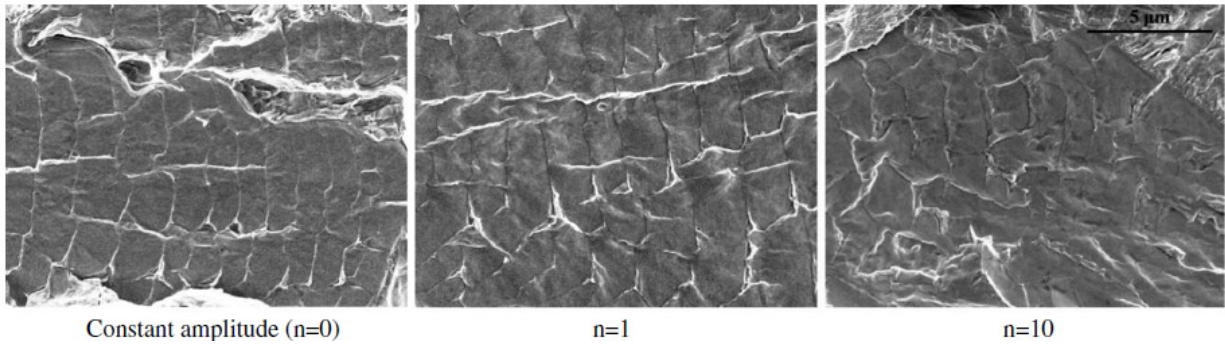
Figure 2-30 SEM images (x7500) showing striations observed on the fracture surface of specimens tested under MC&UL spectrum with varying number 'n' of minor cycles per block in NNpH environment. The striations are evidence of successive blunting and re-sharpening of the crack tip. Reproduced from [10], with permission.
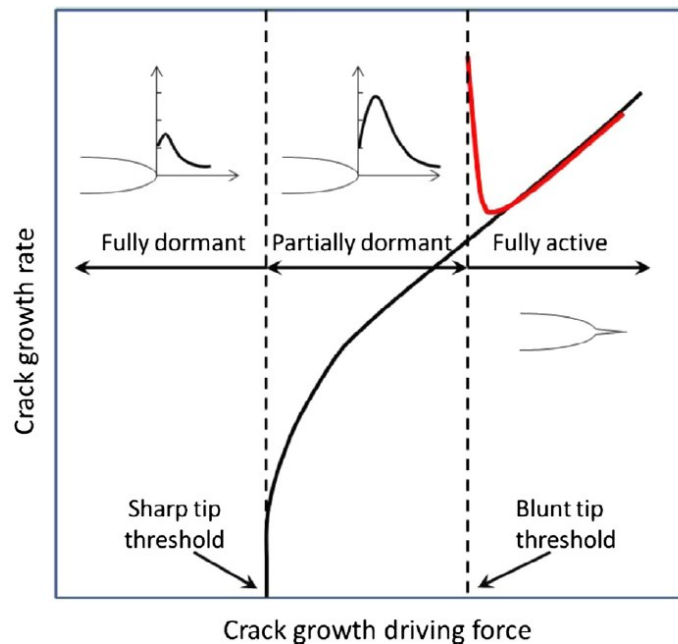
Figure 2-31 Illustration showing different thresholds for a sharp tip and a blunt tip. Reproduced from [114], with permission from Elsevier.

Two thresholds exist for continuous crack growth, one for sharp crack, and another one for blunt crack tips as shown in Figure 2-31 [8,114]. The threshold for blunt tips is much higher than sharp tips, therefore continuous crack propagation from a blunt crack is difficult to achieve unless the mechanical driving forces are very high. However, a blunt tip is still able to create a stress concentration that is sufficient enough to fracture small second-phase particles in front of the crack tip as shown in Figure 2-32 (a). NNpH SCC has quasi-cleavage fracture morphology. For cleavage-type fractures, the local stress must overcome the cohesive strength of the metal in order to break the bonds, but the cohesive strength of the material is usually much higher than

52

the stress achieved ahead of the crack tip [116]. Microcrack formed in front the macroscopic crack is able to provide enough local stress concentration in order to initiate cleavage, and is typically formed at weak links such as grain boundaries, inclusions, or phase interfaces in the FPZ [8,116]. The high hydrogen concentration in the FPZ facilitates the initiation and growth of these microcracks. The microcrack will grow and eventually link up with the main crack [68,112], transforming the blunt macro-crack into a sharp macro-crack that can propagate until it becomes blunt again.

Evidence of microcrack formation in front of the main crack has been found by Chen et al. [117] and Parkins [17]. It is also important to emphasize that it is the fracture of second-phase particles, and not the formation of hydrogen blisters that create microcracks in the FPZ. Chen et al. have found that the amount of diffusible hydrogen generated in an NNpH soil environment at OCP is only 1/10th the minimum hydrogen concentration required to initiate hydrogen blistering in pipeline steel [118].
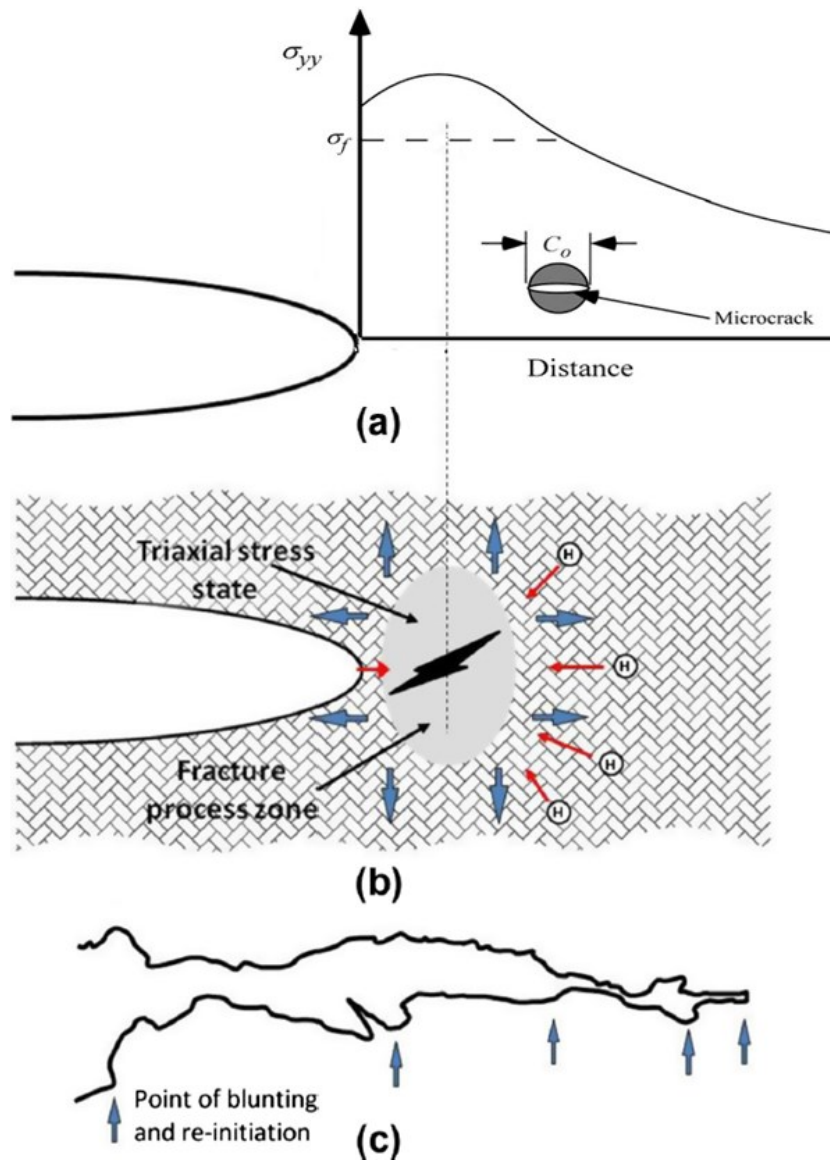
Figure 2-32 Illustration showing the mechanism of discontinuous crack growth: (a) Stress distribution (σ_{yy}) in front of a blunt crack tip is shown. σ_f represents the fracture stress of second-phase particles with size C_o. Microcrack can initiate at weak links such as second-phase particles near the blunt crack tip. (b) Micro-cracks can occur in the FPZ, where hydrogen segregation makes second phase particles highly susceptible to microcrack formation in front of the blunt tip. (c) Traced outline of a crack that has undergone cyclic loading in NNpH environment. The arrows indicate points where resharpening of the crack has occurred. The crack propagated through cycles of blunting, micro-crack initiation, and growth. (a) adapted from [116], with permission from Taylor and Francis Group. (b) & (c) adapted from [114], with permission from Elsevier.

54
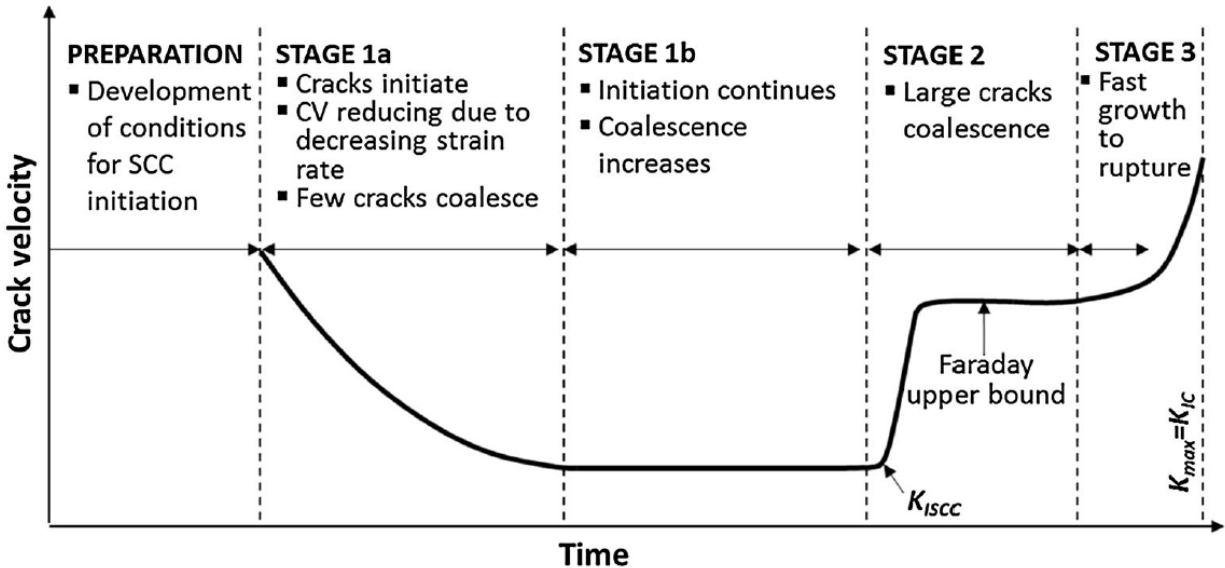
2.5 Bathtub Models

Figure 2-33 Parkin's SCC bathtub model [47]. Reproduced from [111], with permission from Springer.
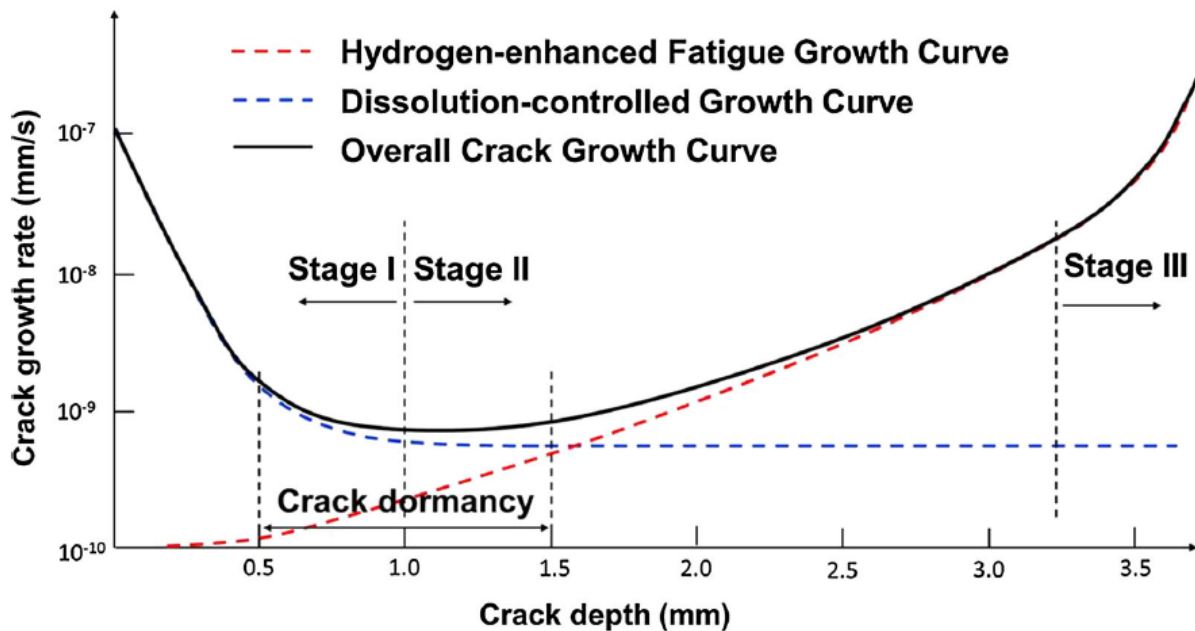
Figure 2-34 Chen's NNpH SCC bathtub model. Reproduced from [111], with permission from Springer.

Several models have been proposed to describe the behaviour of SCC over its life. Parkin's model, shown in Figure 2-33 has been widely used in the pipeline industry, however, the model is only applicable to high pH SCC. The Faraday upper bound shown in Stage 2 indicates time-dependent growth with a film rupture mechanism. Recently, Chen et al. have proposed an improved SCC model for NNpH SCC [8,111] based on decades of knowledge accumulated since

when Parkin's model was first proposed. In Chen et al.'s model, Stage I is controlled by dissolution, and Stage II is controlled by corrosion fatigue mechanisms. The corrosion fatigue models described in section 2.4.4 is applicable only to Stage II cracks. Most pipeline operators are concerned about cracks in stage II, since these are the cracks that can grow to failure. Stage I cracks are typically very shallow (<1mm deep), and are difficult to detect with ILI tools, therefore they are not of priority concern to pipeline operators. It is also difficult to predict the remaining life of Stage I cracks since there is a period of dormancy following stage I, in which the crack does not grow in depth direction. It is unknown how long a crack can stay dormant. It is known however, that only 5 percent of cracks are able to grow past dormancy and reach critical size [111]. In terms of value and safety, pipeline operators should focus more on developing Stage II corrosion fatigue models, which can help them prioritize repairs on significant cracks.
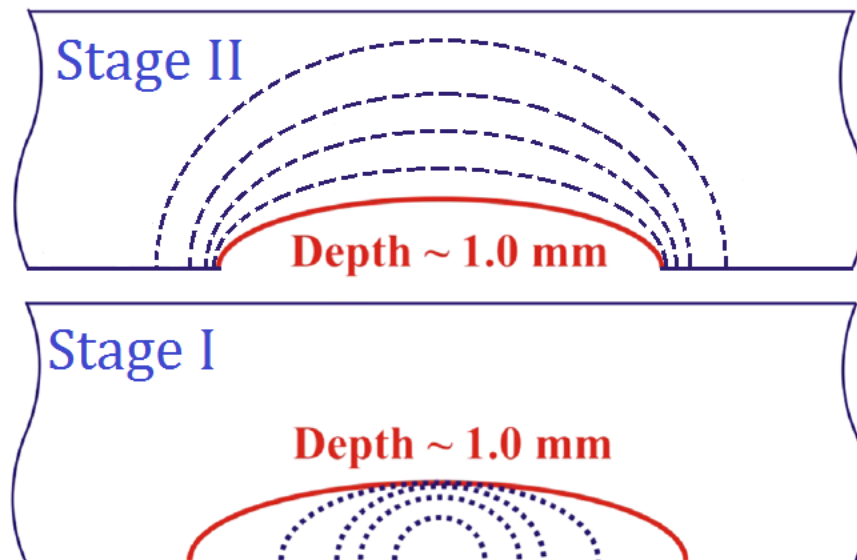
Figure 2-35 SCC crack shape evolution in Stage I and Stage II growth. Reproduced from [111], with permission from Springer.

Figure 2-35 shows the typical shape evolution for a field SCC in Stage I and Stage II growth according to Chen et al.'s model. The red semi-ellipse represents the shape when the crack during dormancy. The shape evolution for the crack in Stage I is very different from the shape evolution of a crack driven by mechanical means. Chapter 3 contains has an in-depth discussion of shape evolution of semi-elliptical surface under purely mechanical driving force. A key finding from that chapter is all surface cracks (regardless of initial shape) tend to grow toward a

semi-circular shape in order to distribute the SIF evenly along the entire crack front. The crack development in Stage I clearly contradict with the shape evolution behaviour described in chapter 3 since the shape is getting more elongated instead of staying semi-circular. The dormancy behaviour in the depth means Stage I crack can only grow in the surface via dissolution mechanism. After dormancy, the crack enters Stage II growth. The shape evolution behaviour during Stage II growth agrees with Chapter 3. The stage II crack in Figure 2-35 is growing toward a more semi-circular shape to distribute the SIF more evenly along its crack front. This suggests mechanical driving force is important during Stage II.

3 Techniques for Preparing Semi-Elliptical Surface Crack Specimens

3.1   List of Variables Used in this Chapter

a — Surface crack depth

$\dfrac{a}{c}$ — Crack aspect ratio, dimensionless variable used in Newman and Raju SIF solution

$\dfrac{a}{t}$ — Crack depth to thickness ratio, dimensionless variable used in Newman and Raju SIF solution

a_m — Precrack depth measured from milled surface to depth tip (crack depth after removal of EDM notch via milling)

a_{m2} — Second stage precrack depth (2nd stage precracking done after milling)

a_o — Precrack depth measured from original surface to depth tip

$a_o{}'$ — Extent of crack influence at depth tip due to precracking, measured from original surface. Includes crack depth and plane strain plastic zone size. $a_o{}' = a_o + r_{p,\mathrm{d}}$

c — Surface crack half-length

C_a — Paris law proportional constant for depth growth , material property

C_c — Paris law proportional constant for surface growth , material property

c_m — Precrack surface half-length at the milled surface

$c_m{}'$ — Extent of crack influence at milled surface due to precracking. Includes plastic zone size.

c_{m2} — Second stage precrack half-length (2nd stage precracking done after milling)

c_o — Precrack half-length measured on the original surface

$c_o{}'$ — Extent of crack influence at original surface due to precracking. Includes crack half-length and plane stress plastic zone size. $c_o{}' = c_o + r_{p,s}$

$K(\phi)$ — Stress intensity factor at a point on the semi-elliptical crack front defined by angle ϕ

K_{max} — Max stress intensity factor during cyclic loading

m	Paris law power constant, a material property
n	Power constant in super-ellipse equation fit
N	Number of load cycles
$r_{p,d}$	Plane strain plastic zone size ahead of crack depth tip
$r_{p,s}$	Plane stress plastic zone size ahead of crack surface tip
t	Thickness of plate containing surface crack
t_f	Final thickness of sample after milling removal of EDM notch
t_m	Amount of thickness milled off to remove EDM notch
t_o	Original thickness of sample with EDM notch
W	Half-width of plate containing surface crack
x	x coordinate of any point along the crack front
y	y coordinate of any point along the crack front
ΔK_a	Range of SIF at depth tip of a surface crack
ΔK_c	Range of SIF at surface tip of a surface crack
σ	Applied remote uniform tensile stress
σ_{YS}	Yield strength of metal
ϕ	Angle of any point along the crack front. Range from 0 to 90°, with 0° at the surface tip, and 90° at the depth tip.

3.2 Introduction

Corrosion fatigue experiments are usually conducted on precracked specimens. Precracking creates sharp cracks from machined notches on the specimens in order to simulate real fatigue cracks. By taking advantage of stress intensity factor (SIF) similitude, the crack can be precracked to any size in order to produce the desired SIF that simulates field conditions. This is a useful strategy for SCC research since the cracks grow slowly due to the low cyclic frequency. A researcher can create a large array of cracks with different starting SIF in order to get crack growth rate measurements at different K values quickly.

Even though researchers are able to replicate the SIF seen in the field, many experiments still cannot reproduce realistic crack growth rates. This is due to the widespread use of thru-wall crack specimens such as the compact tension (CT) specimens. Most corrosion fatigue cracks, including SCC, are part thru-wall surface cracks with an approximate semi-elliptical shape. The two types of cracks specimens (thru-wall & surface cracks) are illustrated in Figure 3-1. It is preferable to use surface crack specimens for SCC studies because it is more realistic. However, replicating surface cracks is challenging. The lack of reliable procedure for precracking a semi-elliptical surface flaw discourages many researchers from using these specimens and producing more accurate results.

(a) **(b)**
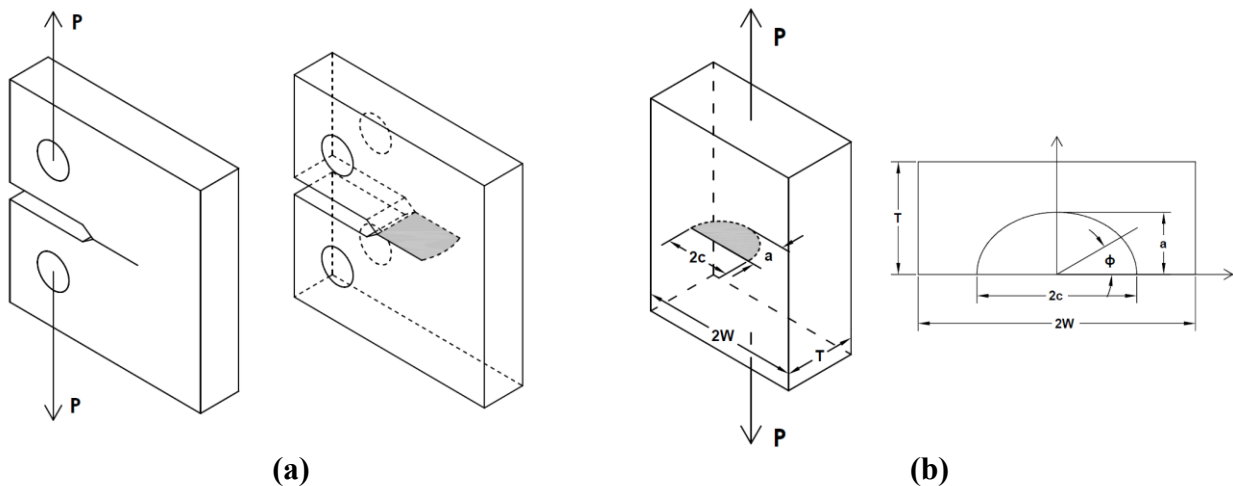
Figure 3-1 Crack specimens used for corrosion fatigue studies: (a) Compact tension specimen, a type of thru-wall crack specimen. (b) Surface crack specimen, where the flaw has only partially penetrated the thickness.

60

The thru-wall crack is essentially a one-dimensional crack in a two-dimensional body. Whereas the surface crack is a two-dimensional crack in a three-dimensional body. The extra dimension in surface cracks brings an additional level of complexity.

For a thru-wall crack specimen with known sample geometry and applied load, the SIF is only dependent on the crack length. The crack length is easily measured and the SIF can then be calculated. Experiments requiring a certain starting SIF can precrack the sample to a target length that corresponds to the required SIF.

For surface cracks, the SIF at any point along the crack front is dependent on both the length and depth of the crack ('c' and 'a' in Figure 3-1). This means the SIF at the surface is dependent on the crack depth, and the SIF at the depth is also dependent on the surface length. The depth and surface growth are deeply related, and growth in one direction is not independent from the other direction. Crack growth should be viewed as the growth of the entire semi-elliptical crack front or the increase in overall crack area. Many SIF solutions for surface cracks have been proposed, but the most widely adopted solution is by Newman and Raju [119–122], which is described in detail in Appendix C. In Newman and Raju's solution, both the length and depth of the crack are required to find SIF at any point on the crack front. Their solution also demonstrates how the shape of the crack can significantly influence crack growth.

For the pipeline industry, there is a focus on predicting the depth growth rate of surface cracks. If the surface crack penetrates the thickness of the pipe wall, it would result in leaks and ruptures. Thru-wall crack specimens have been widely used to study crack growth in the depth direction. However, too much emphasis has been placed on depth growth rate that engineers often overlook how surface and depth growth rates are interconnected. In recent years researchers have conducted SCC studies using surface crack specimens [101,114,115,123]. That is an encouraging development, but these studies used cracks of very different aspect ratios, so direct comparison between these studies is not possible. The precracking procedures used were still based on thru-wall crack specimens. There is a need for a precracking procedure specifically designed for surface cracks that can produce cracks in a wide range of shape and sizes.

The biggest challenge in preparing surface crack specimen is in predicting the depth of the crack. Non-destructive methods of measuring crack depth such as ultrasonic and eddy current are not

accurate enough. The shape of the fatigue cracks also changes as the crack grows, making it difficult to difficult to predict crack depth from surface length alone. A common method of making surface crack samples is to make thin semi-elliptical notches on the surface of the sample through electro-discharge machining (EDM), and then conduct fatigue precracking in order to initiate a fine crack. The fatigue crack that resulted from precracking has a different aspect ratio than the initial EDM notch. The crack does not grow in a manner that maintains the aspect ratio of the starting shape. The surface and depth tip also exhibit different growth rates. A method of predicting crack depth is needed so researchers can accurately calculate initial SIF after precracking has completed.

The objective of this chapter is to present improved methods of preparing semi-elliptical surface cracks for corrosion fatigue experiments. The following issues will be addressed:

- How to accurately recreate in-service fatigue cracks
- How to predict crack depth based on material behaviour and surface measurements
- How to precrack to a wide range of shape and size
- How to design precracking procedures to minimize plastic zone effects

3.3   Shape Evolution of Surface Crack during Fatigue Growth

The stress intensity factor (SIF) for semi-elliptical surface cracks is shown in Appendix C. Predicting the fatigue crack growth rate of semi-elliptical surface crack may seem daunting since each point on the crack front has a unique SIF. The crack growth rate of each point on the crack front must be determined in order to determine how the crack shape will change as it grows. This problem lends itself well to finite-element (FEM) solutions, but that would make the problem impractical to solve. A simpler approach is needed.

Newman and Raju proposed a simple fatigue growth model which has been termed the 'two points plus semi-ellipse' method [119,121]. This method only considers growth at two points on the crack front: the surface and depth tip of the crack ($\phi = 0°$ and $\phi = 90°$). The growths at these two points are calculated with Paris law, and a semi-elliptical profile is assumed to be always maintained between these points. At first glance, it may seem that the surface and depth tip growth are calculated independently, however, the two points are actually coupled through the SIF equations shown in Appendix C. It should be noted that the Newman and Raju SIF solution is a plate solution, and bulging effects were not considered in this thesis.

The 'two points plus semi-ellipse' method has been validated by many experimental results and advanced FEM models [119–122,124–131]. This study has also adopted this method to predict crack growth during precracking due to its good accuracy. Even though the model assumes a semi-elliptical profile is maintained between the surface and depth tip, it is not necessarily so. Many studies have also shown the actual shape deviates from a true semi-ellipse [125,127,130]. Since the shape profile does not affect the crack growth rate calculations, any shape profile can be assumed. It is inconsequential what the shape of the crack is, since the two points most important to remaining-life calculations are already considered: surface tip and depth tip.

The 'two points plus semi-ellipse' method [119,121] is described below. For a crack with known dimensions a and c, the fatigue crack growth rates at the depth ($\frac{da}{dN}$), and surface ($\frac{dc}{dN}$) are found by:

$$\frac{da}{dN} = C_a(\Delta K_a)^m \qquad (3.1)$$

$$\frac{dc}{dN} = C_c(\Delta K_c)^m \tag{3.2}$$

Eqns (3.1) and (3.2) uses the simple Paris law to describe the surface and depth growth. For precracking in air, Paris law is sufficient to describe the fatigue growth behaviour. ΔK_a and ΔK_c are the SIF range for the depth and surface tip, respectively. The SIF equations for surface cracks are shown in Appendix C. K varies along the crack front and is a function of ϕ, therefore ΔK_a and ΔK_c typically have different values. The power constant 'm' is assumed to be an intrinsic material property that is constant in both growth directions. C_a and C_c are proportional Paris law constants at the depth and surface tip. Newman and Raju has proposed two assumptions for the relationship between C_a and C_c:

$$C_c = C_a \tag{3.3}$$

$$C_c = 0.9^m C_a \tag{3.4}$$

Normally C_a and C_c are assumed to be the same, but experimental results [128] have led Newman and Raju to adopt eqn (3.4) in order to account for the observed behaviour in which small semi-circular cracks prefer to grow in almost constant a/c ratio. Newman and Raju argued that the different stress states at the surface and depth (plane stress vs. plane strain) should result in different values of C_a and C_c [122]. Both assumptions were later evaluated by other authors [124–127,129–131], but the conclusions have been mixed. For predicting changes in cracking shape, some studies have shown that $C_c = C_a$ is better [122,124–126,130], but others have shown $C_c = 0.9^m C_a$ is a better [119–121,124,128,129]. For predicting fatigue life, $C_c = 0.9^m C_a$ is generally agreed to be better model [124,131].

An interesting relation can be obtained when eqn (3.1) is divided by eqn (3.2) [124,129]. The result of the division is shown in eqn (3.5) and (3.6):

- For the first assumption $C_c = C_a$:

$$\frac{da}{dc} = \left[\left(\frac{a}{c}\right)^{0.5} \left(1.1 + 0.35 \left(\frac{a}{t}\right)^2\right) \right]^{-m} \tag{3.5}$$

- For the second assumption $C_c = 0.9^m C_a$:

$$\frac{da}{dc} = \left[0.9 \left(\frac{a}{c} \right)^{0.5} \left(1.1 + 0.35 \left(\frac{a}{t} \right)^2 \right) \right]^{-m} \tag{3.6}$$

Full details on the derivation of equations (3.5) and (3.6) can be found in Appendix D. These two equations are the shape evolution equations of the surface crack. Equations (3.5) and (3.6) are differential equations that can be solved numerically after specifying the initial conditions for a and c. The constants 't' and 'm' also need to be specified. The goal of solving these differential equations is to find the shape evolution curves which predict how the aspect ratio and depth ratio of the crack change as it grows. The shape evolution curves are typically plotted as $\frac{a}{c}$ vs. $\frac{a}{t}$. Figure 3-2 shows shape evolution curves for various starting geometry for both $C_c = C_a$ and $C_c = 0.9^m C_a$. The two assumptions show some differences, especially for higher initial a/c ratios and as the crack grows larger. Both assumptions show that cracks with low aspect ratio (low a/c ratio) tend to grow toward a more semi-circular shape (i.e. $a/c = 1$). With the $C_c = 0.9^m C_a$ assumption, small semi-circular cracks (a/c near 1, a/t is small) tend to remain semi-circular for the initial stages of crack growth. With $C_c = C_a$ assumption, there is an initial drop of a/c ratio for small semi-circular cracks.

The material constant 'm' also has an effect on crack shape development as shown in Figure 3-3. Therefore a correct value of 'm' also need to be assumed in order predict the crack shape change, Newman and Raju arbitrarily set 'm' as a material constant that is unaffected by direction of growth.

Figure 3-4 shows the shape evolution experimental results collected by Hosseini and Mahmoud [124]. The trend shown in the experimental data agrees well with the theoretical shape evolution curves shown in Figure 3-2. Again, it is important to point out that shallow cracks with long aspect ratio tend to grow toward a semi-circular shape. These shape predictions are only valid for individual cracks where no coalescence is involved.

In Figure 3-5, a series of shape evolution curves with various initial starting shapes are shown. A few of the initial starting points are highlighted with a blue circle, with diagrams beside them to show the relative size and shape of the initial crack. The initial shapes can be categorized into

four quadrants on the *a/c* vs *a/t* plot. The upper left quadrant is for small, near semi-circular initial cracks (*a/c* ~ 1, low *a/t*). The upper-right quadrant is for large, near semi-circular cracks (*a/c* ~ 1, high *a/t*). The bottom left is long and shallow cracks (low *a/c*, low *a/t*), and the bottom right is long and deep cracks (low *a/c*, high *a/t*).

Most SCC entering stage II that has not coalesced falls in the bottom left quadrant (low *a/c*, low *a/t*), since they are typically long and shallow. Figure 3-6 a) shows the growth sequence of a long shallow sequence crack. The crack approaches a more semi-circular (increasing *a/c* ratio) as it grows. This can be explained using Newman and Raju's SIF solution (see Appendix C). According to the solution, a long shallow crack has a significantly higher *K* at the depth than the surface, resulting larger crack driving force in the depth. This means that a long shallow crack would prefer to grow in the depth instead of the surface in order to approach a semi-circular shape. The crack prefers to grow in a manner that evenly distributes *K* along the entire crack front. Therefore long shallow cracks could be an integrity concern since the crack has a mechanical preference to grow in the depth direction. Of course, this is only applicable to individual cracks that have not coalesced. If coalescence occurs, there would be a sudden increase in crack length, and the mechanical driving force at the depth tip would increase even further.

Even though Newman and Raju came up with a good way to describe the fatigue growth of surface cracks, it also raised more questions. The Paris law constants that most engineers are familiar with were determined through tests done on thru-wall crack specimens such as the CT specimen. But can those Paris law constants determined from thru-wall crack specimens also apply to surface cracks? For a thru-wall crack specimen, only one value of *C* is obtained. Does that *C* represent C_c or C_a in a surface crack? The Paris law constants (both *C* and *m*) for a thru-wall crack specimen are also known to change with thickness of the sample, introducing more uncertainty into the problem. C_c is described as the Paris law proportional constant at the surface where there is plane stress condition, so would fatigue tests done on a thin thru-wall crack specimen produce C_c? Or are C_c or C_a completely unique from any type of thru-wall crack results? The relationship between C_c and C_a in eqns (3.3) and (3.4) are only applicable to isotropic materials. Anisotropic materials, such as pipeline steel, could have unique relation between C_c and C_a. Newman and Raju assumed the constant *m* is the same at the depth and

surface, but the validity of that assumption still need to be proven even though it provides good fit to experimental data. Usually, *m* values obtained from thru-wall crack could be applied to surface cracks with good results. The fact remains there is still a lot not understood about surface crack propagation. More tests need to be done to correlate thru-wall fatigue resistance to surface crack fatigue resistance. With the assumptions in eqns (3.3) and (3.4), a lot of the detail surrounding C_c or C_a are omitted. The user just has to select the correct assumption. Whether those relations between C_c or C_a are true is a matter that requires more research, but these relations allows for crack shape predictions that agree with experimental results.
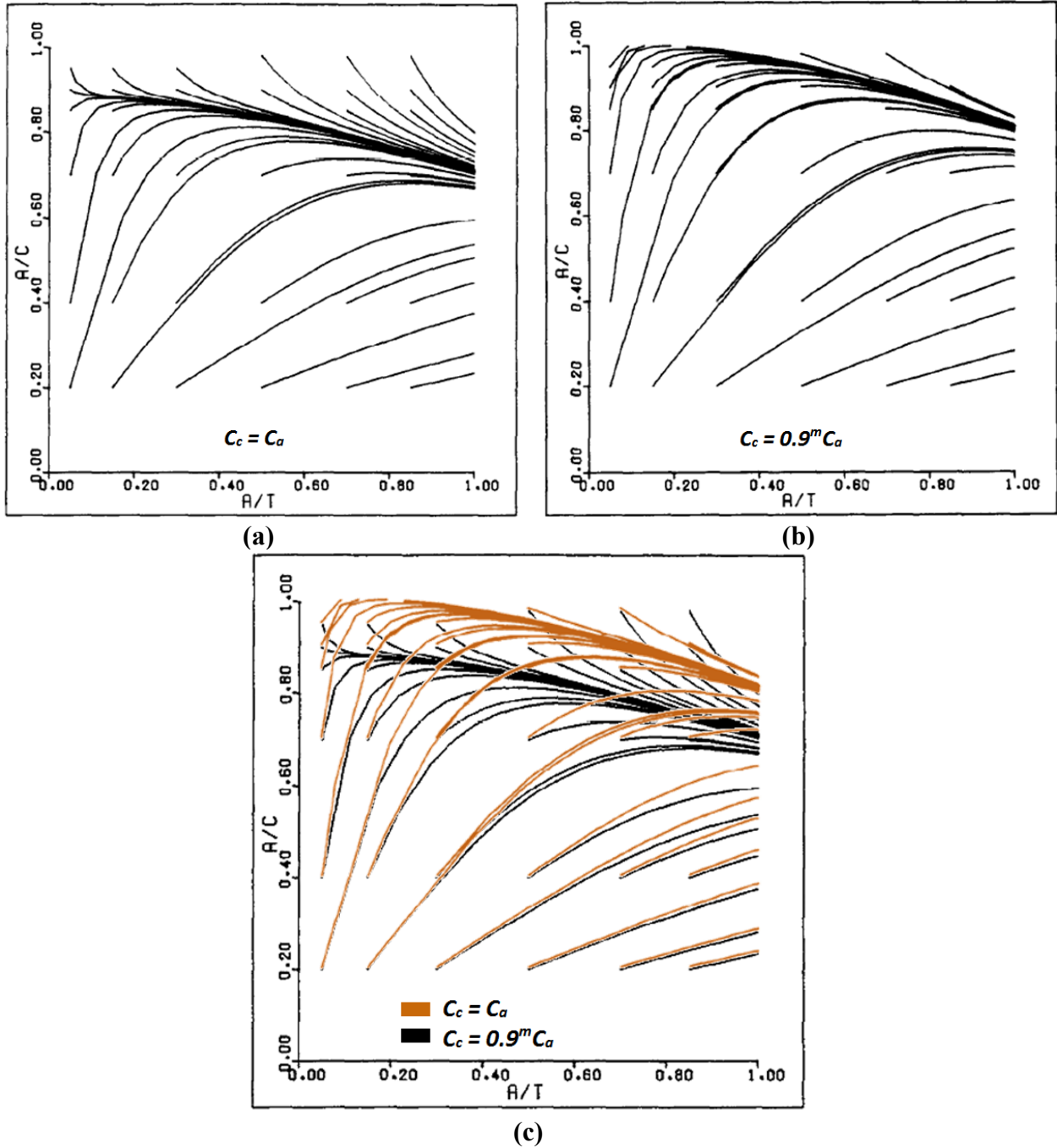
Figure 3-2 Comparison of shape evolution curves, assuming m = 3.5, for various initial crack geometries: (a) $C_c = C_a$ **assumption. (b)** $C_c = 0.9^m C_a$ **assumption. (c) Direct comparison of the two assumptions. Reproduced from [124], with permission from Elsevier.**
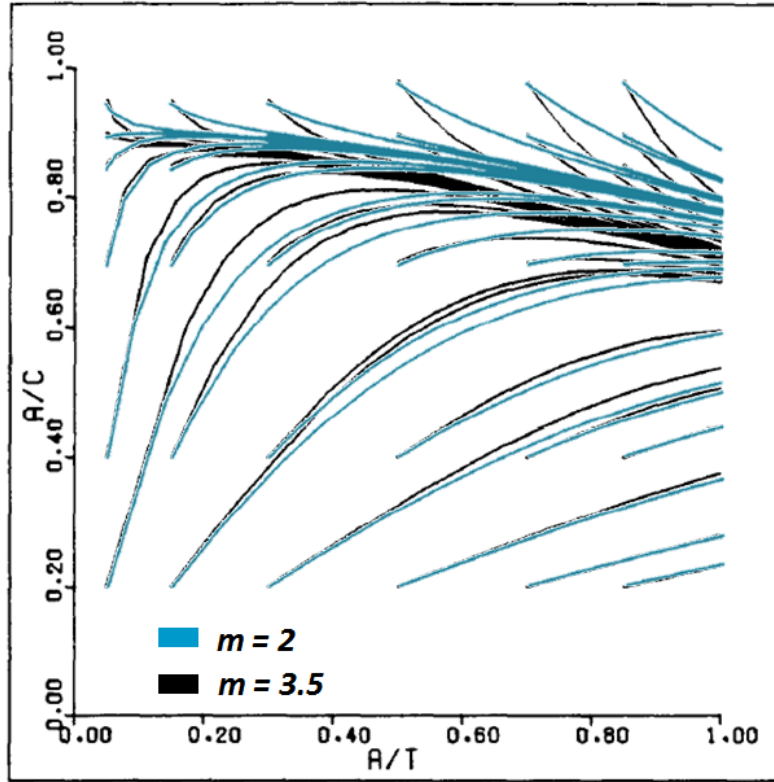
Figure 3-3 The effect of *m* on shape evolution curve. $C_c = C_a$ assumption used. Adapted from [124], with permission from Elsevier.
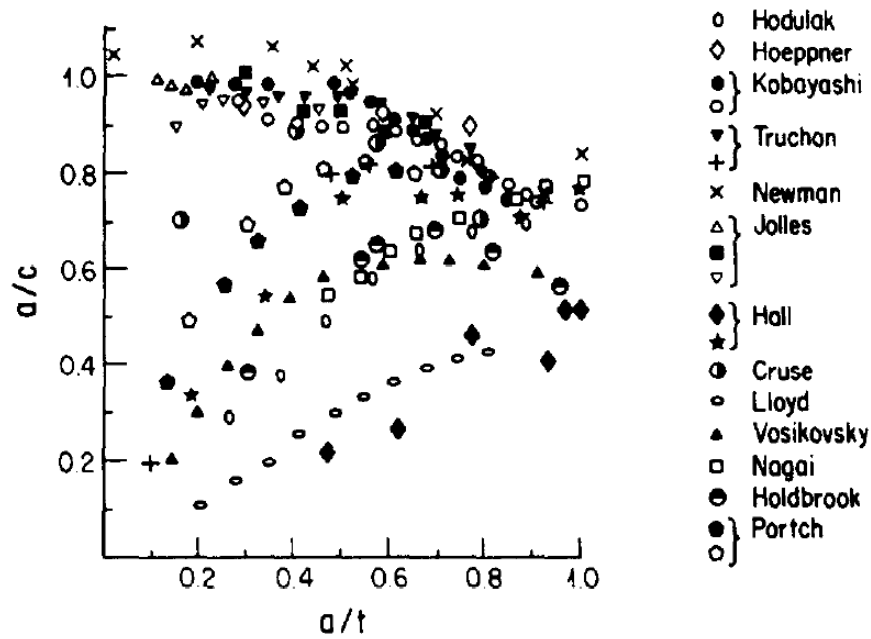
Figure 3-4 Crack Shape changes based on experimental data from various sources. Reproduced from [124], with permission from Elsevier.
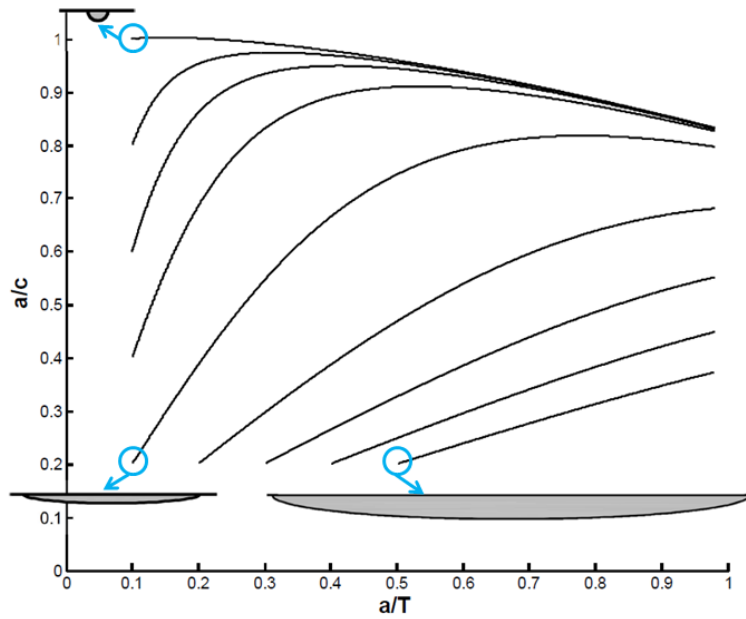
Figure 3-5 Crack shape development's dependency on initial crack geometry (i.e. initial a/c and a/t ratios). The shapes shown are scaled relative to each other to help readers visualize starting geometries. The shape evolution curves are based on m = 3, and the assumption $C_c = 0.9^m C_a$ was used.
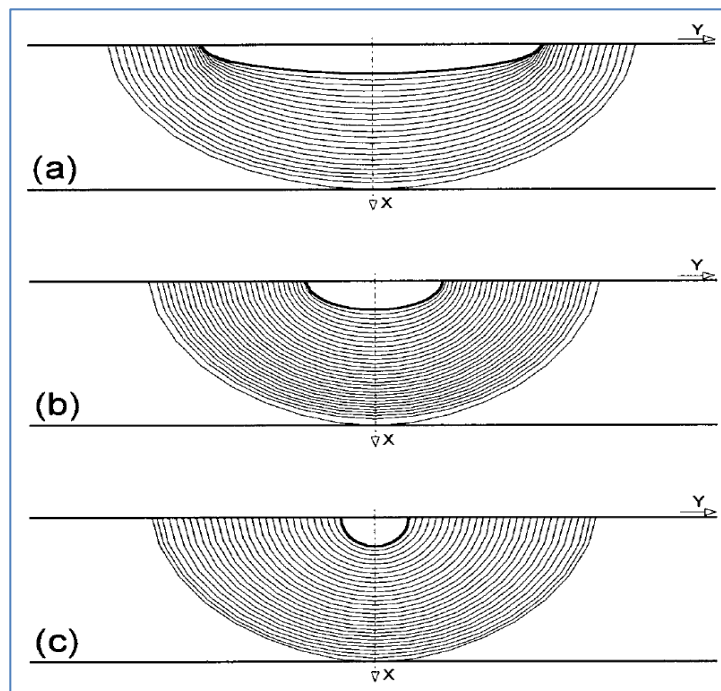
Figure 3-6 Fatigue crack shape development under pure tension for different starting flaw shapes. Reproduced from [130], with permission from Elsevier.

3.4   Experimental Setup
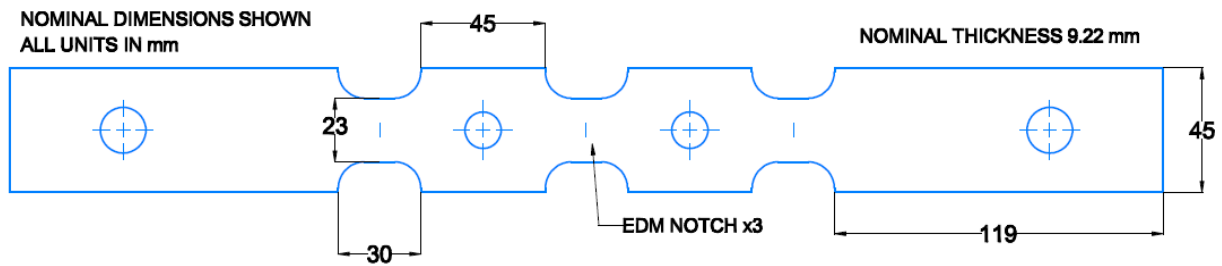
Figure 3-7 Surface crack tensile specimen dimensions
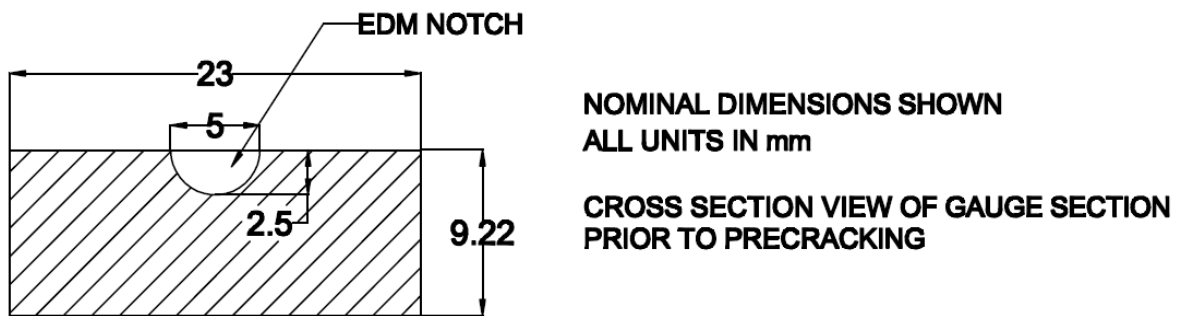
Figure 3-8 Surface crack specimen gauge section – cross-section view

X65 tensile samples containing surface cracks were used for this study. Figure 3-7 and Figure 3-8 shows the initial dimensions of the samples used. The samples were machined from a section of X-65 pipe that has experienced SCC failure. The machined portion came from undamaged portions of the pipe. The long side of the sample is aligned in the longitudinal direction of the pipe. All the EDM notches are aligned in the circumferential direction of the pipe. Precracking was performed on the sample, and then corrosion fatigue tests were later conducted on the precracked specimens. Chapter 4 and 5 covers details regarding the corrosion fatigue tests. This chapter covers the crack growth behaviour during precracking in air.

Each sample contains three reduced gauge sections containing EDM notches. Surface fatigue cracks are initiated from these notches. Each EDM notch on the sample was labelled as top, middle, or bottom (T, M, or B), based on its position when the sample is first placed into a vertical tensile tester. Since the sample is symmetrical, the positions are arbitrarily assigned. Each crack is named in the convention "RL# X", where # refers to the sample number, and X refers to the position (T, M, or B).

The reduced gauge sections measures 30mm x 23 mm x 9.22 mm ($l \times w \times t$) nominally. The EDM notches are semicircular and are nominally 5mm long and 2.5 mm deep ($a = 2.5$mm, $2c = 5$mm). The width of the EDM notches is around 200 μm.

Prior to precracking, the outer surface of the sample was hand ground to a 600 grit finish. The sample was cleaned in an acetone ultrasonic bath and then ethanol bath in order to remove grinding particles. The sample was then dried with compressed air.

The original thickness of the sample prior to milling (t_o) was measured using a micrometer (resolution of 0.001 inches) after grinding is complete. Fatigue precracking was then carried out on the sample using a tensile tester. The sample is taken out of the tensile tester at regular intervals in order to check growth rate and ensure crack length has reached the desired target. The crack growth target is to reach a surface length ($2c_o$) of 10600 μm (±125 μm). The reason this target length was selected is discussed in section 3.6. Crack growth rate may deviate during precracking. To combat this, slow-growing cracks may be isolated using the pin holes shown in Figure 3-7 and placed into the tensile tester with pin adapters attached. Extra fatigue cycles can be applied to slow-growing cracks until they catch up with the longer cracks. The goal is to create cracks of similar size on the same sample prior to corrosion fatigue tests.

Precracking was performed on a computer-controlled MTS series 312 servohydraulic load frame. Fatigue waveforms are inputted through the Instron Wavemaker software. The precracking involves multiple load steps where the load is continuously decreased, in accordance with ASTM standard E647-15 [132]. Samples were precracked in air using a frequency of 5 Hz, and R ratio of 0.1. Table 3-1 summarizes the precracking steps used. Step I was used to initiate the crack only, so little to no growth is achieved during this step. The c_o range in the other steps is a rough guideline only. Step IV used a constant K approach. K is kept relatively constant by maintaining the crack growth rate at the surface at around 1×10^{-8} m/cycle. The crack length is measured regularly to check the growth rate during step IV. If the crack growth rate has started to increase significantly, the load was shed by a small amount in order to maintain the growth rate of 1×10^{-8} m/cycle. Later calculations revealed that the K_{max} at the surface and depth were maintained around 17.4 and 15.9 MPa√m during this step.

Table 3-1 Precracking steps using load shedding method

Precracking Step	% SMYS	c_o range (mm)
Step I	65.0%	2.500
Step II	58.5%	2.500 – 3.060
Step III	52.7%	3.060 – 3.550
Step IV	50% to 33%	3.550 – 5.300

Step IV growth rate was maintained around 1×10^{-8} m/cycle in order to reduce the in-lot variability of the material during precracking. It is well known that when the crack growth rate drops below 10^{-8} m/cycle, the within-lot variability increases significantly [132]. The samples used in this study contain three cracks each, and maintaining the same growth rate among all three cracks is difficult when the surface growth rate is below 10^{-8} m/cycle, therefore the constant growth rate approach was used.

The crack length on the original surface ($2c_o$) was measured under an optical microscope with a manual xy micrometer stage. The micrometer stage has a resolution of 10µm. The optical microscope has a 40x objective lens and a reticle in the eyepiece to allow measurement from crack tip to crack tip. To obtain half-length measurement (c_o), the overall length was divided by two.

After precracking is complete, the outer surface is milled down in order to remove most of the EDM notch. This leaves behind a fine surface crack that is more representative of SCC and ready for corrosion fatigue tests. The average amount of thickness removed was 2.35mm, and that was sufficient to remove the entire EDM notch for most samples. The thickness removed is less than the nominal depth of the EDM notch in most cases, due to the machining tolerance of EDM process. The amount of thickness milled off (t_m) is calculated as the original thickness (t_o) minus the thickness after milling (t_f):

$$t_m = t_o - t_f \qquad (3.7)$$

The thickness after milling (t_f) is measured after the milled surface has being ground and polished to a 1 µm finish. The crack length on the milled surface ($2c_m$) was also measured. The

crack length on the milled surface (c_m) is needed to calculate the SIF prior to the corrosion fatigue test. It is also used for estimating crack depth in the process described in section 3.7.

The actual crack depth that resulted from precracking is needed to verify the shape prediction. The crack depth could only be measured after a sample has been fractured. The sample was fractured after completion of corrosion fatigue testing. The final fracturing process is described in detail in Chapter 4. Figure 3-9 shows a fracture surface that has undergone precracking, milling, and then corrosion fatigue tests. Due to the different environmental and loading conditions during precrack and corrosion fatigue tests, the fracture surface morphologies are also very distinct from each other. The precrack region has a rough morphology, which appears dark when viewed under a stereomicroscope. The corrosion fatigue regions have a quasi-cleavage morphology with large smooth facets that appears shinier under a microscope. Since the precrack and corrosion fatigue region can be easily distinguished, the crack depth (a_m) can be easily measured to verify the shape evolution predictions.
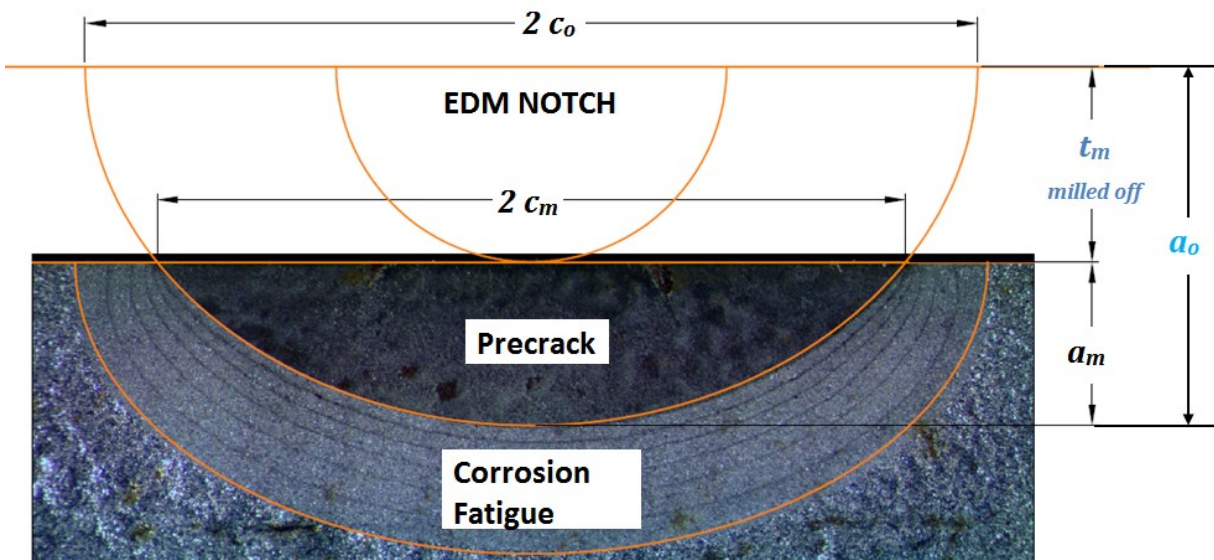
Figure 3-9 The cleaned fracture surface of a crack that has undergone precracking, milling, and then corrosion fatigue tests. The image is taken with a stereomicroscope. The precrack region is dark, and easily distinguishable from the corrosion fatigue region. Dimensions in black are directly measureable. Dimensions shown in blue are derived from other measurements.

3.5   Precracking and Shape Evolution

Eqns (3.5) and (3.6) govern the crack shape evolution of surface cracks under fatigue loading. This section demonstrates how to use these equations to predict the growth of crack during precracking. The crack depth can also be accurately predicted using the shape evolution behaviour. Since precracking is done in air, the Paris law would give a good prediction.

3.5.1 Results and Discussion

Figure 3-10 shows the initial and final geometries of precrack, as well as the shape evolution curves for $m = 2.831$. The m value of 2.831 for X65 is obtained from [133]. The initial starting geometry (red circle) is assumed to be the nominal EDM dimension (5 mm long and 2.5 mm deep). The samples have not been milled, and have a thickness of around 9.22 mm. The blue dots represent the actual shapes at end of precracking (a_o/c_o and a_o/t_o). Note that the depth of crack from the original surface (a_o) is not directly measurable, since the sample had undergone milling and testing before fracturing. The crack depth from the milled surface (a_m) however, is measurable from the fractograph as seen in Figure 3-9. a_o can be calculated as: $a_o = a_m + t_m$. Where t_m is the amount of thickness milled off, which is calculated by subtracting the remaining thickness after milling from the original thickness. Two shape evolution curves are shown, based on equations (3.5) and (3.6). The shape evolution differential equations were solved numerically with the following conditions: $m = 2.831$ [133], $t = 9.22mm$, $c_{o,i} = 2.5mm$, $a_{o,i} = 2.5mm$. From Figure 3-10, it is clear that eqn (3.5), with the assumption $C_c = C_a$, is the better fit for the experimental data.

Table 3-2 and Table 3-3 show the depth prediction results for all of the cracks that had undergone precracking. Equations (3.5) and (3.6) were solved numerically to obtain the relationships between a_o and c_o. The following conditions were used: $m = 2.831$ [133], $t = 9.22mm$, $c_{o,i} = 2.5mm$, $a_{o,i} = 2.5mm$. Both a_o and a_m predictions were compared to measured values. a_o cannot be measured directly, as mentioned in the previous paragraph. Therefore the percentage error for a_m should be used to evaluate prediction accuracy since a_m can be measured directly. From the two tables, it is clear that eqn (3.5), with the assumption $C_c = C_a$, produced very accurate depth predictions, with an average percentage error for a_m of just 7.5%.

These were impressive results since the depth predictions were made based on just one physical measurement of the crack (c_o).
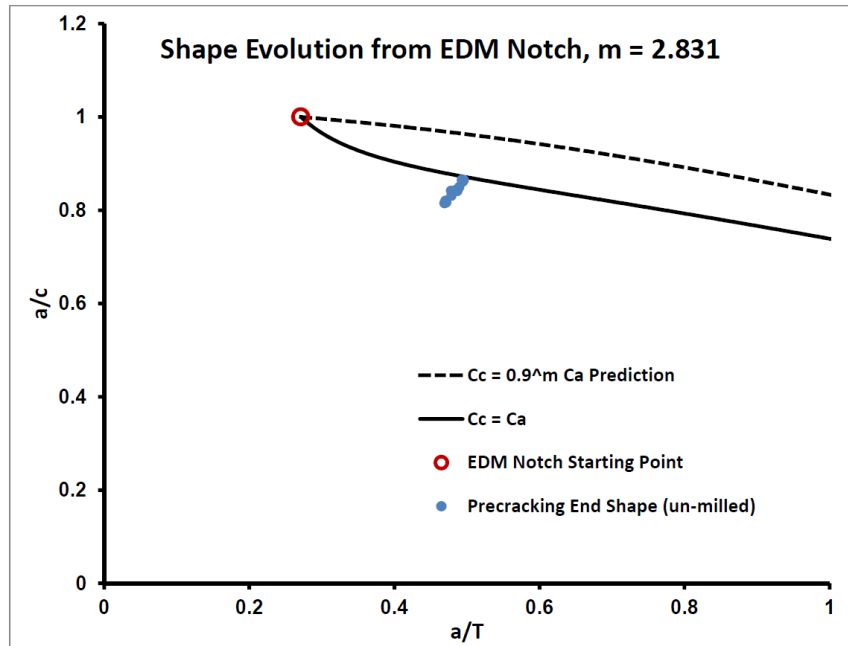
Figure 3-10 Shape evolution for precrack growing from EDM notches on the sample shown in Figure 3-7. The $C_c = C_a$ assumption provides a better fit for the experimental data. The a/c and a/t ratios are calculated from crack dimensions prior to milling. The m value of 2.831 for X65 is obtained from [133]

Table 3-2 Prediction of crack depth using eqn (3.6). $C_c = 0.9^m C_a$ assumption used. m = 2.831 from [133]

$C_c = 0.9^m C_a$ m = 2.831			a_o predictions Depth from original surface			a_m predictions Depth after milling		
Crack Name	C_o (µm)	t_m (µm)	a_o predicted (µm)	a_o measured (µm)	prediction error	a_m predicted (µm)	a_m measured (µm)	prediction error
RL5 T	5313	2347	5062	4414	14.7%	2715	2067	31.4%
RL5 M	5300	2347	5051	4468	13.0%	2704	2122	27.5%
RL5 B	5288	2347	5041	4570	10.3%	2694	2223	21.2%
RL6 T	5255	2357	5013	4546	10.3%	2656	2189	21.3%
RL6 M	5293	2358	5045	4558	10.7%	2687	2200	22.1%
RL6 B	5238	2352	4998	4409	13.4%	2646	2057	28.6%
RL7 T	5320	2350	5068	4500	12.6%	2719	2151	26.4%
RL7 M	5323	2358	5070	4347	16.6%	2712	1988	36.4%
RL7 B	5313	2353	5062	4515	12.1%	2709	2162	25.3%
RL8 T	5338	2336	5083	4491	13.2%	2748	2155	27.5%
RL8 M	5315	2358	5064	4334	16.8%	2706	1976	37.0%
RL8 B	5298	2327	5049	4348	16.1%	2723	2021	34.7%

Table 3-3 Prediction of crack depth using eqn (3.5). $C_c = C_a$ assumption used. m = 2.831 from [133]

$C_c = C_a$			a_o predictions Depth from original surface			a_m predictions Depth after milling		
Crack Name	C_o (µm)	t_m (µm)	a_o predicted (µm)	a_o measured (µm)	prediction error	a_m predicted (µm)	a_m measured (µm)	prediction error
RL5 T	5313	2347	4623	4414	4.7%	2276	2067	10.1%
RL5 M	5300	2347	4613	4468	3.2%	2266	2122	6.8%
RL5 B	5288	2347	4604	4570	0.7%	2257	2223	1.5%
RL6 T	5255	2357	4580	4546	0.7%	2223	2189	1.5%
RL6 M	5293	2358	4608	4558	1.1%	2249	2200	2.2%
RL6 B	5238	2352	4567	4409	3.6%	2215	2057	7.7%
RL7 T	5320	2350	4628	4500	2.9%	2279	2151	6.0%
RL7 M	5323	2358	4630	4347	6.5%	2272	1988	14.3%
RL7 B	5313	2353	4623	4515	2.4%	2269	2162	5.0%
RL8 T	5338	2336	4641	4491	3.4%	2306	2155	7.0%
RL8 M	5315	2358	4625	4334	6.7%	2266	1976	14.7%
RL8 B	5298	2327	4612	4348	6.1%	2285	2021	13.1%

These results above show that using shape evolution equations can be an effective strategy to predict crack depth. However, reasonable assumptions have to be made for the values of m and the relation between C_c and C_a. For pipeline steel, where the initial stress riser is a small semi-circular EDM notch, eqn (3.5) is a better prediction model than eqn (3.6). The assumptions that worked for this case might not apply to other materials or to differently shaped EDM notches. For researchers looking into applying this technique for their application, it is recommended that an extra set of specimens should be made just to confirm the precrack growth behaviour. This allows the user to tweak m values and select whether eqn (3.5) or eqn (3.6) works better for their application.

The numerical solutions to eqns (3.5) and (3.6) can also be used to determine the target surface length required in order to achieve a certain crack depth. In this manner, these equations are valuable tools that can help researchers design fatigue cracks of different sizes. Section 3.5.2 shows how powerful these equations can be.

3.5.2 Precracking Strategy

This section will discuss some of the design strategy that can be used to precrack to a wide range of shape and sizes.

3.5.2.1 Shape of EDM Notch

In the previous section precracking was done on a semicircular EDM notch. Other notch shape could be used as well, but the result could be less predictable as illustrated in Figure 3-11. For a long shallow notch, the crack does not initiate on the entire crack front, so the results might deviate from the predictions. For a semi-circular notch, the stress concentration is very similar on the entire crack front initially, and a sharp crack tip can be quickly established on the entire crack front. Figure 3-6 c) shows the crack prefers to grow evenly all along the crack front for a semi-circular flaw. Shape prediction models are meant for sharp cracks, not blunted notches, therefore the semi-circular notch would produce results closer to predicted values.

Initiating cracks from a long shallow notch also present some technical challenges. As seen in Figure 3-6 a) and Figure 3-11, the crack prefers to grow in the depth direction. The surface grows slowly initially, and will quickly accelerate to match the growth rate in the depth direction.

It is easy to overshoot a crack growth target, especially if the desired crack length is in the range where the surface growth starts to accelerate. Initially, the crack would not appear to grow on the surface for a long time, and can lead the researcher to apply more cycles than necessary in order to encourage growth. When the surface growth rate does pick up, the growth target might have been overshot, and the depth is much deeper than originally anticipated. Since it's difficult to determine an accurate growth rate at the surface for long shallow cracks, precracking needs to be done with caution. The surface length should be still checked at regular interval to avoid overshooting the target. When surface growth rate start to increase, the crack length should be checked at even smaller intervals. Even if no growth is observed at the surface, the depth is still growing.

Based on the above arguments, a semi-circle is the preferred starting notch shape for surface cracks. The precrack behaviour is more likely to follow shape predictions from eqns (3.5) and (3.6). It is also easier to control the growth of semi-circular cracks since the surface grows at a steady pace, so the risk of overshooting growth target is reduced.
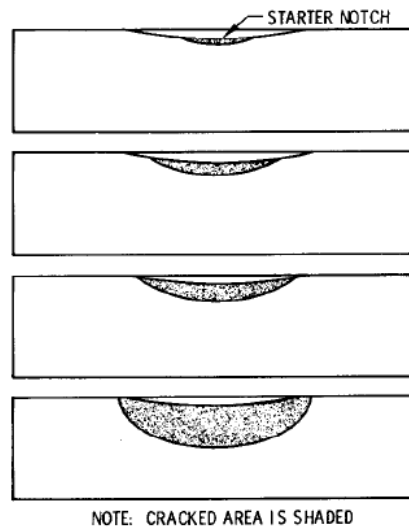
Figure 3-11 Growth sequence of a surface crack initiated from a low a/c ratio EDM notch. Reproduced from [128], with permission from Elsevier.

3.5.2.2 Two-Stage Precrack

This section describes how to achieve different fatigue crack shapes with one-stage precrack and two-stage precrack. Sections 3.4 and 3.5.1 only used one-stage precrack and milling to achieve a final fatigue crack that has a low *a/c* ratio. With two-stage precrack, a fatigue crack with high *a/c* ratio can be produced.

The precracking procedure described below is designed for a semi-circular EDM notch. The goal is to produce fine notchless fatigue cracks of various shapes. Figure 3-12 illustrates the two-stage precracking process. For producing crack shapes suitable for SCC experiments, only the first stage is needed. For the 1st stage precracking (shown in Figure 3-12 (i)), it is carried out on a semi-circular notch. The crack is expected to grow in a manner where the a/c ratio remains close to 1 as the crack grows. The shape evolution equations (eqns (3.5) and (3.6)) can be used to accurately predict shape development as shown in section 3.5.1. The outer surface is then milled to remove the EDM notch, leaving behind a thin notchless crack with low a/c ratio as shown in Figure 3-12 ii). The long shallow crack shape is ideal for SCC experiments.

For other industries where a more semi-circular crack (higher a/c ratio) is common, a second stage precrack can be added. The 2nd stage of precracking is a continuation after 1st stage precracking has completed. Since the initial crack shape for 2nd stage is long and shallow, the crack prefers to grow in depth more than the surface in order to reach higher a/c ratios as shown in Figure 3-5 and Figure 3-6 a). The same precautions mentioned in section 3.5.2.1 should also be applied here because the surface growth is slow initially and accelerates suddenly. Therefore it is important to monitor crack growth and avoid overshooting the crack growth target.

Figure 3-13 shows an example of a crack that has used the two-stage precracking described in this section. The sample is a test piece not relevant to the corrosion fatigue tests done in this study. The sample was milled after first stage precrack, and continued to second stage precrack. Figure 3-14 shows the shape evolution of the crack during 2nd stage precrack. The a/c ratio of the crack has increased as predicted. The shape predictions curves for both eqns (3.5) and (3.6) are shown. In this case however, eqn (3.6) was found to provide the better shape prediction. This highlight the importance of running validation samples for a specific initial crack shape in order to determine which equation would provide the better fit.

The two-stage precracking procedure can be used to create notchless fatigue crack for a wide range of shapes and sizes. The first stage precrack plus milling is suitable for creating shallow cracks with low a/c ratio. The second stage precrack can be added after milling to create notchless cracks with high a/c ratio. Using eqns (3.5) and (3.6), researchers can design

precracking processes based on either one-stage or two-stage precracking by setting a target shape, and then working backwards to determine the required starting crack shape.

i) Unmilled, notched sample with 1st stage precrack

ii) Notchless long aspect ratio crack, c>a

iii) Notchless semicircular crack, c~a
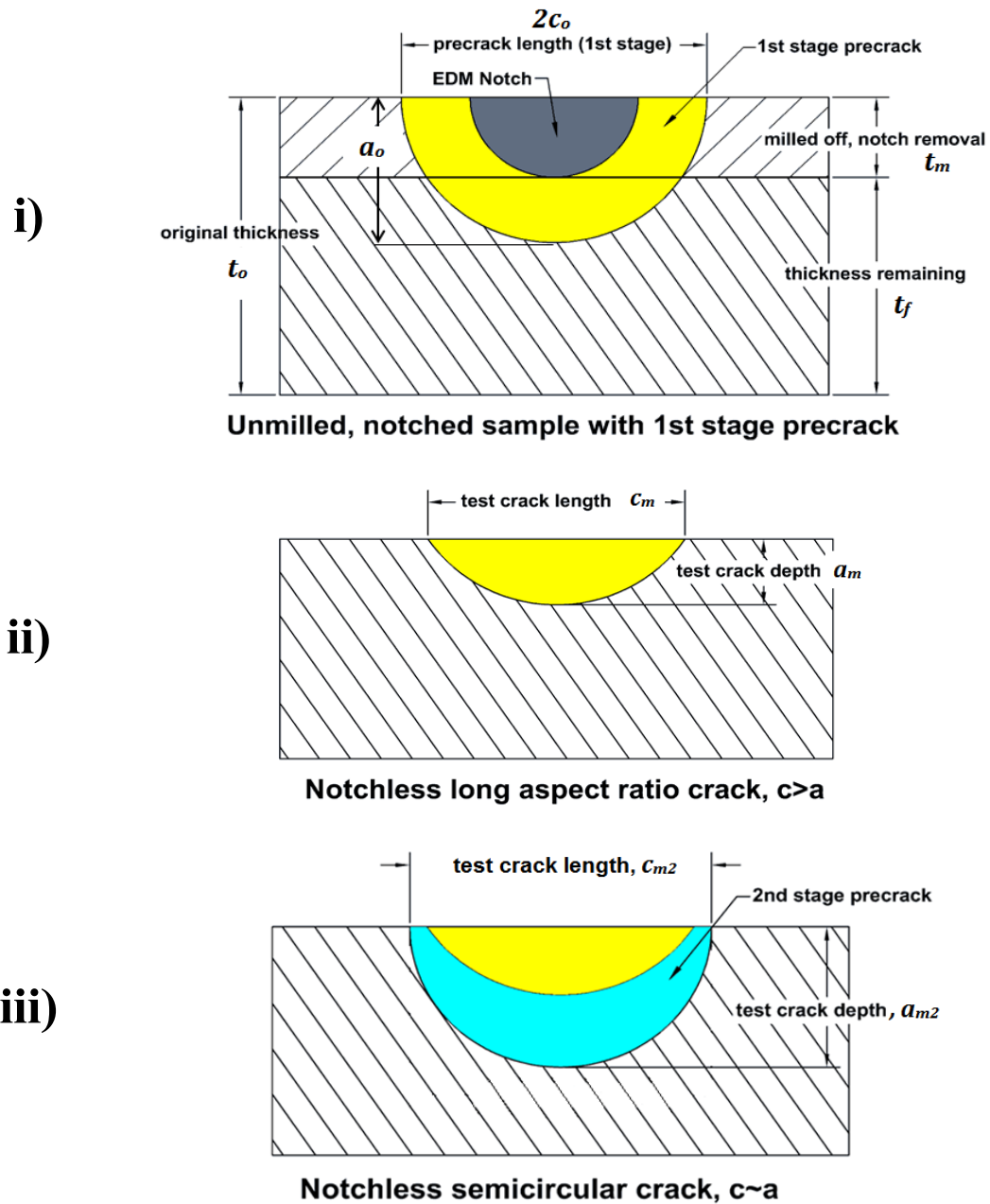
Figure 3-12 Two-stage precracking procedure: i) 1ˢᵗ stage precracking at the original thickness, initiated from semi-circular EDM notch. ii) After milling, the resulting fatigue crack has a long aspect ratio that is suitable for SCC experiments. iii) If a crack with higher *a/c* ratio is desired, 2ⁿᵈ stage precrack can be carried out on the crack shown in step ii.
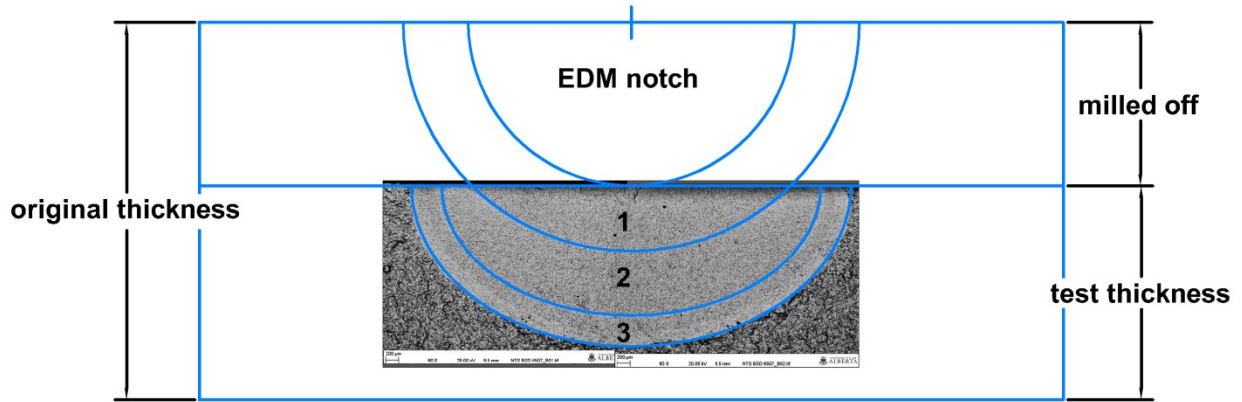
Figure 3-13 Fractograph of a semi-elliptical surface crack specimen made from X65 steel. Region 1 and 2 are 1st and 2nd stage precrack, respectively. The 1st stage precrack was initiated from the EDM notch. The 2nd stage precrack was performed after milling, allowing the crack shape to become more semi-circular. Region 3 is the growth zone of the a corrosion fatigue test.
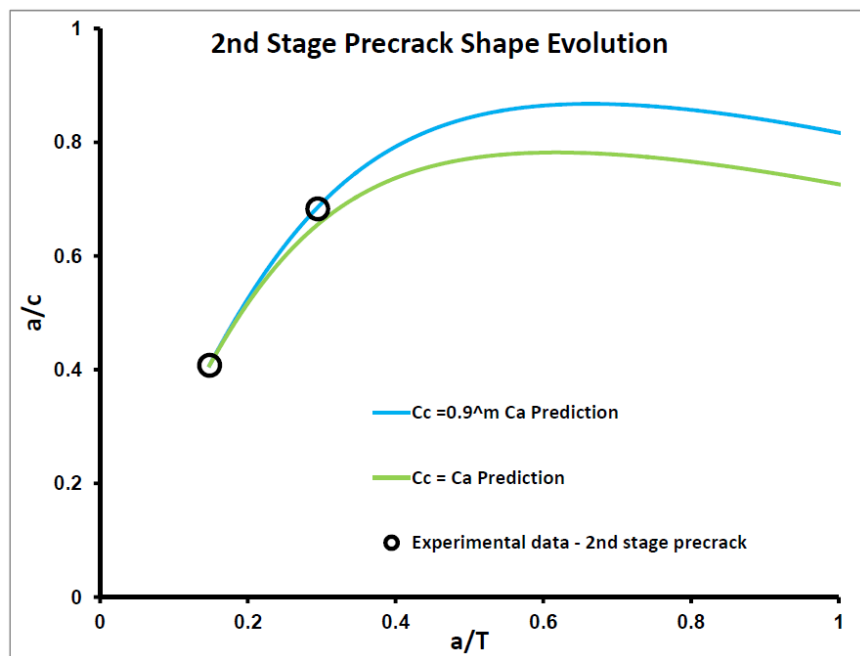
Figure 3-14 Shape evolution curves for the second stage precrack shown in Figure 3-13. m = 2.831 The m value of 2.831 for X65 is obtained from [133]

3.6 Precracking Steps & Consideration for Plastic Zone Size

SCC testing requires notchless precracked samples. As was discussed in the previous sections, the outer surface of the surface crack samples are milled down to remove the EDM notches. However, the milling process also changes the geometry of the sample, and additional consideration has to be made for the plastic zone size during precracking and testing. As stated in ASTM E647-15 [132], the plastic zone size at the start of testing must be larger than the plastic zone formed during precracking in order to avoid retardation effects.
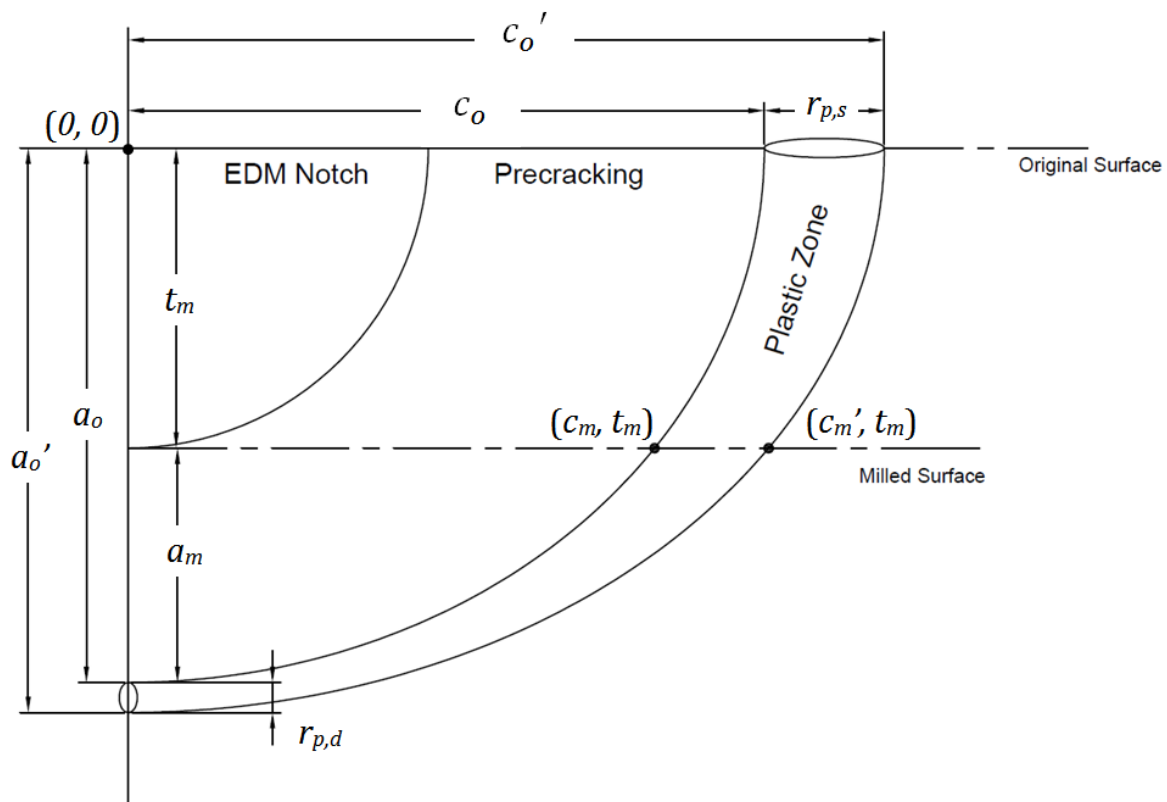
Figure 3-15 Schematic of the plastic zone generated during precracking for a surface crack

Figure 3-15 shows a schematic of a surface crack during precracking and the plastic zone generated. It is assumed that the depth is in plane strain, and the surface is in plane stress. The plastic zone sizes at the depth and surface can be estimated using the Irwin approximation given in eqns (3.8) and (3.9):

Plane strain plastic zone size at depth [134]
$$r_{p,d} = \frac{1}{3\pi}\left(\frac{K_{max,depth}}{\sigma_{YS}}\right)^2 \qquad (3.8)$$

Plane stress plastic zone size at surface [134]
$$r_{p,s} = \frac{1}{\pi}\left(\frac{K_{max,surf}}{\sigma_{YS}}\right)^2 \qquad (3.9)$$

Figure 3-15 also introduced some new variables: c_o', a_o' and c_m':

c_o' and a_o' are the extent of the precrack at the surface and depth, respectively. They capture the both physical dimension of the crack as well as the plastic zone size. c_m' is the extent of the precrack at the milled surface, in the horizontal direction. The stress state at point (c_m, t_m) is in between plane stress and plane strain, but the exact plastic zone size at this location is unknown since it is difficult to obtain the plastic zone profile along the entire crack front. To work around this, a simple elliptical profile is assumed to exist from the edge of the surface plastic zone to the edge of the depth plastic zone. This elliptical profile marks the estimated outermost extent of the plastic zone along the entire crack. It has a major axis length of c_o', and a minor axis length of a_o'. All coordinates along this elliptical front is referenced from the point (0,0), which is the center of the crack at the original surface. Since the profile of the plastic zone during precrack has been established, the value of c_m' can be determined.

Figure 3-16 shows the extent of the plastic zone during testing on the milled sample. The crack undergoing testing is hatched with red lines. Both the sample and crack geometry has changed after milling. The crack area now has a length c_m and a depth of a_m. The max stress during testing has also increased from precracking. The largest stress used during precracking was 65% SMYS, while the largest stress used during testing was 80% SMYS. The smaller dimensions of the crack after milling tend to favour smaller plastic zone. However, the larger stress used during the corrosion fatigue test could increase the plastic zone to extend past the plastic zone created during precracking. Figure 3-16 illustrates the case of a well-designed precracking procedure in which the extent of the plastic zone during testing was able to extend beyond the extent of the plastic zone created during precracking. For the test results to be valid (i.e. not influenced by plastic zone formed during precracking), the following conditions must be met:

$$a_{o,test}' > a_o' \qquad \text{and} \qquad c_{m,test}' > c_m' \qquad (3.10)$$

A common point at the center of the original surface labelled (0,0) in Figure 3-16 was used as the reference point for $a'_{o,test}$, a_o', $c'_{m,test}$, and c_m' measurements. The plastic zone sizes $r_{p,s,test}$ and $r_{p,d,test}$ could be determined using eqns (3.8) and (3.9).
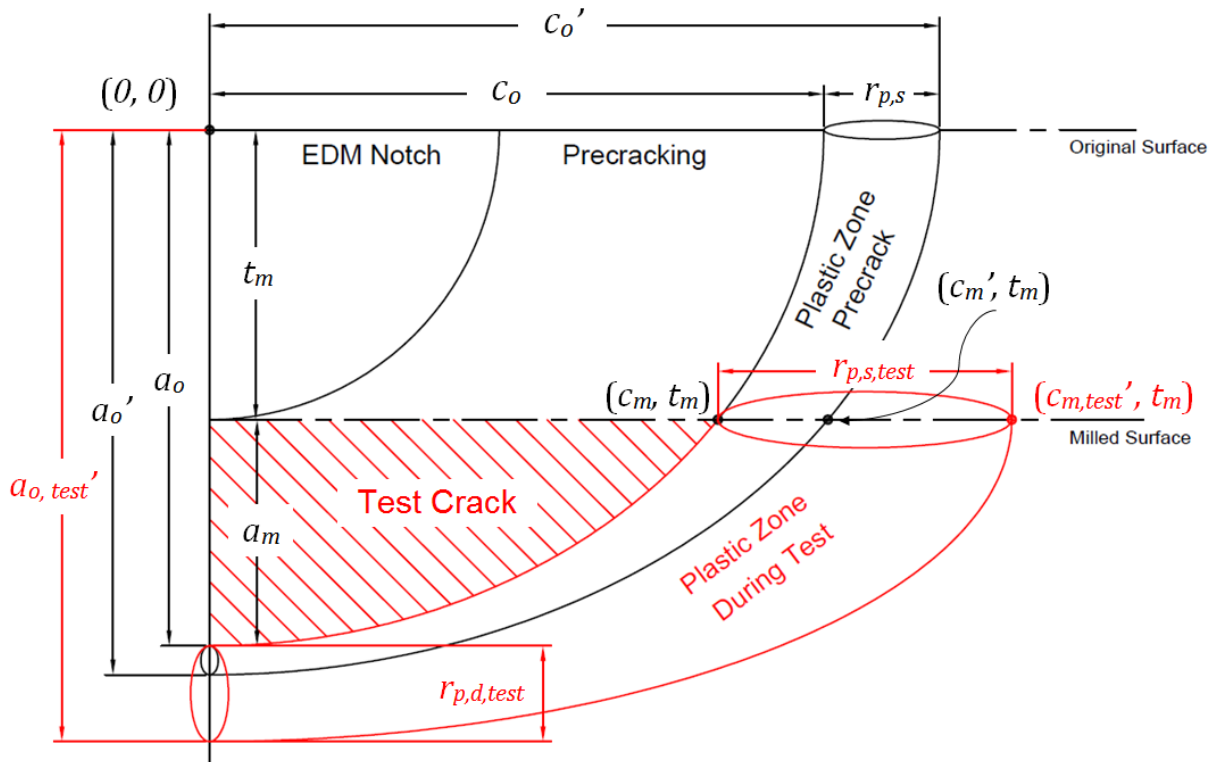
Figure 3-16 A correctly precracked sample in which the plastic zone generated during the test (in red) is able to reach beyond the extent of the plastic zone generated during precracking.

Since $a'_{o,test}$, a_o', $c'_{m,test}$, and c_m' depend on so many factors, it is recommended that the crack extent during precracking and testing are compared for a large range of precrack size in order to ensure the criteria in eqn (3.10) are met. It is easier to meet the criteria if the cracks are precracked to a larger size. For smaller precrack sizes, the extent of the precracking is often greater than the plastic zone generated during the corrosion fatigue test.

The X65 sample and precracking steps used for this study (see section 3.4) are evaluated to see if they would meet the plastic zone extent criteria in eqn (3.10). The process is described below:

85

Calculating the Crack Extent during Precracking (a_o' and c_m')

To determine the extent of the precrack at the milled surface, c_m', the overall process is:

- Find c_o'
- Find a_o'
- Fit elliptical equation with axis lengths of c_o' and a_o'
- Find c_m' at t_m by using the using the elliptical equation from the previous step

First, the plastic zone size must be determined. In order to calculate the plastic zone size during precracking, both c_o and a_o must be determined. c_o is easily measurable, but a_o must be estimated using shape evolution equations or other methods. The differential equations (3.5) and (3.6) could be solved as shown in section 3.5.1 in order to estimate a_o. This approach is not used here since actual crack depth data is available:

Table 3-4 Crack length at original surface and corresponding a/c ratio

	Initial: EDM Notch	Final: Precracking Ended
Average precrack half-length (c_o) at original surface	$c_{o,i} = 2.5\ mm$	$c_{o,f} = 5.3\ mm$
Average precrack depth (a_o) measured from original surface, prior to milling	$a_{o,i} = 2.5\ mm$	$a_{o,f} = 4.452\ mm$

The crack depth a_o for any crack length c_o in between $c_{o,i}$ and $c_{o,f}$ can be obtained via linear interpolation using the data in Table 3-4:

$$a_o = \left(\frac{c_o - c_i}{c_f - c_i}\right)(a_{o,f} - a_{o,i}) + a_{o,i} \tag{3.11}$$

The extent of the crack (refer to Figure 3-15) can then be calculated:

$$c_o' = c_o + r_{p,s} \tag{3.12}$$

$$a_o' = a_o + r_{p,d} \tag{3.13}$$

Where $r_{p,s}$ and $r_{p,d}$ are determined using eqns (3.8) and (3.9). The K_{max} value in the plastic zone size equation depends on the load used in the precracking step, and each precracking step has different loads. The yield strength of the metal σ_{YS} is assumed to be 448 MPa for X65 steel. The original thickness is 9.22mm. The gauge section width (2W) is 23mm.

Next, assume an elliptical profile exist between the surface and depth extents:

$$\left(\frac{x}{c_o'}\right)^2 + \left(\frac{y}{a_o'}\right)^2 = 1 \tag{3.14}$$

Where x and y are the coordinates of any point along the extent elliptical front. The point (c_m', t_m) lies on this elliptical front, and can be plugged into eqn (3.14):

$$\left(\frac{c_m'}{c_o'}\right)^2 + \left(\frac{t_m}{a_o'}\right)^2 = 1 \tag{3.15}$$

The average milled off amount is also known: $t_m = 2.35 \; mm$. Therefore c_m' can be solved:

$$c_m' = \sqrt{\left(1 - \left(\frac{t_m}{a_o'}\right)^2\right) c_o'^2} \tag{3.16}$$

Table 3-5 shows the results of the calculations from eqns (3.11) to (3.16) for each step in the precracking process.

Table 3-5 c_m' results for all of the precracking steps

Precracking Step	Max Stress % SMYS	c_o (mm)	a_o (mm)	Surface - before milling			Depth - before milling			c_m' @ t_m = 2.35 mm (mm)
				K_{max} (MPa√m)	$r_{p,s}$ (mm)	c_o' (mm)	K_{max} (MPa√m)	$r_{p,d}$ (mm)	a_o' (mm)	
Step I initiation	65.0%	2.500	2.500	19.7	0.613	3.113	17.5	0.161	2.661	1.461
Step II start	58.5%	2.500	2.500	17.7	0.497	2.997	15.7	0.131	2.631	1.347
Step II End	58.5%	3.060	2.962	19.7	0.618	3.678	17.7	0.165	3.127	2.427
Step III start	52.7%	3.060	2.962	17.8	0.502	3.562	15.9	0.134	3.096	2.319
Step III End	52.7%	3.550	3.337	19.3	0.594	4.144	17.4	0.160	3.497	3.069
Step IV start*	50% to 33%	3.550	3.337	~17.4	0.480	4.030	~15.9	0.134	3.471	2.966
Step IV End*	50% to 33%	5.300	4.452	~17.4	0.480	5.780	~15.9	0.134	4.586	4.963

* Step IV maintained a relatively constant crack growth by gradually decreasing tensile stress, therefore K_{max} is assumed to be constant in this step.

Calculating the Crack Extent during Testing ($a_{o,test}'$ and $c_{m,test}'$)

The calculation for the plastic zone extent during testing is much simpler. The crack front shape is assumed to be elliptical during precracking, therefore the crack length after milling, c_m, can be estimated as:

$$c_m = \sqrt{\left(1 - \left(\frac{t_m}{a_o}\right)^2\right) c_o{}^2} \tag{3.17}$$

The average milled off amount t_m is 2.35 mm. The sample thickness after milling averages 6.87mm. The crack depth after milling, a_m , can be found by subtracting t_m from the a_o. a_o can be determined in eqn (3.11).The max stress used during the corrosion fatigue tests were all set as 80% SMYS. With these information, the plastic zone size for the crack after milling can be determined with eqns (3.8) and (3.9). The milled surface is now exposed, so the plane stress plastic zone equation applies. The depth is still assumed to be at plane strain.

The extents after milling can be calculated as follows (refer to Figure 3-16):

$$c_{m,test}' = c_m + r_{p,s,test} \tag{3.18}$$

$$a_{o,test}' = a_o + r_{p,d,test} \qquad\qquad (3.19)$$

Comparing the Extents during Precrack and Testing

The $a_{o,test}'$, a_o', $c_{m,test}'$, and c_m' values determined using the calculations above are compared in Figure 3-17 and Figure 3-18 below. A large range of precracking size was included. Recall that the EDM notch has $2c_o$ of 5 mm. The x-axis in the figures below was deliberately chosen to be $2c_o$ since it is directly measurable. This makes it convenient to check how long the precrack must be in order to meet the criteria in eqn (3.10). These figures show that in order to overcome the plastic zone influence at both the depth and milled surface, the precrack length $2c_o$ must be greater than 8.5mm. The precrack $2c_o$ target chosen was 10.6mm, which is well above the 8.5mm threshold. Therefore the crack growth during the corrosion fatigue tests were not retarded by the plastic zone generated during precracking.
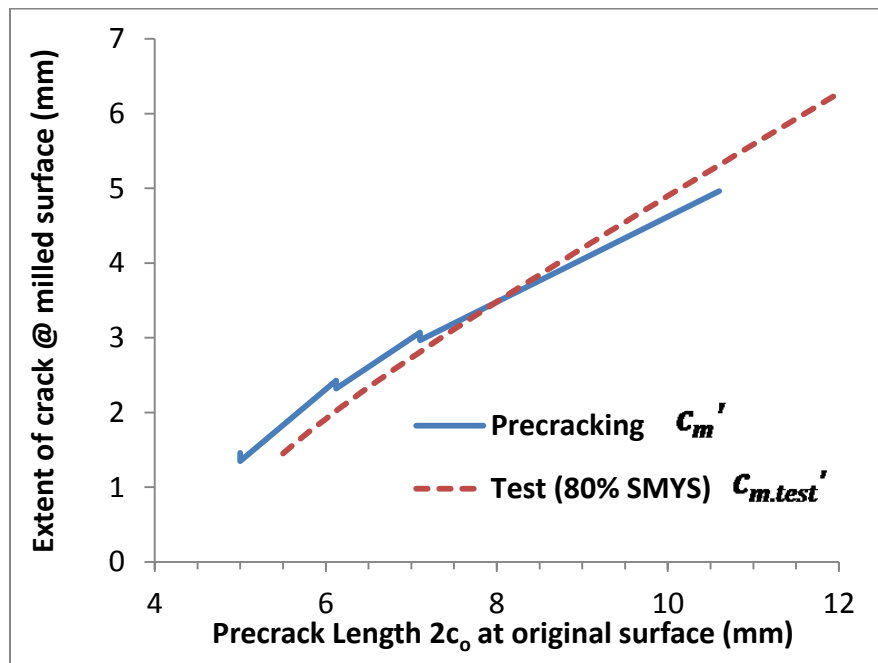
Figure 3-17 Comparison of extent of crack (c_m' and $c_{m,test}'$) at the milled surface for the precracking and testing conditions used
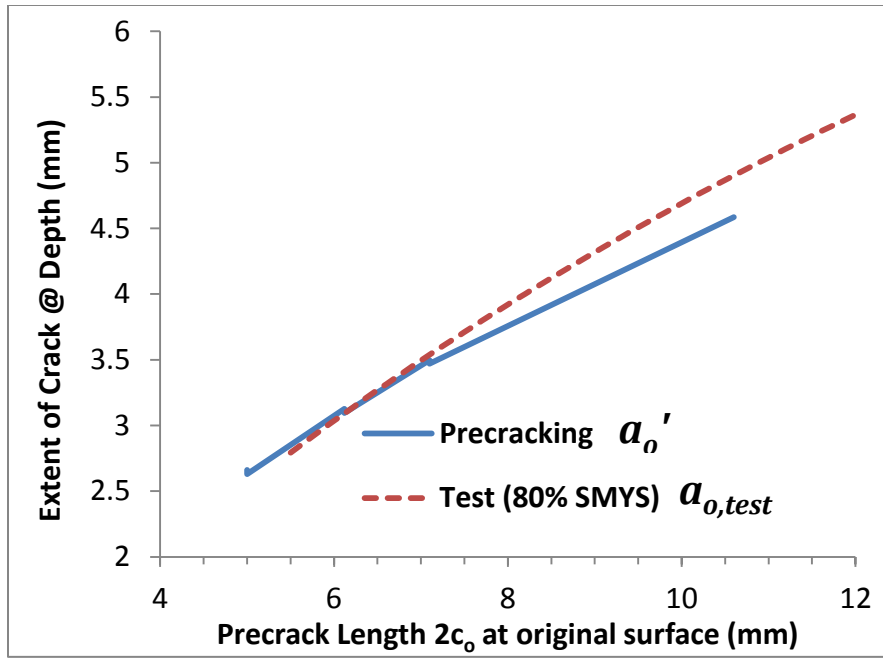
Figure 3-18 Comparison of extent of crack (a_o' and $a_{o,test}'$) at the depth for the precracking and testing conditions used

3.7   Crack Depth Prediction Using Geometrical Method

3.7.1 Introduction

Having accurate prediction of crack depth is critical during the planning phase of corrosion fatigue experiments because the SIF values can be calculated, allowing researchers to estimate crack growth rate and plan the duration of the test. Proper planning of corrosion fatigue test duration can reduce the risk of the sample fracturing during the test. If a sample fractures in a solution cell, the electrolyte can attack the fracture surface and destroy the morphological features.

Various non-destructive examination (NDE) techniques such as ultrasonic and eddy current could also size cracks. However, these methods require expensive equipment that require proper calibration to work effectively. The operator of ultrasonic or eddy current tools must also have extensive training in order to use employ these NDE correctly and be able to correctly interpret the electrical signals generated. The biggest problem with current NDE techniques is they are not accurate for measuring absolute crack depth. It is possible to determine the relative depth of cracks, but to determine absolute depth with accuracy is still a challenge.

Section 3.5.1 described methods to predict the depth of surface cracks during precracking based on the shape evolution behaviour of the crack. However, the accuracy of the technique is highly dependent on whether or not the correct assumptions were made. There are situations where the correct assumptions could not be determined, or there is not enough material to make crack specimens specifically for validating precrack behaviour. In these cases, a geometrical approach could provide an accurate estimate of crack depth.

3.7.2 Description of Technique

The geometrical method employed here only applies individual semi-elliptical surface cracks, not to coalesced cracks. Three measurements are required: surface length c_o, surface length after milling c_m, and thickness milled off t_m. The technique is not a true non-destructive technique since milling is required. It is developed specifically to complement the process of making thin fatigue surface cracks that requires milling.
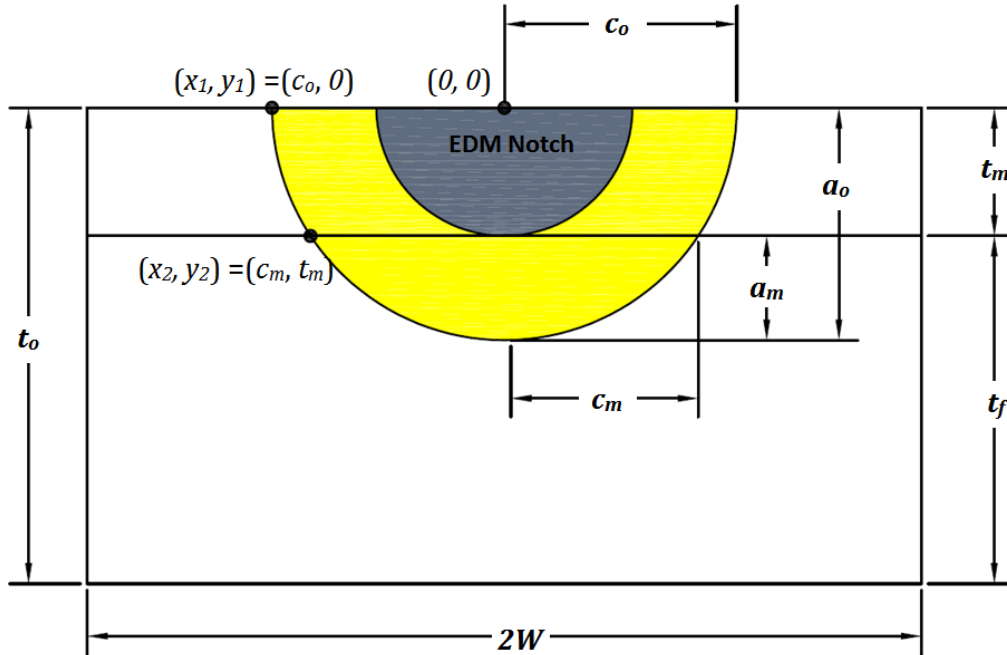
Figure 3-19 Illustration of a semi-elliptical surface crack (yellow) that has grown from an EDM notch after precracking has completed. Two points (x1,y1) and (x2,y2) can be obtained through surface measurements of the crack prior to and after milling. The origin (0,0) is fixed at the midpoint of the original surface. An elliptical/super-elliptical equation can be fitted through the two points shown and used to predict the depth.

Figure 3-19 shows the points of measurement required to use the method: (x_1,y_1) & (x_2, y_2) An equation of ellipse/super-ellipse can be fitted through these two points and used to determine the depth. This method uses the milling operation to its advantage by gaining an additional geometric coordinate in order to fit the elliptical equation. The following variables are required to carry out the fit:

Measurements required:

c_o = Crack surface half-length after precracking, prior to milling
c_m = Crack surface half-length after milling
t_m = Amount of thickness milled off to remove EDM notch

Crack dimensions that need to be determined:

a_o = Crack depth measured from the original surface
$a_m = a_o - t_m$ = Crack depth measured from the milled surface (pre-test depth)

Coordinates required for shape fitting:

(Note: origin is fixed at the midpoint of the original surface prior to milling)

$$x_1 = c_o \qquad \text{Crack surface half-length after precracking, prior to milling}$$
$$y_1 = 0 \qquad \text{y = 0 datum at original surface}$$
$$x_2 = c_m \qquad \text{Crack surface half-length after milling}$$
$$y_2 = t_m \qquad \text{Amount of thickness milled off to remove EDM notch}$$

The elliptical equation can be fitted through the points (x_1, y_1) and (x_2, y_2):

$$\left(\frac{x}{c_o}\right)^2 + \left(\frac{y}{a_o}\right)^2 = 1 \qquad (3.20)$$

However, it was found that a super-ellipse provided a better fit in most cases. A super-ellipse has a similar equation to the elliptical equation, except the power '2' in eqn (3.20) is replaced with the power 'n', which can be any positive number. The equation below is the general equation for a super-ellipse, where a' is the major axis length and b' is the minor axis length.

$$\left(\frac{x}{a'}\right)^n + \left(\frac{y}{b'}\right)^n = 1 \qquad (3.21)$$

A regular ellipse is just a special case of super-ellipse with $n = 2$. The effect of different 'n' values is shown in Figure 3-20. Tweaking the parameter 'n' can result in a better depth prediction.
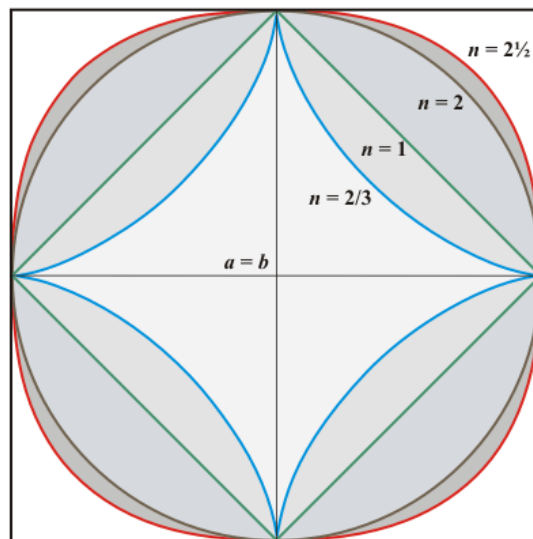
Figure 3-20 Illustration of super-ellipses with different powers of 'n'. Reproduced from [135].

By substituting in the points (x_1, y_1) and (x_2, y_2) into equation (2.13), a system of two equations can be formed:

$$\left(\frac{x_1}{c_o}\right)^n + \left(\frac{y_1}{a_o}\right)^n = 1 \tag{3.22}$$

$$\left(\frac{x_2}{c_o}\right)^n + \left(\frac{y_2}{a_o}\right)^n = 1 \tag{3.23}$$

For eqn (3.22), the second term can be cancelled out since $y_1 = 0$. The variables that need to be determined are a_o and n. The equations can be solved as given below:

$$\alpha = \frac{1}{x_1^n} \tag{3.24}$$

$$\beta = \frac{1 - \alpha x_2^n}{y_2^n} \tag{3.25}$$

$$a_o = \left(\frac{1}{\beta}\right)^{\frac{1}{n}} \tag{3.26}$$

Where α and β are intermediate variables used to calculate a_o. Once a_o is determined, the crack depth after milling can be determined via: $a_m = a_o - t_m$. The most effective way to solve equations (3.24) through (3.26) is to assume a value for 'n' that provides good fit. The optimal values of 'n' can be determined by measuring the actual depth from precracking and comparing that against the predicted depth in equation (3.26). Through trial and error, different n values can be substituted into equations (3.24) through (3.26) in order to find the n value that provides the most accurate predictions of crack depth.

A good first estimate for n is 2, which is a regular ellipse. Small adjustments can then be made to 'n' until an optimal value is reached. Allowing 'n' to be values other than 2 allows the fit to account for deviation from a true ellipse. From experimental measurements and FEM results, surface cracks are known to deviate from a perfect elliptical shape [122,124–127,130]. 'n' could also account for material variations and experimental errors. It is possible that the actual shape of the crack may not conform to the fitted superellipse even though the depth estimate is accurate. Therefore, modifying the value 'n' is just a convenient way to account for shape deviations and other errors in the experiment in order to obtain accurate crack depth measurement, and should not be viewed as a method to predict the true shape of crack.

3.7.3 Results and Discussion

The X65 sample described in section 3.4 was used to evaluate the effectiveness of the crack depth prediction method described here. Table 3-6 shows the coordinate measurements of points (x_1,y_1) and (x_2,y_2) necessary for fitting the super-ellipse equation.

Table 3-6 Coordinate measurements required for elliptical and super-elliptical fit

Sample Name	Crack surface half-length prior to milling $x_1 = c_o$ [μm]	Crack surface half-length after milling $x_2 = c_m$ [μm]	Datum at original Surface $y_1 = 0$ [μm]	Amount of thickness milled off $y_2 = t_m$ [μm]
RL5 T	5313	4599	0	2347
RL5 M	5300	4624	0	2347
RL5 B	5288	4666	0	2347
RL6 T	5255	4549	0	2357
RL6 M	5293	4572	0	2358
RL6 B	5238	4444	0	2352
RL7 T	5320	4633	0	2350
RL7 M	5323	4550	0	2358
RL7 B	5313	4628	0	2353
RL8 T	5338	4520	0	2336
RL8 M	5315	4456	0	2358
RL8 B	5298	4451	0	2327

Table 3-7 shows the predicted value of a_m compared against the measured value on the fracture surface. Predictions using elliptical fit, super-ellipse fit with n = 2.1, and circular fit are shown. The elliptical and super-elliptical fit are performed using eqns (3.24) to (3.26) and the data in Table 3-6. The accuracy of the elliptical fit and super-ellipse fit are similar. The elliptical fit had an average percent error of 8.86%, and the superellipse fit had an average error of 5.97%. The circle fit assumed a semi-circular crack profile centered on the original surface with a radius of c_o. As expected, the circle fit produced the poorest results because the change in a/c ratio was not accounted for.

Various n values were tested in eqns (3.24) to (3.26). For the samples used this study, $n = 2.1$ was found to provide a modest improvement in prediction accuracy. The n value did not deviate much from 2 since the crack shapes only deviated slightly from a true ellipse. For some cracks

the elliptical fit (n=2) produced better results, in other samples the super-elliptical fit (n=2.1) produced better results. Therefore it is recommended that depth prediction should be made with super-elliptical fit using both n = 2 and n = 2.1. This way the range of depth values can be estimated, providing some tolerance in SIF calculations. Depending on the sample and crack shape, other *n* values may provide a better fit.

Table 3-7 Comparison of Geometric Depth Prediction Methods

Sample Name	measured Depth after milling a_m [μm]	Ellipse fit n = 2		Super-ellipse Fit n = 2.1		Circle Fit	
		predicted depth a_m [μm]	Prediction error	predicted depth a_m [μm]	Prediction error	predicted depth a_m [μm]	Prediction error
RL5 T	2067	2343	13.38%	2101	1.68%	2966	43.50%
RL5 M	2122	2456	15.78%	2203	3.83%	2953	39.20%
RL5 B	2223	2644	18.95%	2371	6.65%	2941	32.28%
RL6 T	2189	2352	7.44%	2352	3.65%	2898	32.40%
RL6 M	2200	2323	5.60%	2323	5.30%	2934	33.37%
RL6 B	2057	2093	1.74%	2093	8.77%	2885	40.29%
RL7 T	2151	2429	12.96%	2179	1.30%	2971	38.12%
RL7 M	1988	2187	9.97%	1961	1.38%	2964	49.07%
RL7 B	2162	2439	12.83%	2187	1.18%	2959	36.89%
RL8 T	2155	2057	4.56%	2057	14.42%	3002	39.30%
RL8 M	1976	1969	0.32%	1969	10.63%	2957	49.66%
RL8 B	2021	1964	2.81%	1964	12.86%	2971	47.00%

Figure 3-21 compares the percentage error for the various depth prediction techniques discussed in this chapter. The line chart was used even though the data sets are discrete. This was done to see if any prediction methods showed similar trends. The circle fit and both of the shape evolution predictions showed a similar trend from sample to sample, this was because these predictions depended only on one physical measurement of the crack, which is c_o. As was discussed in section 3.5, the $C_c = C_a$ assumption for crack shape evolution provided good depth estimate, but it is only applicable for a semi-circular notch. Other material and crack shape may demonstrate a preference for $C_c = 0.9^m C_a$ assumption. The elliptical and super-elliptical fit both produced low errors across all samples. They also have the added advantage of being based on physical measurements instead of relying on assumptions.
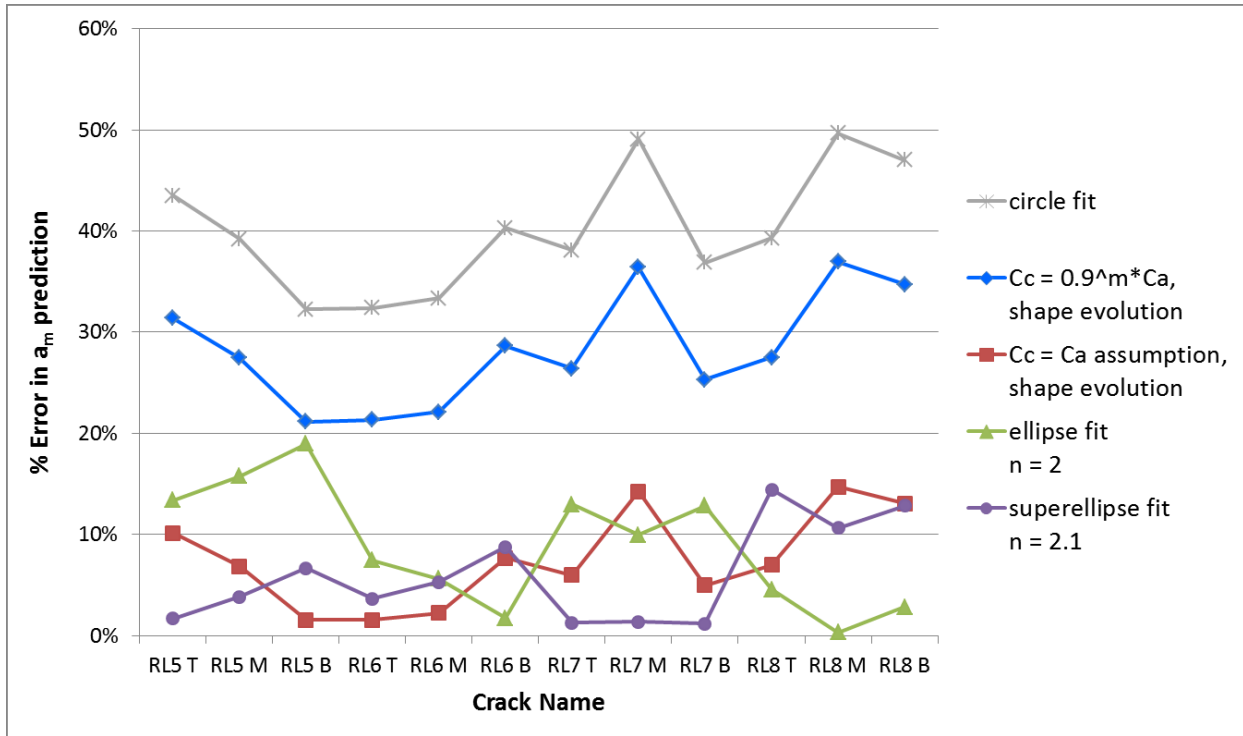
Figure 3-21 Comparison of percentage error for various depth prediction methods

3.8   Conclusions

As more researchers are looking into using surface crack specimens for corrosion fatigue experiments, more robust techniques of preparing the surface crack specimens are necessary. Surface crack specimens are more complex than thru-wall crack specimens because both the surface and depth growth must be considered. This chapter described various techniques that could be used to predict and control the surface crack growth behaviour during precracking. The goal is to introduce techniques that could be used to create fatigue cracks of a wider range of shapes and sizes for corrosion fatigue experiments. The main findings from this chapter are summarized below:

- The crack growth shape evolution during precracking can be predicted accurately using (3.5) and (3.6). For pipeline steel specimen with semicircular EDM notches, eqn (3.5) was able to provide better shape prediction.
- The crack depth after precrack can be accurately predicted using shape evolution curves if correct assumptions for C_c and C_a are made. Eqn (3.5) was able to predict the a_m for the samples in this study with an average of error of only 7.5%.
- The crack depth can also be accurately predicted using super-elliptical fit with 'n' value of 2 and 2.1. With n=2, prediction error averages at 8.86%. For n=2.1, prediction error averages at 5.97%.
- 1st stage precracking followed by milling can create long shallow cracks that are ideal for SCC experiments.
- 2nd stage precrack following 1st stage crack and milling can create cracks with higher a/c ratios
- While milling is necessary to create notchless cracks, it also changes the geometry of the specimen. Additional consideration must be made for the extent of the plastic zone generated during precrack to ensure the test results are not affected by it.

4 Corrosion Fatigue Tests: Experimental Methods

4.1 Introduction

Chapter 3 described the experimental methods used to precrack samples. This chapter focuses on the experimental methods used for the corrosion fatigue tests. Various underload-type spectra are tested on X-65 samples in NNpH environments to study the effect of cycle sequence on crack growth rate. The conditions that need to be simulated during the experiments are:

- NNpH environment with pH in the range of 5 to 7
- Pipe to solution potential at open circuit potential (OCP)
- Pipeline steel samples are from an SCC susceptible pipe
- SCC is in Stage II growth regime according to Chen et al.'s bathtub model [8,111]. During Stage II, crack growth is dominated by corrosion fatigue, with negligible dissolution effect.
- Pipe operating in Class I location with 80% SMYS MAOP
- VAL underload-type spectra applied during testing should simulate oil pipeline operation

4.2 Material

Table 4-1 Composition of X-65 Pipeline Steel Used in Study. Reproduced from [115], with permission from Springer.

Element	C	Mn	Cu	Nb	Cr	Mo	V	Ni	Al	Ti	N	Fe
Composition (wt%)	0.13	1.55	0.05	0.05	0.08	0.01	0.002	0.05	0.042	0.002	0.009	Bal.

X-65 pipe steel was used for this study. Samples were machined from a pipe section that had failed in service. Previous studies by Egbewande et al. [114,115,123] also obtained samples from this same pipe section, and details regarding the chemical composition and microstructure of the steel were already determined in those studies. Table 4-1 shows the composition of the X-65 steel. Figure 4-1 shows the typical microstructure of the steel.
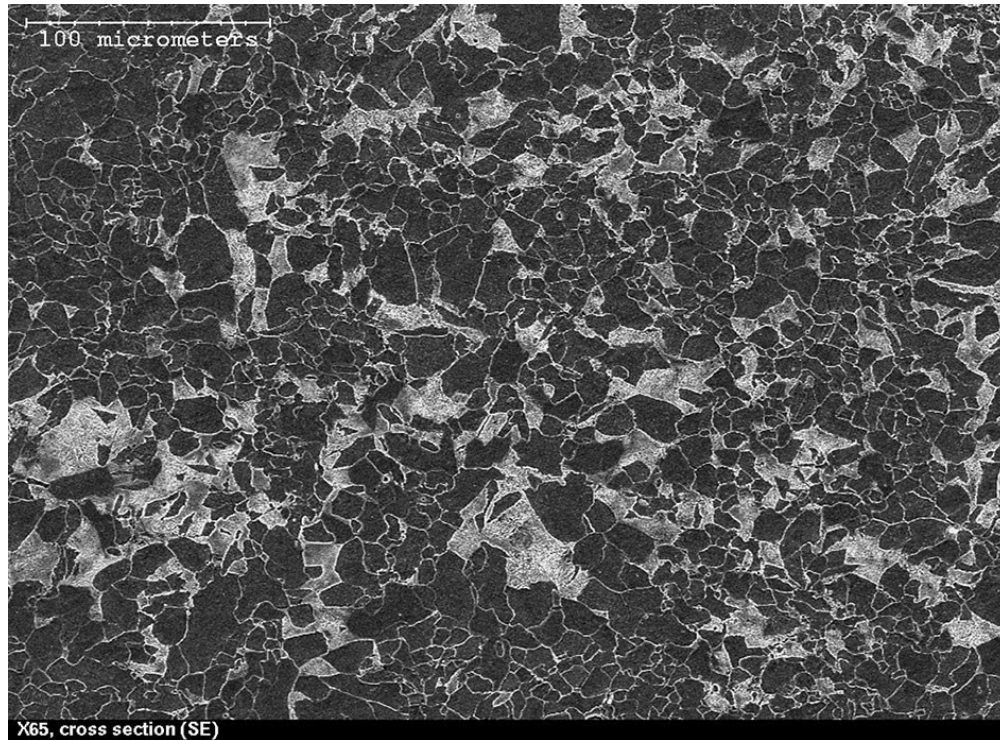
Figure 4-1 Typical microstructure of X-65 pipeline steel used in this study. Reproduced from [115], with permission from Springer.

4.3   Surface Crack Specimens

Surface crack tensile specimens were machined from the X-65 pipe section mentioned in the above section. Each sample contains three reduced gauge sections containing an EDM notch. Surface fatigue cracks are initiated from these notches. Each EDM notch on the sample was labelled as top, middle, or bottom (T, M, or B), based on its position when the sample is first placed into a vertical tensile tester. Since the sample is symmetrical, the positions are arbitrarily assigned. Each crack is named in the convention "RL# X", where # refers to the sample number, and X refers to the position (T, M, or B). The long side of the sample is aligned in the longitudinal direction of the pipe. The EDM notches are aligned in the circumferential direction.
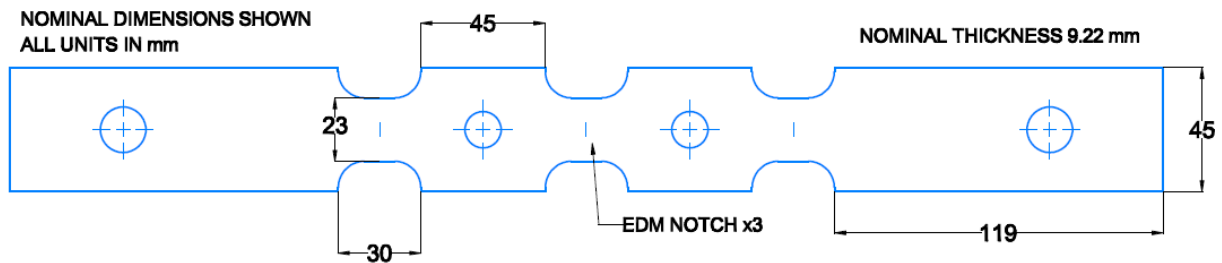
Figure 4-2 Surface crack tensile specimen dimensions
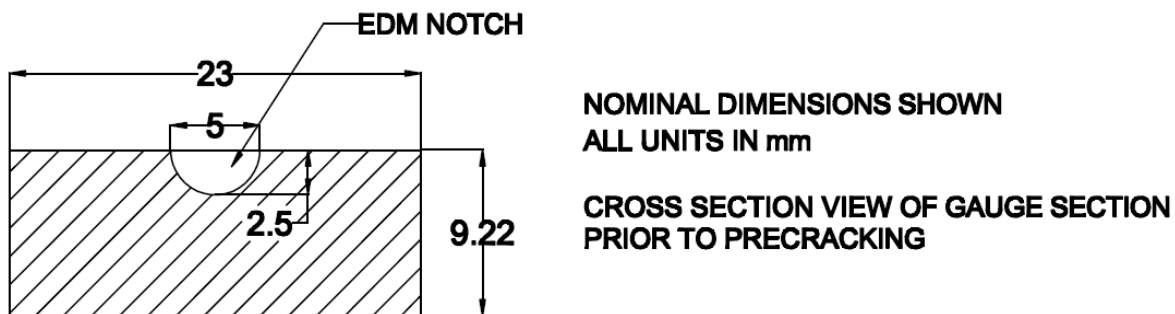
Figure 4-3 Surface crack specimen gauge section – cross-section view

Figure 3-7 and Figure 3-8 shows the initial dimensions of the sample prior to precracking. Detailed precracking procedures can be found in sections 3.4 to 3.6. A brief summary is provided here. The cracks were initiated from the EDM notch and precracked to a surface length ($2c_o$) of around 10.6mm, and then ~2.35mm was milled off from the outer surface to remove the EDM notches. This leaves a behind a long shallow fatigue crack that represents SCC cracks found on a pipe. The samples were precracked to a size that is representative of Stage II SCC. For most samples the actual depths of the EDM notches were slightly less than the 2.5mm shown in Figure 3-8, therefore milling away 2.35mm was sufficient to completely remove the EDM notch in most samples. A few cracks had small amount of left-over EDM notches after milling, but the left-over notches were far too small to influence crack growth (the deepest leftover notch was only 128 microns deep), so the samples were acceptable for use in the corrosion fatigue experiments.

After precracking and milling, the result is a surface crack tensile specimen with long shallow cracks which simulate Stage II SCC. The pre-test dimensions and the corresponding SIF for each crack are shown in Table 4-2. [4] A max stress of 80% SMYS is used for all tests, in accordance

---

[4] In Chapter 3, the crack length and depth after milling were named c_m and a_m. This chapter deals exclusively with milled specimens. For convenience, all crack length and depth after milling in this chapter will simply be referred to as c and a.

with CSA Z662's MAOP requirements for Class I pipes [53]. The SMYS for X-65 steel is assumed to be 448 MPa. The crack depth could only be measured after all the tests were completed and the sample was fractured.

Table 4-2 Pretest crack dimensions and stress intensity factors calculated for 80% SMYS max stress

Crack Name	Pretest Crack Length $2c$ (mm)	Pretest Crack Depth a (mm)	Gauge Section Width $2W$ (mm)	Gauge Section Thickness t (mm)	Pretest K_{max} @ Surface (MPa√m)	Pretest K_{max} @ Depth (MPa√m)
RL5 T	9.199	2.067	23.012	6.873	22.23	29.30
RL5 M	9.248	2.122	23.012	6.873	22.72	29.60
RL5 B	9.333	2.223	23.012	6.873	23.64	30.13
RL6 T	9.098	2.189	23.000	6.863	23.38	29.69
RL6 M	9.144	2.200	23.000	6.862	23.48	29.80
RL6 B	8.888	2.057	23.000	6.868	22.20	28.84
RL7 T	9.265	2.151	23.002	6.871	22.98	29.73
RL7 M	9.100	1.988	23.005	6.862	21.54	28.85
RL7 B	9.256	2.162	23.007	6.867	23.09	29.78
RL8 T	9.041	2.155	23.017	6.890	23.08	29.47
RL8 M	8.913	1.976	23.020	6.881	21.49	28.59
RL8 B	8.902	2.021	23.020	6.913	21.79	28.62

The outer surface of samples were ground and polished to a 1 μm finish after milling. A Buehler IndentaMet 1100 series hardness tester was used to make a series of micro-indents near the crack tips to mark the pre-test crack tip location. These indents were later used as reference points for crack length calibrations. The sample was then cleaned in acetone and ethanol ultrasonic baths. After cleaning, the cracks were imaged under microscopes and the crack lengths were measured.

4.4   Soil Solution

Various soil solutions were developed over the years by different researchers to simulate NNpH environment. The chemical compositions of these solutions are based on groundwater composition of SCC susceptible locations in the field. The solutions are typically purged with a mixture of CO_2 and N_2 gas to create an anaerobic environment. The CO_2 also forms carbonic acid, lowering the pH slightly (see section 2.3.7). The most commonly used gas mixture is 5% CO_2 and 95% N_2. This mixture was found to have a good balance between corrosion activity and

supplying atomic hydrogen to the steel. Higher CO_2 concentration results in more hydrogen generated at the metal surface as discussed in section 2.3.7. However, increasing the CO_2 level above 5% did not have significant impact on crack growth [55].

The most commonly used soil solutions from the literature are NS4 [17], Nova Tap Water (NOVATW) [55], and C2 [81].The composition and pH of these solutions are shown in Table 4-3. For this study, the C2 solution was chosen because of its composition agrees well with field measurements. The C2 solution also has a pH of 6.29 when purged with 5% CO_2, which is very close to the most susceptible pH range for NNpH SCC [7]. Chen & Sutherby found that the crack growth rate in C2 is significantly higher when compared to other soil solutions [72,81]. Therefore experiments performed using C2 should give more conservative results for crack life.

Table 4-3 Composition and pH of commonly used NNpH Solutions. Data from [17,55,81]

Solution / Substance	Composition (g/L)		
	NOVATW	NS4	C2
NaHCO$_3$	0.437	0.483	0.195
KCl	0.015	0.122	0.0035
CaCl$_2$	-	0.137	0.0255
MgSO$_4$·7H$_2$O	-	0.131	0.0274
CaCO$_3$	0.230	-	0.0606
MgCO$_3$	0.354	-	-
CaSO$_4$·2H$_2$O	0.0345	-	-
pH (purged with 5% CO$_2$ + 95% N$_2$)	7.11	6.8	6.29

To prepare the C2 solution, the salts shown in Table 4-3 are mixed with deionized water. The solution is then purged with a gas mixture of 5% CO_2 and 95% N_2 to create an anaerobic environment. The solution undergoes simultaneous purging and mixing for two days so that all the salts can be dissolved. The pH measured ~6.3 at the end mixing. During corrosion fatigue testing, the 5% CO_2 gas is continuously bubbled into the solution to maintain the NNpH environment.

4.5   Coating

Figure 4-4 and Figure 4-5 shows the coating methods used for the corrosion tests. The samples were coated to simulate IHAC conditions during testing. A strip of coating 5mm in width (the red coating shown in Figure 4-5) was applied over each crack to protect the crack from direct dissolution. The back and sides of the sample were also coated (see Figure 4-4) to simulate having only the outer surface of the pipe exposed to the groundwater.

Figure 4-6 shows the schematic of the coating in the gauge section of the tensile specimens. The reason a thin strip of coating is applied over the coating is to simulate IHAC enhanced crack growth. As discussed in section 2.4.7.1, there are two modes of hydrogen embrittlement in pipeline steel: Hydrogen-Environment Assisted Cracking (HEAC), and Internal Hydrogen Assisted Cracking (IHAC). In HEAC, hydrogen is reduced within the crack crevice and diffuses a short distance into the fracture process zone (FPZ) ahead of the crack tip. In IHAC, atomic hydrogen is reduced on the external surface of the sample, and diffuses to the FPZ. Chen et al. [31] showed that Stage II NNpH SCC growth is enhanced mainly through IHAC, and HEAC only has a minor effect (see section 2.4.7.1). Comparing the two HE modes, it is clear that hydrogen has a much shorter diffusion path in HEAC than IHAC, so it would be intuitive to think that HEAC is the dominant process. However for NNpH SCC, the coating disbondments are usually quite large, therefore there is a large amount of exposed bulk surface that is capable of generating hydrogen that can diffuse to the FPZ via IHAC. The exposed external surface area is often much larger than the crack crevice area, therefore IHAC is the dominant process for crack propagation in NNpH SCC.

The strip of coating only allows IHAC as shown in Figure 4-6, which is the main crack propagation mechanism. The coating also blocks HEAC and direct dissolution. HEAC has a negligible contribution to crack growth according to Chen et al. [31], but dissolution could retard crack growth by blunting the crack tips. By blocking direct dissolution, a small amount of conservatism can be included in the experimental results since the crack growth rate for samples with the thin strips of coating would be slightly more aggressive than crack growth rates for fully exposed samples.

The strip coating used was Tuck® Tape (a brand of sheathing tape with excellent adhesion and good water resistance). A length Tuck® Tape (20 to 30 cm long) was cut into 5mm wide strips, and then transferred onto the sample. The strip was made purposely long so it can be wrapped around the gauge section a few times for a better seal. The tape is pressure sensitive, so it is recommended to apply plenty of pressure over the tape to ensure good adhesion. Care should be taken during transfer processes to ensure no dust or grease gets onto the adhesive side of the tape. For cutting the tape into strips, it is recommended to first apply the tape to a clean non-stick surface that can be used as a cutting board, and then cut out the thin strips using an X-Acto or utility knife. The cut out strips can then be peeled off the cutting board and applied to the sample.

For an even better seal, after the strip of Tuck® Tape has been wrapped around the crack, a thin bead of cyanoacrylate was applied along the edges of the tape. Cornstarch was then sprinkled over the wet cyanoacrylate to allow the cyanoacrylate to harden.

After the Tuck® Tape strips were applied over the cracks, a 3D printed plastic shell is installed onto the backside of the sample. The 3D printed shell covers the back and sides of the tensile specimen so only the external surface is exposed to the environment. Two-part epoxy was used as the bonding agent between the sample and 3D printed shell.

For this experiment, sheathing tape was found to be the best coating for the thin strip application. The sample surfaces were highly polished, and it was difficult to find a coating that adheres to polished surfaces. Epoxy was tested as a potential coating method, but it demonstrated poor adhesion to polished surfaces. Solvent-based thermoplastic liquid coating (electrical connector coating) was also tested, and also demonstrated poor adhesion. Tuck® Tape on the other hand, demonstrated excellent adhesion to the polished surface since it was designed to adhere to smooth low surface energy materials such as Tyvek®. Tuck® Tape is also thin, so it conforms to the shape of the sample well.

Additional consideration was also made for ease of removal of the coatings, and Tuck® Tape can be easily removed after a corrosion fatigue test without damaging the sample surface. The tape can be unwrapped at the end of tests. Acetone can be used to soften tape residue on the sample surface so it can be wiped away. Light grinding and polishing removes any stubborn residues.
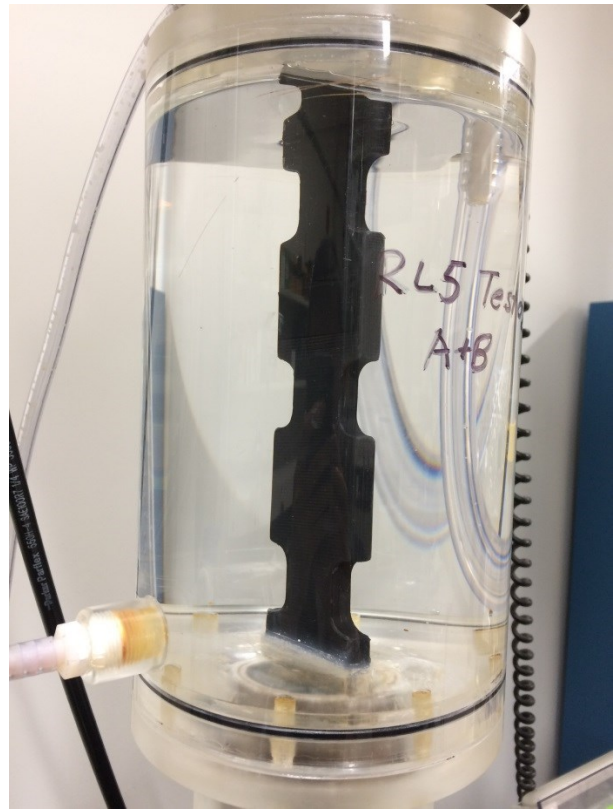
Figure 4-4 Coated sample in solution cell: (a) View of the outer surface of the sample with strips of coating covering the cracks (b) View of back side of the sample showing the 3D printed shell
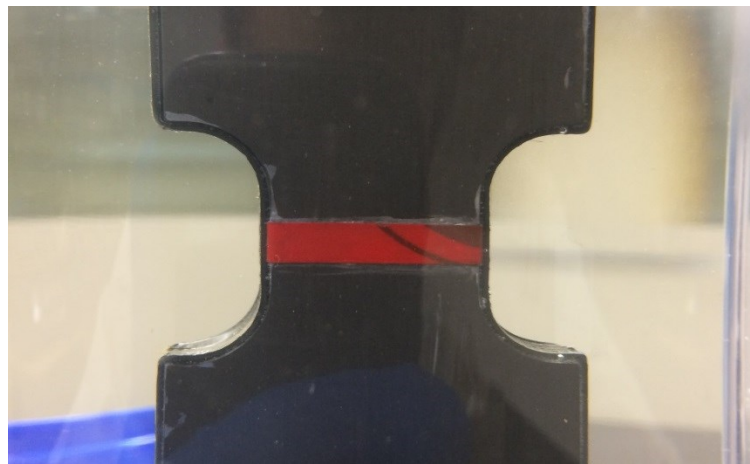
Figure 4-5 Close-up of the strip of coating over the crack
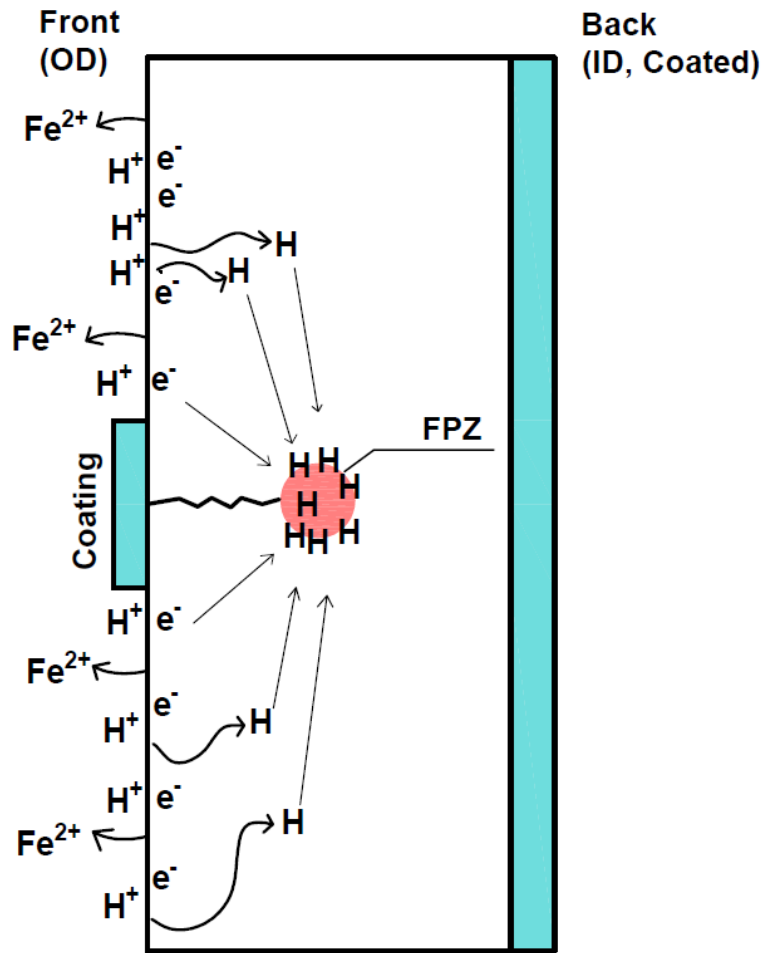
Figure 4-6 Coating method used: a thin strip of coating over the crack blocks out the anodic dissolution of the crack tip. The bulk surface is still exposed, allowing hydrogen ingress through IHAC. The backside of the sample is coated to simulate the internal surface of the pipe wall.

4.6   Cathodic Protection

SCC is typically found under coating disbondment where the undercoating environment is at open circuit potential. It is well known that the disbonded coating shields the CP current from reaching the pipe, allowing an NNpH environment to exist under the coating. To simulate these conditions, no CP was applied to the sample during testing. All of the tests are done at open circuit potential (OCP).

There are also many experimental studies that showed growth rates increased significantly under cathodic polarization in NNpH environment [16]. This had led some researchers to study crack growth in NNpH environment under CP, in order to obtain more conservative remaining life predictions. However, the experimental conditions used in these studies were not representative of field conditions. Some researchers have argued that cathodic protection plays a role in NNpH SCC by producing excess hydrogen that can diffuse into the metal, but studies have shown that CP current has little penetration under disbondment [136–143]. In most cases, there is close to no CP protection under the disbondment, therefore most diffusible hydrogen that is produced must have resulted from the corrosion reaction. Section 2.3.7 has shown that hydrogen is reduced at the metal surface in anaerobic environments. Some of that hydrogen is capable of diffusing into the metal and causing hydrogen embrittlement. There is usually a large area of exposed metal under the disbondment undergoing corrosion which can produce significant amounts of diffusible hydrogen. The samples use this study has a relatively large exposed surface area that is capable of generating enough hydrogen for IHAC.

4.7   Corrosion Cell Setup

After the coating applied in section 4.6 had cured, the sample was then installed into the corrosion cell shown in Figure 4-7. The cells used during the experiments are the same configuration as the cells used in [115]. The corrosion cells are made of acrylic, and were sealed with O-rings and silicone. After the silicone has cured, the premixed C2 solution can be poured into the cell. The sample was then precharged in the solution for 10 days to allow hydrogen concentration to build up within the specimen. 5% CO_2 + 95% N_2 gas was continuously bubbled through the solution during the precharge process to maintain the NNpH environment.

After the precharging was completed, the cell can then be transferred into the tensile tester as shown in Figure 4-7, and corrosion fatigue test can commence. During testing, the 5% CO_2 + 95% N_2 gas was still continuously bubbled through the solution.

An Instron 8516 servo-hydraulic fatigue tensile tester was used to load the sample. The tensile tester was controlled by a computer. Fatigue waveforms were inputted into the WaveEdit program. The WaveRunner program then runs the waveform on the tensile tester.
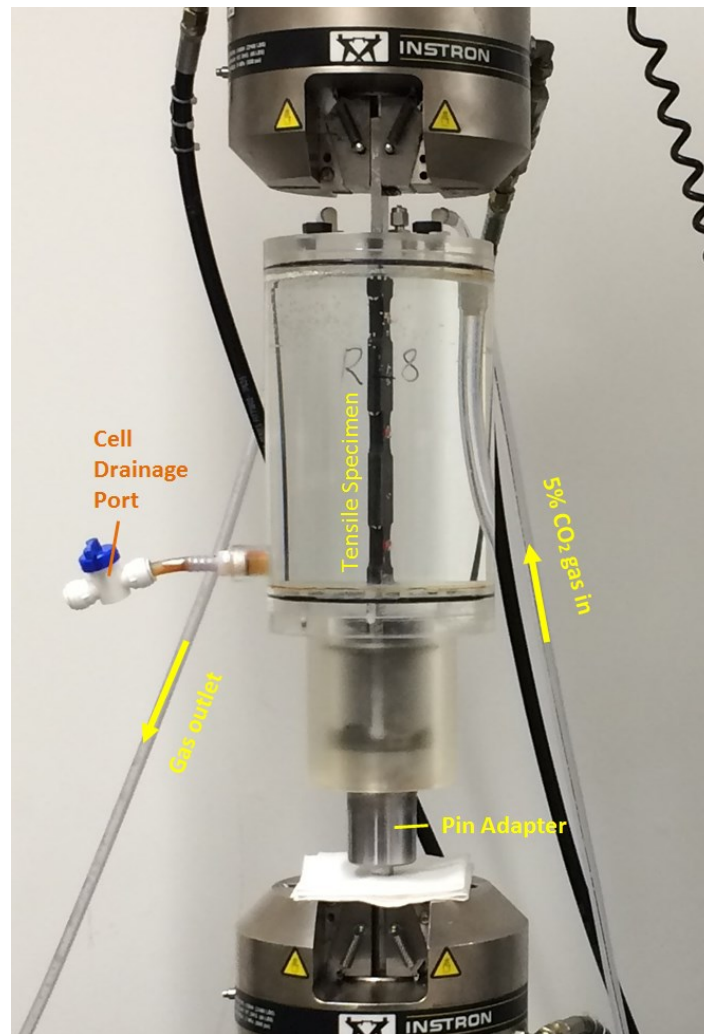
Figure 4-7 Surface crack tensile specimen in the solution cell during corrosion fatigue tests

4.8   Test Spectrum

The VAL underload spectra used in the experiments are presented in

Table 4-4. The frequencies and the number of minor cycles in the test spectra agree with the oil pipeline operating conditions shown in Table 4-5. The spectra are composed of minor cycles (MC) and underload cycles (UL).

Two types of UL's are used in the spectra, one mild UL cycle (named 'A') with R ratio of 0.4, and one severe UL cycle (named 'B') with R ratio of 0.1. The R-ratio of 0.4 for 'A' is close to the UL R ratio of 0.5 used by Yu et al.'s VAL tests [9,10,94], this could offer some comparison of results. An aggressive UL cycle was included in the tests spectra to test if load interaction effects can affect the damage done during an aggressive cycle. For the 7MC-(A/B) and 7MC-(12A/12B) spectra, two R ratios for minor cycles (R_{MC}) were used. The R_{MC} of 0.9 corresponds to the mild UL 'A' and R_{MC} of 0.85 corresponds to the aggressive UL 'B'. These R_{MC} values were chosen since they had the same loading/unloading rate as their corresponding underload. The remaining spectra, 14MC-AB, 14MC-BA, 28MC-ABAB, and 28MC-BABA, used a unified minor cycle with R ratio of 0.875. The value of 0.875 was chosen since it is the average of 0.9 and 0.85. This was done to simplify the waveforms for input into the tensile tester and reduce the variables in arranging the sequences. These differences in R_{MC} values are not expected to affect the outcome of the experiments. Also, the combined factor $\Delta K^2 K_{max}/f^{0.1}$ values of all the R_{MC} used are well below the threshold set by Chen & Sutherby [81]. For the remainder of the thesis, no distinction is made between the different minor cycle R ratios in the spectra. They are all regarded as just one type of minor cycle.

The frequency of UL (f_{UL}) for 7MC-(A/B) and 7MC-(12A/12B) spectra was chosen to be 0.001 Hz, which is the critical frequency determined by Yu et al. [9] that that maximizes crack growth rate for underload spectra (refer to Figure 2-24). The minor cycle frequency (f_{MC}) for 7MC-(A/B) and 7MC-(12A/12B) was 0.006 Hz. For later experiments, the frequencies were increased due to time constraints so experiments could be completed faster. For 14MC-AB, 14MC-BA, 28MC-ABAB, and 28MC-BABA spectra, f_{UL} was increased to 0.0032 Hz, and f_{MC} was increased to 0.0192 Hz. For all of the spectra, an f_{MC}:f_{UL} ratio of 6 was maintained.

All spectra are based on a set of composition rules. The overall MC:UL ratio for all spectra is 7:1. 50% of UL must be 'A' type with R = 0.4, the the other 50% of UL must be 'B' type with R = 0.1. The sequencing and agglomeration level of cycles are altered to create the different spectra seen in

Table 4-4. Agglomeration refers to grouping together similar types of cycles. For example, 7MC-(A/B) and 7MC-(12A/12B) spectra have a basic pattern of 7 MC + 1 UL, which is the most distributed and also the least agglomerated patterns. 28MC-ABAB and 28MC-BABA spectra on the other hand, have a basic pattern of 28 MC + 4 UL, which is the most agglomerated pattern tested.

One important concept used in this study is Fundamental Blocks (FB). The number of cycles in a fundamental block is the sum of the numerator and denominator in the reduced MC:UL ratio. For this study, the reduced MC:UL ratio for all spectra is 7:1. Therefore the FB for all the spectra tested consists of 7 MC and 1 UL, with a length of 8 cycles. FB allows for fair comparison of different waveforms. All crack growth rates are calculated per fundamental block since the waveform pattern that is looped in the tensile tester have different lengths. For example, 28MC-ABAB and 28MC-BABA spectra have a repeating pattern (28MC + 4UL) which is equivalent to 4 fundamental blocks. To compare the growth rate from 28MC-ABAB test to a 7MC-(A/B) test, the growth rate value in 28MC-ABAB must be divided by 4 to obtain the growth rate per FB.

Since two different types of UL were used, they can be sequenced in different ways. For the 7MC-(A/B) spectrum, the pattern is alternating between 7 MC + 1 'A' UL and 7 MC + 1 'B' UL. The 7MC-(12A/12B) spectrum is the same as 7MC-(A/B) in terms of agglomeration level, but instead of alternating between the patterns, the 7 MC + 1 'A' UL pattern is repeated for 12 times before repeating the 7 MC + 1 'B' UL 12 times. 14MC-AB and 14MC-BA spectra differ in that the order of the two UL cycles is switched. 28MC-ABAB and 28MC-BABA also differ in just the sequencing of the UL's. Figure 4-8 shows all spectra repeating their basic pattern until a total FB length of 24 has been reached. Within these 24 FB's, all spectra have the same number of MC's, A type UL's, and B type UL's.

Table 4-4 Description of Spectrum Waveforms Used during Testing

Spectrum Name	Basic Pattern	Waveform Illustration
7MC-(A/B)	7 MC + 1 UL	R = 0.9, f = 0.006 Hz; R = 0.85, f = 0.006 Hz; R = 0.4, f = 0.001 Hz; R = 0.1, f = 0.001 Hz
7MC-(12A/12B)	7 MC + 1 UL	R = 0.9, f = 0.006 Hz; × 12; R = 0.85, f = 0.006 Hz; × 12; R = 0.4, f = 0.001 Hz; R = 0.1, f = 0.001 Hz
14MC-AB	14 MC + 2 UL	R = 0.875, f = 0.0192 Hz; R = 0.4, f = 0.0032 Hz; R = 0.1, f = 0.0032 Hz
14MC-BA	14 MC + 2 UL	R = 0.875, f = 0.0192 Hz; R = 0.1, f = 0.0032; R = 0.4, f = 0.0032 Hz
28MC-ABAB	28 MC + 4 UL	R = 0.875, f = 0.0192 Hz; R = 0.4, f = 0.0032 Hz; R = 0.1, f = 0.0032 Hz

Table continued next page
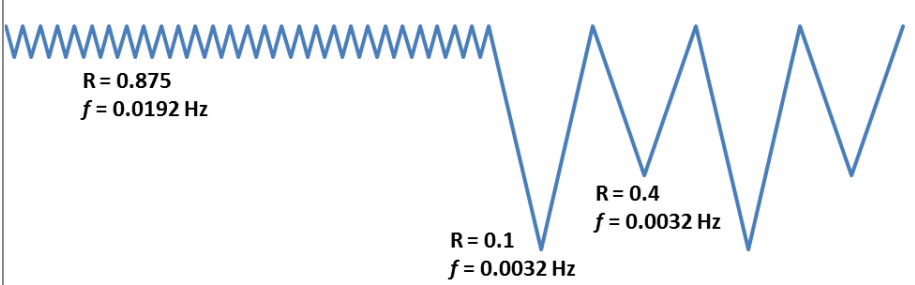
Spectrum Name	Basic Pattern	Waveform Illustration
28MC-BABA	28 MC + 4 UL	R = 0.875 f = 0.0192 Hz R = 0.4 f = 0.0032 Hz R = 0.1 f = 0.0032 Hz

Table 4-5 Characteristic of Underload Spectrum in Oil Pipelines [11]

Item	Range of Values
Range of unloading frequency (Hz)	6.89×10^{-6} to 1.0×10^{-1}
Range of loading frequency (Hz)	5.11×10^{-6} to 1.0×10^{-2}
Number of minor cycles between adjacent underloads	0 - 26
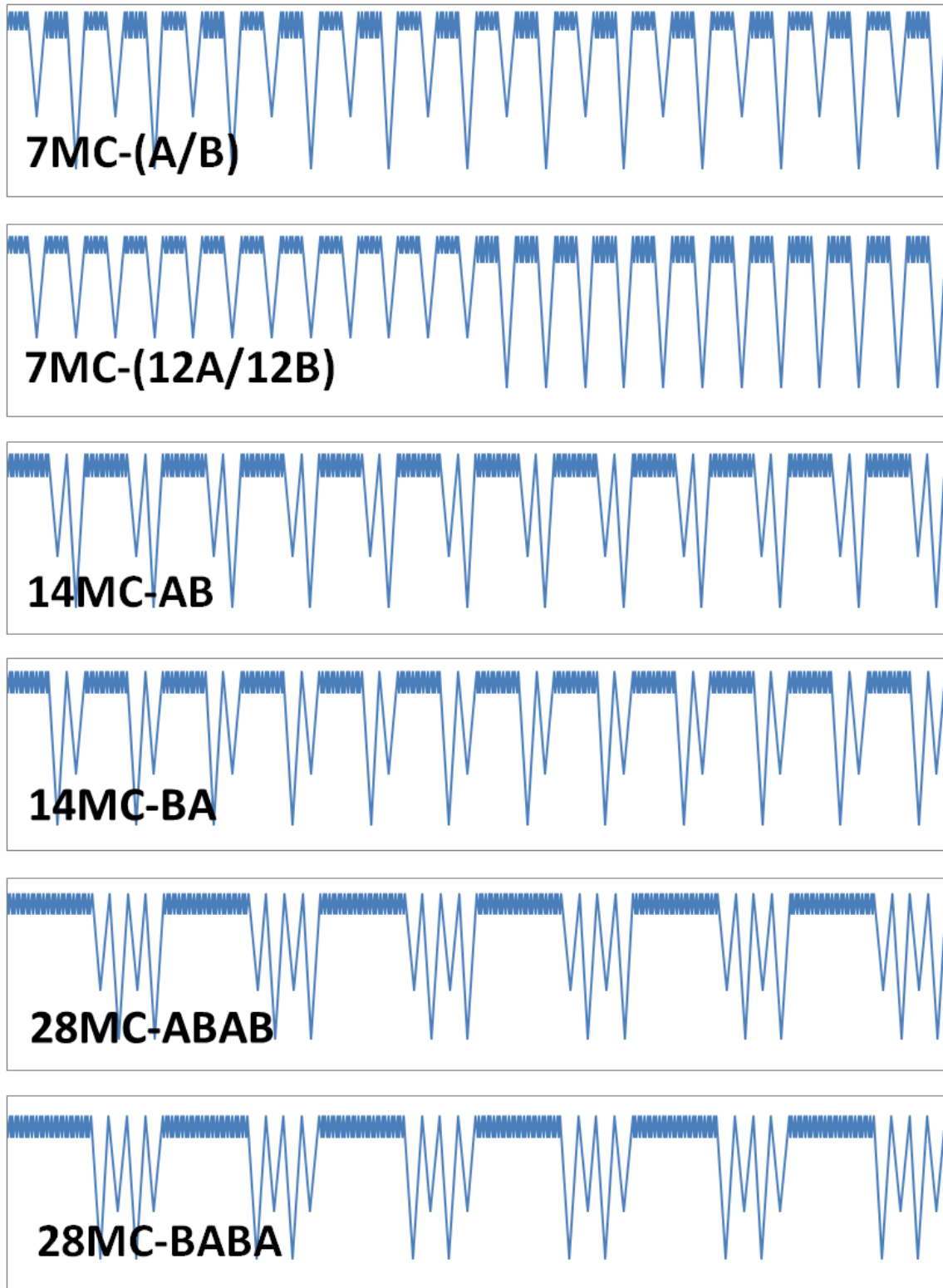
Figure 4-8 Comparison of the spectra used in the experiments. 24 fundamental blocks of each spectrum is shown.

114

4.9   Beachmark

The beach mark strategy was chosen as a replacement for the potential drop systems. Each spectrum was tested multiple times on a single sample to obtain crack growth rates at different crack sizes. Beachmarks were inserted between tests to demarcate the different test regions so crack growth can be easily measured.

The potential drop system was not adopted for several reasons. As seen in Figure 4-7, all gauge sections on the specimen were submerged in the C2 solution. Creating a watertight seal around all electrical connections for the potential drop system is challenging, and there is a high risk of unwanted galvanic reactions. Since there were multiple cracks on a sample, there was also a risk of signal interference between the different cracks. Calibration is also difficult for surface cracks, because the potential drop data need to be calibrated to the change in crack area instead of the change in crack length. It is well known that surface crack deviate more from a true elliptical shape as it grows, so converting the area growth into surface and depth growth requires many assumptions to be made.

For RL5 and RL6, various beachmark methods were tested. By RL7, a beachmarking procedure had been established. The beachmark parameters used for each sample can be found in Table 4-6 thru Table 4-9 (beachmarks are labelled "BM" in the table). All the beachmark processes were able to produce distinct bands on the fracture surface, but the procedures used for RL7 and RL8 were the most consistent. The beach marking process used for RL7 and RL8 is described below:

- The sample remained in the corrosion cell during the entire beachmarking procedure. The cell does not need to be disassembled, and there is also no need to take the cell assembly off the tensile tester.
- The samples were held at zero-load for at least 12 hours after a test has completed.
- After the hold period, beachmark cycles were applied to the sample
- The beachmark parameters were: 60% SMYS max load, R = 0.3, f = 1.5 Hz.
  - The max load during testing was 80% SMYS, so the beachmark max load must be lower. Therefore 60% SMYS was chosen.

- For a crack with initial pre-test surface K_{max} of around 23 MPa√m and initial depth K_{max} of around 30 MPa√m, the number of beachmark cycles applied in between later tests should range from 1000 to 3000 cycles.
- The first beachmark step should have the highest number of cycles. Subsequent beachmark steps should reduce the number of cycles gradually. This is to ensure the widh of the beachmark stays consistently thin. For example, in Table 4-9, RL8 went through 5 beachmark steps (each named as 'BM##'), and each step decreased the number of cycles applied. BM01 had 3000 cycles; BM02 had 2500 cycles, BM03 with 2000 cycles, BM04 with 1800 cycles, and finally BM05 with 1600 cycles.
- The frequency used during beachmarking should be several orders of magnitude higher than the corrosion fatigue frequency. If the corrosion fatigue test frequencies were in the range of 10^{-3} Hz, then the beach mark frequency should be at least 1.5 Hz. The faster frequency was needed to reduce the amount of time the crack is interacting with the environment during the beachmarking cycles. This resulted in a fracture morphology that is similar to the one produced by fatigue loading in air. This made the beachmark easily distinguishable from the quasi-cleavage morphology of the corrosion fatigue test. Earlier beachmarking attempts on RL5 and RL6 were done in air, which required the cell to be disassembled. However it was later discovered there was no need to perform the beachmarking in air. RL7 and RL8 underwent beachmarking in C2 solution and still produced beachmark morphology that was similar to fatigue in air. As long as the beachmarking frequency is sufficiently high, beachmarking can be done within the C2 solution

- After the beachmarks were completed, the sample was held at zero-load for another 12 hours. The next corrosion fatigue could commence after the 12 hour wait period.

4.10   Order of Tests

Table 4-6 to Table 4-9 show the lists of corrosion fatigue tests and beach marks conducted on each of the samples. While beachmark can be used to generate more data points, the number is limited when compared to potential drop technique. However, the crack measurements obtained from beachmarks can be more accurate since the exact crack shape at the end of each test can be recorded onto the fracture surface. By exploiting the small differences in initial crack size, and arranging the test in a leapfrog manner, a large number data points could be generated with beachmarks. Using these methods, 9 data points were generated for each of the spectrum tested.

As shown in Table 4-6 to Table 4-9, each sample went through a specific set of tests. Therefore all three cracks on the sample also went through the same tests. This may seem like redundancy since the cracks were precracked to similar sizes, however this can greatly improve accuracy and reproducibility of the results. Figure 4-9 shows how two similarly sized cracks could generate a "filled in" crack growth trend that is better suited for trend fitting. Even though the cracks on a sample have similar sizes, small differences still exist, and the slightly larger crack always grows faster. Most fatigue growth models are based on the power law, so even small differences in SIF can be significant (e.g. for Paris law the driving force ΔK is to the power of m). The small size difference between the cracks on a sample can be exploited to obtain a more "filled in" set of data.

A leapfrogging technique was used to arrange order of tests so two spectra can be tested simultaneously on one sample. This technique is demonstrated in Figure 4-10. In this figure, the growth rate data for two spectra is generated from one single crack that has undergone 6 tests. Beachmark cycles are added in between each test to demarcate boundaries on the fracture surface. The order in which Spectrum A and Spectrum B tests are arranged is done in a leapfrogging manner. Spectrum A test is followed by a Spectrum B test, and then followed by a Spectrum A test, and so on. The green arrows track the actual movement of the data points as the test progresses. The end result is a trend for each set of data can be obtained.

For RL5 and RL6, the leapfrogging between 7MC-(12A/12B) and 7MC-(A/B) waveform was done across two samples as shown in Table 4-6 and Table 4-7. These were the first two samples tested, so the crack growth rates were unknown. To be on the safe side, only three tests were

done on each sample because limited crack growth was expected. It was feared adding too much beach marks for small growth can make the data difficult to interpret. However, the crack growth rate obtained for RL5 and RL6 was faster than expected, so the duration of tests for RL7 and RL8 were shortened so 6 tests could be fitted onto one sample. The tests on RL7 and RL8 were done in a leap frog fashion like the example shown in Figure 4-10. Beachmarks were also inserted between each test to demarcate them.

Table 4-6 RL5 Sequence of Tests and Beach Marks

				Test Duration (No. FB)	Beach Mark Cycles (No. Cycles)
Test	**Max Stress (% SMYS)**	**Environment**	**Description**		
Test 01	80%	C2	7MC-(12A/12B)	360	-
BM 01*	70%	Air	R = 0.3, 1 Hz	-	5000
Test 02	80%	C2	7MC-(A/B)	550	-
BM 02	65%	C2	R = 0.3, 0.5 Hz	-	4000
Test 03	80%	C2	7MC-(12A/12B)	600	-

* Sample was taken out of the cell using the procedure in section 4.11. The beachmarking was then completed in air. After beachmarking, the cell + sample assembly was re-built, filled with C2 solution, and precharged for 10 days before starting the next test.

Table 4-7 RL6 Sequence of Tests and Beach Marks

				Test Duration (No. FB)	Beach Mark Duration (No. Cycles)
Test	**Max Stress (% SMYS)**	**Environment**	**Description**		
Test 01	80%	C2	7MC-(A/B)	586	-
BM 01*	65%	Air	R = 0.3, 1 Hz	-	4000
Test 02	80%	C2	7MC-(12A/12B)	600	-
BM 02*	65%	Air	R = 0.3, 1 Hz	-	500
Test 03	80%	C2	7MC-(A/B)	558	-

* Sample was taken out of the cell using the procedure in section 4.11. The beachmarking was then completed in air. After beachmarking, the cell + sample assembly was re-built, filled with C2 solution, and precharged for 10 days before starting the next test.

Table 4-8 RL7 Sequence of Tests and Beach Marks

Test	Max Stress (% SMYS)	Environment	Description	Test Duration (No. FB)	Beach Mark Duration (No. Cycles)
Test 01	80%	C2	14MC-AB	258	-
BM 01	60%	C2	R = 0.3, 1.5Hz	-	2600
Test 02	80%	C2	28MC-ABAB	256	-
BM 02	60%	C2	R = 0.3, 1.5Hz	-	2200
Test 03	80%	C2	14MC-AB	256	-
BM 03	60%	C2	R = 0.3, 1.5Hz	-	1800
Test 04	80%	C2	28MC-ABAB	256	-
BM 04	60%	C2	R = 0.3, 1.5Hz	-	1400
Test 05	80%	C2	14MC-AB	254	-
BM 05	60%	C2	R = 0.3, 1.0Hz	-	1500
Test 06	80%	C2	28MC-ABAB	256	-

Table 4-9 RL8 Sequence of Tests and Beach Marks

Test	Max Stress (% SMYS)	Environment	Description	Test Duration (No. FB)	Beach Mark Duration (No. Cycles)
Test 01	80%	C2	14MC-BA	284	-
BM 01	60%	C2	R = 0.3, 1.5Hz	-	3000
Test 02	80%	C2	28MC-BABA	292	-
BM 02	60%	C2	R = 0.3, 1.5Hz	-	2500
Test 03	80%	C2	14MC-BA	296	-
BM 03	60%	C2	R = 0.3, 1.5Hz	-	2000
Test 04	80%	C2	28MC-BABA	292	-
BM 04	60%	C2	R = 0.3, 1.5Hz	-	1800
Test 05	80%	C2	14MC-BA	288	-
BM 05	60%	C2	R = 0.3, 1.5Hz	-	1600
Test 06	80%	C2	28MC-BABA	288	-
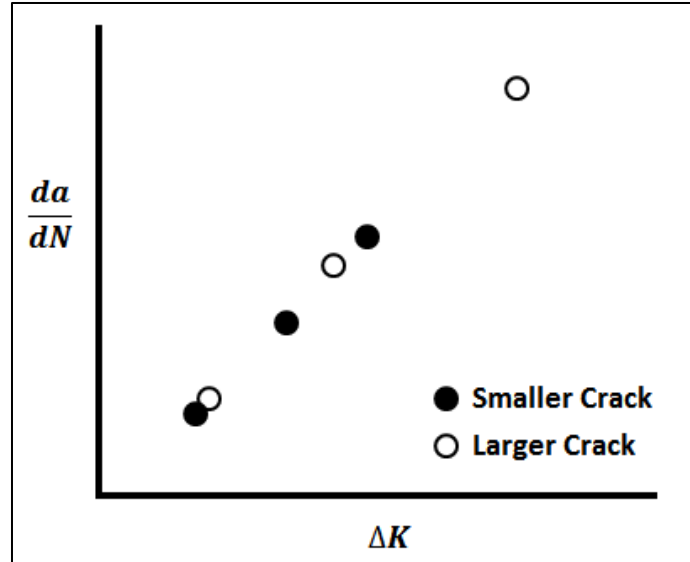
Figure 4-9 Schematic illustration of crack growth data generated for the same spectrum from two cracks with a small differences in initial size. In this hypothetical example, a spectrum was tested 3 times on each crack to produce 3 data points per crack. The smaller crack could provide additional data points to fill in the gaps in the data trend of the larger crack.
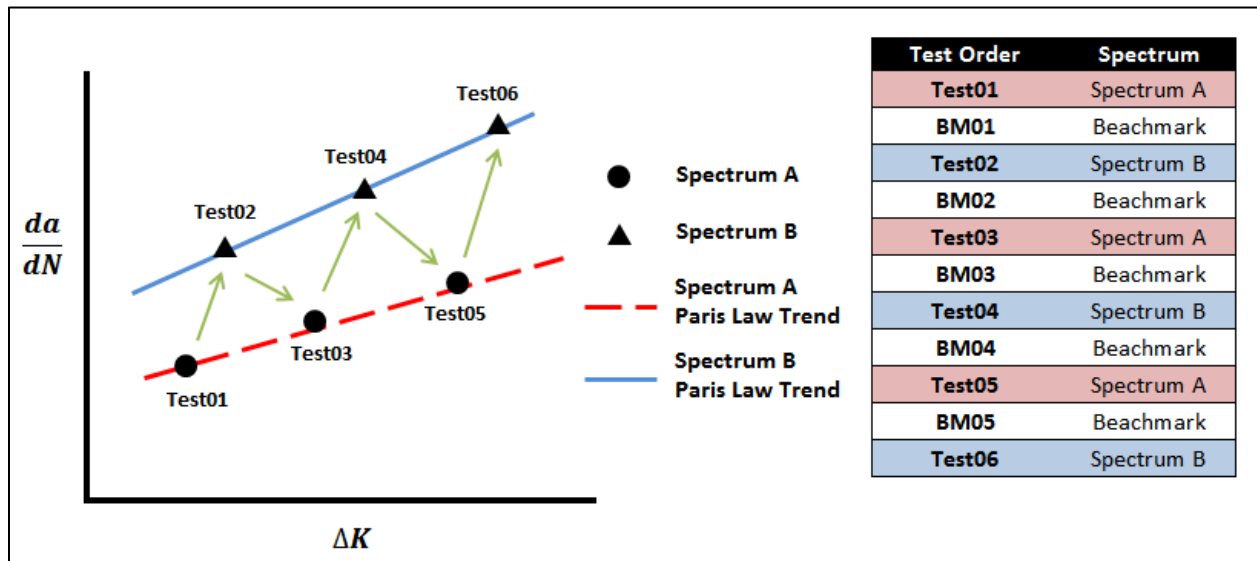
Figure 4-10 Schematic illustration of crack growth data of two spectra generated via leap frogging technique from one single crack. The list of tests the crack has gone through is shown on the right.

4.11   Cell Disassembly, Fracturing Open the Crack, and Cleaning the Fracture Surface

After a sample had completed its tests, the cell assembly was taken out of from the tensile tester to prepare for the removal of the sample from the solution cell. During this process, the gas inlet and outlet ports were sealed to prevent oxygen from entering the cell. A small sample of fluid was taken from the cell to measure the pH to ensure it was still within the NNpH range. Next, the solution in the cells was drained through the cell drain port shown in Figure 4-7. A liberal amount of ethanol was sprayed onto the sample from the top as the cell was draining to prevent oxidation. After the fluid had drained, the cells were disassembled and the sample removed.

With the coating still intact, the samples were gently wiped clean with Kimwipes and ethanol. The 3D printed sleeve was also removed. The tape coating was left on to protect the crack areas. Fine-grit sandpaper was used to clean the sample of stubborn corrosion deposits and silicone residues. Ethanol was regularly sprayed on during grinding to provide lubrication. After the grinding cleaning process is complete, the tape coating was removed. The sample was then placed in an ethanol ultrasonic bath to remove grinding particles.

After the ultrasonic bath, the gauge sections undergo fine grinding and polishing to remove any tape residue and corrosion deposits. Manual in-situ polishing was performed to reach a finish of 1 μm. The crack tip area was difficult to polish since it had sunken into the material due to plastic deformation. To polish this area, a small polishing tool was made by wrapping Kimwipes around a cotton swab. The tool was dipped in diamond abrasive suspension and was used to polish the area around the crack tip. The end result of polishing is shown in Figure 4-11. The entire gauge section in this figure had been polished to the same finish, however the tape covered area was still much shinier. This was because the tape coated section had a relatively uncorroded surface while the areas outside were covered with small pits.

The samples underwent one more ultrasonic bath after polishing, and then the crack areas were cleaned by cellulose acetate replica described in [144]. For a better replica clean, small bending loads can be applied with clamps as shown in Figure 4-12 to open the crack a bit, and then replica film can be applied over the crack. After the surface has been thoroughly cleaned, the

crack surface was imaged under optical microscopes, and the length was measured using the techniques shown in section 4.12.

To prepare the samples for final fracturing, they were cut down to a manageable size. Notches were made on the sides and back of the sample in the sample plane as the crack using a hacksaw and files. The samples were then cooled in liquid nitrogen for four hours. After that, the samples were fractured by striking the backside with a cold chisel. The fractured pieces were immediately placed into acetone to prevent oxidation of the crack face due to condensation. After the samples warmed to room temperature, they were taken out of the acetone and dried with compressed air. The fracture surfaces could then be imaged.

The fracture surfaces were first cleaned using replicating film described in [144]. One disadvantage of using replicating tape is it could leave behind residue on the rough fracture surface, even ultrasonic cleaning in acetone might not be able to dislodge stubborn replica residue. An alternative is scotch tape which can be gently pressed onto the fracture surface and peeled off. The replica cleaning only removed loosely attached corrosion deposits as seen in Figure 5-13. For a deeper clean, the sample was etch-cleaned with 5% acetic acid for 30 to 60 seconds. The sample was then immediately dipped into a slightly basic sodium bicarbonate solution to neutralize the acid. The sample was then rinsed with deionized water, then ethanol, and dried with compressed air. Water-based detergent cleaning [144] was also used if acid etching wasn't enough. The detergent used was Fisherbrand Sparkleen. 15g was mixed in per 350 mL of hot water (~95°C). The detergent solution was placed in an ultrasonic bath, and samples were placed in to be cleaned for 20 to 30 minutes. After the detergent bath was completed, the sample was placed in plain hot water ultrasonic bath for 5 minutes to remove any soap residue. Once complete, the sample was rinsed with ethanol and dried with air.
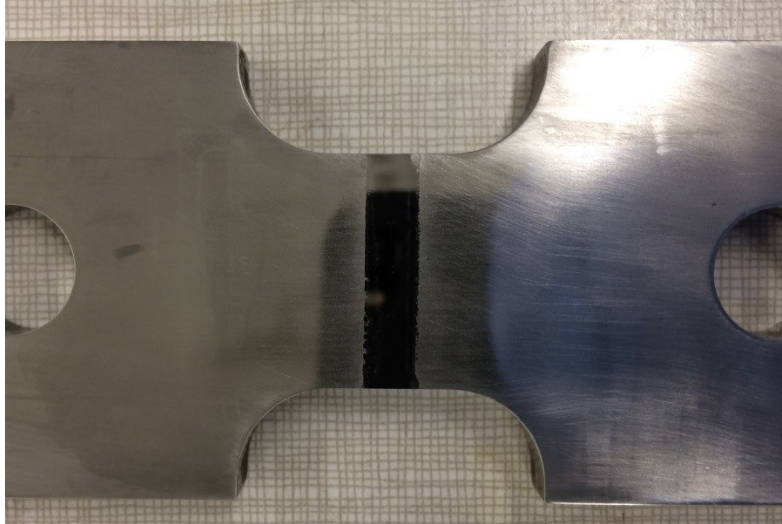
Figure 4-11 the gauge section of a sample after tests had completed. The coating was removed. The surfaces were then cleaned and polished. Note the shiny strip is where the tape coating was.

Figure 4-12 Demonstration of small bending load applied with clamps to open up the crack surface slightly so better replica cleaning results can be obtained.

4.12   Crack Characterization

This section describes the methods used to obtain measurements of crack length and crack depths. First, the crack surface lengths before and after testing were measured from the surface of the sample. These length measurements were then used to calibrate the fracture surface measurements. Since the beachmarks were visible on the fracture surface, the surface and depth growth from each test could also be determined.

Before starting crack length measurements, the gauge sections were polished to 1 μm finish as described in section 4.3 and 4.11. Prior to testing, micro-indents were also made near the crack tips using the procedure described in section 4.3.

4.12.1   Surface Characterization

Direct Measurement

The easiest method to crack surface length was to have a high powered optical microscope (with 100x objective and eyepiece reticles) that has a stable micrometer x-y stage with a movement resolution of 1μm. The crack length is measured directly by moving the stage from crack tip to crack tip and reading the distance on the micrometer. The crack tips from the experiments were very thin, so it was difficult to find the exact location of the crack tip with an objective less than 100x. A high measurement precision is also needed since the cracks grew only grew a small amount, hence the requirement for an X-Y stage with precision of 1 μm. However such equipment was cost-prohibitive and not available, so other methods of measuring crack lengths had to be found. Another problem with using this method was that the sample must be aligned in the same way each time the crack was measured. A small amount of deviation in angular alignment can cause significant length measurement error. It was also preferable to have a permanent record of the crack such as a replica or an image of the entire crack so comparisons can be made before and after testing.

Surface Replica

One method tried was creating plastic replicas of the crack on the surface of the sample with cellulose acetate tape using the process described in [144], and then examining the replica in an

124

SEM. The samples used were too large to fit into the SEM chamber, therefore replicas were used instead. Acetone was first applied over the crack area, and then 120 μm thick replicating tape was applied over the sprayed area. The tape was allowed to dry, and a carbon conductive double-sided adhesive tab was applied onto the tape, right over the crack area. The replica can then be transferred to an SEM stub by pressing the stub into the double-sided adhesive. The replica was then sputtered coated with carbon and examined in an SEM. Replicating film was purported to have resolution as small as 50 Å [145], however this level of resolution could not be achieved during testing. After comparing the optical micrographs of the crack tip and the SEM images of the replica crack tip, it was found that the replica underestimated the true extent of the crack tip by as much as 60 micron. The other problem with replicas was the stretching that occurs when the replica is peeled off the sample surface. The stretching was also found to be non-uniform, making it difficult to apply correction factors. Therefore replicating tapes were not used for crack length measurements.

Optical Microscope Surface Imaging

A method that was found to work well was taking a series of overlapping images along the crack length with a camera attached to an optical microscope, and then stitching the images to form one single image of the entire crack. Optical microscopes are easy to calibrate, so pixel measurements on the crack image could be converted to distance measurements. A key benefit of having a stitched image is it's a permanent record. Stitched images can be produced for the crack prior to testing and after testing, allowing side-by-side comparison of before and after. The method also doesn't require expensive x-y micrometer stages and can significantly reduce random errors. The method is described in detail below:

The surface of the samples was imaged with an Olympus GX41 metallurgical microscope with an Infinity 1-2 CMOS USB camera attached. The GX41 microscope has objective lenses from 10x to 100x. The microscope also has a simple manual x-y stage that could move the sample, but it had no measurement capability. The Infinity 1-2 camera has a max resolution of 1600 x 1200 pixels, and is controlled through a computer with the Lumenera Infinity Capture software. The microscope + camera system was also calibrated with a stage micrometer (not to be confused

with micrometer stage) for each objective lens. Pixel to micrometer conversion could be carried out with calibration factors.

The 20X objective lens was used to take overlapping images along the entire crack length. The pre-test micro-indents were also included in the image set since they are required for calibration. The minimum amount of overlap between two images was around 50%. The stage translation does not need to be precise and equal. After the low mag 20x image of the entire crack was taken, 15 - 20 overlapping images were taken at each crack tip with both the 50x and 100x objectives. The high magnification images were needed to find the crack tip.

After all the images were taken, the images were stitched with the open source photo-stitching software Hugin. Various settings in Hugin were tweaked to make it suitable for stitching microscopy images. When stitching was completed, each crack had the following set of stitched images: one image of the entire crack with 20x magnification, including the indents; one 50x image of the first crack tip; one 100x image of the first crack tip; one 50x image of the second crack tip; and one 100x image of the second crack tip.

The stitched images were then imported into AutoCAD. Scaling and rotation corrections were also applied to each image according to Table 4-10. The 20x stitch of the entire pretest crack was scaled using the microscope calibration factor to convert the pixel dimension into microns. It was also used as the rotation reference for other images. One advantage of working with stitched images in AutoCAD is that random errors in scaling and rotation can be significantly reduced. Systematic errors are also easy to correct since all the images hare a common reference.

Table 4-10 Scaling and rotation correction applied for surface images imported into AutoCAD

Image ID	Stitched Image Description	Scaling Reference	Rotation Reference
1	Pretest 20x entire crack	Calibration Factor	Used as ref.
2	Pretest Surface Tip#1 50x	image 1	image 1
3	Pretest Surface Tip#2 50x	image 1	image 1
4	Pretest Surface Tip#1 100x	image 1	image 1
5	Pretest Surface Tip#2 100x	image 1	image 1
1'	Post-test 20x entire crack	image 1	image 1
2'	Post-test Surface Tip#1 50x	image 1'	image 1'
3'	Post-test Surface Tip#2 50x	image 1'	image 1'
4'	Post-test Surface Tip#1 100x	image 1'	image 1'
5'	Post-test Surface Tip#2 100x	image 1'	image 1'

Figure 4-13 shows the surface images listed in Table 4-10 imported into AutoCAD along with the fracture surface image. The surface images had scaling and rotation corrected according to Table 4-10. The images were all aligned vertically and compared side by side. Image 1' was rotated and scaled with reference to image 1 using the micro-indents. If image 1' was also scaled using the calibration factor, there would be a small amount of random error, and the images would not align perfectly. Therefore image 1 was assumed to be accurate and was used as the reference. Figure 4-14 shows how high magnification crack tip images were overlaid on top of lower magnification images in AutoCAD to determine the location of crack tips. The high magnification close-up of the crack tips were scaled and aligned to their respective 20x image. Features on sample surface such as dots, pits, inclusions, scratches, etc. were chosen as reference points to scale and align the high magnification images of crack tips. After the close up images were properly aligned and overlaid, accurate tip to tip measurements of pre-test and post-test crack measurements can be made.

SEM Imaging

It was already mentioned in this section that the samples were too large to fit into the SEM chamber. Therefore obtaining an SEM image of the pretest crack surface is not possible. However for the post-test sample, it could be cut up and be able to fit inside the SEM. This could provide high-resolution pictures, but is not advisable since the measurement process would still

be the same as optical microscopy, and would require large amounts of overlapping images. It would be prohibitively expensive and time-consuming to create low magnification scans of the entire crack.

The SEM can however be used effectively to scan the crack tips. This was done for a few cracks that had cracks that were too fine for optical microscopes, so the crack tips images were taken under the SEM, but the low magnification stitch was still made using optical images. The SEM used was Zeiss EVO LS15 EP-SEM. In most cases, it was found that the 100x objective lens in an optical system would suffice for finding the crack tip.

4.12.2   Fracture Surface Characterization

After the samples were fractured, the fracture faces were imaged using SEM and stereomicroscopes. The fracture surface images were then calibrated and scaled so measurements can be obtained for crack growth during every test. Since the beachmarks were visible, the different tests were clearly demarcated.

SEM Imaging of Fracture Surface

The Zeiss EVO lS15 EP-SEM was used to image the fracture surfaces for some of the samples. The SEM was equipped with a 4-quadrant BSE detector that was well suited for looking at fracture surface. A major challenge with SEM was dealing with the large fracture surface area. The SEM had a minimum magnification, so multiple scans were required to capture the entire crack area. Another downside to using low magnification was the increased aberration which was noticeable. Higher magnification up to 2000x was also used to locate beach mark boundaries. However it was not always easy to differentiate the beachmarks from an SEM image. Some beach marks that were easily observable with the naked eye were difficult to find under the SEM, especially if the sample had been etched. The SEM was mainly used to determine the fracture surface morphology rather than to obtain measurements on a fracture surface.

The SEM software also provides scaling factors for their images to convert pixels to microns. However, it was found that the particular program used by the Zeiss EVO SEM calculated the scaling factor as a function of magnification only. In actual operation, the field of view of SEM is dependent on the gun and lens parameters used. Changing the focus also affects the field of

view. Therefore calibrating an SEM is difficult since so many factors have to be considered. Distance measurements on stitched SEM images showed increased random error when compared to optical images. This was expected since the calibration for optical microscope is more stable. As long as the image is in focus, the calibration factor would apply to the optical image. For these reasons, the SEM images were not used as references for scaling. The SEM images were instead scaled to the surface images when imported into AutoCAD.

Stereomicroscope Imaging of Fracture Surface

A Wild M3 manual stereomicroscope with an attached OMAX 10MP USB microscope camera was used to image the fracture surface for most of the samples. The magnification of the stitched images was around ~12x. Around 5 to 6 focus stacks were taken across the crack for stitching. Since optical microscopes have limited depth of field, the focus stacking technique was used to bring all features on the fracture surface into focus. The focused stacked images were also easier to stitch in Hugin since the program has an easier time finding control points. The focus stacking was performed with Picolay. Image stitching was done in Hugin.

Figure 4-13 discussed earlier shows a stitched stereomicroscope image of a fracture surface imported into AutoCAD. The fractograph is scaled using the surface lengths measurements as a reference. After the fractograph is scaled, the growth during each test can be measured with the help of beach marks. The different regions (precrack, quasi-cleavage, and beachmark) were easily distinguishable since they had different textures that reflected light differently.
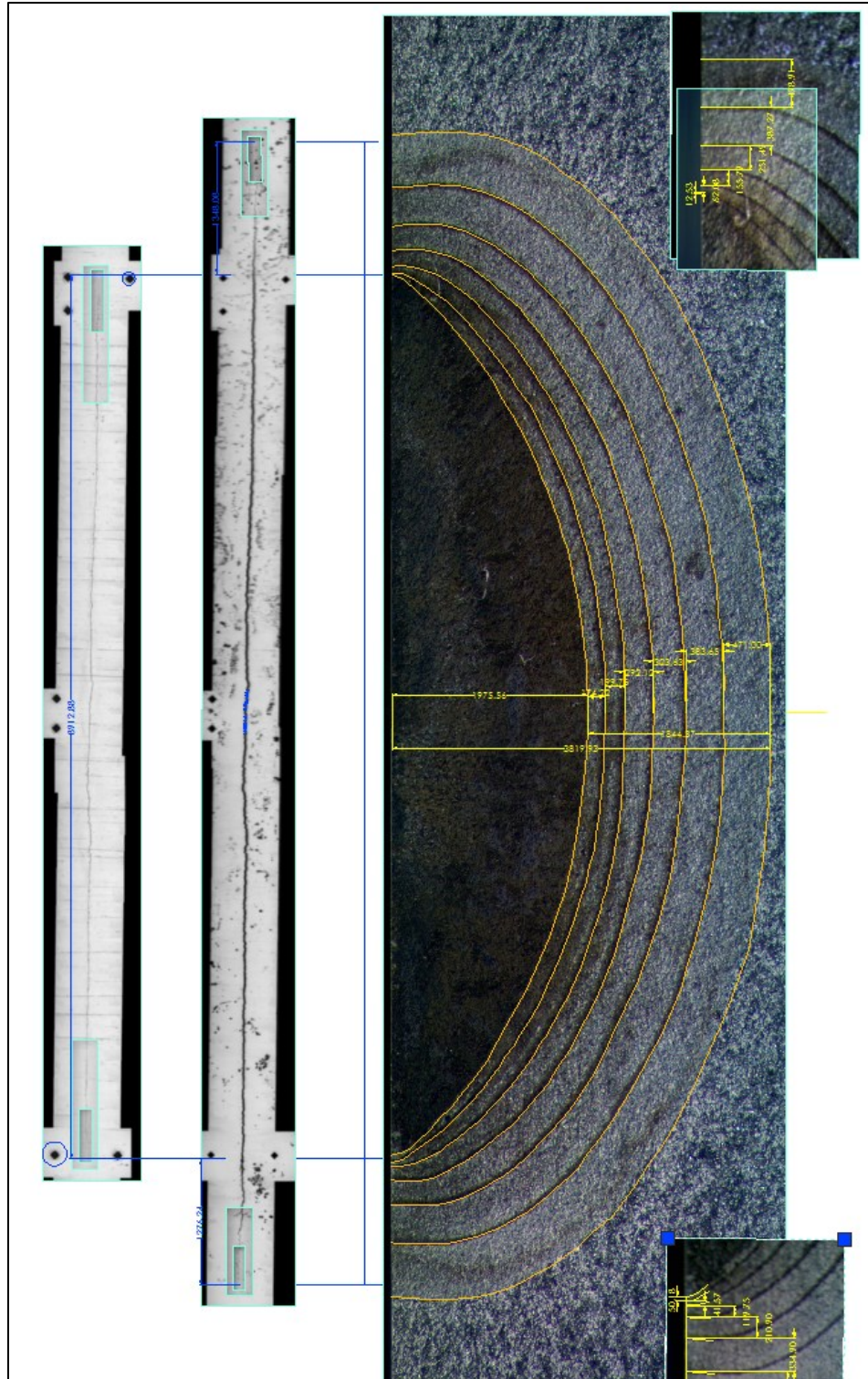
Figure 4-13 Screenshot of crack measurements in AutoCAD. The images were scaled properly and relative rotations were corrected. From Left to right: pretest surface stitch, post-test surface stitch, and fracture surface with beach marks.

130
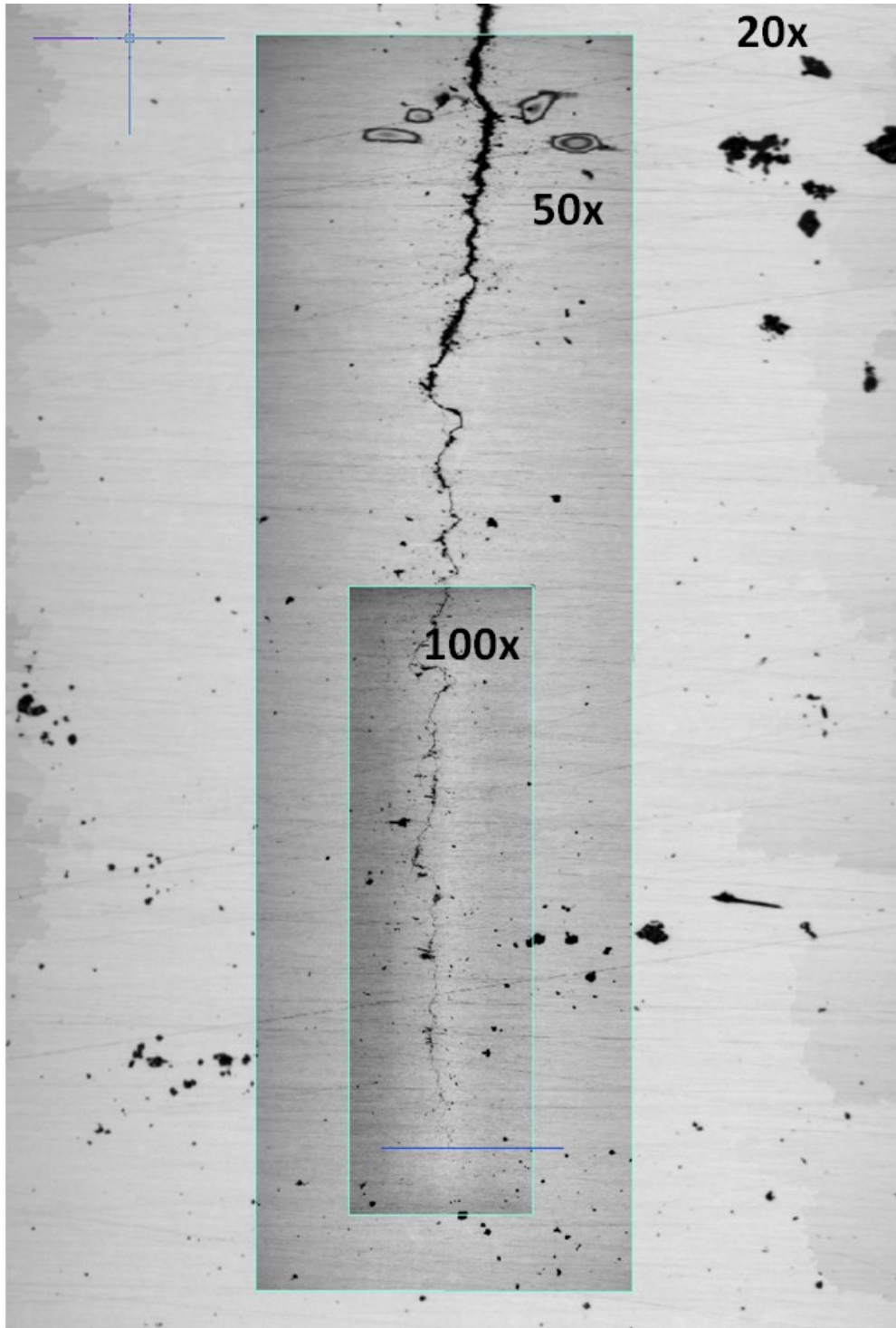
Figure 4-14 Screenshot in AutoCAD showing the overlay of high magnification crack tip images on top of low magnification images to determine the exact location of crack tip. The crack length can then be accurately measured from tip to tip.

5 Corrosion Fatigue Tests: Results & Discussion

5.1 Surface Characterization

A full collection of crack surface images can be found in Appendix B.

5.1.1 Crack Tip Morphology and Crack Width

Figure 5-1 shows the comparison of the crack tips before and after testing. Both sets of crack tip image were taken after the samples were cleaned and polished to 1µm finish. The crack shown has undergone multiple tests (~1700 FB's), and the crack tip was still as sharp as the pretest crack. All the crack tips from the experiment produced sharp crack tips during testing (See Appendix B). This is strong evidence of hydrogen embrittlement in the fracture process zone during corrosion fatigue tests. Even though there were small amounts of corrosion under the coating, the crack tip remained sharp, suggesting dissolution was negligible.
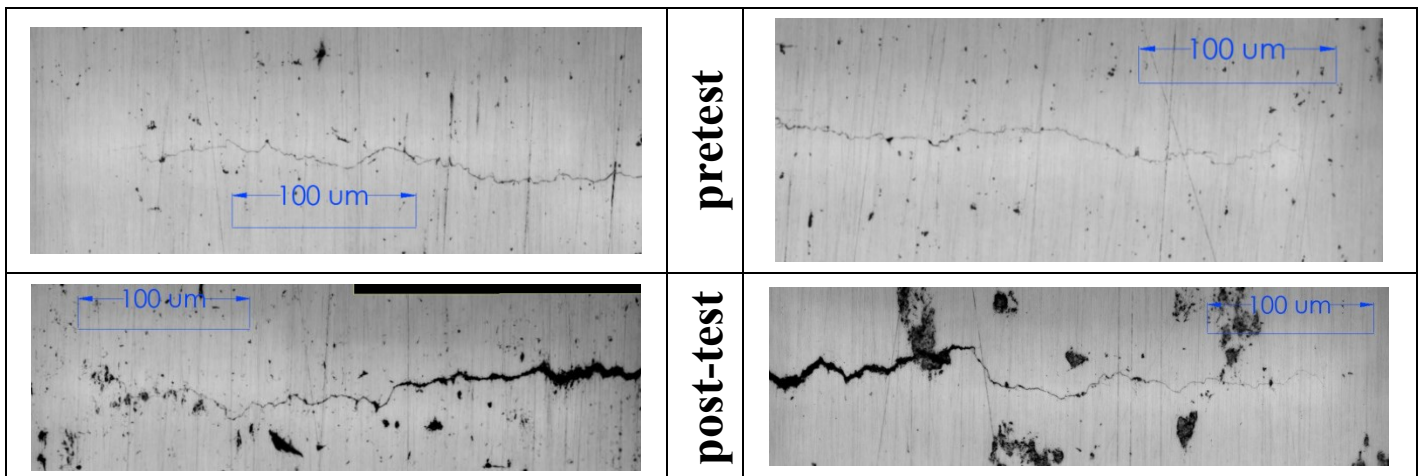
Figure 5-1 Comparison of pretest and post-test crack tip morphology for one of the cracks.

Figure 5-2 has a low magnification stitched image of the entire crack. The two sets of indents near the ends of crack marked where the pre-test crack tip location was. The crack width gradually became thinner as the crack grew beyond the indent marks. The thin crack tips seen in Figure 5-1 suggest a discontinuous crack growth mechanism, discussed in section 2.4.7.3. For discontinuous crack growth, a microcrack initiates just ahead of the macro-crack tip in the hydrogen-rich FPZ. The sharp microcrack propagates both forward and backward under cyclic loading, and is eventually able to link up with the macro-crack. The result is a sharp crack tip

132

after the corrosion fatigue tests. The significant amount of crack widening observed at the center of the crack in Figure 5-2 indicates a strong blunting mechanism was also competing with the microcrack sharpening mechanism.

Crack widths were measured at the center of each crack as seen in Figure 5-2 to study if any trends could be found. It was found that the crack width correlates strongly with the size of the crack as seen in Figure 5-3. In the figure, the crack width was plotted against three different crack dimensions: crack length, crack depth, and crack front length. The crack front length is the length of the semi-elliptical crack front. The pretest crack widths were not included in the graph since they were considered negligible, so only post-test crack widths were included. Post-test crack widths for all cracks were included in the plot. Since different cracks grew to different sizes, width measurements over a large range of sample size could be obtained. RL5 and RL6 were also taken out of the cell after each test for measurements, so a lot of crack widths data for smaller crack sizes were also obtained.

Exponential regression provided good fit for all three trends in Figure 5-3. The trends showed minimal scatter and the regression model has high R-squared value. Different crack underwent different spectra and still produced data that fitted in with the fitted trend. This suggests that the spectra did not affect the crack widening process. Therefore the crack widening process was controlled by the max stress and environment.

A key observation from Figure 5-3 is: the larger the crack, the wider it is. This suggests K_{max} has an effect on crack widening. The long period of minor cycles combined with the high max load of 80% SMYS makes it sound plausible. However, the large width measurements (up to 103 μm) also suggest that mechanical factors were not the only cause for crack widening, and other factors, most likely environmental factors, also played a role. Yu, in chapter 6 of this thesis, also studied the crack widening on CT specimens after corrosion fatigue tests in NNpH environment [105]. Yu conducted corrosion fatigues tests with two coating conditions. The first is using a bare sample with no coating. The second is a thin strip coating applied over the crack (seen in Figure 5-5) to prevent direct dissolution of crack but still allows IHAC process to occur. The second type of coating is very similar to the coating method used in this thesis. Yu used an underload type spectrum and ran the test for 46 days. Samples in the air were also tested. The

results of his experiments can be found in Figure 5-4 and Figure 5-5. Yu found that the 46 day test had little effect on the crack width of the sample in air. The crack was only widened by around 1 micron. This suggests that mechanical loading has only a small role in widening the cracks. The bare sample in C2 produced the widest crack due to the dissolution of the crack walls. The most interesting results were that of the coated samples tested in C2. The coated samples experienced significantly more widening when compared to samples tested in air, but since the dissolution was blocked, the widening effect had to be attributed something else. Yu argued that the crack widening observed for coated samples in C2 was due to hydrogen enhanced localized plasticity (HELP). Even though dissolution was blocked at the crack tip, hydrogen was still reduced at the steel surface and could easily diffuse into the metal surrounding the crack and cause HELP.

The HELP mechanism is also a plausible explanation for the large widening observed on the samples in this study. The strip of coating over the surface blocked most of the dissolution, so the crack widening could not be attributed to corrosion. However, hydrogen produced on the bulk surface could still diffuse to the regions around the crack and cause HELP. Even though no tests were done in air in the current study, it is expected that the crack width increase for an in-air test would be similar to what Yu had observed for his specimens tested in air, since the K_{max} used by Yu (~33 MPa√m) was similar to the K_{max} value used for this study.
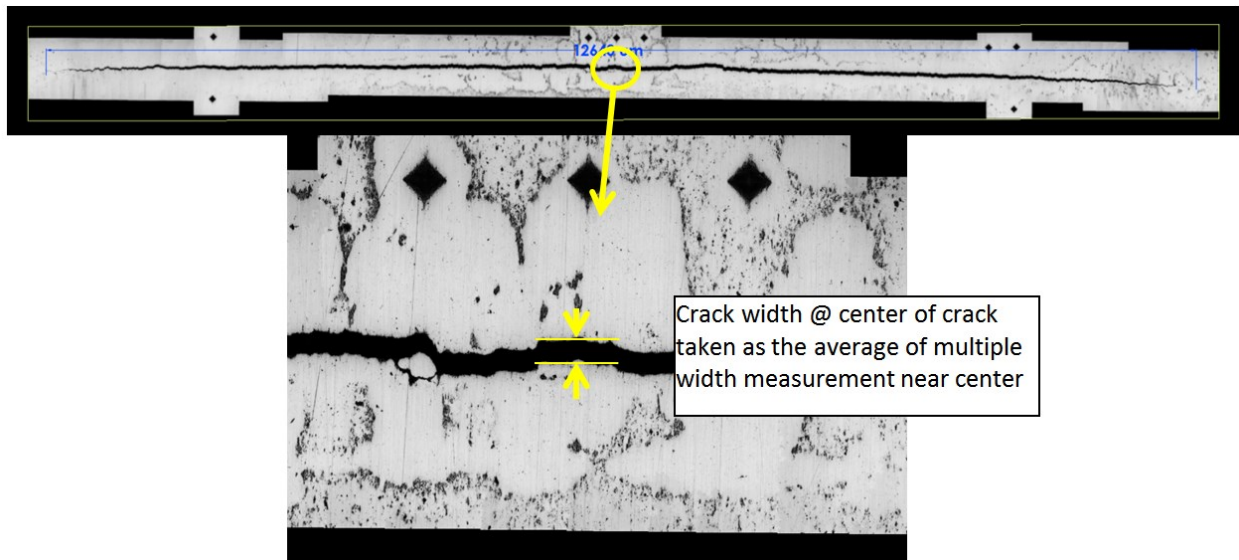
Figure 5-2 Crack width measurements were taken at the center of the crack.
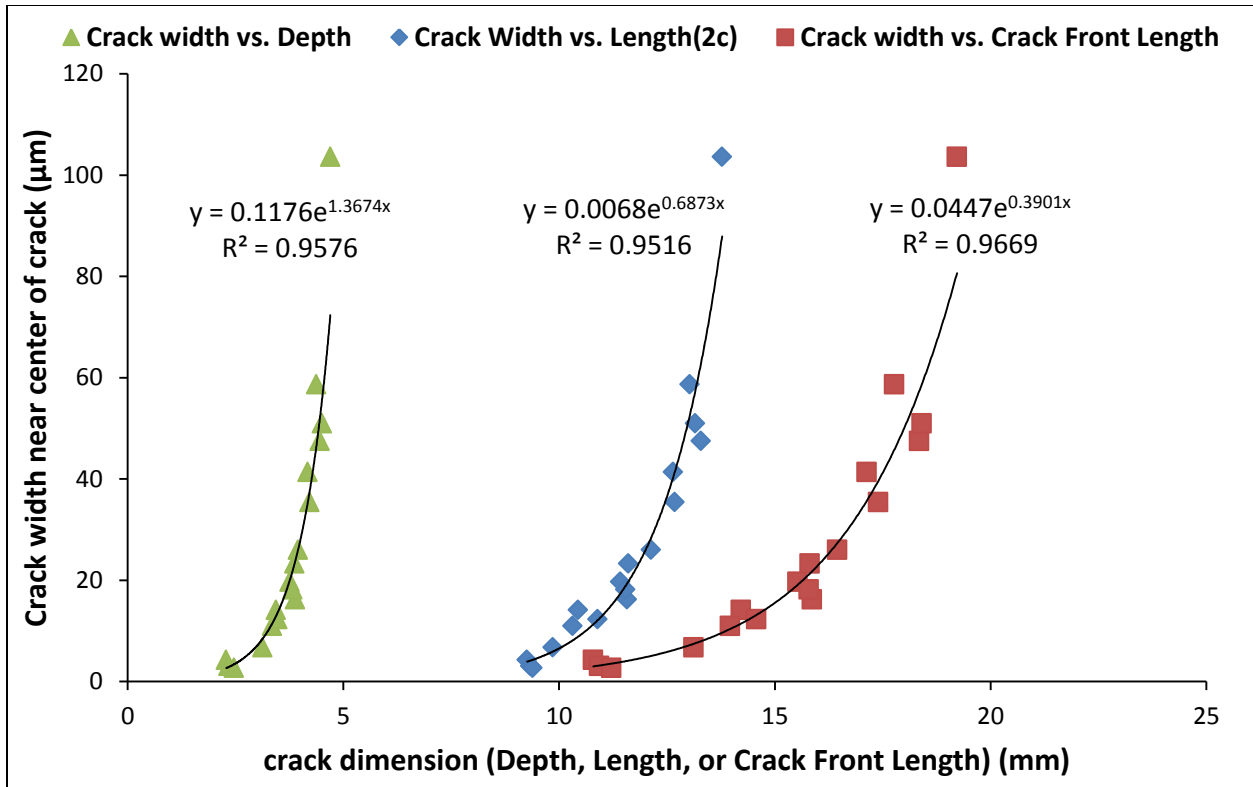
Figure 5-3 The relationship between the crack opening width at the outer surface (measured near the midpoint of the crack length), and other geometries of the crack (crack length, crack depth, and crack front perimeter)
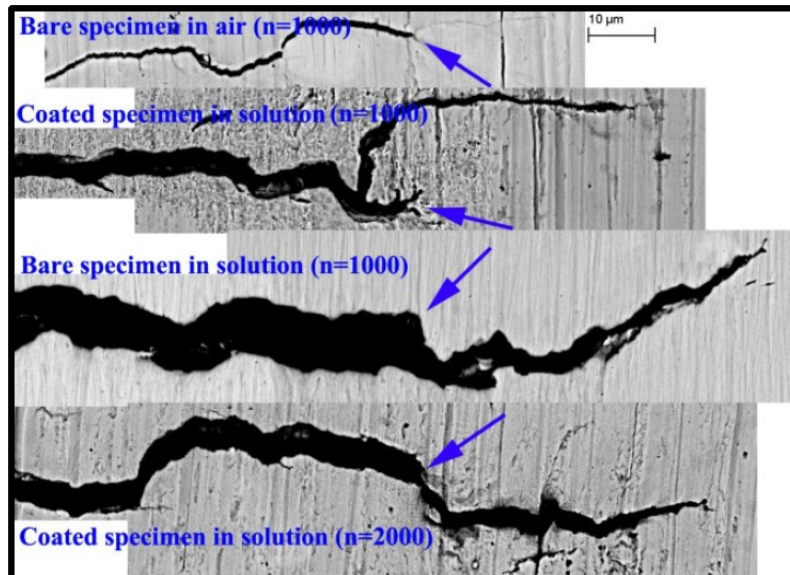
Figure 5-4 Crack tip morphology of CT specimen with different coating conditions tested with VAL underload-type spectrum. Significant crack widening was observed for both coated and uncoated samples tested in C2 solution. Reproduced from [105], with permission from M. Yu.

135
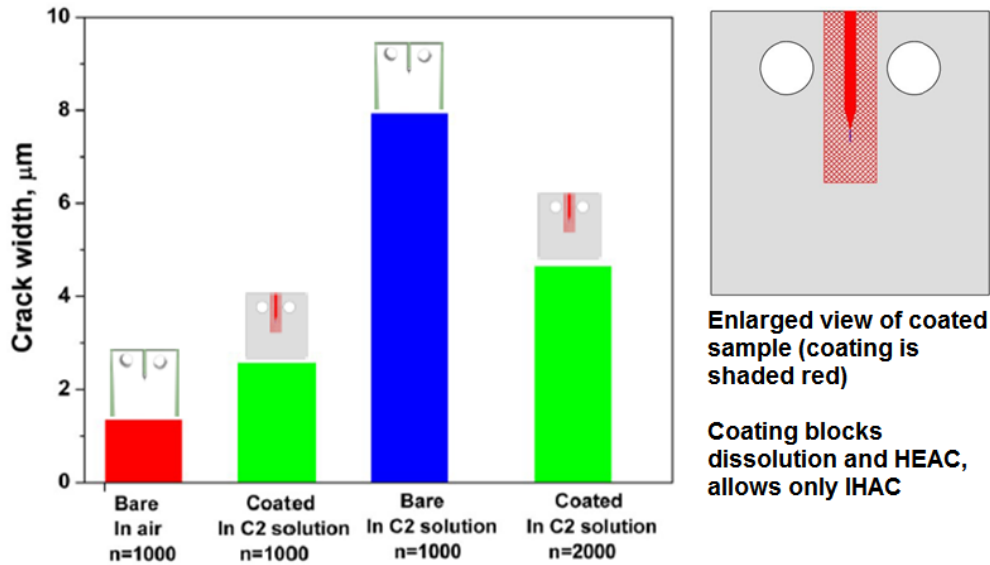
Figure 5-5 Crack width measured behind precrack tip after underload-type test on CT specimens. All tests were 46 days in duration, except for the coated n = 2000 test which took 52 days. K_{max} = 33 Mpa$\sqrt{}$m. An enlarged view of coated sample is shown on the right. Reproduced from [105], with permission from M. Yu.

5.1.2 Corrosion on the Sample Surface

The ability of Tuck® Tape to block corrosion under the coated strip is demonstrated in Figure 5-6. A small amount of water is still able to penetrate into the coating as shown in (a), leaving some corrosion deposit on the surface. After polishing, however, these corrosion deposits under the tape were easily removed as seen in (b). Because the amount of moisture that is able to diffuse under the tape is so small, very few corrosion pits are formed under the tape. In (b), the boundary between coated and uncoated areas on the sample is clearly visible. The uncoated areas were filled with corrosion pits, while the coated area remains relatively pristine. The crack tips under the tape coating also remained sharp throughout the corrosion fatigue tests (Figure 5-1), providing further evidence that the tape is effective in blocking out dissolution.

Figure 5-7 shows two images taken with an optical microscope with different focus level at the coating boundary. Optical microscopes have a narrow depth of field therefore only a narrow Z range can be in focus. The image on the left was focused on a higher plane, which puts the coated region in focus. The image on the right was focused on a lower plane, which put the corroded region in focus. This height difference shows that the tape was effective in preventing

136

corrosion. These two images also show that the uncoated region underwent both pitting and general corrosion (the difference in height indicates general corrosion).

The corrosion pitting density also showed variation as shown in Figure 5-8. The pitting density was noticeably higher right next to the coating boundary, and decreased a constant pitting density over a span of about 1 mm. Figure 5-9 shows the high magnification images of the corrosion pits right next to the coating boundary and at a distance of 1.5mm away. The difference in pitting density is clearly shown. In the left image of Figure 5-9, some fine cracks also seem to have initiated from the corrosion pits.

It is not clear what causes the higher corrosion pit density at the coating boundary. Some studies have also reported that crack initiation can occur near the edge of well-bonded coatings [22,69]. For the current study, it is possible that certain corrosion deposits were formed right at the edge of the tape, and the deposit enhanced the corrosion right at the tape boundary. More research is needed into this phenomenon to fully understand the cause.
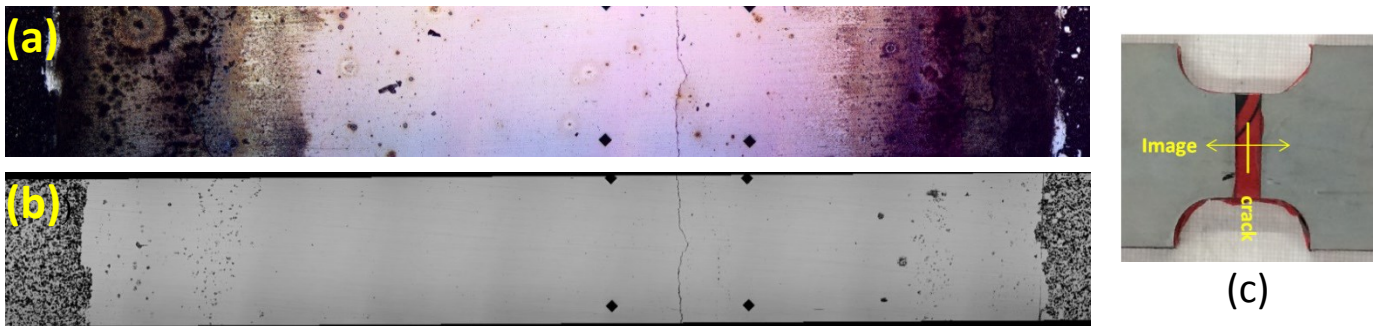
Figure 5-6 Images of the crack area coated with Tuck Tape after coating was removed at the end of corrosion fatigue tests: (a) Tape was removed, and the taped area was cleaned with acetone. (b) The same sample is then polished to 1 μm finish, revealing little corrosion had occurred under the tape (c) The alignment of the image relative to the crack. The image was taken perpendicular across the crack
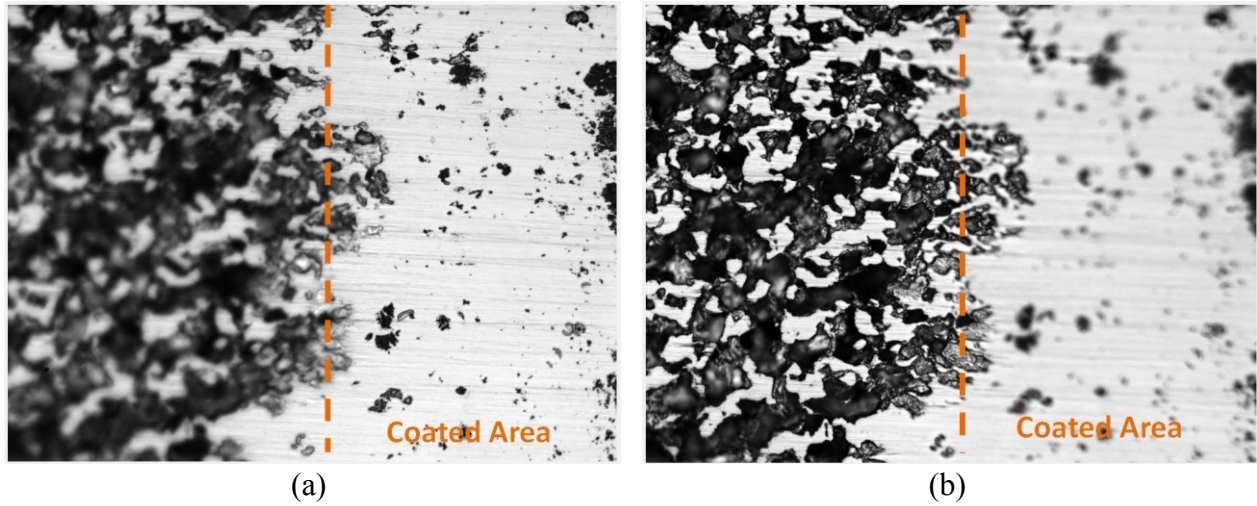
Figure 5-7 Optical microscope image of the coating boundary at different focus levels: (a) the image is focused at a higher plane. The coated region is in focus. (b) The image is focused at a lower plane. The corroded region is in focus.
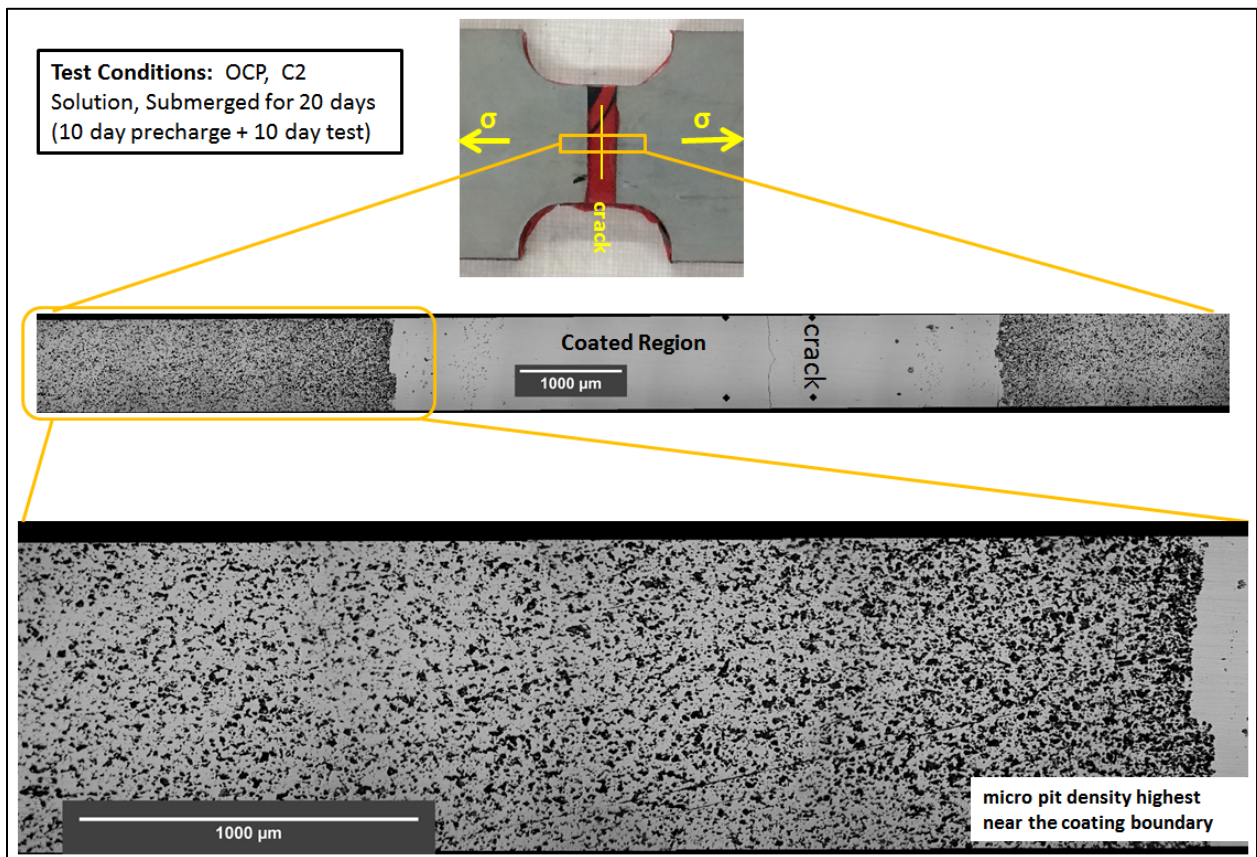
Figure 5-8 Low-magnification stitched image taken across the coated region on the gauge section. The top image indicates the orientation and the location where the image was taken. The bottom image is a zoomed in view of the corroded region, showing the change in micro pit density from the coating boundary.
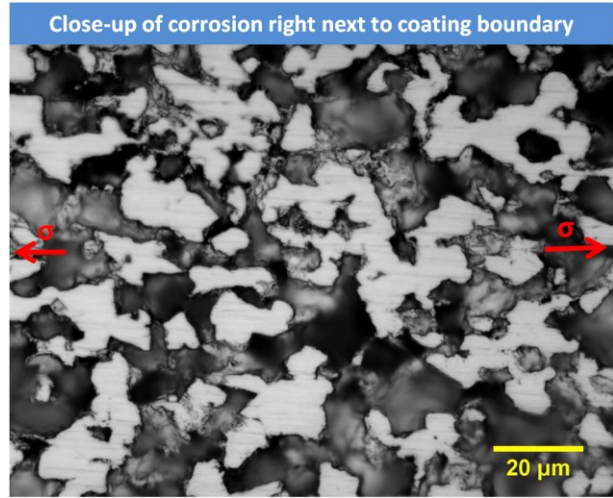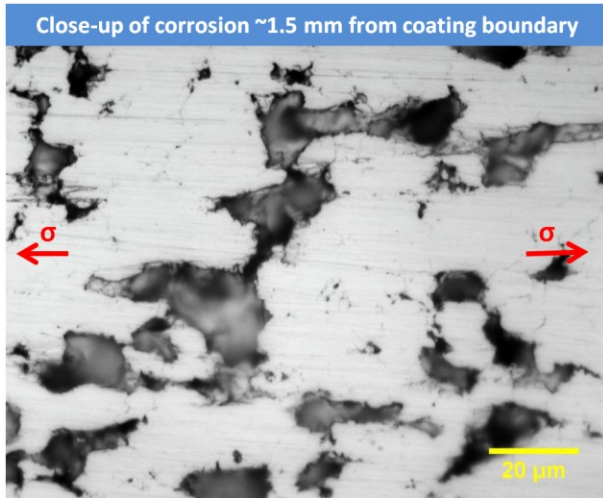
Figure 5-9 High magnification optical images of the corrosion pits near the coating boundary. Left: image taken at ~1.5mm away from the coasting boundary. Right: image taken right next to the coating boundary

5.2   Fracture Surface Characterization

A full collection of crack images be found in Appendix B.

5.2.1   Beachmark Results

The max load during beachmark was significantly lower than the max load during corrosion fatigue tests. As a result, a large plastic zone is created ahead of the crack tip during testing. The beachmark max load is unable to overcome this plastic zone initially. Therefore the crack seeks out other paths to propagate during beachmark cycles. This leads to bifurcation and branching during beachmark as shown in Figure 5-10. The crack bifurcates along the entire crack front during beachmarking, and creates dark crack like crevices on the fracture surface as seen in Figure 5-12 that are distinct from the quasi-cleavage morphology created during the corrosion fatigue tests. The beachmark cycles also produce striations similar to those seen for precracking in air, as evidenced in Figure 5-11.

These striations and crevices in the crack wall that resulted from beachmarking create a rough texture with a large amount of surface area. This makes the beachmark bands particularly susceptible to corrosion as seen in Figure 5-13 (a). The crevices in the crack wall and the rough texture create a lot of pockets where moisture can get trapped and form precipitates. The corrosion fatigue regions, with their large smooth facets, are relatively unaffected by moisture accumulation. As discussed in section 5.1.2, it was difficult to completely block out moisture with a thin strip of coating. A small amount of moisture was expected to diffuse through the adhesive layer on the tape, but it was not expected to affect the results since there was little evidence of corrosion on the quasi-cleavage regions. Cleaning the fracture surface with replicating tape and acetone (as seen in Figure 5-13 (b)) resulted in a cleaner fracture surface, but the beach mark regions were still covered with corrosion deposit. This suggests that there was excellent adhesion of the corrosion deposit due to the rougher texture. Further cleaning using etching and detergent bath as seen in Figure 5-13 (c) was able to remove corrosion deposits from the beach mark areas, and the beachmarks were still clearly visible. The beachmarks appeared darker than the corrosion fatigue regions because the beachmark regions had a rougher texture that reflected less light, whereas the corrosion fatigue region had large quasi-cleavage facets that reflected more light. It should also be pointed out that the precrack region had the same

appearance as the beachmarks in Figure 5-13. This is because the beachmark region had similar morphology as the precracking region (shown in Figure 5-14).

The widths of the beachmark bands are also important, because thinner beachmarks allow for more accurate measurements. The beachmark widths were confirmed under the SEM. For RL5 and RL6, there was considerable growth during beachmarking to the higher load, slower frequency and larger numbers of cycles. For RL7 and RL8, the beachmarks were much thinner (in the range of 5 to 20 μm). However, the beachmark was not a continuous band. As shown in Figure 5-11 and Figure 5-12, there were many points along the crack front where the quasi-cleavage facets spans across the beach mark bands. Therefore, the widths of the beachmarks were considered negligible on RL7 and RL8. As long as thin beachmarks were visible on the macroscopic images, accurate measurements can be made. It is recommended to check the widths of the beachmarks under a SEM to confirm that they are negligible.

Some fracture surfaces were imaged both before and after etching. However, it is not necessary to etch the fracture surface for imaging. The corrosion deposits can be beneficial since they make the beachmarks easier to see. For some samples the beachmarks on the etched surface were too thin to see clearly, but the corrosion deposits were able to clearly show the location of the beachmarks. For other samples where the corrosion deposits obscured the beachmarks, the etched fractograph is more useful. Information obtained from both the etched and unetched images can be pieced together to obtain the complete set of crack growth measurements.
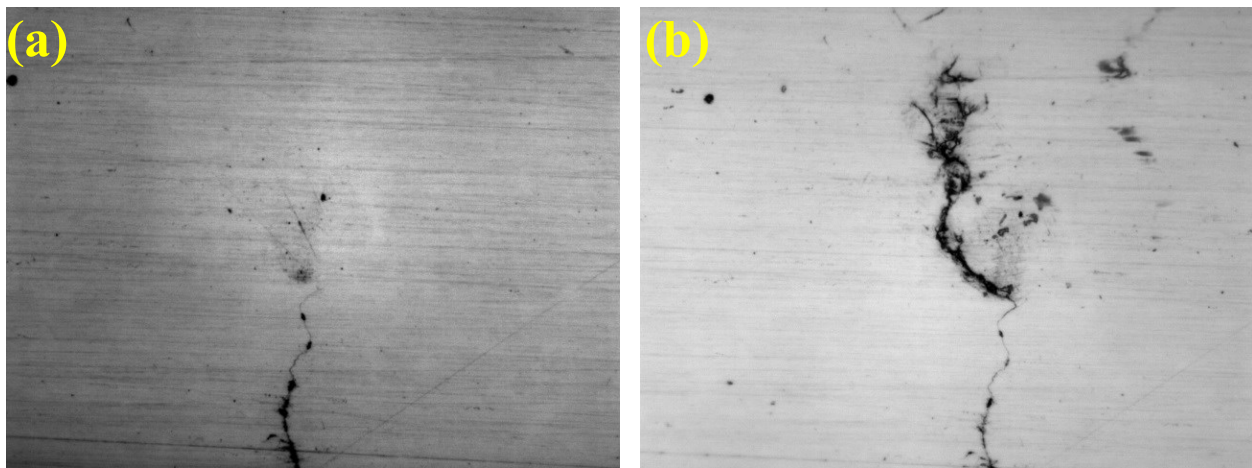
Figure 5-10 Crack tip on the surface: (a) before beachmark cycles (b) after beach mark cycles
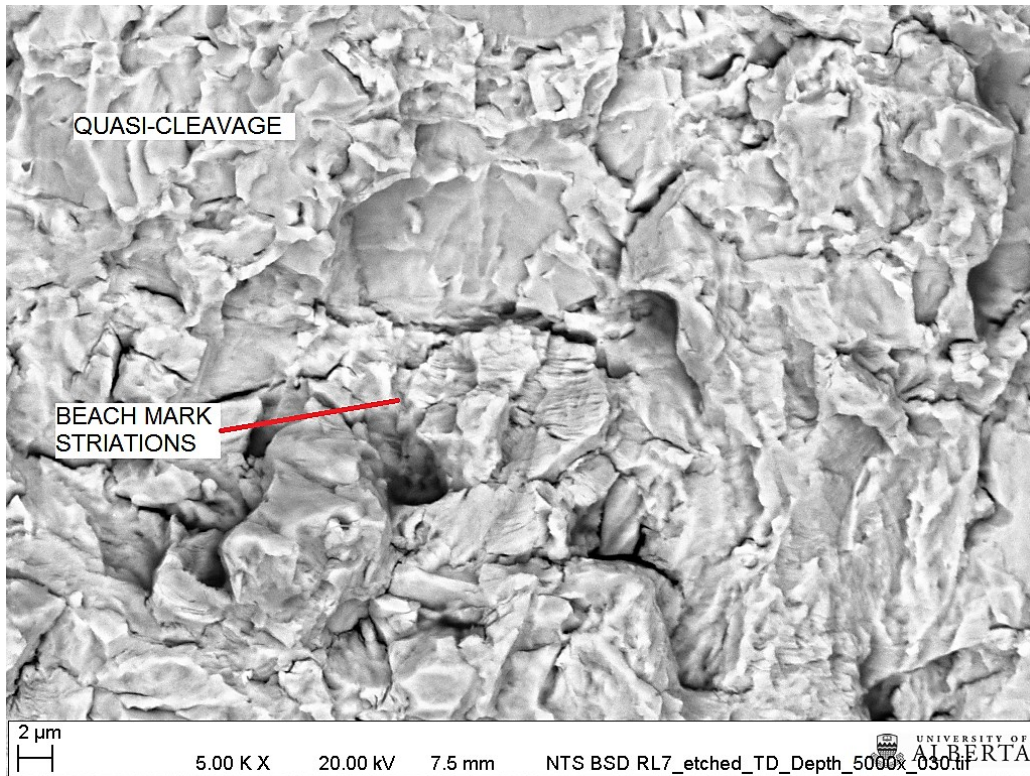
Figure 5-11 Beachmark morphology under SEM, showing beach mark striations.
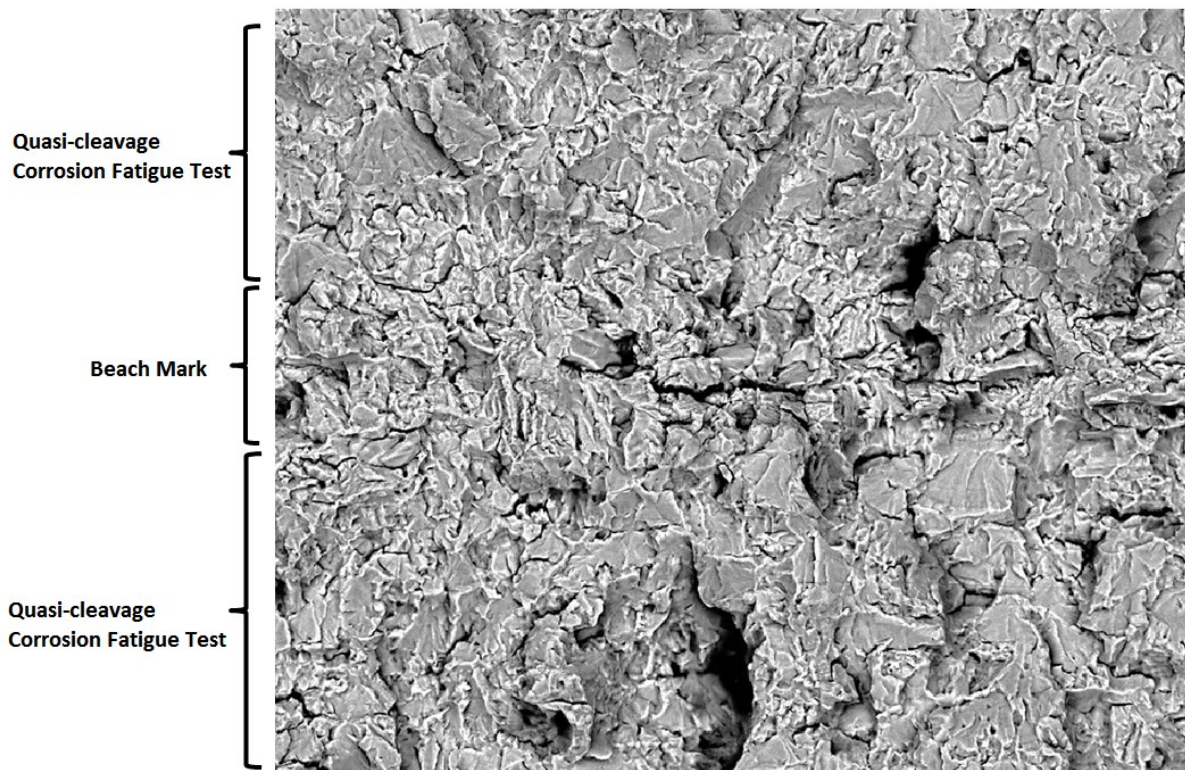
Figure 5-12 2000x SEM image of beachmark region in between two corrosion fatigue test regions.
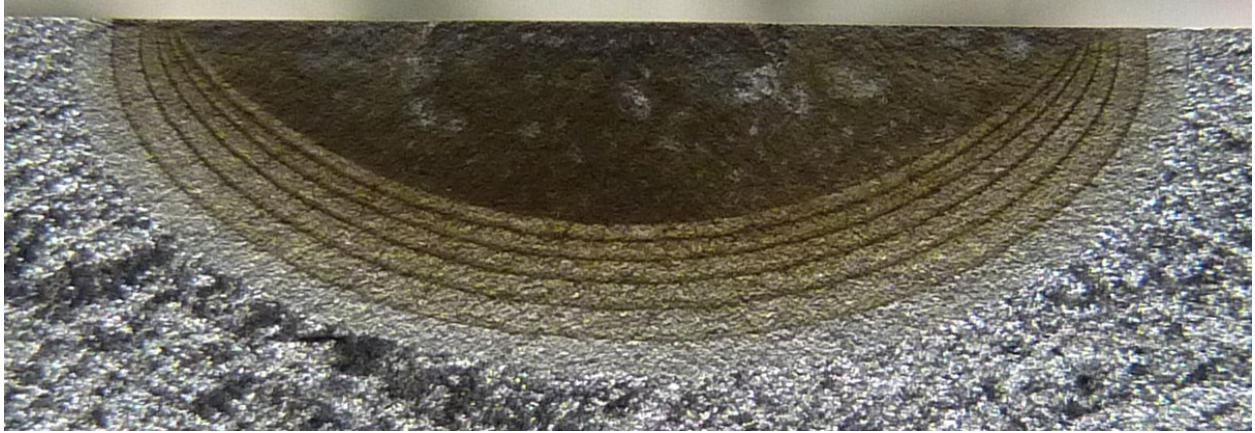
(a) as is after fracture
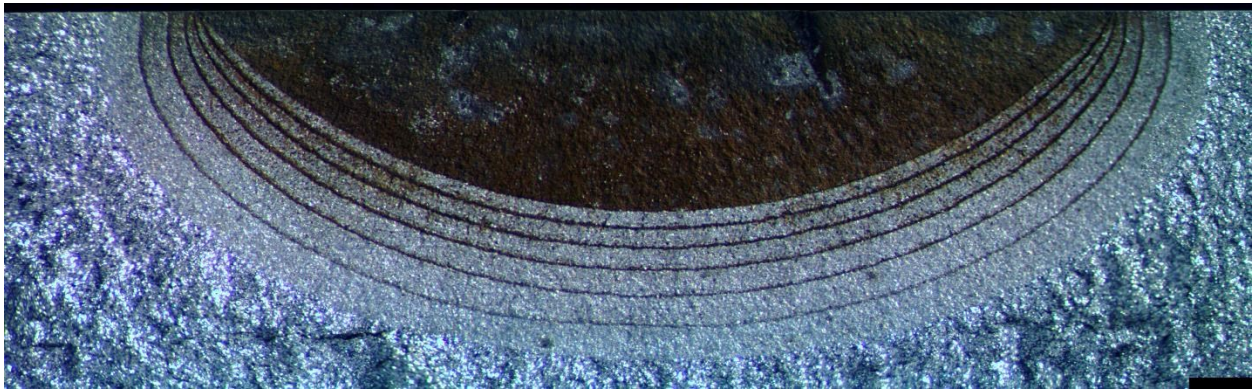
(b) cleaned with replicating film
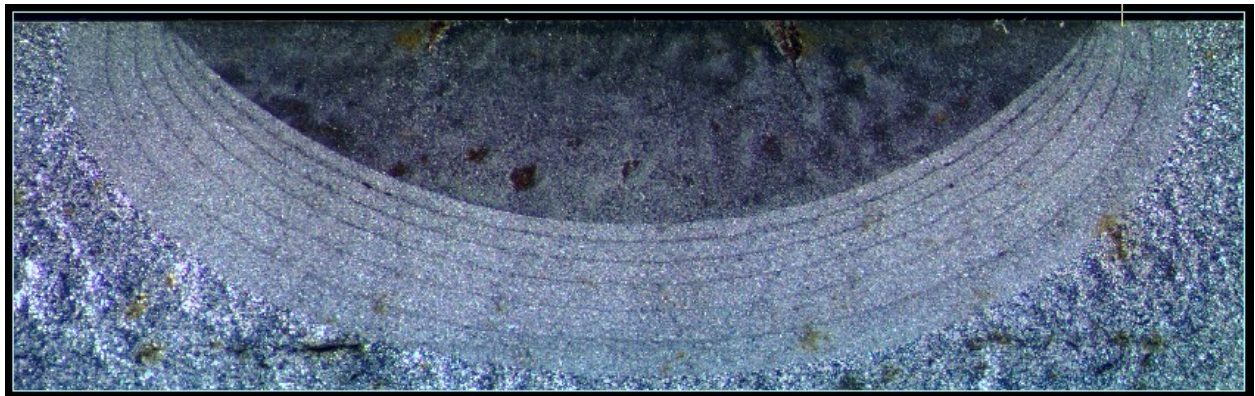
(c) cleaned with 5% acetic acid and detergent solution

Figure 5-13 Fracture surface for RL7-M showing the beach marks generated: (a) Image take right after fracture, with a regular camera (b) Image taken using stereo-microscope after cleaning with replicating film (c) Image taken using stereo-microscope after cleaning with 5% acetic acid and detergent solution
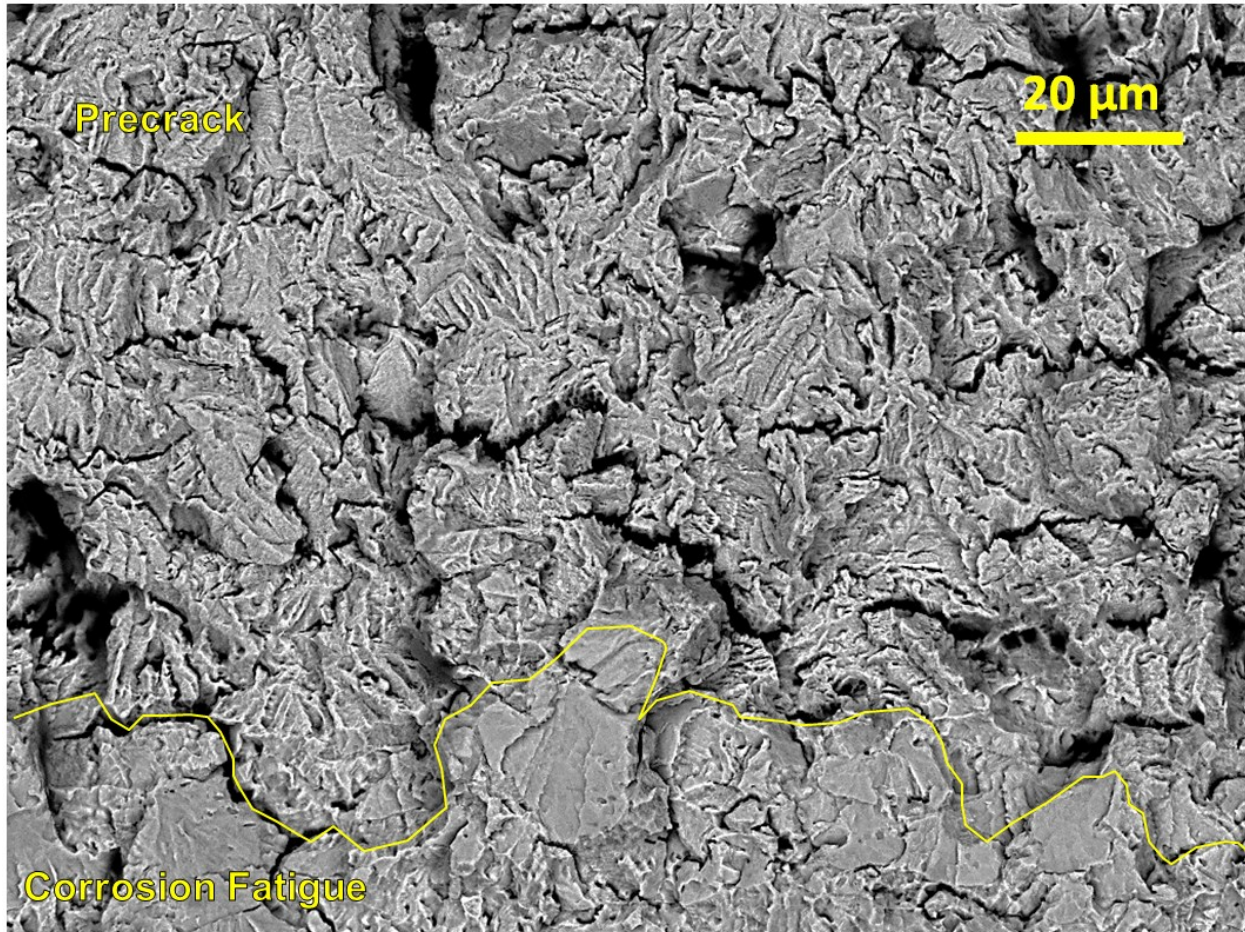
Figure 5-14 Difference in morphology between precrack and corrosion fatigue test

5.2.2   Surface Growth Lagging

As the crack grew larger, it was also observed that the surface tip growth lagged behind the growth just beneath the surface. This is shown in Figure 5-15. This is a well-known phenomenon that's commonly observed for thru-wall crack specimens as well, and is illustrated in Figure 5-16. The lagging behaviour is due to the larger plastic zone on the surface which causes crack closure effects. For this study, all surface lengths were measured on the outer surface of the sample to be consistent. The extended length just beneath the surface was not used for measurements.

Figure 5-15 Close-up of a surface tip showing growth at the surface is lagging behind growth just beneath the surface.

crack growth direction

successive positions
of crack front

(a) Curved crack fronts of through crack

crack growth
directions

lagging behind
of crack front

(b) Deviations of semi-elliptical
crack front at material surface
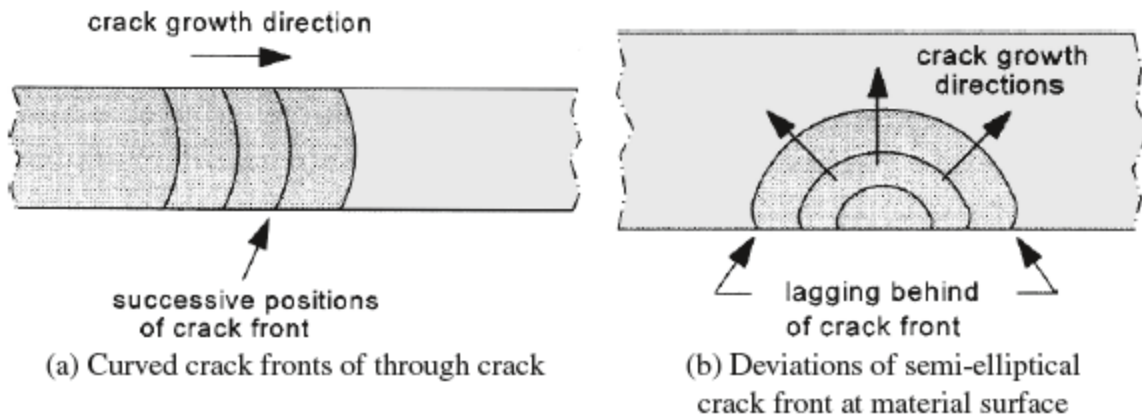
Figure 5-16 Crack growth lagging on the material surface due to closure effects. Reproduced from [146], with permission from Springer.

5.2.3　　　More SEM Images of Fracture Surface

Quasi-cleavage is the predominant fracture morphology observed in the corrosion fatigue regions on the fracture surface, as shown in Figure 5-17 to Figure 5-19. This is strong indicator of hydrogen embrittlement during crack growth. Direct dissolution and HEAC was blocked with the coating, therefore IHAC was the main mechanism behind the HE. Pockets of ductile dimples could also be found, especially in later test regions. This suggests an elastic-plastic model would be more accurate for crack growth prediction. The fracture surface morphology also agreed with the field findings, which demonstrated that the coating condition used during the experiment was able to accurately simulate Stage II SCC.
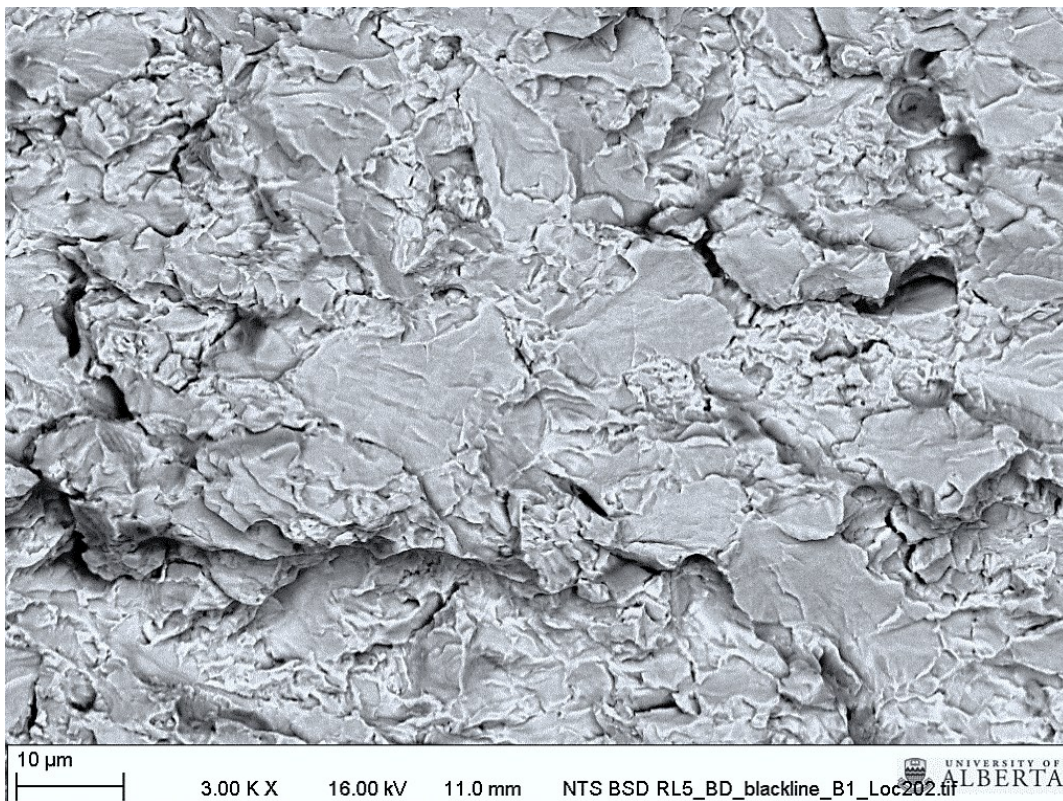
Figure 5-17 Fracture surface morphology in the corrosion fatigue region, showing quasi-cleavage fracture mode

146
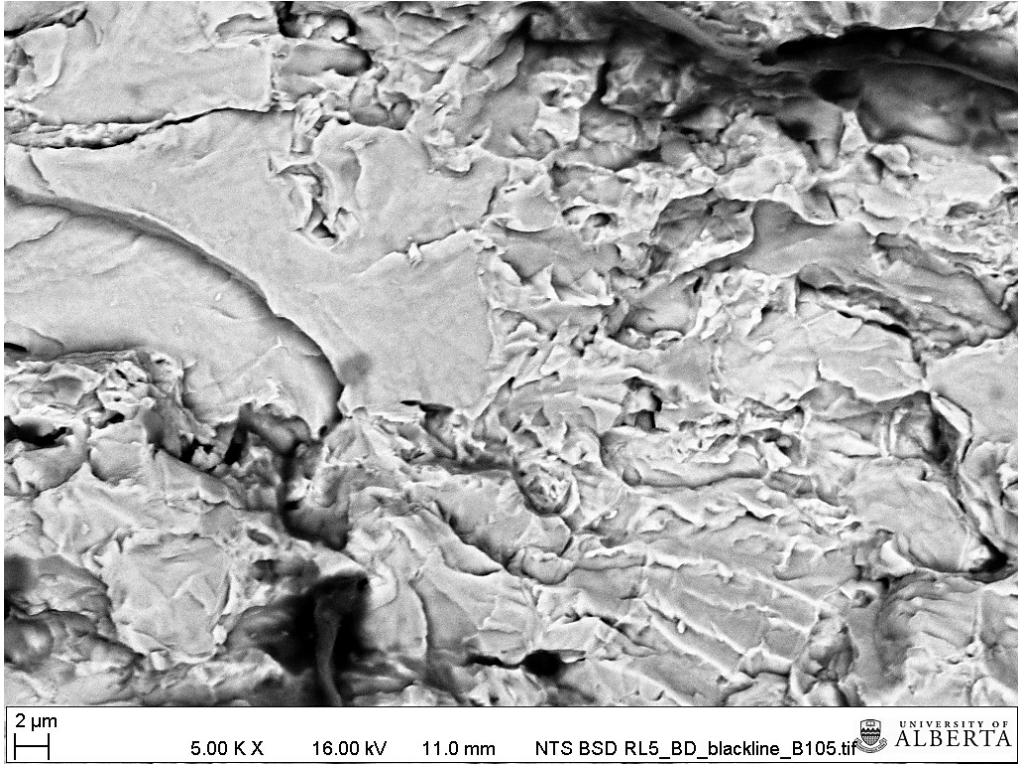
Figure 5-18 Fracture surface morphology in the corrosion fatigue region, showing quasi-cleavage fracture mode
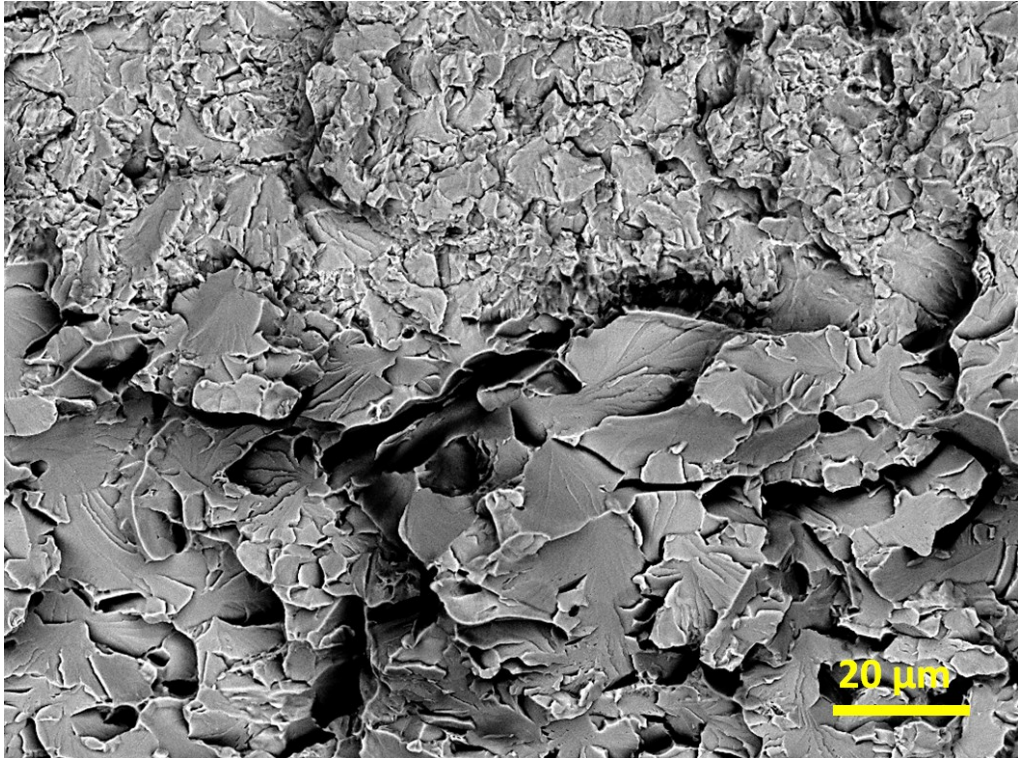
Figure 5-19 SEM image showing the end of corrosion fatigue tests and the start of final brittle fracture. The fracture morphology makes a sudden transition from quasi-cleavage to brittle cleavage.

5.3   Crack Growth Rates of Spectra

Note: The growth data for all of the cracks, including SIF, growth rate, and combined factors results were tabulated in <mark>Appendix A.</mark>

With the aid of beachmarks, the crack growth during each test in both the surface and depth direction can be measured. The crack growth rate of a test is calculated as the growth amount in each test divided by the number of fundamental blocks tested. As discussed in section 4.8, the number of cycles in a fundamental block is the sum of the numerator and denominator in the reduced MC:UL ratio. For all the spectra tested, the MC:UL ratio is 7:1. Therefore the FB length is 8 cycles. Growth rate is calculated per FB so fair comparisons between different spectra can be made. The FB captures the load interaction effects between the minor cycles and underload cycles. The minor cycles by themselves contribute little to crack growth in constant amplitude loading, but they can enhance the growth of underload cycle following after them [10].

The stress intensity factor for a test region is calculated using the midpoint dimensions c_{mid} and a_{mid}. Since a test region is bounded in between two beachmarks, the initial and final crack dimensions for the test can be easily measured. c_{mid} is the midpoint surface length between initial and final surface length for a test region. a_{mid} is the midpoint crack depth between the initial and final depth for a test region.

The combined factor [81] was used as driving force parameter for crack growth. As discussed in section 2.4.4.4, the combined factor accounts for both the mechanical and environmental influence on crack growth. Eqn (2.15) shows the equation of the combined factor model for constant amplitude loading:

$$\frac{da}{dN} = A \left[\frac{\Delta K^{\alpha} K_{max}{}^{\beta}}{f^{\gamma}} \right]^{n} + h \qquad (5.1)$$

The $\frac{\Delta K^{\alpha} K_{max}{}^{\beta}}{f^{\gamma}}$ term is the combined factor, where $\alpha = 0.67$, $\beta = 0.33$, and $\gamma = 0.033$. The frequency f accounts for the environmental effect on crack growth. A and n are constants analogous to C and m in Paris law, and are determined through curve fitting on experimental data. h is crack growth due to dissolution, however in this study all of the samples were coated, so h

148

was assumed to be zero for all tests. K_{max} was calculated using the midpoint crack dimensions c_{mid} and a_{mid} described earlier. ΔK was calculated for the UL's. However, two types of UL's were used, R = 0.1 and R = 0.4, so two sets of combined factor were calculated, one for type 'A' UL with R = 0.4 and one for type 'B' UL with R = 0.1.

The UL is the main driver behind crack growth, so it makes sense to calculate the combined factor for the UL cycles. Since two sets of combined factors were calculated, comparison with other studies' results is more difficult because one now has to ask which set of data should be used for comparison, R = 0.1 or R = 0.4? The combined factor was designed for constant amplitude loading, and can only handle one type of waveform in the spectrum. This is a challenge faced by all VAL fatigue experiments. Currently there is no solution to address this issue. More research is needed in order to find better ways to compare different VAL spectrum results. However in this study, the combined factor model can be used to internally compare the spectra tested to find their relative severity.

Since the growth rate is based on FB and the dissolution is negligible, eqn (2.15) can be modified to:

$$\frac{da}{d(FB)} = A \left[\frac{\Delta K^\alpha K_{max}{}^\beta}{f^\gamma} \right]^n \tag{5.2}$$

Eqn (5.2) is used as the corrosion fatigue model for this experiment. The crack growth rate per FB was plotted against the combined factor in Figure 5-20 to Figure 5-23.

In Figure 5-20 and Figure 5-21, the corrosion fatigue data points at the surface and depth were plotted. Two sets of data were plotted on each chart, one for type 'A' UL with R = 0.4, and the other for type 'B' UL with R = 0.1. The two sets of data points share the same growth rate values (on vertical axis). The difference comes from the combined factor value which depends on the R ratio. As a result, the two data sets were shifted horizontally from each other. It can also be seen that the R = 0.4 dataset is a more conservative dataset, showing faster growth rates than the R = 0.1 data for any particular value of combined factor. The growth trend from Chen & Sutherby's combined factor study [81] were also included in Figure 5-20 and Figure 5-21 as the grey curves. The growth curve is obtained from Figure 2-16 (b), which was drawn by Chen & Sutherby after

normalizing the growth rate data obtained from the CT specimens in C2 solution. This curve represents the predicted crack growth rate for different combined factor values in C2 solution for constant amplitude loading. In Figure 5-20 and Figure 5-21, the growth rate for this curve is in mm/cycle, where 1 block = 1 cycle. In both figures, the curve lies between the R = 0.1 and R = 0.4 data sets. This makes sense because R = 0.4 data set is over-conservative, while the R = 0.1 data set is under-estimating crack growth rate. The spectra were also designed to have 50% of UL with R = 0.4, and the other 50% of UL with R = 0.1. This means the combined effect of these two underloads should fall somewhere in between. Chen & Sutherby's growth trend shows an approximate location of where this "combined effect" trend would be.

In Figure 5-20, the experimental data sets for surface growth have the same shape as the Chen & Sutherby's trend. The near-threshold behaviour is observed for the curve as well as the data points. But in Figure 5-21, the experimental data sets for depth growth showed more deviation from Chen & Sutherby's trend, especially as the crack grew larger. This suggests that thru-wall crack specimens such as the CT specimen used by Chen & Sutherby model the surface growth behaviour better than the depth growth behaviour for semi-elliptical surface cracks. This has implications for other test results from CT specimens. Researchers have relied on CT specimens to provide test results that could represent crack depth growth in a pipe wall, but this study shows the CT specimens is more suited for modelling surface growth behaviour. The stress state within a thru-wall crack is important in determining its behaviour. It is likely that Chen's CT specimens had a stress state closer to plane stress throughout the thickness of the sample. More studies with thicker CT specimens should be done to check if it models the depth growth behaviour better, since thicker CT specimen is more likely to have stress state closer to plane strain at the centre of the sample.

In Figure 5-22 and Figure 5-23, lines based on the power law shown in eqn (5.2) were fitted for each spectrum's data points. The goal was to obtain a set of fitted lines where the data can be visualized more clearly and allow for easier comparison of the severity of different spectra. Since the goal was for comparison within this study, either R = 0.1 or R = 0.4 data sets could do the job. This is because on a log-log plot, the two data sets are merely offsetted horizontally from each other. For clarity, only R = 0.1 data points and their fitted lines were shown in Figure 5-22 and Figure 5-23. For the surface growth plot (Figure 5-22), the points near threshold were not

included in the regression. The crack measurements for these initial surface points were not as accurate as the measurements for later tests because the growth amount was small (as small as 25μm growth). For some spectra, there was noticeable change in the slope of the data points midway through, so two lines were fitted instead of one. The two-line fitting was only done for 28MC-ABAB and 28MC-BABA spectra.

Table 5-1 and Table 5-2 list the parameters of the fitted lines in Figure 5-22 and Figure 5-23. The parameters A and n from eqn (5.2) were determined through linear regression of the log-log data. The parameters for both R=0.4 and R = 0.1 data were shown. The power n is the same between both R = 0.4 and R = 0.1 since the slopes are the same between the two datasets. $A_{0.4}$ is the A value determined for the R = 0.4 data, and $A_{0.1}$ is the A value determined for the R = 0.1 data.
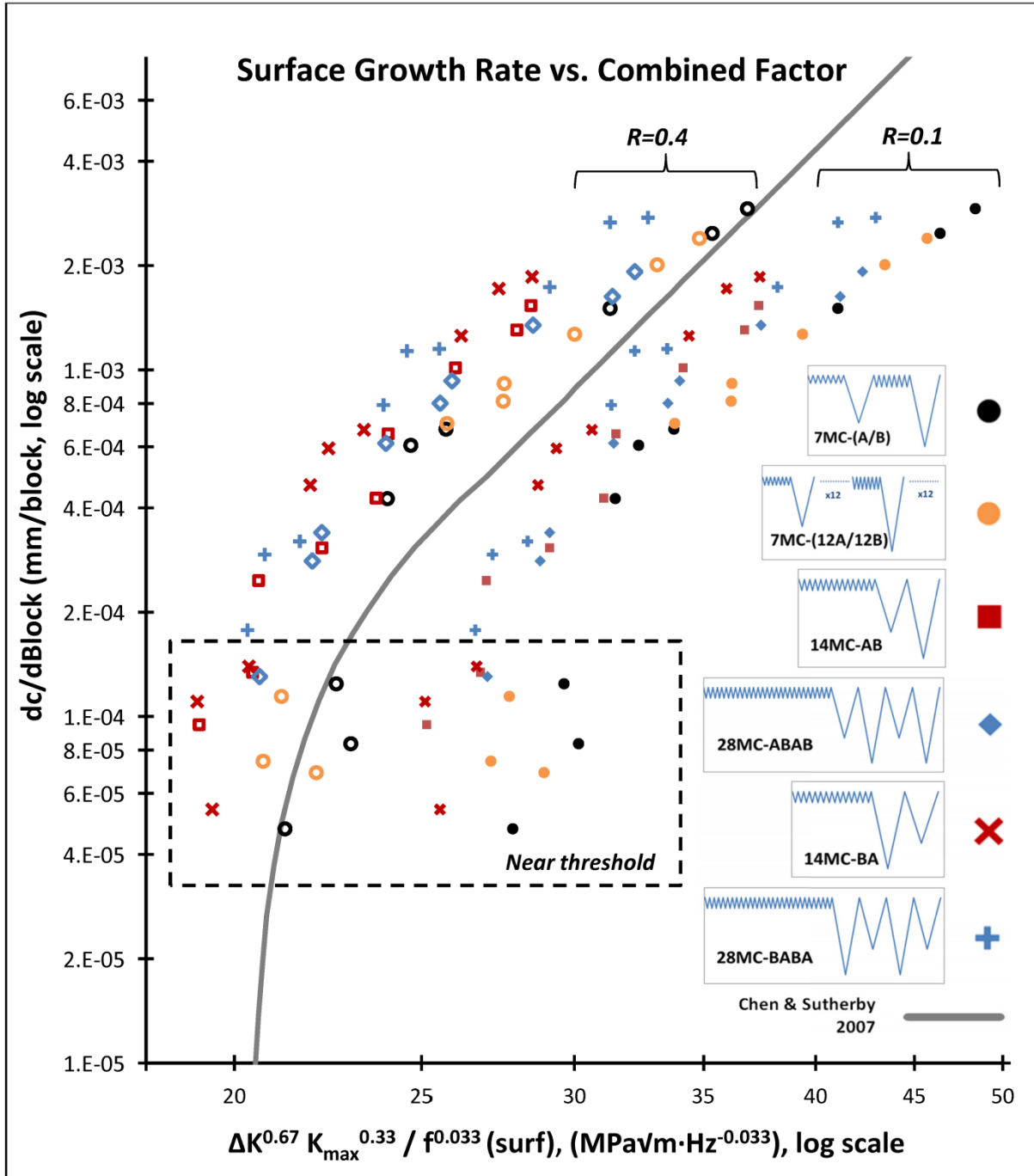
Figure 5-20 Experimental data points for crack growth at surface. The combined factor is calculated for the UL cycle in the spectrum. Since two types of UL were used (R=0.4 & R=0.1), the data points for both R ratios were plotted. Chen's experimental combined factor crack growth curve for C2 solution [81] is shown with a grey line.

152
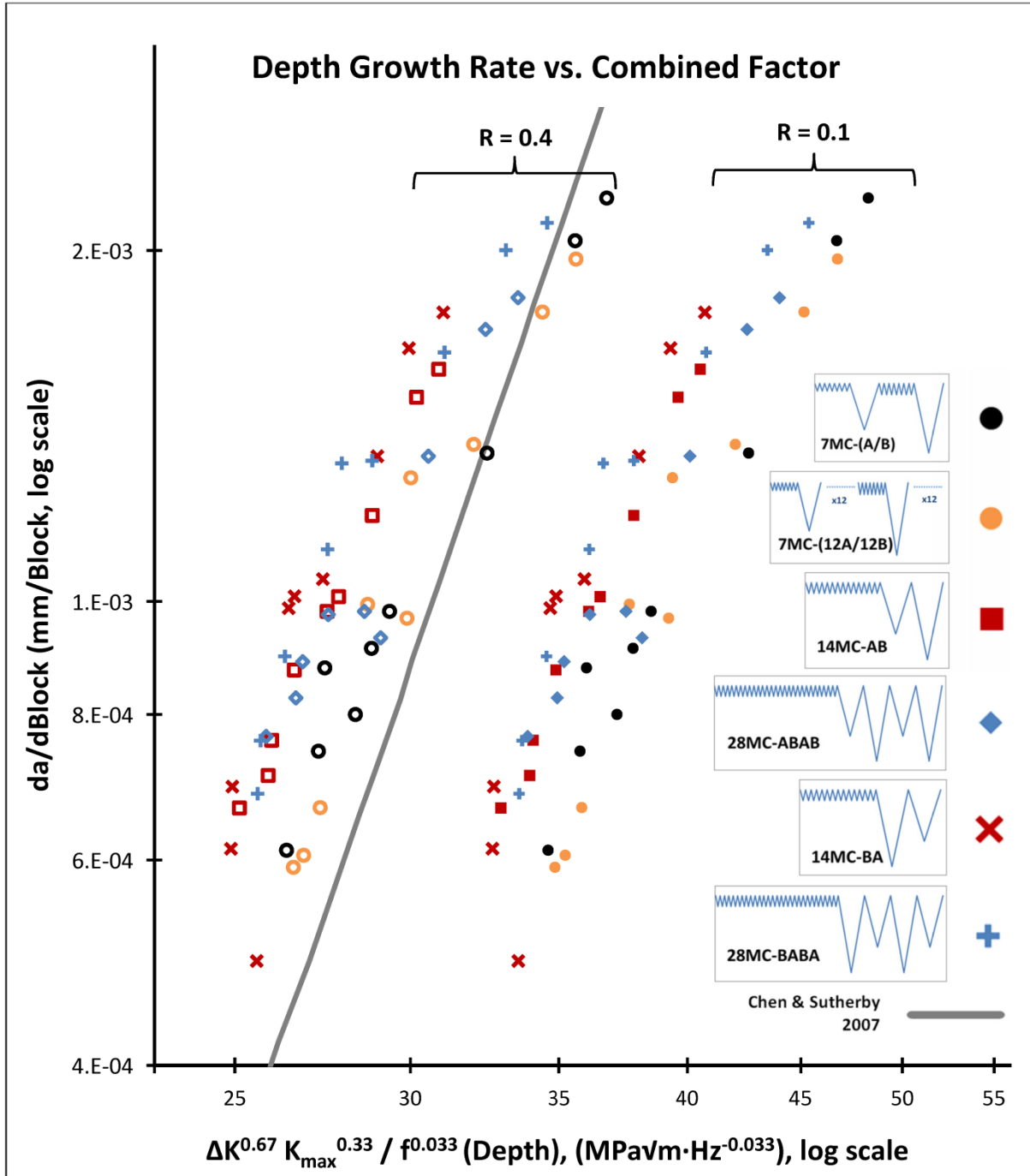
Figure 5-21 Experimental data points for crack growth at depth. The combined factor is calculated for the UL cycle in the spectrum. Since two types of UL were used (R=0.4 & R=0.1), the data points for both R ratios were plotted. Chen's experimental combined factor crack growth curve for C2 solution [81] is shown with a grey line.
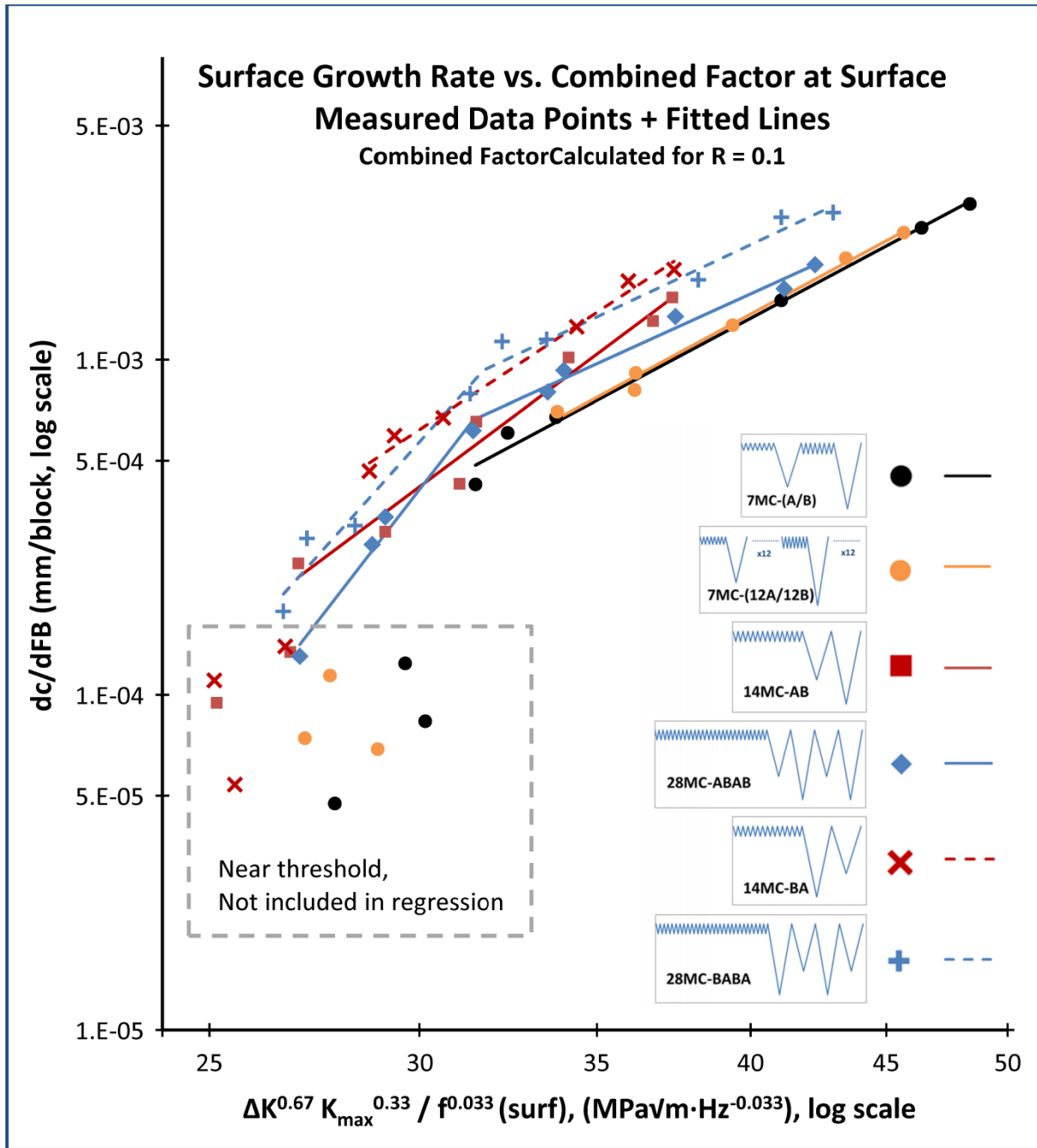
Figure 5-22 Experimental data points for surface growth fitted with regression lines based on power law. Only the data for R = 0.1 UL is shown for clarity.
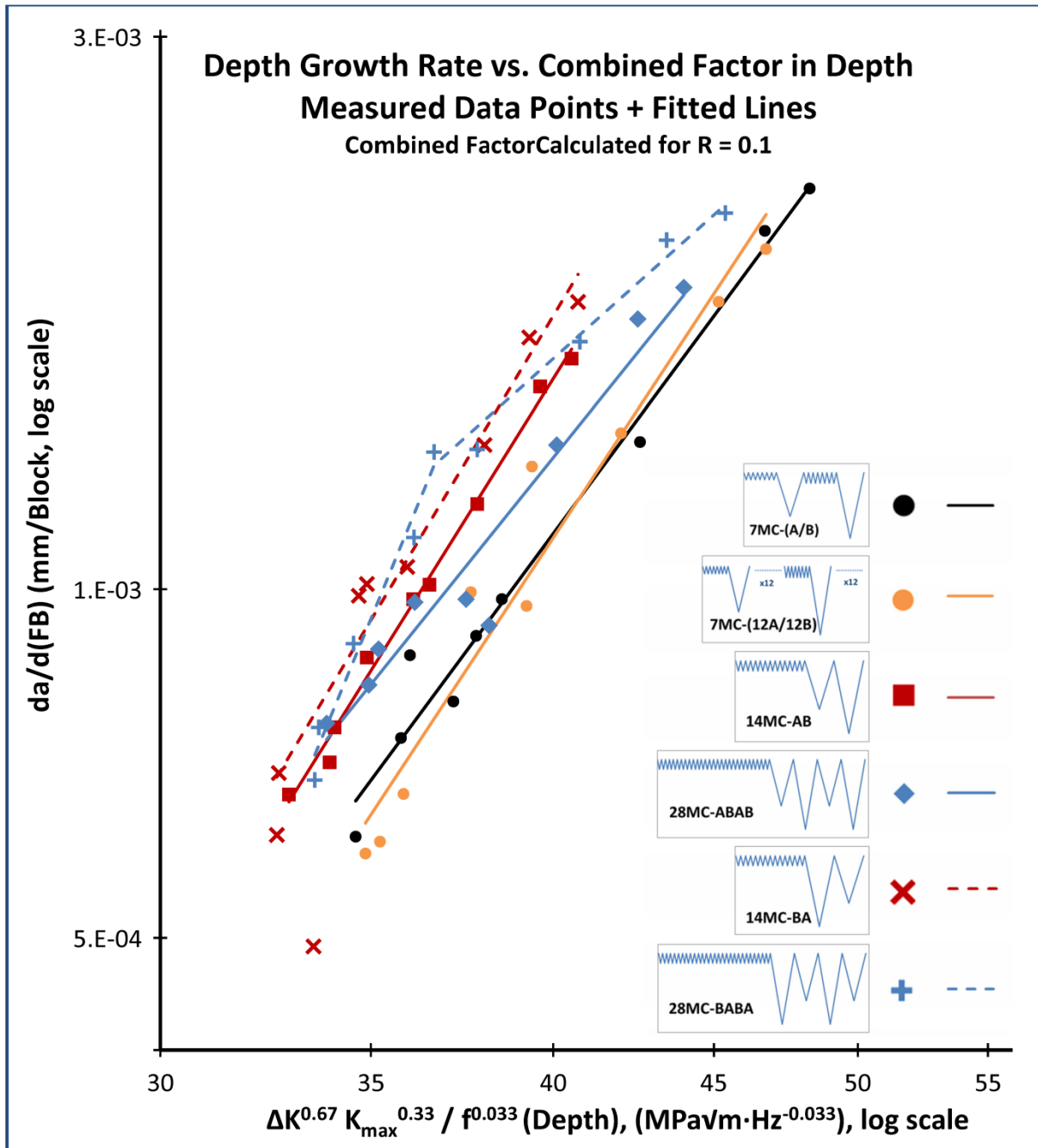
Figure 5-23 Experimental data points for depth growth fitted with regression lines based on power law. Only the data for R = 0.1 UL is shown for clarity.

Table 5-1 Combined factor crack growth equation constants (A & n) at surface

A & n Values for Surface Growth Units: mm/FB & MPa$\sqrt{m}\cdot$Hz$^{-0.033}$			
Spectrum	$A_{0.4}$	$A_{0.1}$	n
7MC-(A/B)	7.2696E-10	2.3105E-10	4.2193
7MC-(12A/12B)	6.1223E-10	1.9152E-10	4.2779
14MC-AB	3.9151E-12	7.8681E-13	5.9066
28MC-ABAB (line 1)	4.8498E-18	2.9976E-19	10.2469
28MC-ABAB (line 2)	6.0783E-09	2.2574E-09	3.6462
14MC-BA	4.7866E-11	1.1555E-11	5.2319
28MC-BABA (line 1)	5.3271E-16	4.8126E-17	8.8498
28MC-BABA (line 2)	6.6626E-09	2.4257E-09	3.7192

Table 5-2 Combined factor crack growth equation constants (A & n) at depth

A & n Values for Depth Growth Units: mm/FB & MPa$\sqrt{m}\cdot$Hz$^{-0.033}$			
Spectrum	$A_{0.4}$	$A_{0.1}$	n
7MC-(A/B)	3.9320E-09	1.4492E-09	3.6745
7MC-(12A/12B)	8.4290E-10	2.7502E-10	4.1227
14MC-AB	5.3400E-10	1.6384E-10	4.3489
28MC-ABAB	1.2610E-08	5.0376E-09	3.3777
14MC-BA	3.2490E-10	9.4894E-11	4.5309
28MC-BABA (line 1)	3.7530E-13	6.2617E-14	6.5914
28MC-BABA (line 2)	3.5590E-07	1.8259E-07	2.4568

5.4 Comparison of Spectrum Severity

5.4.1 Ranking of Spectrum Severity

Figure 5-24 and Figure 5-25 shows the fitted lines only from Figure 5-22 and Figure 5-23. The data points were hidden for clarity so easier comparison can be made between the different spectra. The surface and depth direction showed a similar ranking of spectrum severity.

Figure 5-26 shows the approximate ranking of all the spectra tested.

The 7MC-(A/B) and 7MC-(12A/12B) have very similar rates with almost no differences. Therefore they were ranked the same. They were also the least severe spectra tested.

14MC-BA and 28MC-BABA were grouped together on the ranking since they had similar growth rates for most part of Figure 5-24 and Figure 5-25. The 14MC-AB and 28MC-ABAB were also grouped together for the same reason.

Even though 14MC-BA and 28MC-BABA had similar severity for most crack sizes, the 14MC-BA is ranked slightly higher. This is because 14MC-BA is more severe than 28MC-BABA for larger crack sizes.

Within the ranking group of 14MC-AB and 28MC-ABAB, the 14MC-AB is ranked slightly higher. This is because 14MC-AB is more severe than 28MC-ABAB for larger crack sizes.
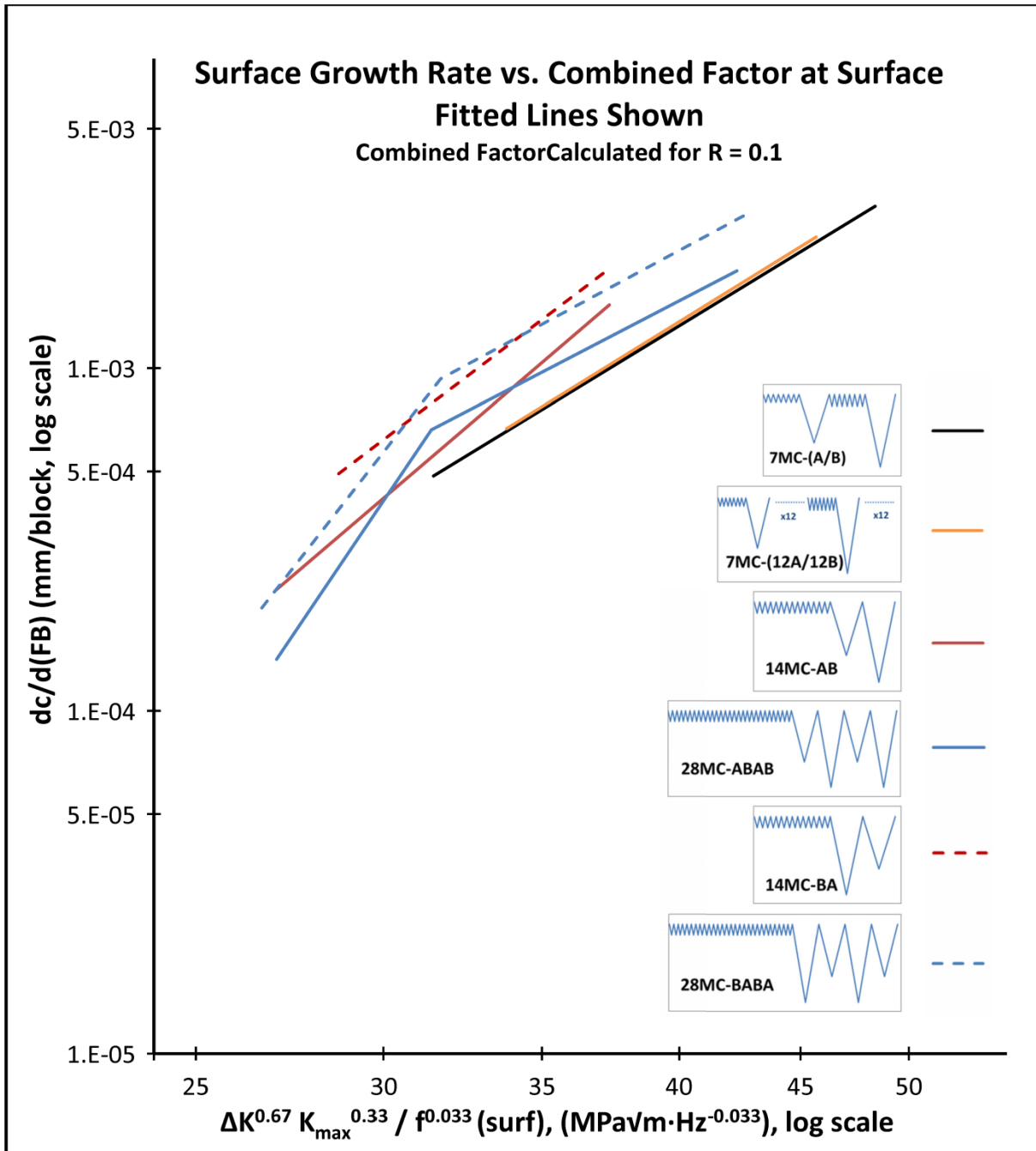
Figure 5-24 The fitted lines for surface growth based on combined factor. Data points are removed to allow easier comparison of trends. Only the results for R = 0.1 UL are shown.
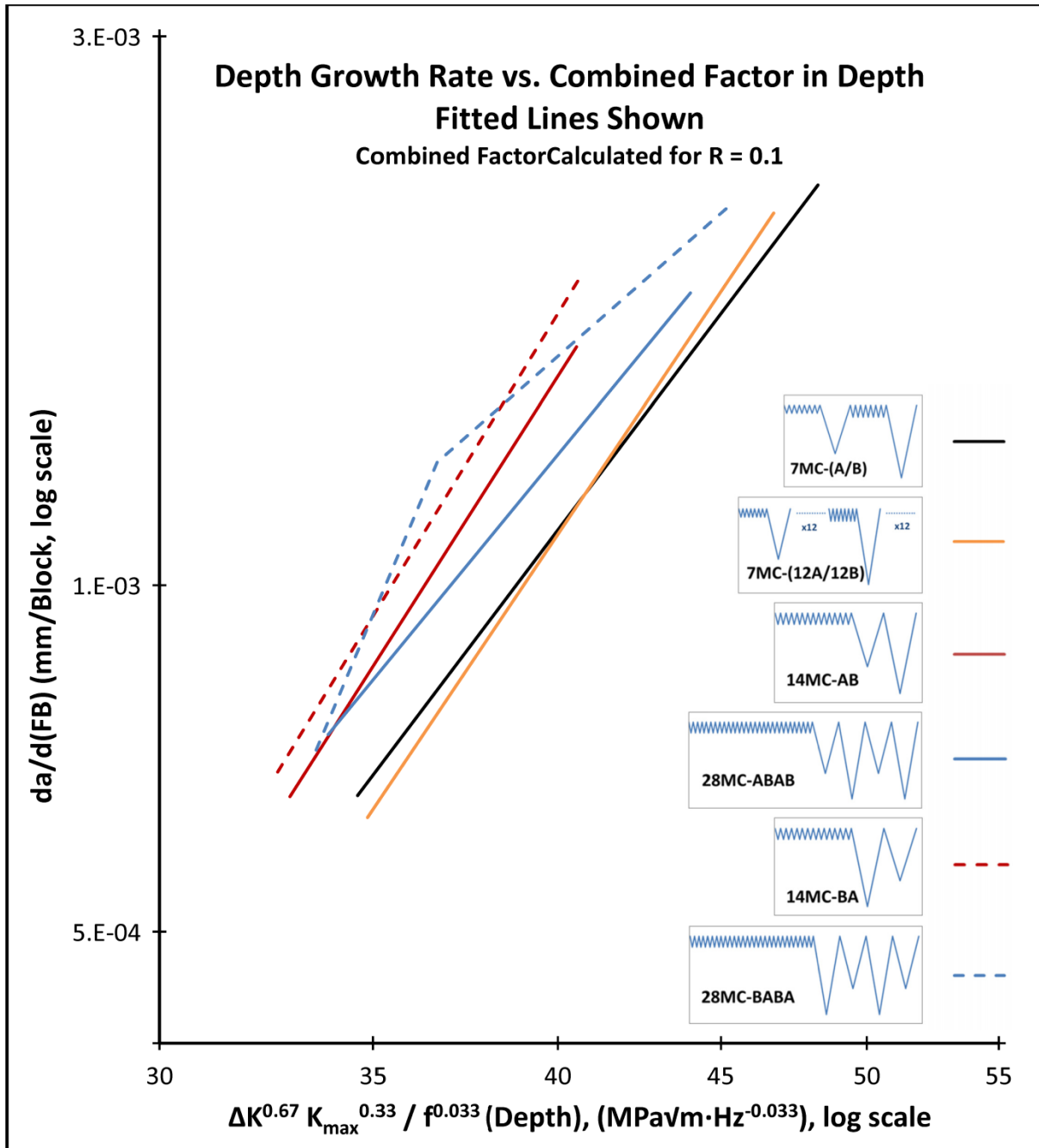
Figure 5-25 The fitted lines for depth growth based on combined factor. Data points are removed to allow easier comparison of trends. Only the results for R = 0.1 UL are shown.

159
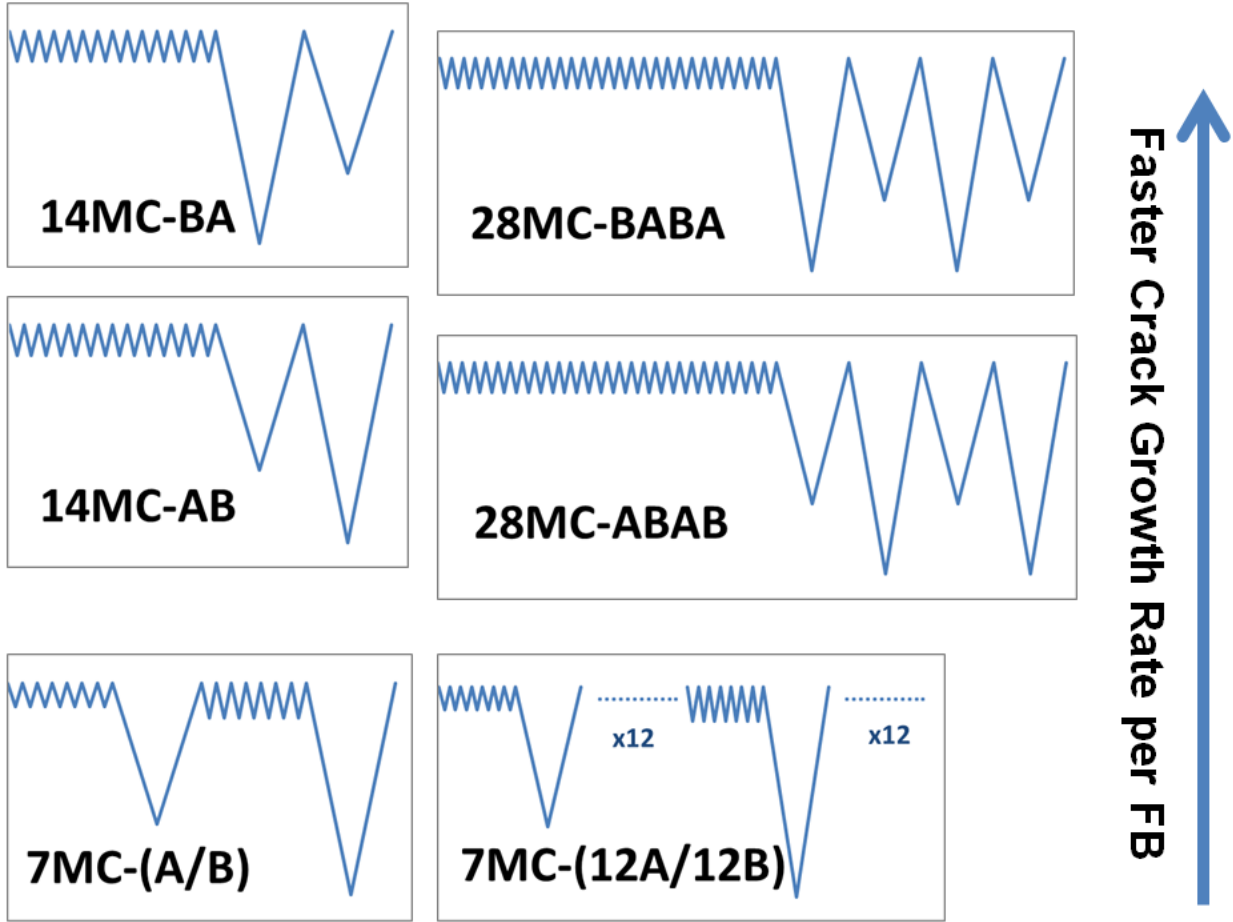
Figure 5-26 Approximate ranking of the spectrum severity

5.4.2   Agglomeration

Agglomeration refers to how dispersed are different types of cycles within a spectrum. Higher agglomeration means a larger number of similar types of cycles are sequenced consecutively within a spectrum. Table 5-3 shows the agglomeration level of the different spectra tested and the corresponding length of MC chain and the number of interaction of events. The 7MC-(A/B) and 7MC-(12A/12B) spectra were the least agglomerated because the UL's are evenly distributed among the MC's. 14MC-AB and 14MC-BA spectra have an increased agglomeration level because 2 UL's are grouped together. 28MC-ABAB and 28MC-BABA spectra have the highest agglomeration level because 4 UL's are grouped together. Increasing the agglomeration level increases length of the MC chain in between UL's (i.e. number of MC in between UL's). Increasing the agglomeration level also decreases the number of interaction events, which is the number of instance where a MC is followed by an UL. Since hydrogen is accumulating in the fracture process zone (FPZ) during the MC chain, the first UL that follows the MC chain is most affected by hydrogen embrittlement (HE). Therefore the number of interaction events in a spectrum could be thought as the number of instances where an UL is exposed to the highest hydrogen level in the FPZ, and is able to do more damage.

Table 5-3 Summary of Agglomeration Effect on MC Chain Length and the Number of Interaction Events

Spectrum	Agglomeration Level	Length of MC chain in between UL's (number of MC)	Number of Interaction Events within 'x' FB (i.e. number of instances where MC is followed by UL)
7MC-(A/B) 7MC-(12A/12B)	I	7	x
14MC-AB 14MC-BA	II	14	x/2
28MC-ABAB 28MC-BABA	III	28	x/4

The two effects of increased agglomeration level are illustrated in Figure 5-27. The first effect is the increases in the length of the MC chains, which allows for a longer period of time for hydrogen to segregate to the FPZ. Hydrogen segregation is dependent on the triaxial stress in the FPZ. During the long chain of MC preceding the UL cycles, hydrogen is accumulating in the FPZ due to hydrogen segregation effects [67,106]. Since the load fluctuations are small, a high

stress level is maintained in the FPZ during the MC chain, which encourages hydrogen segregation. A longer MC chain means the hydrogen level in the FPZ at the end of chain is higher since hydrogen has more time to segregate to the FPZ. Therefore subsequent UL following a longer MC chain is able to cause more damage, which would increase crack growth rate.

The second effect of increased agglomeration level is the decrease in the number of interaction events. At the end of the MC chain, hydrogen level in the FPZ is at its highest level, and the spectrum is at its maximum potential to cause damage. The hydrogen concentration in the FPZ also does not increase indefinitely as the MC chain gets longer. There is a saturation level beyond which a longer MC chain would not build up more hydrogen, and the number of interaction events becomes important. A lower number of interaction events means less UL's are directly exposed to the max hydrogen level in the FPZ at the end of a MC chain. The higher agglomeration level also means more UL's are shielded from HE effects by other UL's before it. Therefore the reduction in interaction events decreases crack growth rate.

The competition between the two effects shown in Figure 5-27 determines the resultant crack growth rate of a spectrum. From the figure, it can be seen that predicting the crack growth rate of a spectrum can be complex due to these competing factors.
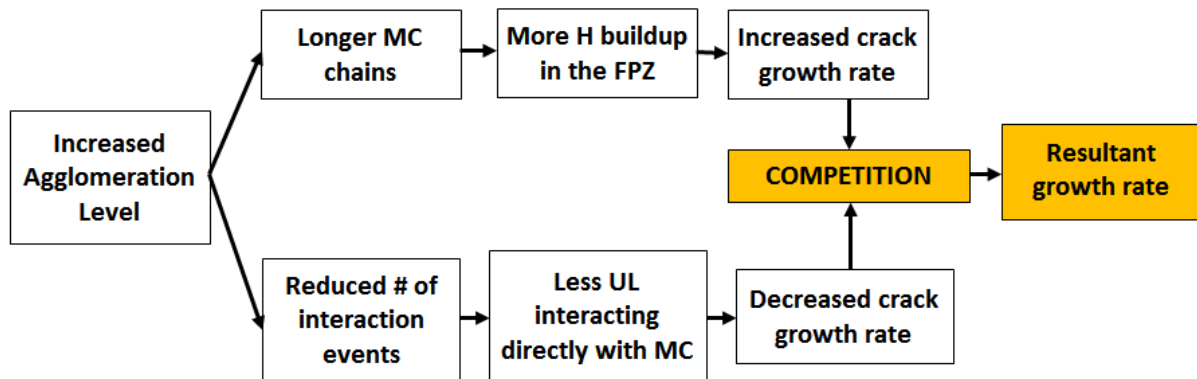
Figure 5-27 The effect of increased agglomeration level on crack growth rate

5.4.3 Spectrum Severity for the Lowest Agglomeration Level

The 7MC-(A/B) and 7MC-(12A/12B) spectra had the lowest agglomeration and also the slowest crack growth rates. Having the lowest agglomeration meant that the number of interaction events was maximized, which favours increased crack growth rate. However, lowering the agglomeration level also decreased the length of the MC chain to only 7 cycles, which provided limited time for hydrogen segregation. For these two spectra, the reduced MC chain length was more dominant, and resulted in slower crack growth rate.

This result seems to suggest that the spectrum with the lowest agglomeration level would have the lowest severity. However, consideration must also be made for the MC:UL ratio. All of the spectra tested in this study only had an overall MC:UL ratio of 7:1. For other spectrum with higher MC:UL ratio, the lowest agglomeration level may not be the least severe spectrum. It is reasonable to predict that for spectra with high MC:UL ratio, the lowest agglomeration level may even be the most dangerous spectrum. This is because hydrogen level in the FPZ does not increase indefinitely and there is a saturation level. If a spectrum has a high enough MC:UL ratio, it could reach hydrogen saturation in the FPZ at the end of the MC chain even at the lowest agglomeration level. In such a case, increasing the length of the MC chain by increasing the agglomeration level would not provide additional enhancement to crack growth. In fact, further increases in agglomeration level would reduce spectrum severity since the number of interaction events will be reduced.

Another observation of the 7MC-(A/B) and 7MC-(12A/12B) growth rate results was that they were very similar. Different arrangements of the dispersed UL for the lowest agglomeration level did not have significant impact on crack growth rate. This is because when the UL's are distributed throughout the MC's, the UL's are isolated from each other and there are limited load interaction effects between the UL's. So each 7 MC + 1 UL block is effectively an independent block not affected by the surrounding blocks.

5.4.4   Effect of UL Sequence for Agglomeration Level II and Above

The next comparison is between the spectra with the same agglomeration level, for agglomeration level II and above (i.e. 14MC-AB vs. 14MC-BA and 28MC-ABAB vs. 28MC-BABA). In these higher agglomeration levels, the UL's cycles are agglomerated into groups of two or more. From Figure 5-24 and Figure 5-25, it is shown that 14MC-BA is more severe than 14MC-AB, and 28MC-BABA is more severe than 28MC-ABAB. The common theme between both of the more severe spectra (14MC-BA and 28MC-BABA) is that they have the 'BA' style arrangement of UL cycles, where the first UL cycle after the MC chain is the more aggressive R=0.1 UL cycle. From these comparisons, it could be seen that the sequence of UL's after MC is important in determining the spectrum severity for underload spectrums with higher agglomeration.

There are two main mechanisms that determine the relative severity of underload spectra:

1. the accumulation of hydrogen in the fracture process zone (FPZ) during the MC chain due to hydrogen segregation effects [67,106]. Illustrated in Figure 5-28
2. The enhanced growth rate of MC's in underload spectra due to load interaction effects. Illustrated in Figure 5-29

Hydrogen segregation is dependent on the triaxial stress in the FPZ. During the long chain of MC preceding the UL cycles, hydrogen is accumulating in the FPZ due to hydrogen segregation effects [67,106]. Since the load fluctuations are small, a high stress level is maintained in the FPZ during the MC chain, which encourages hydrogen segregation. A long chain of MC's also provides more time for hydrogen diffusion into the FPZ. At the end of the MC chain, the hydrogen level in the FPZ is at its highest level, and the spectrum is at its maximum potential to cause damage. Any UL following the MC chain would have enhanced crack growth rates due to HE, especially the first UL after the MC chain, and the severity of a spectrum was observed to be dependent on the R ratio of the first UL cycle to follow the MC chain.

Subsequent UL that follows the first UL are less enhanced by HE since they are shielded from the maximum hydrogen level in the FPZ. Each UL cycle would deplete a certain amount of hydrogen in the FPZ. Since hydrogen segregation takes time, the up-ramp loading portions of the

UL cycles would not provide sufficient time to restore the hydrogen level in the FPZ to its maximum. So special attention must be paid to the first UL because it is at its maximum potential to cause damage.

Figure 5-28 illustrates the influence of the UL sequencing and hydrogen segregation during MC chain on crack growth rates. As shown in the figure, the MC chain hovers just below the maximum stress, so the mean stress during MC chain is high, which allows time for hydrogen segregation. The hydrogen concentration [H] in the FPZ is at its highest at the end of the MC chain. The crack growth during the first UL following the MC chain will be most enhanced by HE.

From a mechanical perspective, more aggressive UL cycle (i.e. lower R ratio) would cause more damage. When combined with HE effects, such as right after a chain of MC's, a more aggressive UL cycle would be enhanced even further. So it makes sense that spectra with 'BA' style of UL sequencing (e.g. 14MC-BA and 28MC-BABA) would have higher crack growth rates than spectra with 'AB' style of UL sequencing (e.g. 14MC-AB and 28MC-ABAB). Recall that the 'B' type UL cycle has R = 0.1, and the 'A' type UL cycle has R = 0.4. The R = 0.1 'B' UL cycle is the most dangerous cycle in the spectra tested since it has the lowest R ratio. In the 'BA' style of UL sequencing, the first UL to follow the MC chain is the more aggressive R = 0.1 UL, therefore it has higher crack growth rates.

The other reason 14MC-BA and 28MC-BABA are more severe than 14MC-AB and 28MC-ABAB is because of the underload effect. The underload effect describes the acceleration of crack growth for minor cycles that follows an underload cycle. This effect has been observed in different metallic materials [99,147], and also pipeline steel [9,10,93,101].

First a special note needs to be made about minor cycles. "Minor Cycle" is a subjective term. For the pipeline industry, minor cycles typically mean small pressure fluctuations just below the MAOP with R ratio of around 0.9. But for other studies, minor cycles generally refer to cycles that have smaller amplitude (or higher R ratio) than the most aggressive UL cycle. For many authors, the R=0.4 UL used in this study would be considered a MC relative to the R=0.1 UL. A more accurate description of the underload effect should be: the enhanced crack growth rate of mild underload cycles following a major underload cycle.

165

The mechanisms behind the underload effect are not well understood. Some authors [99,148] believed that strain hardening of the material in front of the crack tip was the reason for the enhanced crack growth of minor cycles following an underload. However, this is not a valid explanation for underload spectra because the maximum stress is kept constant. Recently Yu et al. have suggested that strain softening is a more plausible explanation of the underload effect [10], but more study is needed to confirm this.

The underload effect in the tested spectra is illustrated in Figure 5-29. The figure compares 28MC-ABAB and 28MC-BABA as an example. The cycles in black are major UL cycle that accelerates the growth rates of MC's following it. The cycles colored orange are smaller amplitude cycles that act as MC's to the preceding UL. From the figure, it is clear that the 28MC-BABA spectrum has a larger number of cycles that act as MC's to a preceding UL. The R=0.4 UL should be viewed as a MC relative to the R=0.1 UL. If a R=0.4 UL is placed after a R=0.1 UL, the R=0.4 UL would have accelerated growth due to the underload effect. In the 28MC-BABA spectrum, both of the R=0.4 UL are enhanced due to the underload effect, therefore it would have a higher spectrum severity.

In summary, spectra with 'BA' style UL sequence (such as 14MC-BA and 28MC-BABA) are more severe than spectra with 'AB' style UL sequence (such as 14MC-AB and 28MC-ABAB), because:

- The first UL following the MC chain for 'BA' style spectra is the more aggressive R=0.1 UL, and this UL is able to achieve most damage since hydrogen level in the FPZ is at its maximum
- The arrangement of cycles in 'BA' style spectra allows for more R=0.4 UL cycles to be enhanced via the underload effect because the R=0.4 UL act as a minor cycle to the R=0.1 UL.

Figure 5-28 Comparison of 14MC-BA and 14MC-AB spectra showing the differences in damage caused by the first UL after the MC chain

Figure 5-29 Illustration of underload effects in 28MC-ABAB and 28MC-BABA spectra, where cycles following an underload are enhanced by load interaction effects

5.4.5   Implications for Pipeline Integrity

The ranking shown in Figure 5-26 provide some interesting insight. It shows that the UL sequencing has a bigger influence on crack growth rate than the agglomeration level. Based on the results from Yu et al [10], increasing the number of minor cycles between underloads should increase the crack growth during the UL. Increasing the agglomeration level also increases the number of minor cycles in between UL's as shown in Table 5-3. The expectation was that the highest agglomeration level would produce highest crack growth rates. What the rankings showed instead is that level II and level III agglomeration with the same UL sequence could have similar growth rates. For some crack sizes the level II agglomeration was ranked higher and for others the level III was ranked higher. There are multiple intersections that occurred between the two trends. The result is a complex relationship between the two agglomeration levels. However, if the trends from level II and level III agglomerations are extrapolated (e.g. compare 14MC-AB to 28MC-ABAB or 14MC-BA to 28MC-BABA), the level II agglomeration would produce faster growth rates than the level III agglomeration. The extrapolation also shows that 14MC-AB spectrum would eventually be able to intersect 28MC-BABA's trend and produce faster growth rate. Past this intersection point, both 14MC-AB and 14MC-BA will have faster growth rates than 28MC-ABAB and 28MC-BABA.

The behaviour of these trends show that there are multiple factors affecting crack growth rates. Figure 5-27 is a good illustration of the competing effects that are present when the agglomeration is increased. Figure 5-28 and Figure 5-29 shows how different sequencing of UL's for spectra with agglomeration level II and above affect the crack growth rate. All these effects must be considered when determining spectrum severity. For some situations, an increased agglomeration level is more beneficial due to the decreased number of interaction events. For other situations, a decreased agglomeration level is more beneficial due to shorter MC chains in between underloads. Currently there is no prediction model that can account for these competing effects. Adding in the effect of sequencing in agglomerated UL bocks, the prediction model could become even more complex. It is recommended that more corrosion fatigue experiments should be carried out to study these effects. In general, the most severe spectra are usually not the most agglomerated spectra. Instead, they are the spectra that balance

the two opposing forces (MC chain length and number of interaction events) to optimize the crack growth enhancement

5.5 Comparison of Acceleration Factors of the Spectra

A shortcoming of the comparison shown in section 5.3 and 5.4 is that it can only be used for internal comparison since different UL cycles would produce different set of trends. The traditional crack growth curves could not capture the effect of all the cycles in a VAL spectrum. To compare VAL spectra, a commonly used method is through the comparison of acceleration factor (γ), which is calculated as:

$$\gamma = \frac{\text{measured growth rate per block}}{\substack{\text{predicted growth rate per block by a} \\ \text{linear summation of the constant} \\ \text{amplitude crack growth response}}} \tag{5.3}$$

In order to account for both types UL cycles in the acceleration factor, eqn (5.3) was modified to eqn (5.4):

$$\gamma = \frac{\text{actual growth rate in one FB} \times 2}{\substack{\text{predicted growth rate for} \\ \text{14 MC} + 1 \text{ UL(R=0.4)} + 1\text{UL(R=0.1)}}} \tag{5.4}$$

Since half of the UL's were R =0.4 and the other half R=0.1, extending the γ calculation over two fundamental blocks captures the averaged effect of both types of UL. Eqn (5.4) is used to calculate γ for all data points and spectra. Confusion may arise because it may appear the above equation is only meant to be used for 14MC-AB or 14MC-BA spectra, but it is applied to all spectra. The cycles within these two fundamental blocks consist of 14 MC, one UL with R=0.4, and one UL with R = 0.1. These cycles are the most reduced composition of all the spectra (14MC:1UL(R=0.4):1UL(R=0.1)). The two fundamental block unit used in this section should be used a virtual reference unit that captures the effects of all types of cycles that exist in the spectra.

The predicted growth rate in γ is calculated using two models. The first model used was Chen & Sutherby's combined factor model [81], and the acceleration factor calculated using this model is shown in Figure 5-30. The second model was Been et al.'s model from [80], the acceleration factor results of which is shown in Figure 5-31.

To use the combined model for prediction, the dashed curve shown in Figure 2-16 (b) was digitized. The growth rate corresponding to a combined factor value was obtained graphically from the digitized curve.

Been et al.'s corrosion fatigue model in NNpH environment was based on non-linear curve fitting of the experimental data obtained. The tests were performed on CT specimens. The equation of the model is given below:

$$\frac{da}{dN} = 3.27 \times 10^{-8} \cdot \Delta K^{2.88} \cdot K_{max}^{0.42} \tag{5.5}$$

In both prediction models, the crack growths due to the minor cycles were negligible when compared the crack growth during the underload cycles.

As shown in Figure 5-30 and Figure 5-31, the acceleration factor was calculated for both the surface and depth direction. The ranking of the spectrum severity from these figures are also similar to the rankings seen in Figure 5-24 and Figure 5-25. Figure 5-30 tends to show better agreement with the previous rankings because the predicted model is also based on the combined factor model, which considered the environmental effects. Figure 5-31 based on Been et al.'s model only considered the mechanical driving forces, therefore the agreement with the previous ranking was worse.

γ Calculated with the Combined Factor Model

In Figure 5-30, the change in acceleration factor with the crack growth shows some interesting behaviour. For the surface plot, γ initially increased, and then gradually declined as the crack grew larger in size. As shown in Figure 5-20, the initial data points for surface growth was near the threshold regime, so more error is expected in the acceleration factor. The initial increase in γ for the surface plot is due to these data points being near the threshold regime. The combined factor model likely overestimates the crack growth in the near-threshold regime. Once the surface growth enters the linear region on a growth curve, the acceleration factor quickly reaches a peak, before showing a steady decline. The same decline is observed in the depth plot of Figure

171

5-30. Since the SIF in the depth direction is already well past the threshold regime, no initial increase in γ was observed.

The decline in γ for both the surface and depth direction after the crack has entered the linear growth regime is due to several causes. The first cause is the difference in hydrogen concentration profile within the surface crack specimen used in this study and the CT specimen used by Chen & Sutherby. In Chen & Sutherby's experiments, uncoated bare CT specimens were tested in C2 solution. Hydrogen was generated on all sides of the specimen since the entire CT specimen was submerged in the C2 solution. This results in a relatively constant bulk hydrogen concentration throughout the CT specimen. This hydrogen profile differs significantly from that in actual pipe walls. A pipe wall only generates hydrogen on the external surface, and the internal surface is free from hydrogen. Therefore the hydrogen concentration is decreasing with thickness, with the highest level at the external surface. The surface crack specimen used in this study simulates the real pipeline conditions in the field, with coating on the back and sides of the sample to prevent hydrogen generation on those surfaces (see Figure 4-4). The hydrogen concentration in the surface crack specimen is therefore decreasing with thickness. A small decrease in hydrogen concentration is also expected near the edge of the sample since the sides were also coated. The crack growth relation observed by Chen & Sutherby is actually more aggressive than that in an actual pipe. The hydrogen embrittlement effect in the CT specimens remains relatively constant as the crack grows larger. But for the surface crack specimens, the influence of hydrogen is decreasing as the crack grows due to the decreasing hydrogen profile. The result is the acceleration factor will decline as the crack grows larger.

The strip of coating covering the crack could also contribute to the declining γ trend. In Chen & Sutherby's experiments, the specimen was bare, so the crack growth was under the constant influence of both HEAC and IHAC. In the current study, HEAC is effectively blocked with the tape, so only IHAC was present. On top of that, the IHAC effect is decreasing as the crack grows deeper because the bulk hydrogen concentration is also decreasing.

γ Calculated with Been et al.'s Model

The γ trend calculated with Been et al.'s model shown in Figure 5-31 offers an interesting comparison to the γ trend calculated with the combined factor. The biggest difference between

the two models is the behaviour of γ in the active growth region. In Been et al.'s γ trend, the γ value stabilized during the active growth phase and remained relatively constant. This could be explained by noticing that Been et al.'s model only considered the mechanical driving forces. No environmental factor was considered. The mechanical driving forces between the surface crack specimen and CT specimens would be comparable. Therefore γ is expected to stabilize.

<u>Why is $\gamma < 1$?</u>

A noticeable feature in both Figure 5-30 and Figure 5-31 is that for most Kmax values, the γ value is less than 1. The same behaviour has also been observed by Yu et al. [10]. Details about Yu et al.'s study were discussed in section 2.4.6.1. In this study, Yu et al. found that for VAL underload-type spectra, when n is less than ~32 (n is the number of MC between adjacent UL's), the acceleration factor was less than 1. The acceleration factor that Yu et al. calculated was based on constant amplitude test that was conducted in the same study using the same environmental conditions, so the acceleration factor results are reliable. For the current study, the number of minor cycles between UL's ranged from 7 to 28, and the acceleration factor results agree with what Yu et al. has found.

Yu et al. also found that for $R_{UL} < 0.25$, the crack growth rate was less than 1 for underload-type spectrum [94] (see section 2.4.6.3). The lowest R ratio used during the test was 0.1, which is below 0.25. This means the growth rate of the R = 0.1 UL was possibly retarded with a similar mechanism as that seen in [94].

The reason why $\gamma < 1$ during the corrosion fatigue tests is not well understood, but the findings in the current study do agree with Yu et al.'s findings. It is possible that HELP take place during the MC's, and that has a slight retardation effect. More research is needed to find out why this behaviour occurs.
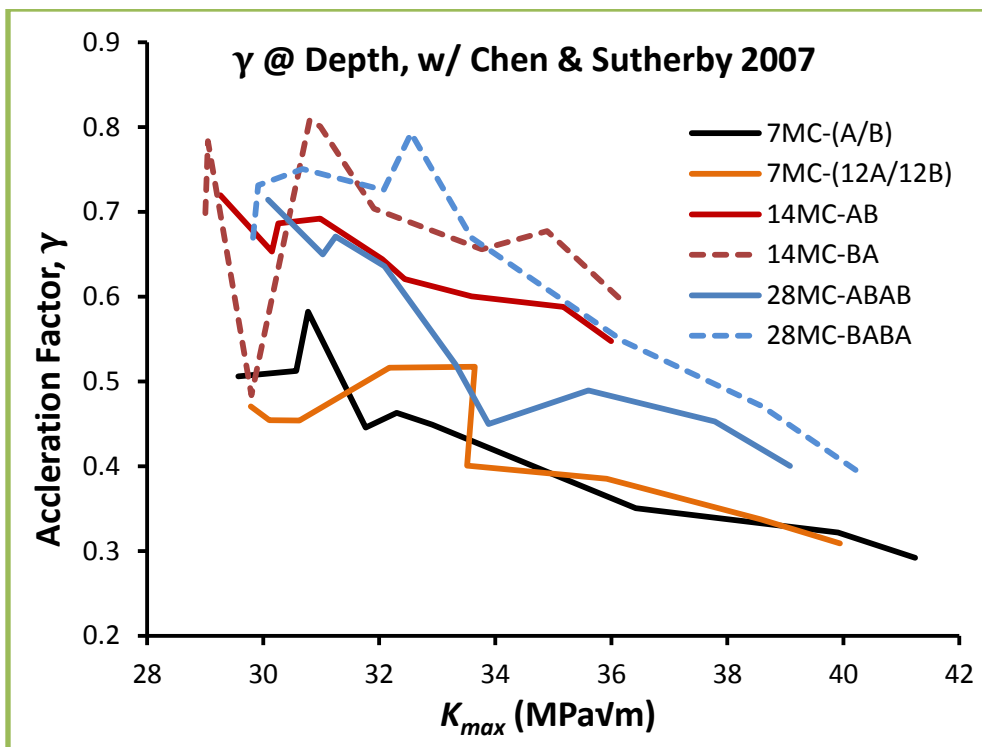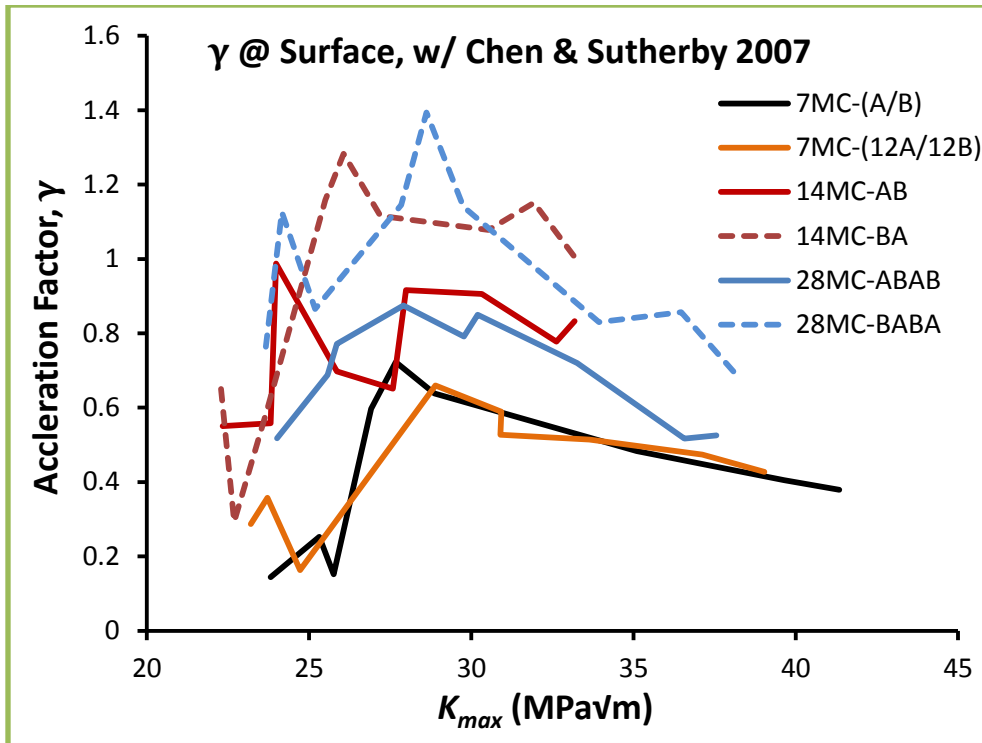
Figure 5-30 Acceleration factor for different test spectra. Predicted growth rates calculated with Chen & Sutherby's combined factor model [81]
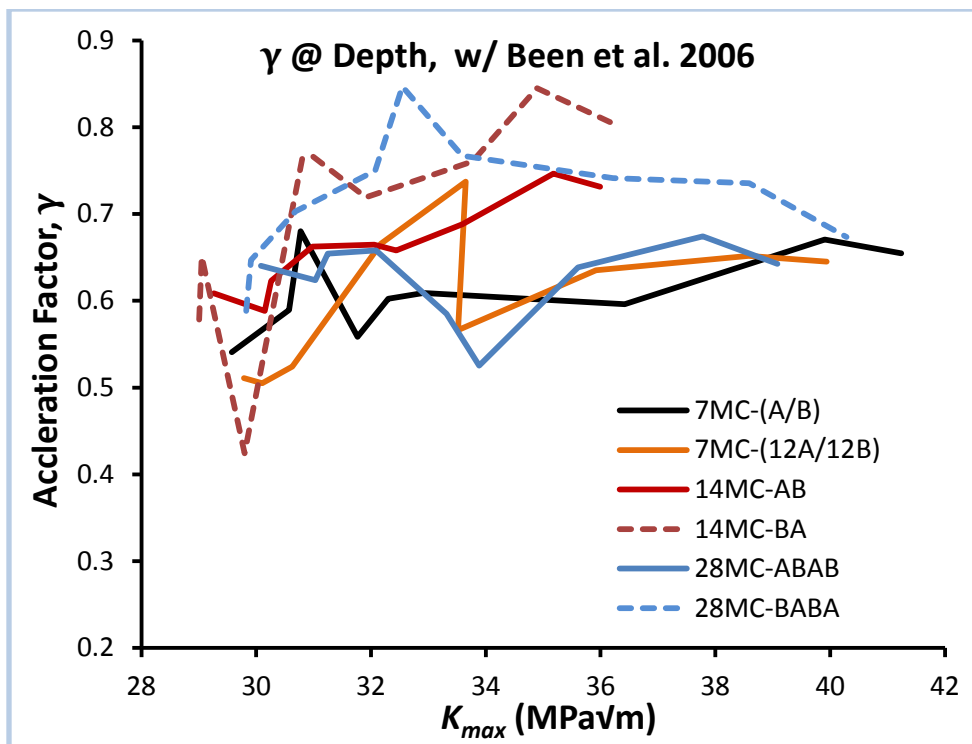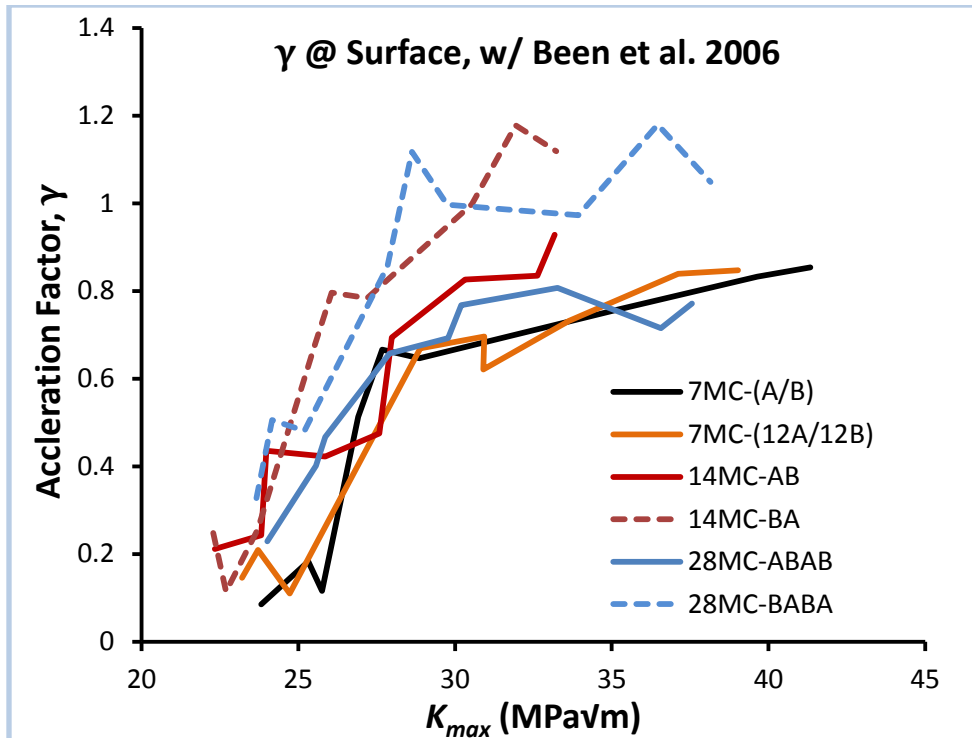
Figure 5-31 Acceleration factor for different test spectra. Predicted growth rates calculated with Been et al.'s model [80]

5.6 Comparison of Crack Growth Rates on the Same Sample

The crack growth rates for each individual crack on the sample were tracked as shown in Figure 5-32. Crack area could be easily measured on the fracture surface images using AutoCAD by digitizing the beachmarks. The crack area growth rate was chosen since it captures both surface and depth growth. The area is a better measure of a crack's size. The results clearly show that cracks with larger initial sizes grow faster. This result is not surprising, but what is surprising is how the tests were able to distinguish such small differences in initial crack size. It shows the experiment is done with high precision. It also shows the growth rate is highly sensitive to small differences in dimensions. For pipelines, it means the largest crack is always going to be the biggest threat.
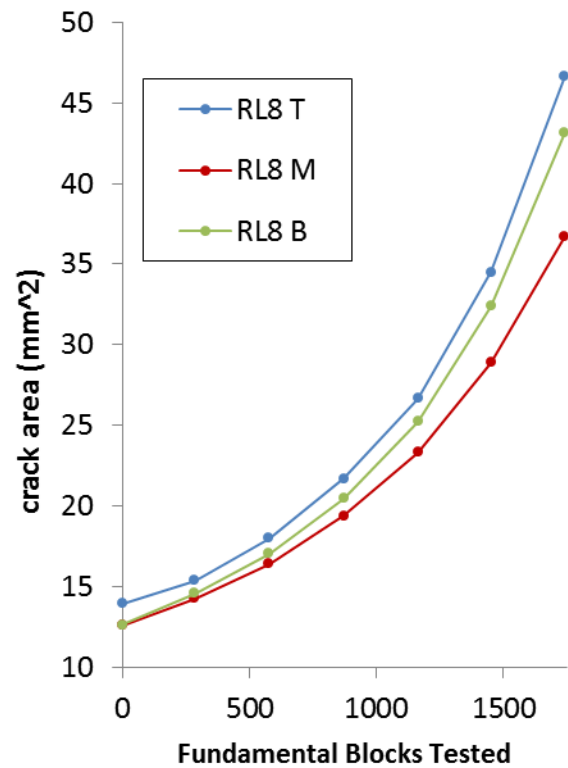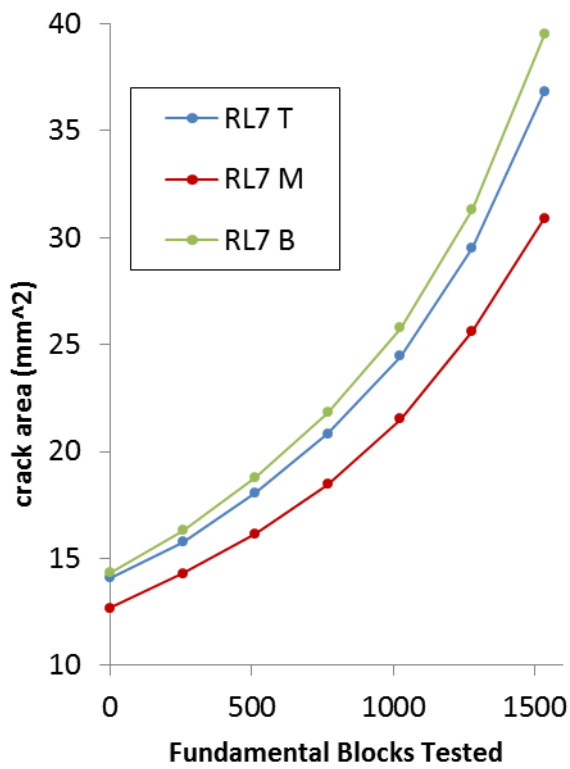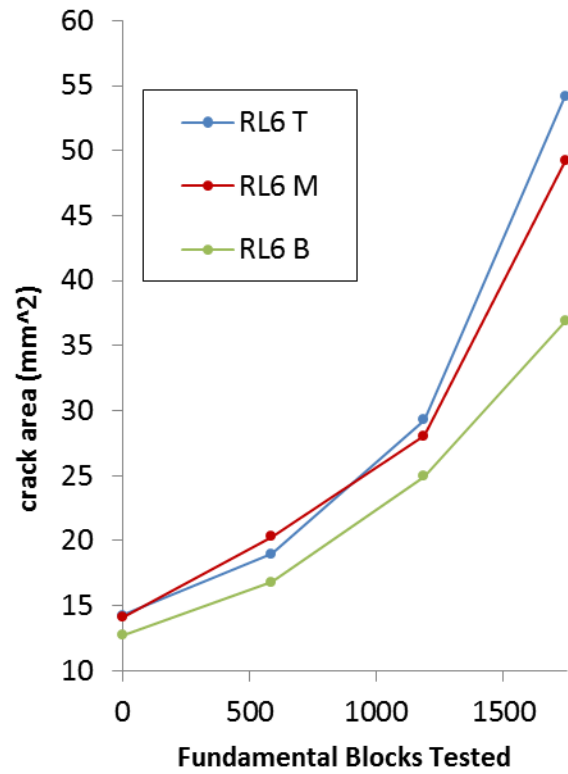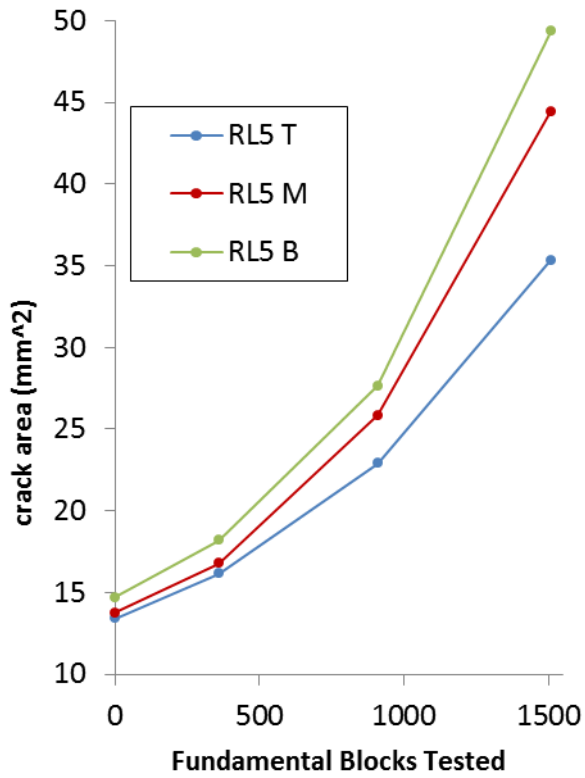
Figure 5-32 Crack growth progression for each individual crack on samples RL5 to RL8. On samples with multiple cracks, the larger cracks will grow faster, even if the differences at the start are small.

5.7   Deviation from Elliptical Shape

As discussed in section 3.3, it is typically assumed that the crack shape maintains a semi-elliptical shape as the crack grows. However it is not the case as shown in Figure 5-33 and Figure 5-34. The 1:1 line in Figure 5-33 represents if the measured crack area completely agrees with the theoretical ellipse area. If the data points all line up on the 1:1 line, it means the crack maintained a semi-elliptical shape. If the points lie above the line, then the actual crack area is "fuller" and has larger area than an ellipse. If the point lies below the line, the crack shape is not filling up the ellipse shape. The theoretical crack area is calculated as:

$$A = \frac{\pi \, a \, c}{2}$$

(5.6)

At the beginning, the crack area all fall below the 1:1 line since the crack shape is not a true ellipse. The sample has undergone milling, so the precrack area left over is a cropped portion of a circle, which has less area than a true ellipse. As the crack grows, however, the shape becomes more elliptical, and eventually have an area larger than an ellipse. This is caused by surface growth lagging behind due to surface closure effects, which was discussed in section 5.2.2. Since the surface growth lagged behind, the *c* measurement is reduced and as a result the theoretical crack areas are underestimated.
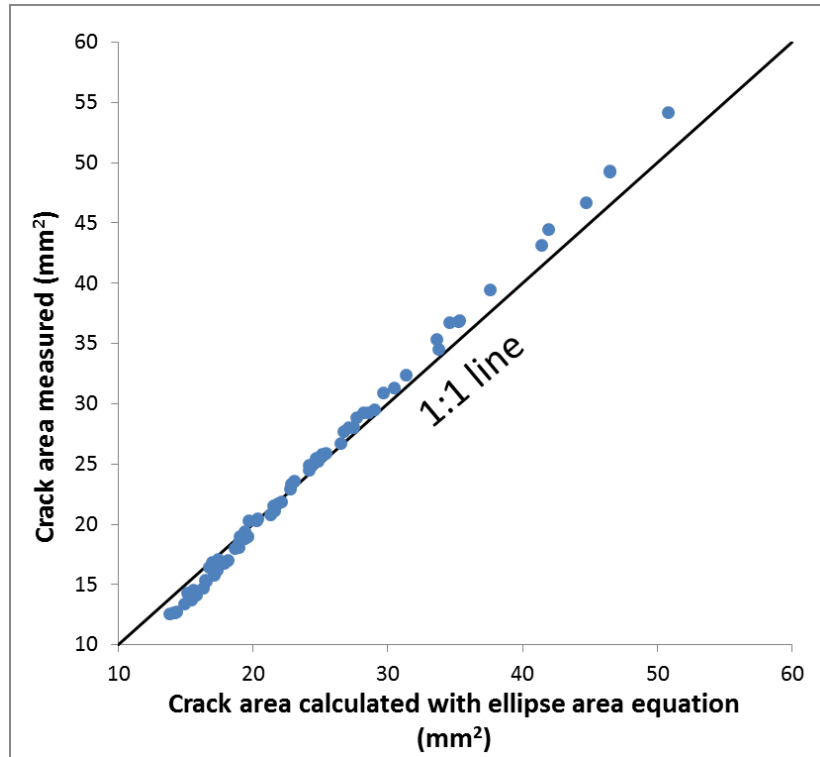
Figure 5-33 Comparison of measured crack area to theoretical area of an ellipse.

demonstrating the crack area deviation of the actual crack compared to an ideal ellipse, especially at later stages of crack growth, the area is bigger than an ellipse → caused by crack front lagging behind on the surface due to closure effects. Also caused by shape deviation (superellipse n>2). The initial area is less than the ellipse area because of geometry and milling.
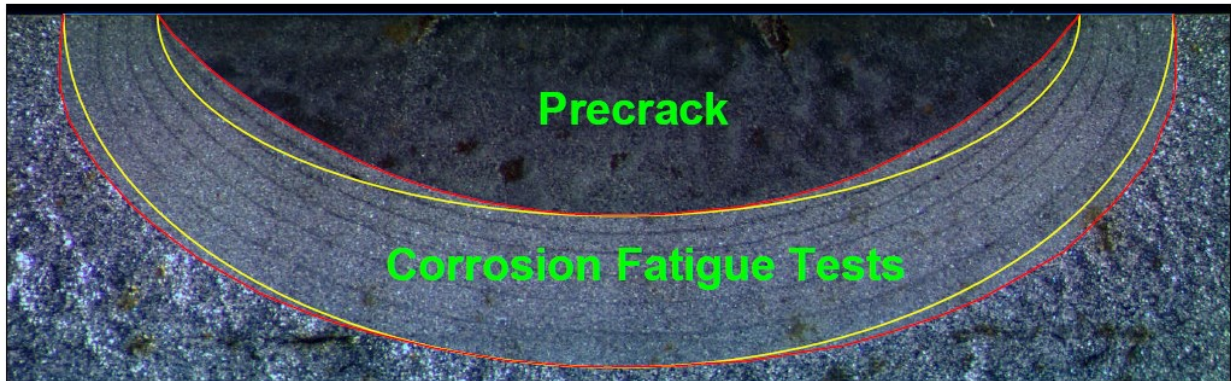
Figure 5-34 Deviation from true elliptical shape observed on a fracture surface. The red lines trace the actual crack front. The yellow lines represent true ellipses.

5.8　　　Difference in Field SCC Shape and Experiment Crack Shape

As shown in Figure 5-15, the crack grew little for the initial tests. Since the pretest crack shape was long and shallow, the crack has much higher initial SIF in the depth direction, so depth the preferred growth direction as shown in Figure 5-13. Analysis of the tabulated data in Appendix A shows that the *a/c* ratio of the crack is increasing as the crack grows, which agrees with the shape prediction behaviour of surface cracks discussed in section 3.3. The shape evolution during the corrosion fatigue tests is shown in Figure 5-35. The cracks were growing toward a more semi-elliptical shape in order to distribute the stress intensity evenly along its crack front. The shape evolution prediction is only valid for individual cracks that haven't coalesced with other cracks. In the field, it's rare to find SCC with a shape close to a semi-circle due to coalescence. As shown in Figure 5-36, most SCC found in the field have a long aspect ratio (i.e. longer length than depth) due to SCC coalescence (shown in Figure 5-37). Closer examination of Figure 5-37 also reveals that the individual cracks that joined to form the coalesced crack originally grew in the manner predicted in section 3.3. It could be seen from the beachmarks that the individual cracks were growing toward a more semi-circular shape. This suggests that if a lone individual SCC is initiated in the field, it would grow in the manner shown in section 3.3. However if coalescence occurs, as it often does in the field, then the SCC would have a much longer aspect ratio.
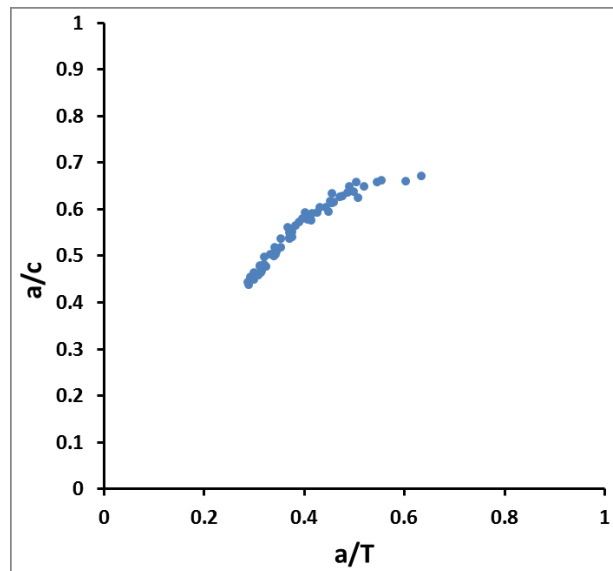
Figure 5-35 a/c vs. a/T data from all the corrosion fatigue tests in this study
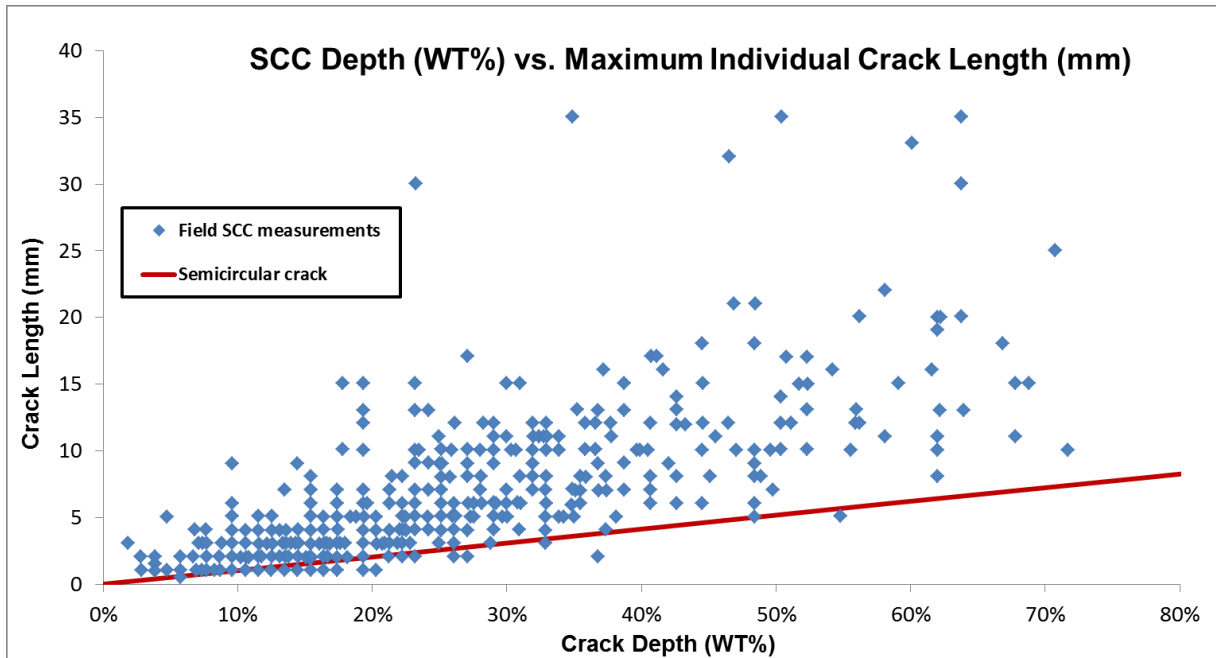
Figure 5-36 Individual crack geometry measurements for SCC's found Suncor Energy's 16" OSPL Pipeline through their SCC inspection program. Note most cracks found have a long aspect ratio above the red semicircular shape line. Interlinked crack length not shown. Reproduced from [54], with permission from ASME.
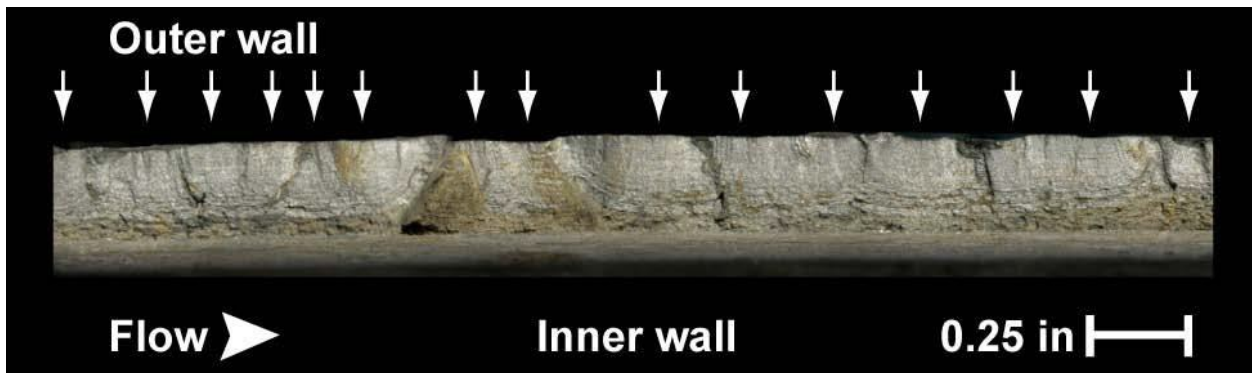
Figure 5-37 Fracture surface of a coalesced SCC crack that caused an in-service rupture caused by SCC/corrosion fatigue that occurred on Enbridge Line 6B in Marshall, Michigan in 2010. The surface has been cleaned to remove corrosion scales. Curving beach marks on individual cracks can be seen. White arrows indicate origins of individual SCC cracks that later coalesced and joined. Ratchet marks are also visible where two cracks have joined. Reproduced from [29], courtesy of the National Transportation Safety Board.

5.9   Comparison with Other Studies
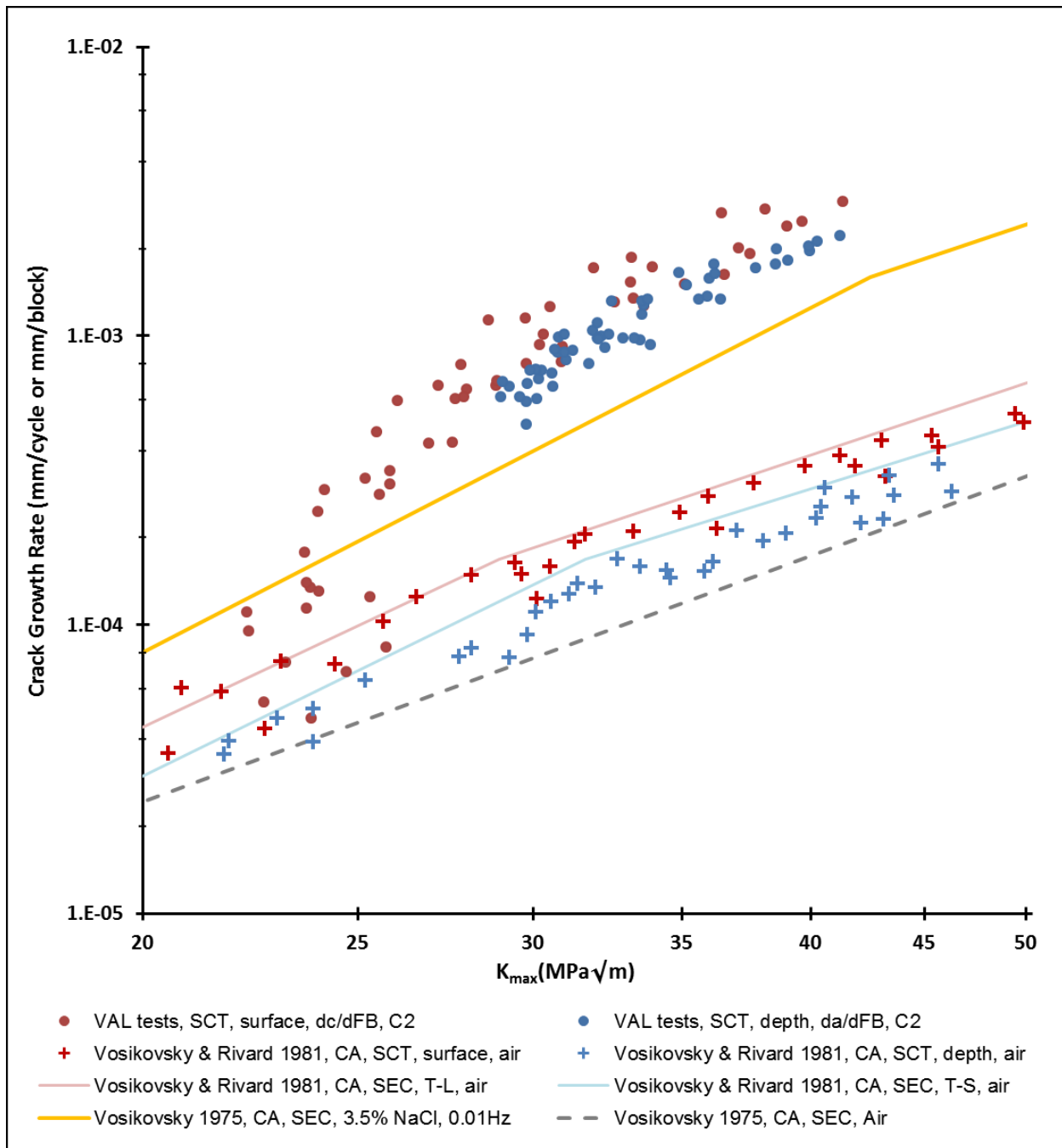
Figure 5-38 Comparison of the experimental data to other experiments done with X65 steel. The red and blue dots are results from this study. Data from other studies came from [133,149].[5]

182

Figure 5-38 compares the experimental data from this study to other experimental results on X65 steel. The red and blue dots represent the surface and depth data from the current study. No distinction is made between the different spectra tested. The goal of this comparison is to compare the growth in the surface and depth direction. Select results from other studies were included in the figure:

Vosikovsky & Rivard's Surface Crack Tests (SCT) on X65 Steel [149]

- Samples machined from X65 pipeline steel skelp
- Semi-elliptical surface cracks were initiated from an EDM notch
- The starting notch shape had an elongated aspect ratio similar to the current study ($a < c$)
- $f = 10$ Hz, R = 0.05, constant amplitude waveform, in air
- Observed faster growth in the surface direction than the depth direction

Vosikovsky & Rivard's Single Edge Crack Specimen (SEC) Tests on X65 Steel [149]

- Samples machined from X65 pipeline steel skelp
- SEC specimens with notches in two different orientation were made:
  - T-L direction (longitudinal direction along pipe)
  - T-S direction (thickness direction of pipe wall)
- $f = 10$ Hz, R = 0.05, constant amplitude waveform, in air
- Faster crack growth was observed in the T-L direction, which was caused by the anisotropy of the steel skelp
- Observed numerous elongated inclusions that interfered with the growth in the depth direction. Vosikovsky & Rivard postulated that the depth growth was slowed down by the presence of elongated inclusions.

Vosikovsky's Single Edge Crack Specimen (SEC) Tests on X65 Steel in Air [133]

- Samples machined from X65 pipeline steel skelp
- Cracks aligned in T-L (longitudinal direction)
- $f = 0.1$ to 15 Hz, R = 0.2, constant amplitude waveform, in air

183

Vosikovsky's Single Edge Crack Specimen (SEC) Tests on X65 Steel in 3.5% NaCl [133]

- Samples machined from X65 pipeline steel skelp

- Cracks aligned in T-L (longitudinal direction)

- Tested in salt water solution with 3.5% NaCl (similar to NNpH environment)
  - OCP (-680 mV$_{SCE}$)
  - pH 6.5 to 7.5

- $f = 0.01$ Hz, R = 0.2, constant amplitude waveform

In the above figure, the comparison of the surface crack growth data from the current study shows that the surface growth rate is actually higher than the depth growth rate for a certain SIF. This is supported by Vosikovsky & Rivard's surface crack tests and Vosikovsky's SEC tests. The results from the SEC tests done in both T-L and T-S direction demonstrated that the difference in growth rates was due to the anisotropy of the material, and the crack propagation is easier in the longitudinal direction of the pipe wall. Vosikovsky and Rivard believed that the depth growth was slowed down by the presence of elongated inclusions. This is a plausible explanation since all pipeline steel is anisotropic due to the manufacturing processes.

It should also be pointed out that the surface cracks in the current study are aligned in the circumferential direction of the pipe. So to be more accurate, the experimental results of the current study show that the growth in the circumferential direction is faster than the depth direction. From all the surface crack experimental data in Figure 5-38, it can be concluded that both the longitudinal and circumferential direction have faster crack growth rates than the depth direction.

In an isotropic material, the expected behaviour of a surface crack is that the depth would grow faster than the surface for the same SIF value. This is due the depth having a plane-strain stress state, while the surface is at plane stress. However, in all of the surface crack results in Figure 5-38, the surface growth rate was higher than the depth growth rate. This means the anisotropy of the pipeline steel has a greater effect on the crack growth behaviour than the stress state. Furthermore, the results from the current study also imply that anisotropy has an effect on corrosion fatigue. This has major implications for SCC research because the anisotropy of the pipeline steel is not considered in current SCC models.

Even with the faster surface growth rate, the shape evolution of a Stage II SCC is still expected to grow toward a semi-circular shape, although the shape is going to be somewhat flatter than those predicted using Newman and Raju's method [119,121]. In terms of absolute growth rates, the difference between the surface and depth direction is relatively small. Therefore it is not expected to alter the shape evolution behaviour drastically. As shown in Figure 5-35, the shape evolution for the current study is still growing toward a more semi-circular shape.

Experimental results from Vosikovsky's SEC tests in 3.5% NaCl solution offers an interesting comparison to the corrosion fatigue results from the current study. The 3.5% NaCl environment is similar to the C2 solution in terms of pH and potential. Vosikovsky also observed quasi-cleavage fracture morphology which indicated hydrogen embrittlement. The main reason slower crack growth rate was observed for Vosikovsky's test is most likely due to the constant amplitude waveform and the faster frequency used. Vosikovsky used a frequency an order of magnitude higher than the frequency in the current study, and according to [9], that would result in a slower crack growth rate because 0.01 Hz is above the critical frequency of 10^{-3} Hz.

The crack growth enhancement due to the C2 solution is clearly demonstrated by the comparison in the above figure. The crack growth rate in the current study is about an order of magnitude higher than the growth rates obtained in air from other studies for larger K_{max} values. However, since most of the dissolution is blocked due to the coating over the crack, the crack growth enhancement must be caused by IHAC. The data shows that direct exposure to the solution is not required to accelerate crack growth, which can be interpreted as Stage II SCC can be enhanced through IHAC alone.

185

6 Conclusion and Recommendation

6.1   Conclusions

The objective of this thesis was to study the effects of agglomeration and sequencing in a VAL underload spectrum on the corrosion fatigue of pipeline steel in an NNpH environment. Corrosion fatigue experiments were carried out on surface crack samples that simulated stage II SCC. However, surface cracks samples are not commonly used by researchers and there are many challenges associated with the precracking of these specimens. Chapter 3 presented additional improvements that were made to the precracking procedures of surface crack specimens. Generating large amounts of crack growth data without the use of a risky potential drop system was also a big challenge. Chapter 4 presented beachmarking techniques that were used to demarcate the boundaries between corrosion fatigue tests and to generate more data points. For the corrosion tests, various underload spectra with different agglomeration level and sequencing were applied to the samples. After the completion of the corrosion fatigue tests, the samples were fractured. Measurements were made on the fracture surface to determine the crack growth for each test. Chapter 5 contains the analysis of these results. The growth rate data were plotted using the combined factor model so the relative severity of different spectra could be compared. The acceleration factors for the spectra were also compared. Lastly, the crack growth data from this study were compared to results from other studies. The main conclusions from this thesis are summarized below:

6.1.1   Surface Crack Precracking

- The precrack shape can be predicted accurately using the shape evolution curves based on Newman and Raju's 'two points plus semi-ellipse' fatigue model
- Elliptical/super-elliptical fit through geometrical points generated from measurement of surface length of the precrack before and after milling process could accurately predict crack depth with an average error of less than 6%.
- While milling is necessary to create notchless cracks, it also changes the geometry of the specimen. Additional consideration must be made for the extent of the plastic zone during precrack to ensure the test results are not affected by it.

6.1.2   Crack Characterization Techniques

- Beachmarks can be generated in between two corrosion fatigue tests by:
    - Holding the sample at zero load for 12 hours after a test has completed
    - Apply a few thousand cycles of fatigue cycles with max stress lower than the corrosion fatigue test max stress, and frequency several orders of magnitude higher than the test frequency
    - Holding the sample again at zero load for 12 hours before starting the next test
- By arranging tests in a leapfrog manner and adding in beachmarks in between tests, a large amount of crack growth data can be generated simultaneously for two test waveforms without the use of potential drop systems.

6.1.3   Crack Characterization Observations

- The crack widths on the surface of the samples were widened significantly after the corrosion fatigue tests. The crack widths correlated strongly with crack size. HELP is likely the mechanism behind crack widening.
- Crack tips at the surface remained sharp throughout all corrosion fatigue tests, which is indicative of crack tip sharpening due to HE and discontinuous crack growth mechanism
- The Tuck Tape coating strip was effective in blocking out crack tip dissolution and simulating IHAC conditions
- The corrosion pit density was the highest along the boundary of the strip of tape coating, suggesting SCC susceptibility is the highest right next to the edge of disbondment.
- The crack shape deviated from the true semi-elliptical shape as it grew larger.
- Surface growth lagged behind growth just beneath the surface as the crack grew larger due to plastic zone closure effects at the surface
- The shape evolution behaviour of the surface cracks during the corrosion fatigue tests agreed with the shape evolution curves derived from Newman and Raju's surface crack fatigue growth equations. The crack grew toward a more semi-circular shape. This suggests lone individual SCC would also grow into a more semi-circular shape. Long critical cracks found in the field are formed by coalesced cracks that individually grew in

a manner that followed the shape evolution curves (i.e. individually growing toward more a semi-circular shape).

- The fracture surface morphology within the corrosion fatigue regions is predominantly quasi-cleavage. This is a strong indicator of hydrogen embrittlement during crack growth.

6.1.4 Agglomeration and Sequence Effects on VAL Underload Spectra

- Changing the agglomeration level in underload spectra can affect the crack growth rates. Increasing the agglomeration level increases the length of the MC chain, but it also reduces the number of interaction events (occurrences where UL directly follows a chain of MC's). The increase in MC chain length enhances crack growth rates while the decrease in interaction events slows down crack growth. The competition between these two effects determines the final growth rate. However, this competition also makes the prediction of the resultant crack growth rate more difficult.

- Three levels of agglomeration were tested in this study. It was found that level II agglomeration produced similar growth rates to level III agglomeration even though level III agglomeration had longer MC chains. This result could only be explained with the competition effect described above.

- The most severe spectra are usually not the most agglomerated spectra. Instead, they are the spectra that balance the two opposing forces (MC chain length and number of interaction events) to optimize the crack growth enhancement

- For agglomeration level II and above, the sequencing of consecutive UL's is important. When the most severe UL is the first UL after a chain of MC's, the spectrum is more severe because the first UL is capable of doing maximum damage due to the FPZ hydrogen level being at its maximum at the end of the MC chain

- For agglomeration level II and above, the sequencing of consecutive UL's also affect spectrum severity due to the underload effect. Milder underload cycles following a major underload have accelerated growth due to the underload effect.

6.1.5   Acceleration Factor

- The acceleration factors in the surface and depth direction were calculated using the combined factor model [81] and Been et al.'s model [80]

- The acceleration factor calculated using the combined factor showed a decreasing trend for cracks in the stable growth regime. This was caused by the differences in hydrogen concentration gradient in the CT specimens and the surface crack specimens. The combined factor model was based on results from CT specimens, which had a relatively constant bulk hydrogen concentration throughout the sample. Whereas the surface crack specimens used in this study had a more realistic hydrogen concentration gradient. Therefore SCC models should be developed using surface crack specimens instead of CT specimens

- The acceleration factor calculated with Been et al.'s model showed a relatively constant trend as the crack grew. This was because Been et al.'s model was based on mechanical driving forces only

- The acceleration factors for most SIF values were less than 1. The same behaviour was also observed by Yu et al. [10] for MC chain length < 32 cycles and for $R_{UL} < 0.25$ [94]. The reason for this behaviour is not known and requires further study.

6.1.6   Comparison with Other Studies

- Through comparison of crack growth data with other studies, it was confirmed that the anisotropy of pipeline steel causes different fatigue resistance in different crack growth directions.

- The results from this study and other studies showed that crack growth rate was higher in the surface direction (longitudinal & circumferential direction) than the thickness direction. This means the fatigue resistance of the pipeline material is higher in the depth direction

- The crack growth rate from this study is an order of magnitude higher than the growth rates obtained in air, indicating significant crack growth enhancement through IHAC in an NNpH environment

6.2 Recommendations for Pipeline Operators

- Since the competition between MC chain length and number of interaction events makes it difficult to predict the relative severity of the spectra when the agglomeration level is changed, it is recommended that corrosion fatigue experiments are carried out to verify the resultant crack growth rate

6.3 Recommendations for Future Studies

- In this study as well as other studies, it was found SCC susceptibility is higher right next to the edge of disbondment. A comprehensive field study should be conducted to confirm this finding. Additional laboratory studies should be conducted to determine the reason for the behaviour.

- Future corrosion fatigue studies should be conducted using surface crack specimens rather than thru-wall crack specimens such as the CT specimen. Surface crack specimens simulate real cracks on the pipeline more accurately. The difference in hydrogen gradient within these two types of samples causes growth rate discrepancies.

- Studies should be conducted to investigate why the acceleration factor is less than 1 for VAL underload spectra where the MC chain length has less than 32 cycles.

- Corrosion fatigue models such as the combined factor model should be modified so the effect of load interaction in VAL spectrum can be captured

- The effect of agglomeration levels on VAL underload spectra with higher MC:UL ratio should also be studied. It would be interesting to see how the increase in MC:UL ratio would affect the competition between MC chain length and the number of interaction events in determining the resultant crack growth rate.

- The anisotropy of the pipeline steel was not considered in previous SCC models. The results of this study and other studies have confirmed that anisotropy affects the fatigue resistance of the pipeline material in different directions. More work is needed to incorporate the effect of anisotropy into SCC models.

Bibliography

[1]   Green, K. P., and Jackson, T., 2015, *Safety in the Transportation of Oil and Gas: Pipelines or Rail?*, Fraser Institute.

[2]   Government of Canada, N. E. B., 2016, "NEB – Who Regulates Canada's Pipelines?" [Online]. Available: https://www.neb-one.gc.ca/bts/nws/rgltrsnpshts/2016/01rgltrsnpsht-eng.html. [Accessed: 10-Mar-2018].

[3]   Canadian Energy Pipeline Association, "Safety," About Pipelines: How safe are pipelines [Online]. Available: https://www.aboutpipelines.com/en/safety/. [Accessed: 10-Mar-2018].

[4]   Government of Canada, N. E. B., 2014, "NEB – Pipeline Ruptures" [Online]. Available: https://www.neb-one.gc.ca/sftnvrnmnt/sft/pplnrptr/index-eng.html. [Accessed: 10-Mar-2018].

[5]   National Energy Board, 1996, *Public Inquiry Concerning Stress Corrosion Cracking on Canadian Oil and Gas Pipelines: Report of the Inquiry*, MH-2-95, National Energy Board.

[6]   Paviglianiti, J., Murray, A., and Harrison, J., 2008, "The Importance of 'Significant' SCC Data Reported to the National Energy Board: An Update," *Proceedings of IPC2008 7th International Pipeline Conference*, pp. 867–874.

[7]   Delanty, B., and O'Beirne, J., 1992, "MAJOR FIELD STUDY COMPARES PIPELINE SCC WITH COATINGS," Oil and Gas Journal, **90**(24).

[8]   Chen, W., 2016, "An Overview of Near-Neutral PH Stress Corrosion Cracking in Pipelines and Mitigation Strategies for Its Initiation and Growth," CORROSION, **72**(7), pp. 962–977.

[9]   Yu, M., Xing, X., Zhang, H., Zhao, J., Eadie, R., Chen, W., Been, J., Boven, G. V., and Kania, R., 2015, "Corrosion Fatigue Crack Growth Behavior of Pipeline Steel under Underload-Type Variable Amplitude Loading Schemes," Acta Materialia, **96**, pp. 159–169.

[10]   Yu, M., Chen, W., Kania, R., Van Boven, G., and Been, J., 2015, "Underload-Induced Crack Growth Behaviour of Minor Cycles of Pipeline Steel in near-Neutral PH Environment: UNDERLOAD-INDUCED CRACK GROWTH BEHAVIOUR OF MINOR CYCLES OF PIPELINE STEEL IN NEAR-NEUTRAL PH ENVIRONMENT," Fatigue & Fracture of Engineering Materials & Structures, **38**(6), pp. 681–692.

[11]   Zhao, J., Chevil, K., Yu, M., Been, J., Keane, S., Van Boven, G., Kania, R., and Chen, W., 2016, "Statistical Analysis on Underload-Type Pipeline Spectra," Journal of Pipeline Systems Engineering and Practice, **7**(4), p. 04016007.

[12]   Anderson, T. L., 2005, "Chapter 11: Environmentally Assisted Cracking in Metals," *Fracture Mechanics Fundamentals and Applications*, Taylor & Francis, Boca Raton (Fla.); London; New York (etc.), pp. 511–552.

[13]   Parkins, R. N., 1994, *Overview of Intergranular Stress Corrosion Cracking Research Activities*, Report to Line Pipe Research Supervisory Committee of the American Gas Association, PR-232-9401.

[14]   CEPA Pipeline Integrity Working Group, 2015, *CEPA Recommended Practices for Managing Near-Neutral PH Stress Corrosion Cracking 3rd Edition*, Canadian Energy Pipeline Association.

[15] Fang, B. Y., Atrens, A., Wang, J. Q., Han, E. H., Zhu, Z. Y., and Ke, W., 2003, "Review of Stress Corrosion Cracking of Pipeline Steels in 'Low' and 'High' PH Solutions," Journal of Materials Science, **38**(1), pp. 127–132.

[16] King, F., 2010, *Development of Guidelines for Identification of SCC Sites and Estimation of Re-Inspection Intervals for SCC Direct Assessment*, PR-377-063528-R01, Pipeline Research Council International.

[17] Parkins, R. N., Blanchard, W. K., and Delanty, B. S., 1994, "Transgranular Stress Corrosion Cracking of High-Pressure Pipelines in Contact with Solutions of Near Neutral PH," CORROSION, **50**(5), pp. 394–408.

[18] Parkins, R. N., 1992, *Environment Sensitive Cracking of High-Pressure Pipelines in Contact with Carbon Dioxide Containing Solutions*, Topical report to Line Pipe Research Supervisory Committee of the American Gas Association, NG-18 Report no. 205.

[19] Krishnamurthy, R. M., Martens, B., Feser, D., Marreck, P., and MacDonald, R., 2000, "Liquid Pipeline Stress Corrosion Cracking," *2000 3rd International Pipeline Conference*, ASME.

[20] ROSEN Group, 2017, *The Encyclopedia of Pipeline Defects, Third Ed*, published in 2017 on behalf of ROSEN Group by: Clarion Technical Publishers and Tiratsoo Technical (a Division of Great Southern Press).

[21] Beavers, J. A., 1992, *Assessment of the Effects of Surface Preparation and Coatings on the Susceptibility of Line Pipe to Stress-Corrosion Cracking*, Report to Corrosion Supervisory Committee, PR186-917, Final Report, Pipeline Research Council International.

[22] Parkins, R. N., 1999, *A Review of Stress Corrosion Cracking of Pipelines in Contact with Near-Neutral (Low) PH Solutions*, Report to Line Pipe Research Supervisory Committee of the American Gas Association, PR-232-9701.

[23] Beavers, J. A., and Worthingham, R. G., 2002, "The Influence of Soil Chemistry on SCC of Underground Pipelines," pp. 1671–1678.

[24] Been, J., King, F., Yang, L., Song, F., and Sridhar, N., 2005, "The Role Of Coatings In The Generation Of High-And Near-Neutral Ph Environments That Promote Environmentally Assisted Cracking," NACE International.

[25] NACE International, 2013, *Control of External Corrosion on Underground or Submerged Metallic Piping Systems*, NACE-SP0169-2013.

[26] Transportation Safety Board of Canada, 1995, *Commodity Pipeline Occurrence Report - Natural Gas Pipeline Ruptures - TransCanada PipeLines Limited - Line 100-3, 914-Millimetre (36-Inch) Main Line - Kilometre Post Main Line Valve 30-3 +0.245 Kilometres - Line 100-4, 1,067-Millimetre (42-Inch) Main Line - Kilometre Post Main Line Valve 30-4 +0.220 Kilometres - Rapid City, Manitoba - 29 July 1995*, Report Number P95H0036.

[27] Transportation Safety Board of Canada, 2004, *Pipeline Investigation Report - Natural Gas Pipeline Rupture - TransCanada PipeLines - Line 100-3, 914-Millimetre-Diameter Line - Main-Line Valve 31-3 + 5.539 Kilometres - Near the Village of Brookdale, Manitoba - 14 April 2002*, Report Number P02H0017.

[28] Transportation Safety Board of Canada, 2010, *Natural Gas Pipeline Rupture - TransCanada Pipeline Inc. - 914-Millimeter-Diameter Pipeline - Line 2 – MLV 107-2 + 6.031 KM - Near Englehart, Ontario - 12 September 2009*, Report Number P09H0074.

[29] National Transportation Safety Board, 2012, *Enbridge Incorporated Hazardous Liquid Pipeline Rupture and Release, Marshall, Michigan, July 25, 2010.*, Pipeline Accident Report NTSB/PAR-12/01, Washington, D.C.

[30] Transportation Safety Board of Canada, 2012, *Natural Gas Pipeline Rupture - TransCanada PipeLines Limited - 914.4 -Millimetre-Diameter Pipeline - Line 100-2 – MLV 76-2 + 09.76 KM - Near Beardmore, Ontario - 19 February 2011*, Report Number P11H0011.

[31] Chen, W., Kania, R., Worthingham, R., and Boven, G. V., 2009, "Transgranular Crack Growth in the Pipeline Steels Exposed to Near-Neutral PH Soil Aqueous Solutions: The Role of Hydrogen," Acta Materialia, **57**(20), pp. 6200–6214.

[32] Harle, B. A., Beavers, J. A., and Jaske, C. E., 1995, "Mechanical and Metallurgical Effects on Low-PH Stress Corrosion Cracking of Natural Gas Pipelines," *Proc. CORROSION/95, Paper No. 646*, NACE International, Orlando, FL.

[33] Eadie, R., Hung, L. W., Sutherby, R., Roy, G., Shen, G., Luo, J., Chen, W., Hamré, T. C., King, F., and Jack, T., 2002, "Long Seam Welds in Gas and Liquids Pipelines and Near-Neutral PH Stress Corrosion Cracking and Corrosion Fatigue," *Proceedings of IPC'02 4th International Pipeline Conference*, ASME, pp. 1629–1633.

[34] TOUZET, M., LOPEZ, N., and PUIGGALI, M., 1998, "Effect of Applied Potential on Cracking of Low-Alloyed Pipeline Steel in Low PH Soil Environment," *Proc. EUROCORR'98, European Federation of Corrosion, Paper No. 226*, p. 12.

[35] Wang, Y.-Z., Revie, R. W., and Parkins, R. N., 1999, "Mechanistic Aspects of Stress Corrosion Crack Initiation and Early Propagation," NACE International.

[36] Qin, Z., Demko, B., Noël, J., Shoesmith, D., King, F., Worthingham, R., and Keith, K., 2004, "Localized Dissolution of Millscale-Covered Pipeline Steel Surfaces," CORROSION, **60**(10), pp. 906–914.

[37] Sherar, B. W. A., Keech, P. G., Qin, Z., King, F., and Shoesmith, D. W., 2010, "Nominally Anaerobic Corrosion of Carbon Steel in Near-Neutral PH Saline Environments," CORROSION, **66**(4), pp. 045001-045001–11.

[38] Beavers, J. A., Johnson, J. T., and Sutherby, R. L., 2000, "Materials Factors Influencing the Initiation of Near-Neutral PH SCC on Underground Pipelines," ASME, pp. IPC2000-221.

[39] Chen, W., Vanboven, G., and Rogge, R., 2007, "The Role of Residual Stress in Neutral PH Stress Corrosion Cracking of Pipeline Steels – Part II: Crack Dormancy," Acta Materialia, **55**(1), pp. 43–53.

[40] Van Boven, G., Rogge, R., and Chen, W., 2006, "Residual Stress and Stress Corrosion Cracking of High Pressure Hydrocarbon Transmission Pipelines," *Proceedings of IPC 2006 International Pipeline Conference*, ASME, pp. 725–742.

[41] Van Boven, G., Chen, W., and Rogge, R., 2007, "The Role of Residual Stress in Neutral PH Stress Corrosion Cracking of Pipeline Steels. Part I: Pitting and Cracking Occurrence," Acta Materialia, **55**(1), pp. 29–42.

[42] King, F., Ikeda-Cameron, K., Jack, T., and Been, J., 2004, *Long-Term Environmental Monitoring of near-Neutral and High-PH SCC Sites and the Basis of an Improved SCC Site Selection Model*, Gas Research Institute Report, GRI-04/0098.

[43] King, F., Jack, T., and Yang, L., 2004, *Assessment of the Aggressiveness of Various Types of Soil towards Low-PH SCC*, Gas Research Institute Report, GRI-04/0097.

[44] Van Boven, G., Jack, T. R., and King, F., 2004, *Environmental Factors: Effect on SCC Growth*, Gas Research Institute Report, GRI-04/0161.

[45] Beavers, J. A., and Harle, B. A., 2001, "Mechanisms of High-PH and Near-Neutral-PH SCC of Underground Pipelines," J. Offshore Mech. Arct. Eng, **123**(3), pp. 147–151.

[46] Beavers, J. A., and Harle, B. A., 1996, "Mechanisms of High-PH and Near-Neutral-PH SCC of Underground Pipelines," *1996 1st International Pipeline Conference*, pp. 555–564.

[47] Parkins, R. N., 2000, "A Review of Stress Corrosion Cracking of High Pressure Gas Pipelines," NACE International.

[48] Parkins, R. N., 1988, *Investigations Relating to the Environment Sensitive Fracture in the TransCanada Pipelines System*, Confidential report to TransCanada PipeLines.

[49] Tran, T., Brown, B., and Nesic, S., 2015, "Corrosion of Mild Steel in an Aqueous CO_2 Environment – Basic Electrochemical Mechanisms Revisited," NACE International.

[50] Nešić, S., 2011, "Carbon Dioxide Corrosion of Mild Steel," *Uhlig's Corrosion Handbook*, R.W. Revie, ed., John Wiley & Sons, Inc., pp. 229–245.

[51] Parkins, R. N., 1998, *Effects of Hydrogen on Low PH Stress Corrosion Crack Growth*, Report to Line Pipe Research Supervisory Committee of the American Gas Association, final report, PR-232-9704.

[52] Fang, B., Eslami, A., Kania, R., Worthingham, R., Been, J., and Chen, W., 2008, "Stress Corrosion Crack Initiation in X-65 Pipeline Steel Under Disbonded Coating With Cathodic Protection," *Proceedings of IPC2008 7th International Pipeline Conference*, ASME, pp. 723–733.

[53] CSA Group, and Standards Council of Canada, 2015, *Oil and Gas Pipeline Systems*, CSA Group, Toronto, Ont.

[54] Leeson, R., and Spitzmacher, D. K., 2006, "SCC Inspection and Mitigation Program on Suncor OSPL Pipeline: Field Data Trends and Observations," *2006 International Pipeline Conference*, pp. 35–48.

[55] Gu, B., Yu, W. Z., Luo, J. L., and Mao, X., 1999, "Transgranular Stress Corrosion Cracking of X-80 and X-52 Pipeline Steels in Dilute Aqueous Solution with Near-Neutral PH," CORROSION, **55**(3), pp. 312–318.

[56] Chen, W., Wang, S.-H., Chu, R., King, F., Jack, T. R., and Fessler, R. R., 2003, "Effect of Precyclic Loading on Stress-Corrosion-Cracking Initiation in an X-65 Pipeline Steel Exposed to near-Neutral PH Soil Environment," Metallurgical and Materials Transactions A, **34**(11), pp. 2601–2608.

[57] Parkins, R. N., and Beavers, J. A., 2003, "Some Effects of Strain Rate on the Transgranular Stress Corrosion Cracking of Ferritic Steels in Dilute Near-Neutral-PH Solutions," CORROSION, **59**(3), pp. 258–273.

[58] Lu, B. T., and Luo, J. L., 2006, "Relationship between Yield Strength and Near-Neutral PH Stress Corrosion Cracking Resistance of Pipeline Steels—An Effect of Microstructure," CORROSION, **62**(2), pp. 129–140.

[59] Asher, S. L., Leis, B., Colwell, J., and Singh, P. M., 2007, "Investigating a Mechanism for Transgranular Stress Corrosion Cracking on Buried Pipelines in Near-Neutral PH Environments," CORROSION, **63**(10), pp. 932–939.

[60] Fang, B., Han, E.-H., Wang, J., and Ke, W., 2007, "Mechanical and Environmental Influences on Stress Corrosion Cracking of an X-70 Pipeline Steel in Dilute Near-Neutral PH Solutions," CORROSION, **63**(5), pp. 419–432.

[61] Asher, S. L., and Singh, P. M., 2009, "Role of Stress in Transgranular Stress Corrosion Cracking of Transmission Pipelines in Near-Neutral PH Environments," CORROSION, **65**(2), pp. 79–87.

[62] Liu, Z. Y., Li, X. G., Du, C. W., Wang, L. X., and Huang, Y. Z., 2010, "Effect of Dissolved Oxygen on Stress Corrosion Cracking of X70 Pipeline Steel in Near-Neutral PH Solution," CORROSION, **66**(1), pp. 015006-015006–6.

[63] Pan, B. w., Li, J. x., Su, Y. j., Chu, W. y., and Qiao, L. j., 2012, "Role of Hydrogen in Stress Corrosion Cracking of X-60 Pipeline Steel in Soil Containing Water," CORROSION, **68**(11), pp. 1029–1036.

[64] Javidi, M., and Bahalaou Horeh, S., 2014, "Investigating the Mechanism of Stress Corrosion Cracking in Near-Neutral and High PH Environments for API 5L X52 Steel," Corrosion Science, **80**, pp. 213–220.

[65] Wang, X. z., Liu, Z. y., Ge, X., Zhan, X. l., Du, C. w., and Li, X. g., 2014, "Growth Behavior of Stress Corrosion Cracks of X80 Pipeline Steel in Underground Water of Acidic Soil," CORROSION, **70**(9), pp. 872–879.

[66] Rhodin, T. N., 1959, *Physical Metallurgy of Stress Corrosion Fracture*, New York, Interscience Publishers [c1959].

[67] Sofronis, P., and McMeeking, R. M., 1989, "Numerical Analysis of Hydrogen Transport near a Blunting Crack Tip," Journal of the Mechanics and Physics of Solids, **37**(3), pp. 317–350.

[68] Troiano, A. R., 2016, "The Role of Hydrogen and Other Interstitials in the Mechanical Behavior of Metals: (1959 Edward De Mille Campbell Memorial Lecture)," Metallography, Microstructure, and Analysis, **5**(6), pp. 557–569.

[69] King, F., Jack, T. R., Chen, W., Revie, R. W., Elboujdaini, M., and Worthingham, R. G., 2001, "Development of a Predictive Model for the Initiation and Early Stage Growth of Near Neutral PH SCC of Pipeline Steels," *CORROSION 2001*, NACE International.

[70] Kushida, T., Nose, K., Asahi, H., Kimura, M., Yamane, Y., Endo, S., and Kawano, H., 2001, "Effects of Metallurgical Factors and Test Conditions on Near Neutral PH SCC of Pipeline Steels," NACE International.

[71] Wang, S.-H., Chen, W., King, F., Jack, T. R., and Fessler, R. R., 2002, "Precyclic-Loading-Induced Stress Corrosion Cracking of Pipeline Steels in a Near-Neutral-PH Soil Environment," CORROSION, **58**(6), pp. 526–534.

[72] Chen, W., and Sutherby, R., 2004, "Environmental Effect of Crack Growth Rate of Pipeline Steel in Near-Neutral PH Soil Environments," *Proceedings of IPC2004 International Pipeline Conference*, ASME, pp. 123–132.

[73] Zheng, W., Bibby, D., Li, J., Bowker, J. T., Gianetto, J. A., Revie, R. W., and Williams, G., 2006, "Near-Neutral PH SCC of Two Line Pipe Steels Under Quasi-Static Stressing Conditions," *Proceedings of IPC 2006 International Pipeline Conference*, pp. 95–105.

[74] Fang, B. Y., Eadie, R., Chen, W. X., and Elboujdaini, M., 2009, "Passivation/Immersion Method to Grow Pits in Pipeline Steel and a Study of Pit Nucleation and Growth Resulting from the Method," Corrosion Engineering, Science and Technology, **44**(1), pp. 32–42.

[75] Fang, B. Y., Eadie, R. L., Chen, W. X., and Elboujdaini, M., 2010, "Pit to Crack Transition in X-52 Pipeline Steel in near Neutral PH Environment Part 1 – Formation of Blunt Cracks from Pits under Cyclic Loading," Corrosion Engineering, Science and Technology, **45**(4), pp. 302–312.

[76] Beavers, J. A., and Jaske, C. E., 1998, "Near-Neutral PH SCC of Pipelines: Effects of Pressure Fluctuations on Crack Propagation," NACE International.

[77] Beavers, J. A., and Jaske, C. E., 2004, *Effects of Pressure Fluctuations on SCC Propagation*, Pipeline Research Council International Report, Catalog no. L51872e.

[78] Beavers, J. A., and Harper, W. V., 2004, "Stress Corrosion Cracking Prediction Model," *CORROSION 2004*, NACE.

[79] Beavers, J. A., 2004, *Near-Neutral Ph Scc: Dormancy and Re-Initiation of Stress Corrosion Cracks*, Gas Research Institute Report GRI-7045.

[80] Been, J., Eadie, R., and Sutherby, R., 2006, "Prediction of Environmentally Assisted Cracking on Gas and Liquid Pipelines," *Proceedings of IPC 2006 International Pipeline Conference*, pp. 517–531.

[81] Chen, W., and Sutherby, R. L., 2007, "Crack Growth Behavior of Pipeline Steel in Near-Neutral PH Soil Environments," Metallurgical and Materials Transactions A, **38**(6), pp. 1260–1268.

[82] Eadie, R. L., Szklarz, K. E., and Sutherby, R. L., 2005, "Corrosion Fatigue and Near-Neutral PH Stress Corrosion Cracking of Pipeline Steel and the Effect of Hydrogen Sulfide," Corrosion, **61**(02).

[83] Been, J., Fessler, R. R., Keane, S., and Kresic, W., 2006, "History of Pressure Fluctuations Related to Severity of Near-Neutral PH SCC," *Proceedings of IPC 2006 International Pipeline Conference*, pp. 579–588.

[84] Been, J., King, F., and Sutherby, R., 2008, "Environmentally Assisted Cracking of Pipeline Steels in Near-Neutral PH Environments," *Environment-Induced Cracking of Materials*, Elsevier, Amsterdam, pp. 221–230.

[85] Gangloff, R. P., 1990, "Corrosion Fatigue Crack Propagation in Metals," Sep. 1988, United States.

[86] Anderson, T. L., 2005, "Chapter 10: Fatigue Crack Propagation," *Fracture Mechanics Fundamentals and Applications*, Taylor & Francis, Boca Raton (Fla.); London; New York (etc.), pp. 451–509.

[87] Shoji, T., Suzuki, S., and Ballinger, R. G., 1995, "Theoretical Prediction of SCC Growth Behavior -- Threshold and Plateau Growth Rate," Proc. 7th Int. Symp. Environmental Degradation of Materials in Nuclear Power Plants (Houston, TX: NACE, 1995), p. 881.

[88] Scott, P. M., and Truswell, A. E., 1983, "Corrosion Fatigue Crack Growth in Reactor Pressure Vessel Steels in PWR Primary Water," J. Pressure Vessel Technol, **105**(3), pp. 245–254.

[89] Beavers, J. A., Maier, C. J., Jaske, C. E., and Worthingham, R., 2007, "Methodology For Ranking Scc Susceptibility Of Pipeline Segments Based On The Pressure Cycle History," *Corrosion Conference and Expo (CORROSION 2007)*, NACE International.

[90] Van Boven, G., Sutherby, R., and King, F., 2002, "Characterizing Pressure Fluctuations on Buried Pipelines in Terms Relevant to Stress Corrosion Cracking," *4th International Pipeline Conference, Parts A and B*, pp. 1687–1698.

[91] Lambert, S. B., Beavers, J. A., Delanty, B., Sutherby, R., and Plumtree, A., 2000, "Mechanical Factors Affecting Stress Corrosion Crack Growth Rates in Buried Pipelines," *2000 3rd International Pipeline Conference, Volume 2: Integrity and Corrosion; Offshore Issues; Pipeline Automation and Measurement; Rotating Equipment*, p. V002T06A039.

[92]   Zhang, X.-Y., Lambert, S. B., Sutherby, R., and Plumtree, A., 1999, "Transgranular Stress Corrosion Cracking of X-60 Pipeline Steel in Simulated Ground Water," CORROSION, **55**(3), pp. 297–305.

[93]   Yu, M., Chen, W., Kania, R., Van Boven, G., and Been, J., 2014, "Depressurization-Induced Crack Growth Enhancement for Pipeline Steels Exposed to Near-Neutral PH Environments," *Proceedings of the 2014 10th International Pipeline Conference IPC2014*, ASME, p. V002T06A076.

[94]   Yu, M., Chen, W., Kania, R., Van Boven, G., and Been, J., 2016, "Crack Propagation of Pipeline Steel Exposed to a Near-Neutral PH Environment under Variable Pressure Fluctuations," International Journal of Fatigue, **82**, pp. 658–666.

[95]   Semiga, V., 2016, *Fatigue Considerations for Natural Gas Transmission Pipelines*, BMT Fleet Technology Limited 30348.FR (Rev.02), BMT Fleet Technology Limited.

[96]   Zhao, J., Chen, W., Keane, S., Been, J., and Van Boven, G., 2014, "Development and Validation of Load-Interaction Based Models for Crack Growth Prediction," p. V002T06A077.

[97]   Zheng, W., Tyson, W. R., Revie, R. W., Shen, G., and Braid, J. E. M., 1998, "Effects of Hydrostatic Testing on the Growth of Stress-Corrosion Cracks," ASME, pp. 459–472.

[98]   Chen, W., Kang, Y., Eadie, R., Kania, R., Van Boven, G., and Worthingham, R., 2012, "Achieving Maximum Crack Remediation Effect From Optimized Hydrotesting," *Proceedings of the 2012 9th International Pipeline Conference*, ASME, Calgary, Alberta, Canada.

[99]   Fleck, N. A., 1985, "Fatigue Crack Growth Due to Periodic Underloads and Overloads," Acta Metallurgica, **33**(7), pp. 1339–1354.

[100] Skorupa, M., 1998, "Load Interaction Effects During Fatigue Crack Growth Under Variable Amplitude Loading—a Literature Review. Part I: Empirical Trends," Fatigue & Fracture of Engineering Materials & Structures, **21**(8), pp. 987–1006.

[101] Williams, B. W., Lambert, S. B., Sutherby, R., and Plumtree, A., 2004, "Environmental Crack Growth under Variable Amplitude Loading of Pipeline Steel," CORROSION, **60**(1), pp. 95–103.

[102] Wang, S.-H., and Chen, W., 2001, "Room Temperature Creep Deformation and Its Effect on Yielding Behaviour of a Line Pipe Steel with Discontinuous Yielding," Materials Science and Engineering: A, **301**(2), pp. 147–153.

[103] Wang, S.-H., Zhang, Y., and Chen, W., 2001, "Room Temperature Creep and Strain-Rate-Dependent Stress-Strain Behavior of Pipeline Steels," Journal of Materials Science, **36**(8), pp. 1931–1938.

[104] Wang, S.-H., and Chen, W., 2002, "A Study on the Pre-Cyclic-Load-Induced Burst of Creep Deformation of a Pipeline Steel under Subsequent Static Load," Materials Science and Engineering: A, **325**(1–2), pp. 144–151.

[105] Yu, M., 2015, "Crack Growth Behavior of Pipeline Steels under Variable Pressure Fluctuations in a Near-Neutral PH Environment," Doctor of Philosophy Thesis, University of Alberta.

[106] Matsumoto, R., Taketomi, S., Matsumoto, S., and Miyazaki, N., 2009, "Atomistic Simulations of Hydrogen Embrittlement," International Journal of Hydrogen Energy, **34**(23), pp. 9576–9584.

[107] Gu, B., Luo, J., and Mao, X., 1999, "Hydrogen-Facilitated Anodic Dissolution-Type Stress Corrosion Cracking of Pipeline Steels in Near-Neutral PH Solution," CORROSION, **55**(1), pp. 96–106.

[108] Cheng, Y. F., 2007, "Fundamentals of Hydrogen Evolution Reaction and Its Implications on Near-Neutral PH Stress Corrosion Cracking of Pipelines," Electrochimica Acta, **52**(7), pp. 2661–2667.

[109] Le Friant, D., Bayle, B., Adam, C., and Magnin, T., 2000, "Stress Corrosion Cracking of Pipeline Steels in Simulated Ground Water: From Mechanisms to a Ranking Test," *Proc. EUROCORR 2000, 10-14 September, 2000, London, UK (Institute of Metals, London, UK)*.

[110] Ahmed, T. M., Lambert, S. B., Sutherby, R., and Plumtree, A., 1997, "Cyclic Crack Growth Rates of X-60 Pipeline Steel in a Neutral Dilute Solution," CORROSION, **53**(7), pp. 581–590.

[111] Zhao, J., Chen, W., Yu, M., Chevil, K., Eadie, R., Van Boven, G., Kania, R., Been, J., and Keane, S., 2017, "Crack Growth Modeling and Life Prediction of Pipeline Steels Exposed to Near-Neutral PH Environments: Dissolution Crack Growth and Occurrence of Crack Dormancy in Stage I," Metallurgical and Materials Transactions A, **48**(4), pp. 1629–1640.

[112] Gangloff, R. P., 2003, "6.02 - Hydrogen-Assisted Cracking," *Comprehensive Structural Integrity*, I. Milne, R.O. Ritchie, and B. Karihaloo, eds., Pergamon, Oxford, pp. 31–101.

[113] Kang, Y., Chen, W., Kania, R., Boven, G. V., and Worthingham, R., 2011, "Simulation of Crack Growth during Hydrostatic Testing of Pipeline Steel in Near-Neutral PH Environment," Corrosion Science, **53**(3), pp. 968–975.

[114] Egbewande, A., Chen, W., Eadie, R., Kania, R., Van Boven, G., Worthingham, R., and Been, J., 2014, "Transgranular Crack Growth in the Pipeline Steels Exposed to Near-Neutral PH Soil Aqueous Solutions: Discontinuous Crack Growth Mechanism," Corrosion Science, **83**, pp. 343–354.

[115] Egbewande, A., Chen, W., Eadie, R., Kania, R., Van Boven, G., Worthingham, R., and Been, J., 2014, "Surface Crack Growth Behavior of Pipeline Steel Under Disbonded Coating at Free Corrosion Potential in Near-Neutral PH Soil Environments," Metallurgical and Materials Transactions A, **45**(11), pp. 4946–4959.

[116] Anderson, T. L., 2005, "Chapter 5: Fracture Mechanisms in Metals," *Fracture Mechanics Fundamentals and Applications*, Taylor & Francis, Boca Raton (Fla.); London; New York (etc.), pp. 219–256.

[117] Chen, W., King, F., and Vokes, E., 2002, "Characteristics of Near-Neutral-PH Stress Corrosion Cracks in an X-65 Pipeline," CORROSION, **58**(3), pp. 267–275.

[118] Chen, W., Wang, S.-H., King, F., Jack, T. R., and Wilmott, M. J., 2000, "Hydrogen Permeation Behavior of X-70 Pipeline Steel in a Near-Neutral PH Soil Environment," p. V002T06A038.

[119] Newman, J. C., 1979, *Analysis of Surface Cracks in Finite Plates under Tension or Bending Loads*, NASA Technical Paper 1578.

[120] Newman, J. C., 1984, *Stress-Intensity Factor Equations for Cracks in Three-Dimensional Finite Bodies Subjected to Tension and Bending Loads*, NASA-TM-85793, NAS 1.15:85793.

[121] Newman, J. C., and Raju, I. S., 1981, "An Empirical Stress-Intensity Factor Equation for the Surface Crack," Engineering Fracture Mechanics, **15**(1), pp. 185–192.

[122] Newman Jr., J. C., and Raju, I. S., 1984, "Prediction of Fatigue Crack-Growth Patterns and Lives in Three-Dimensional Cracked Bodies," *Fracture 84, Proceedings of the 6th International Conference on Fracture (ICF6)*, Pergamon, pp. 1597–1608.

[123] Egbewande, A. T., Eslami, A., Chen, W., Worthingham, R., Kania, R., and VanBoven, G., 2010, "Growth of Surface-Type Stress Corrosion Cracks in Near-Neutral PH Environments Under Disbonded Coatings," *Proceedings of the 8th International Pipeline Conference IPC2010*, ASME, pp. 653–662.

[124] Hosseini, A., and Mahmoud, M. A., 1985, "Evaluation of Stress Intensity Factor and Fatigue Growth of Surface Cracks in Tension Plates," Engineering Fracture Mechanics, **22**(6), pp. 957–974.

[125] Smith, C. W., 1981, "Observations on Prediction of Non-Self-Similar Subcritical Crack Growth and Stress Intensity Distributions," *International Conference on Fracture 1981, Cannes (France)*.

[126] Smith, C. ., 1984, "Stress Intensity Distributions and Width Correction Factors for Natural Cracks Approaching 'Benchmark' Crack Depths," *Fracture Mechanics: Fifteenth Symposium*, ASTM International, 100 Barr Harbor Drive, PO Box C700, West Conshohocken, PA 19428-2959, pp. 118–129.

[127] Carter, D., Canda, W., and Blind, J., 1990, "Experimental Evaluation of Stress-Intensity Solutions for Surface Flaw Growth in Plates," *Surface-Crack Growth: Models, Experiments, and Structures*, W. Reuter, J. Underwood, and J. Newman, eds., ASTM International, 100 Barr Harbor Drive, PO Box C700, West Conshohocken, PA 19428-2959, pp. 215-215–22.

[128] Corn, D. L., 1971, "A Study of Cracking Techniques for Obtaining Partial Thickness Cracks of Pre-Selected Depths and Shapes," Engineering Fracture Mechanics, **3**(1), pp. 45–52.

[129] Wu, S.-X., 1985, "Shape Change of Surface Crack during Fatigue Growth," Engineering Fracture Mechanics, **22**(5), pp. 897–913.

[130] Lin, X. B., and Smith, R. A., 1999, "Finite Element Modelling of Fatigue Crack Growth of Surface Cracked Plates: Part II: Crack Shape Change," Engineering Fracture Mechanics, **63**(5), pp. 523–540.

[131] Lin, X. B., and Smith, R. A., 1999, "Finite Element Modelling of Fatigue Crack Growth of Surface Cracked Plates: Part III: Stress Intensity Factor and Fatigue Crack Growth Life," Engineering Fracture Mechanics, **63**(5), pp. 541–556.

[132] 2015, *ASTM E647-15e1 Standard Test Method for Measurement of Fatigue Crack Growth Rates*, ASTM International, West Conshohocken, PA.

[133] Vosikovsky, O., 1975, "Fatigue-Crack Growth in an X-65 Line-Pipe Steel at Low Cyclic Frequencies in Aqueous Environments," J. Eng. Mater. Technol, **97**(4), pp. 298–304.

[134] Suresh, S., 1998, "9.5 Plastic Zone Size in Monotonic Loading," *Fatigue of Materials, Second Edition*, Cambridge University Press.

[135] Darling, D., "Superellipse" [Online]. Available: http://www.daviddarling.info/encyclopedia/S/superellipse.html. [Accessed: 05-Apr-2018].

[136] Gan, F., Sun, Z.-W., Sabde, G., and Chin, D.-T., 1994, "Cathodic Protection to Mitigate External Corrosion of Underground Steel Pipe Beneath Disbonded Coating," CORROSION, **50**(10), pp. 804–816.

[137] Brousseau, R., and Qian, S., 1994, "Distribution of Steady-State Cathodic Currents Underneath a Disbonded Coating," CORROSION, **50**(12), pp. 907–911.

[138] Yan, M. C., Wang, J. Q., Han, E. H., and Ke, W., 2007, "Electrochemical Measurements Using Combination Microelectrode in Crevice Simulating Disbonded of Pipeline Coatings under Cathodic Protection," Corrosion Engineering, Science and Technology, **42**(1), pp. 42–49.

[139] Yan, L., Arafin, M., and Gravel, J.-P., 2017, "Penetration of Cathodic Protection into Pipeline Coating Disbondment," NACE International.

[140] Eslami, A., Fang, B., Kania, R., Worthingham, B., Been, J., Eadie, R., and Chen, W., 2010, "Stress Corrosion Cracking Initiation under the Disbonded Coating of Pipeline Steel in Near-Neutral PH Environment," Corrosion Science, **52**(11), pp. 3750–3756.

[141] Eslami, A., Marvasti, M., Chen, W., Eadie, R., Kania, R., Worthingham, R., and Van Boven, G., 2010, "The Role of Electrochemical Conditions in Near-Neutral PH SCC Initiation Mechanism(S)," *Proceedings of the 8th International Pipeline Conference IPC2010*, ASME, pp. 315–321.

[142] Eslami, A., Kania, R., Worthingham, B., Boven, G. V., Eadie, R., and Chen, W., 2011, "Effect of CO2 and R-Ratio on near-Neutral PH Stress Corrosion Cracking Initiation under a Disbonded Coating of Pipeline Steel," Corrosion Science, **53**(6), pp. 2318–2327.

[143] Eslami, A., 2012, "Near-Neutral PH Stress Corrosion Crack Initiaion under Simulated Coating Disbondment," Doctor of Philosophy Thesis, University of Alberta.

[144] Zipp, R. D., and Dahlberg, E. P., 1987, "Preparation and Preservation of Fracture Specimens," *ASM Handbook, Volume 12: Fractography*, ASM International, p. 6.

[145] Ted Pella Inc., *Technical Notes: Cellulose Acetate Replicating Film*.

[146] Schijve, J., 2009, "Fatigue Crack Growth. Analysis and Predictions," *Fatigue of Structures and Materials*, Springer, Dordrecht, pp. 209–256.

[147] Doré, M. J., and Maddox, S. J., 2013, "Accelerated Fatigue Crack Growth in 6082 T651 Aluminium Alloy Subjected to Periodic Underloads," Procedia Engineering, **66**, pp. 313–322.

[148] Schijve, J., 1976, "The Effect of Pre-Strain on Fatigue Crack Growth and Crack Closure," Engineering Fracture Mechanics, **8**(4), pp. 575–581.

[149] Vosikovsky, O., and Rivard, A., 1981, "Growth of Surface Fatigue Cracks in a Steel Plate," International Journal of Fatigue, **3**(3), pp. 111–115.

[150] Anderson, T. L., 2005, "Appendix 9: Stress Intensity and Fully Plastic J Solutions for Selected Configurations," *Fracture Mechanics Fundamentals and Applications*, Taylor & Francis, Boca Raton (Fla.); London; New York (etc.), pp. 434–448.

Appendix A -   Crack Growth Data

Columns 1 - 9

Row Number	Crack Name	Test #	Spectrum	f_{UL} (Hz)	f_{MC} (Hz)	Test Duration (Days)	Test Duration (# FB)	Pretest Surface Length $2c_i$ (µm)	Post-test Surface Length $2c_f$ (µm)
1	RL5 T	Test01	7MC-(12A/12B)	0.001	0.006	9.0278	360	9199	9252
2	RL5 M	Test01	7MC-(12A/12B)	0.001	0.006	9.0278	360	9248	9331
3	RL5 B	Test01	7MC-(12A/12B)	0.001	0.006	9.0278	360	9333	9382
4	RL5 T	Test02	7MC-(A/B)	0.001	0.006	13.7924	550	9316	9783
5	RL5 M	Test02	7MC-(A/B)	0.001	0.006	13.7924	550	9373	10039
6	RL5 B	Test02	7MC-(A/B)	0.001	0.006	13.7924	550	9459	10201
7	RL5 T	Test03	7MC-(12A/12B)	0.001	0.006	15.0463	600	9901	11421
8	RL5 M	Test03	7MC-(12A/12B)	0.001	0.006	15.0463	600	10264	12675
9	RL5 B	Test03	7MC-(12A/12B)	0.001	0.006	15.0463	600	10414	13287
10	RL6 T	Test01	7MC-(A/B)	0.001	0.006	14.6952	586	9098	9244
11	RL6 M	Test01	7MC-(A/B)	0.001	0.006	14.6952	586	9144	9242
12	RL6 B	Test01	7MC-(A/B)	0.001	0.006	14.6952	586	8888	8944
13	RL6 T	Test02	7MC-(12A/12B)	0.001	0.006	15.0463	600	9346	10441
14	RL6 M	Test02	7MC-(12A/12B)	0.001	0.006	15.0463	600	9341	10315
15	RL6 B	Test02	7MC-(12A/12B)	0.001	0.006	15.0463	600	9010	9851
16	RL6 T	Test03	7MC-(A/B)	0.001	0.006	13.9931	558	10522	13777
17	RL6 M	Test03	7MC-(A/B)	0.001	0.006	13.9931	558	10388	13150
18	RL6 B	Test03	7MC-(A/B)	0.001	0.006	13.9931	558	9895	11573
19	RL7 T	Test01	14MC-AB	0.0032	0.0192	2.0218	258	9265	9334
20	RL7 M	Test01	14MC-AB	0.0032	0.0192	2.0218	258	9100	9149
21	RL7 B	Test01	14MC-AB	0.0032	0.0192	2.0218	258	9256	9383
22	RL7 T	Test02	28MC-ABAB	0.0032	0.0192	2.0062	256	9334	9478
23	RL7 M	Test02	28MC-ABAB	0.0032	0.0192	2.0062	256	9149	9215
24	RL7 B	Test02	28MC-ABAB	0.0032	0.0192	2.0062	256	9383	9557
25	RL7 T	Test03	14MC-AB	0.0032	0.0192	2.0062	256	9478	9697
26	RL7 M	Test03	14MC-AB	0.0032	0.0192	2.0062	256	9215	9372
27	RL7 B	Test03	14MC-AB	0.0032	0.0192	2.0062	256	9557	9892
28	RL7 T	Test04	28MC-ABAB	0.0032	0.0192	2.0062	256	9697	10107
29	RL7 M	Test04	28MC-ABAB	0.0032	0.0192	2.0062	256	9372	9687
30	RL7 B	Test04	28MC-ABAB	0.0032	0.0192	2.0062	256	9892	10368
31	RL7 T	Test05	14MC-AB	0.0032	0.0192	1.9905	254	10107	10770
32	RL7 M	Test05	14MC-AB	0.0032	0.0192	1.9905	254	9687	10202
33	RL7 B	Test05	14MC-AB	0.0032	0.0192	1.9905	254	10368	11147

Row Number	Crack Name	Test #	Spectrum	f_{UL} (Hz)	f_{MC} (Hz)	Test Duration (Days)	Test Duration (# FB)	Pretest Surface Length $2c_i$ (μm)	Post-test Surface Length $2c_f$ (μm)
34	RL7 T	Test06	28MC-ABAB	0.0032	0.0192	2.0062	256	10770	11603
35	RL7 M	Test06	28MC-ABAB	0.0032	0.0192	2.0062	256	10202	10891
36	RL7 B	Test06	28MC-ABAB	0.0032	0.0192	2.0062	256	11147	12130
37	RL8 T	Test01	14MC-BA	0.0032	0.0192	2.2256	284	9041	9120
38	RL8 M	Test01	14MC-BA	0.0032	0.0192	2.2256	284	8913	8976
39	RL8 B	Test01	14MC-BA	0.0032	0.0192	2.2256	284	8902	8933
40	RL8 T	Test02	28MC-BABA	0.0032	0.0192	2.2883	292	9120	9307
41	RL8 M	Test02	28MC-BABA	0.0032	0.0192	2.2883	292	8976	9079
42	RL8 B	Test02	28MC-BABA	0.0032	0.0192	2.2883	292	8933	9104
43	RL8 T	Test03	14MC-BA	0.0032	0.0192	2.3196	296	9307	9704
44	RL8 M	Test03	14MC-BA	0.0032	0.0192	2.3196	296	9079	9355
45	RL8 B	Test03	14MC-BA	0.0032	0.0192	2.3196	296	9104	9455
46	RL8 T	Test04	28MC-BABA	0.0032	0.0192	2.2883	292	9704	10376
47	RL8 M	Test04	28MC-BABA	0.0032	0.0192	2.2883	292	9355	9817
48	RL8 B	Test04	28MC-BABA	0.0032	0.0192	2.2883	292	9455	10118
49	RL8 T	Test05	14MC-BA	0.0032	0.0192	2.2569	288	10376	11445
50	RL8 M	Test05	14MC-BA	0.0032	0.0192	2.2569	288	9817	10539
51	RL8 B	Test05	14MC-BA	0.0032	0.0192	2.2569	288	10118	11106
52	RL8 T	Test06	28MC-BABA	0.0032	0.0192	2.2569	288	11445	13028
53	RL8 M	Test06	28MC-BABA	0.0032	0.0192	2.2569	288	10539	11537
54	RL8 B	Test06	28MC-BABA	0.0032	0.0192	2.2569	288	11106	12640

Columns 10 - 19

Row Number	Pretest Crack Depth a_i (μm)	Post-test Crack Depth a_f (μm)	Surface Length @ midpoint of test region $2c_{mid}$ (μm)	Depth @ midpoint of test region a_{mid} (μm)	a/T initial	a/c initial	a/T final	a/c final	a/T mid-point	a/c mid-point
1	2067	2279	9226	2173	0.3007	0.4493	0.3316	0.4927	0.3162	0.4711
2	2122	2339	9290	2230	0.3087	0.4588	0.3404	0.5015	0.3245	0.4802
3	2223	2463	9358	2343	0.3234	0.4764	0.3583	0.5249	0.3408	0.5007
4	2372	2812	9550	2592	0.3451	0.5092	0.4091	0.5748	0.3771	0.5428
5	2428	2929	9706	2679	0.3533	0.5181	0.4262	0.5836	0.3897	0.5519
6	2545	3084	9830	2815	0.3703	0.5381	0.4487	0.6047	0.4095	0.5727
7	2934	3752	10661	3343	0.4268	0.5926	0.5459	0.6570	0.4864	0.6271
8	3152	4215	11470	3683	0.4586	0.6142	0.6132	0.6650	0.5359	0.6423
9	3272	4452	11850	3862	0.4761	0.6284	0.6477	0.6701	0.5619	0.6518
10	2189	2625	9171	2407	0.3189	0.4811	0.3824	0.5679	0.3507	0.5248
11	2200	2714	9193	2457	0.3206	0.4812	0.3955	0.5873	0.3581	0.5345
12	2057	2415	8916	2236	0.2995	0.4628	0.3516	0.5401	0.3256	0.5016
13	2673	3439	9894	3056	0.3895	0.5721	0.5011	0.6588	0.4453	0.6178
14	2764	3344	9828	3054	0.4028	0.5918	0.4874	0.6484	0.4451	0.6215
15	2530	3127	9431	2828	0.3684	0.5616	0.4552	0.6348	0.4118	0.5998
16	3459	4697	12150	4078	0.5040	0.6575	0.6843	0.6818	0.5942	0.6713
17	3364	4502	11769	3933	0.4903	0.6477	0.6561	0.6847	0.5732	0.6684
18	3137	3884	10734	3510	0.4567	0.6340	0.5655	0.6713	0.5111	0.6541
19	2151	2333	9300	2242	0.3130	0.4642	0.3396	0.5000	0.3263	0.4822
20	1988	2160	9124	2074	0.2898	0.4370	0.3148	0.4722	0.3023	0.4547
21	2162	2358	9319	2260	0.3148	0.4671	0.3434	0.5026	0.3291	0.4850
22	2333	2545	9406	2439	0.3396	0.5000	0.3704	0.5370	0.3550	0.5186
23	2160	2356	9182	2258	0.3148	0.4722	0.3433	0.5113	0.3291	0.4918
24	2358	2585	9470	2471	0.3434	0.5026	0.3765	0.5410	0.3599	0.5220
25	2545	2796	9587	2671	0.3704	0.5370	0.4070	0.5767	0.3887	0.5571
26	2356	2579	9294	2468	0.3433	0.5113	0.3759	0.5505	0.3596	0.5310
27	2585	2843	9724	2714	0.3765	0.5410	0.4141	0.5749	0.3953	0.5582
28	2796	3047	9902	2922	0.4070	0.5767	0.4435	0.6030	0.4252	0.5901
29	2579	2829	9530	2704	0.3759	0.5505	0.4123	0.5841	0.3941	0.5675
30	2843	3082	10130	2963	0.4141	0.5749	0.4488	0.5945	0.4314	0.5849
31	3047	3427	10438	3237	0.4435	0.6030	0.4988	0.6365	0.4711	0.6202
32	2829	3130	9944	2979	0.4123	0.5841	0.4561	0.6136	0.4342	0.5992

Row Number	Pretest Crack Depth a_i (μm)	Post-test Crack Depth a_f (μm)	Surface Length @ midpoint of test region $2c_{mid}$ (μm)	Depth @ midpoint of test region a_{mid} (μm)	a/T initial	a/c initial	a/T final	a/c final	a/T mid-point	a/c mid-point
33	3082	3483	10757	3283	0.4488	0.5945	0.5073	0.6250	0.4780	0.6103
34	3427	3865	11186	3646	0.4988	0.6365	0.5626	0.6662	0.5307	0.6519
35	3130	3471	10547	3300	0.4561	0.6136	0.5058	0.6374	0.4810	0.6259
36	3483	3950	11638	3717	0.5073	0.6250	0.5752	0.6513	0.5412	0.6387
37	2155	2295	9080	2225	0.3128	0.4768	0.3331	0.5032	0.3229	0.4900
38	1976	2150	8944	2063	0.2871	0.4433	0.3124	0.4790	0.2998	0.4612
39	2021	2218	8917	2119	0.2924	0.4540	0.3209	0.4966	0.3066	0.4754
40	2295	2557	9213	2426	0.3331	0.5032	0.3711	0.5494	0.3521	0.5266
41	2150	2350	9027	2250	0.3124	0.4790	0.3415	0.5176	0.3269	0.4984
42	2218	2440	9018	2329	0.3209	0.4966	0.3529	0.5360	0.3369	0.5165
43	2557	2866	9506	2711	0.3711	0.5494	0.4160	0.5907	0.3935	0.5705
44	2350	2642	9217	2496	0.3415	0.5176	0.3839	0.5648	0.3627	0.5415
45	2440	2739	9280	2589	0.3529	0.5360	0.3962	0.5793	0.3746	0.5581
46	2866	3252	10040	3059	0.4160	0.5907	0.4720	0.6268	0.4440	0.6093
47	2642	2965	9586	2803	0.3839	0.5648	0.4309	0.6041	0.4074	0.5849
48	2739	3122	9786	2931	0.3962	0.5793	0.4517	0.6172	0.4240	0.5989
49	3252	3761	10911	3507	0.4720	0.6268	0.5459	0.6573	0.5089	0.6428
50	2965	3349	10178	3157	0.4309	0.6041	0.4867	0.6355	0.4588	0.6204
51	3122	3597	10612	3360	0.4517	0.6172	0.5204	0.6478	0.4861	0.6332
52	3761	4370	12237	4066	0.5459	0.6573	0.6342	0.6708	0.5901	0.6645
53	3349	3820	11038	3584	0.4867	0.6355	0.5552	0.6622	0.5209	0.6495
54	3597	4174	11873	3886	0.5204	0.6478	0.6038	0.6604	0.5621	0.6545

Columns 20 - 25

Row Number	K_{max} @ Surface Midpoint (MPa√m)	K_{max} @ Depth Midpoint (MPa√m)	Combined Factor @ Surface for R=0.4 UL (MPa√m·Hz$^{-0.033}$)	Combined Factor @ Depth for R=0.4 UL (MPa√m·Hz$^{-0.033}$)	Combined Factor @ Surface for R=0.1 UL (MPa√m·Hz$^{-0.033}$)	Combined Factor @ Depth for R=0.1 UL (MPa√m·Hz$^{-0.033}$)
1	23.2029	29.7856	20.6968	26.5685	27.1572	34.8617
2	23.7162	30.1038	21.1547	26.8523	27.7580	35.2341
3	24.7201	30.6267	22.0502	27.3188	28.9330	35.8462
4	26.9099	31.7669	24.0035	28.3358	31.4960	37.1807
5	27.6728	32.3014	24.6839	28.8126	32.3888	37.8063
6	28.8602	32.9137	25.7431	29.3588	33.7787	38.5229
7	33.6419	35.9172	30.0084	32.0379	39.3753	42.0382
8	37.1166	38.5772	33.1078	34.4106	43.4421	45.1516
9	39.0331	39.9413	34.8173	35.6273	45.6852	46.7482
10	25.3160	30.5718	22.5817	27.2698	29.6305	35.7819
11	25.7593	30.7739	22.9771	27.4501	30.1493	36.0185
12	23.8152	29.5727	21.2430	26.3787	27.8738	34.6126
13	30.9296	33.6495	27.5890	30.0151	36.2007	39.3841
14	30.8967	33.5161	27.5596	29.8961	36.1622	39.2280
15	28.8902	32.1751	25.7698	28.7000	33.8137	37.6585
16	41.3409	41.2379	36.8758	36.7839	48.3863	48.2657
17	39.6409	39.9077	35.3594	35.5974	46.3966	46.7089
18	35.0937	36.4197	31.3033	32.4861	41.0744	42.6264
19	23.8102	30.1509	20.4388	25.8817	26.8186	33.9605
20	22.3370	29.2648	19.1741	25.1210	25.1592	32.9624
21	23.9790	30.2601	20.5836	25.9754	27.0087	34.0834
22	25.5650	31.0272	21.9451	26.6338	28.7951	34.9474
23	24.0069	30.0835	20.6076	25.8237	27.0401	33.8844
24	25.8582	31.2499	22.1967	26.8250	29.1253	35.1982
25	27.5825	32.0543	23.6769	27.5155	31.0675	36.1043
26	25.8577	30.9824	22.1963	26.5954	29.1247	34.8969
27	27.9854	32.4383	24.0227	27.8451	31.5212	36.5368
28	29.7733	33.3175	25.5575	28.5999	33.5351	37.5271
29	27.9070	32.0903	23.9555	27.5464	31.4330	36.1448
30	30.1947	33.8847	25.9193	29.0868	34.0098	38.1660
31	32.6260	35.1763	28.0063	30.1954	36.7482	39.6207
32	30.3200	33.5929	26.0268	28.8362	34.1508	37.8372

Row Number	K_{max} @ Surface Midpoint (MPa√m)	K_{max} @ Depth Midpoint (MPa√m)	Combined Factor @ Surface for R=0.4 UL (MPa√m·Hz$^{-0.033}$)	Combined Factor @ Depth for R=0.4 UL (MPa√m·Hz$^{-0.033}$)	Combined Factor @ Surface for R=0.1 UL (MPa√m·Hz$^{-0.033}$)	Combined Factor @ Depth for R=0.1 UL (MPa√m·Hz$^{-0.033}$)
33	33.1795	35.9939	28.4814	30.8973	37.3716	40.5417
34	36.5641	37.7835	31.3867	32.4335	41.1838	42.5574
35	33.2672	35.6071	28.5566	30.5652	37.4704	40.1060
36	37.5556	39.0784	32.2379	33.5450	42.3007	44.0159
37	23.7045	29.7950	20.3480	25.5761	26.6995	33.5596
38	22.2883	29.0056	19.1323	24.8985	25.1043	32.6704
39	22.6890	29.0477	19.4763	24.9347	25.5557	32.7179
40	25.1884	30.6821	21.6218	26.3376	28.3709	34.5587
41	23.6656	29.8227	20.3146	25.5999	26.6557	33.5907
42	24.1570	29.9113	20.7364	25.6760	27.2091	33.6906
43	27.1926	31.9112	23.3423	27.3927	30.6284	35.9431
44	25.5023	30.7998	21.8913	26.4387	28.7245	34.6913
45	26.0654	30.9830	22.3746	26.5959	29.3587	34.8977
46	29.7481	33.5913	25.5358	28.8349	33.5067	37.8355
47	27.8333	32.0731	23.8922	27.5316	31.3500	36.1254
48	28.6214	32.5479	24.5687	27.9392	32.2376	36.6602
49	33.2242	36.1638	28.5197	31.0431	37.4220	40.7330
50	30.5326	33.7694	26.2093	28.9878	34.3904	38.0361
51	31.9332	34.8935	27.4116	29.9527	35.9679	39.3022
52	38.1502	40.2861	32.7482	34.5817	42.9703	45.3761
53	33.9349	36.2129	29.1298	31.0852	38.2225	40.7883
54	36.4691	38.5920	31.3052	33.1275	41.0769	43.4680

Columns 26 - 29

Row Number	Acceleration Factor @ Surface, Calculated w/ Combined Factor	Acceleration Factor @ Depth, Calculated w/ Combined Factor	Acceleration Factor @ Surface, Calculated with Been et al. 2006 model	Acceleration Factor @ Depth, Calculated with Been et al. 2006 model
1	0.29	0.47	0.15	0.51
2	0.36	0.45	0.21	0.51
3	0.16	0.45	0.11	0.52
4	0.60	0.45	0.51	0.56
5	0.72	0.46	0.67	0.60
6	0.64	0.45	0.65	0.61
7	0.51	0.39	0.73	0.64
8	0.47	0.34	0.84	0.65
9	0.43	0.31	0.85	0.65
10	0.25	0.51	0.18	0.59
11	0.15	0.58	0.12	0.68
12	0.14	0.51	0.09	0.54
13	0.59	0.52	0.70	0.74
14	0.53	0.40	0.62	0.57
15	0.66	0.52	0.67	0.67
16	0.38	0.29	0.85	0.65
17	0.41	0.32	0.83	0.67
18	0.48	0.35	0.76	0.60
19	0.56	0.65	0.24	0.59
20	0.55	0.72	0.21	0.61
21	0.99	0.69	0.44	0.62
22	0.69	0.65	0.40	0.62
23	0.52	0.71	0.23	0.64
24	0.77	0.67	0.47	0.65
25	0.65	0.64	0.47	0.66
26	0.70	0.69	0.42	0.66
27	0.92	0.62	0.69	0.66
28	0.79	0.52	0.69	0.59
29	0.87	0.64	0.66	0.66
30	0.85	0.45	0.77	0.53
31	0.78	0.59	0.83	0.75
32	0.91	0.60	0.83	0.69

Row Number	Acceleration Factor @ Surface, Calculated w/ Combined Factor	Acceleration Factor @ Depth, Calculated w/ Combined Factor	Acceleration Factor @ Surface, Calculated with Been et al. 2006 model	Acceleration Factor @ Depth, Calculated with Been et al. 2006 model
33	0.83	0.55	0.93	0.73
34	0.52	0.45	0.71	0.67
35	0.72	0.49	0.81	0.64
36	0.53	0.40	0.77	0.64
37	0.59	0.48	0.26	0.42
38	0.65	0.70	0.25	0.58
39	0.29	0.78	0.11	0.65
40	0.87	0.75	0.48	0.70
41	0.76	0.67	0.33	0.59
42	1.13	0.73	0.51	0.65
43	1.12	0.70	0.78	0.72
44	1.16	0.81	0.67	0.76
45	1.28	0.80	0.80	0.77
46	1.14	0.67	1.00	0.77
47	1.15	0.73	0.86	0.75
48	1.39	0.79	1.12	0.85
49	1.00	0.60	1.12	0.81
50	1.08	0.66	1.00	0.76
51	1.15	0.68	1.18	0.84
52	0.69	0.39	1.05	0.67
53	0.83	0.55	0.97	0.74
54	0.86	0.47	1.18	0.74

Appendix B -   Crack Images

This appendix contains the images used to obtain the crack growth measurements. Full detail on how the images were measured can be found in section 4.12. The images were scaled, aligned, and measured in AutoCAD. The images in this appendix were exported from AutoCAD along with their respective scale bars.

The surface images were all taken after polishing. They were imaged with an optical microscope unless stated otherwise. The fractographs were taken with SEM for some samples and stereomicroscopes for other samples. It was not necessary to etch the fracture surface to obtain good measurements. The corrosion deposits along the beachmarks can even be helpful for measurements.

RL5-B	RL5-M	RL5-T
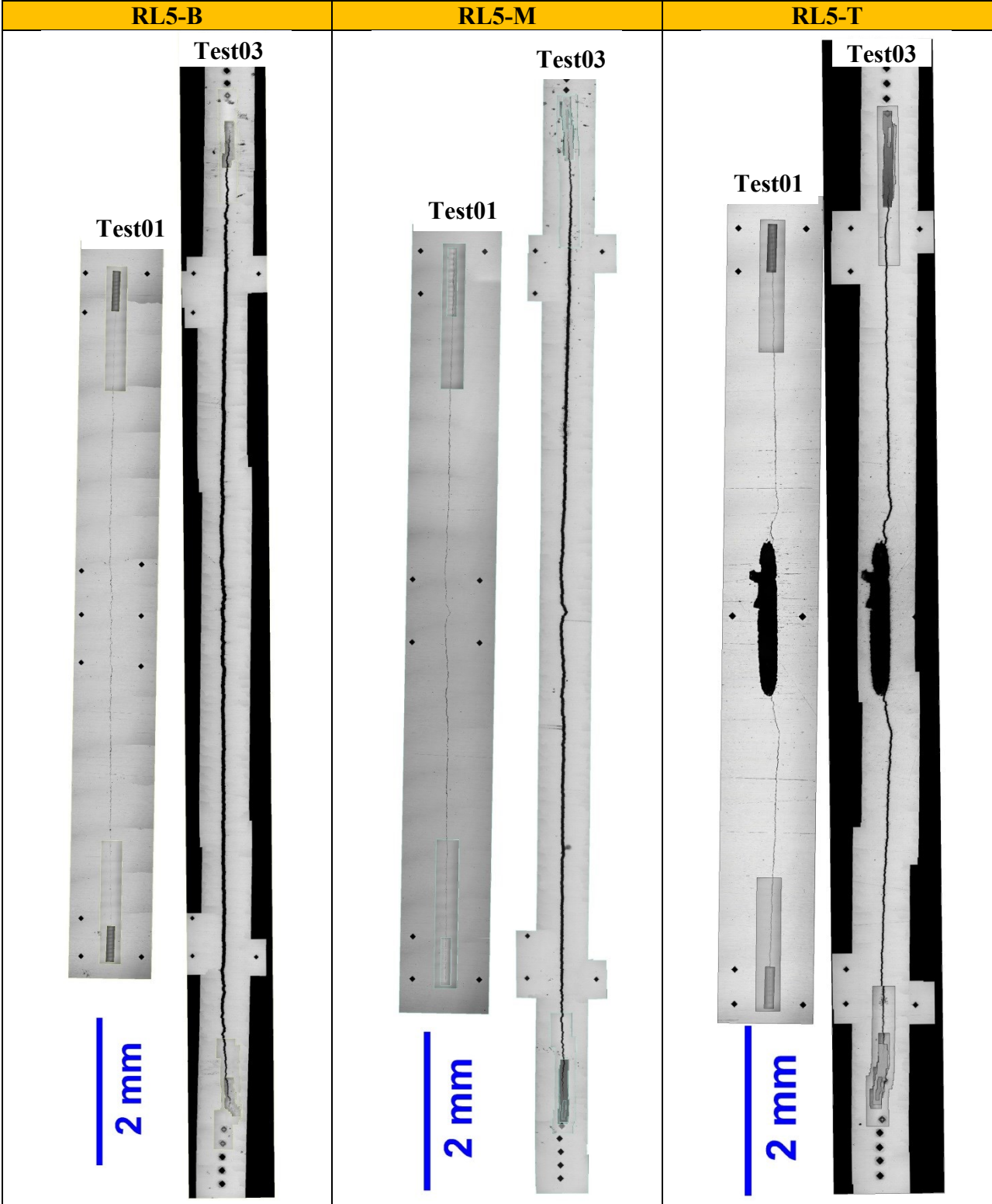
Figure B-1 Surface images taken after Test01 and Test03 for RL5 cracks.
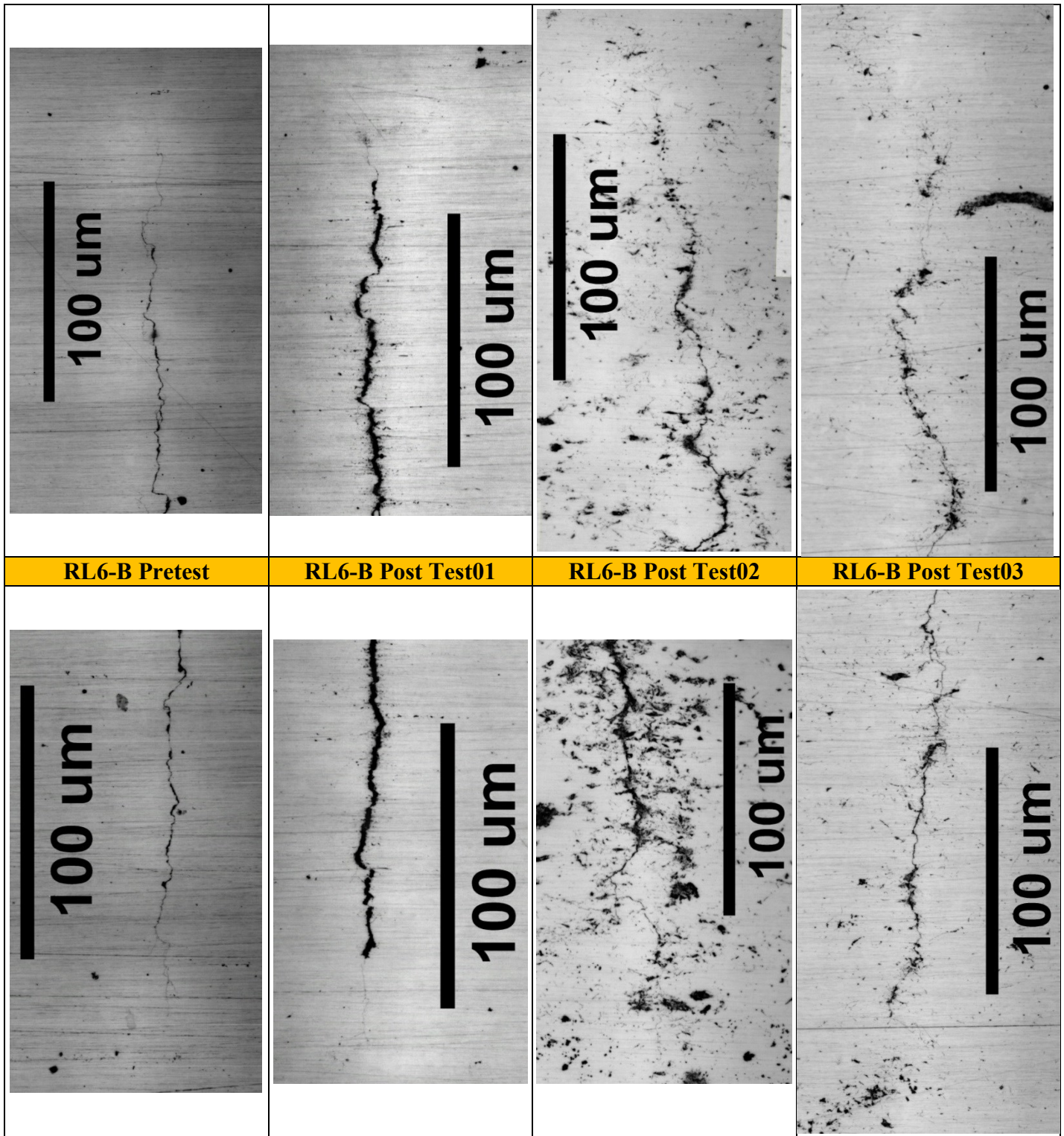
| RL5-B Pretest | RL5-B Post Test01 | RL5-B Post Test03 |
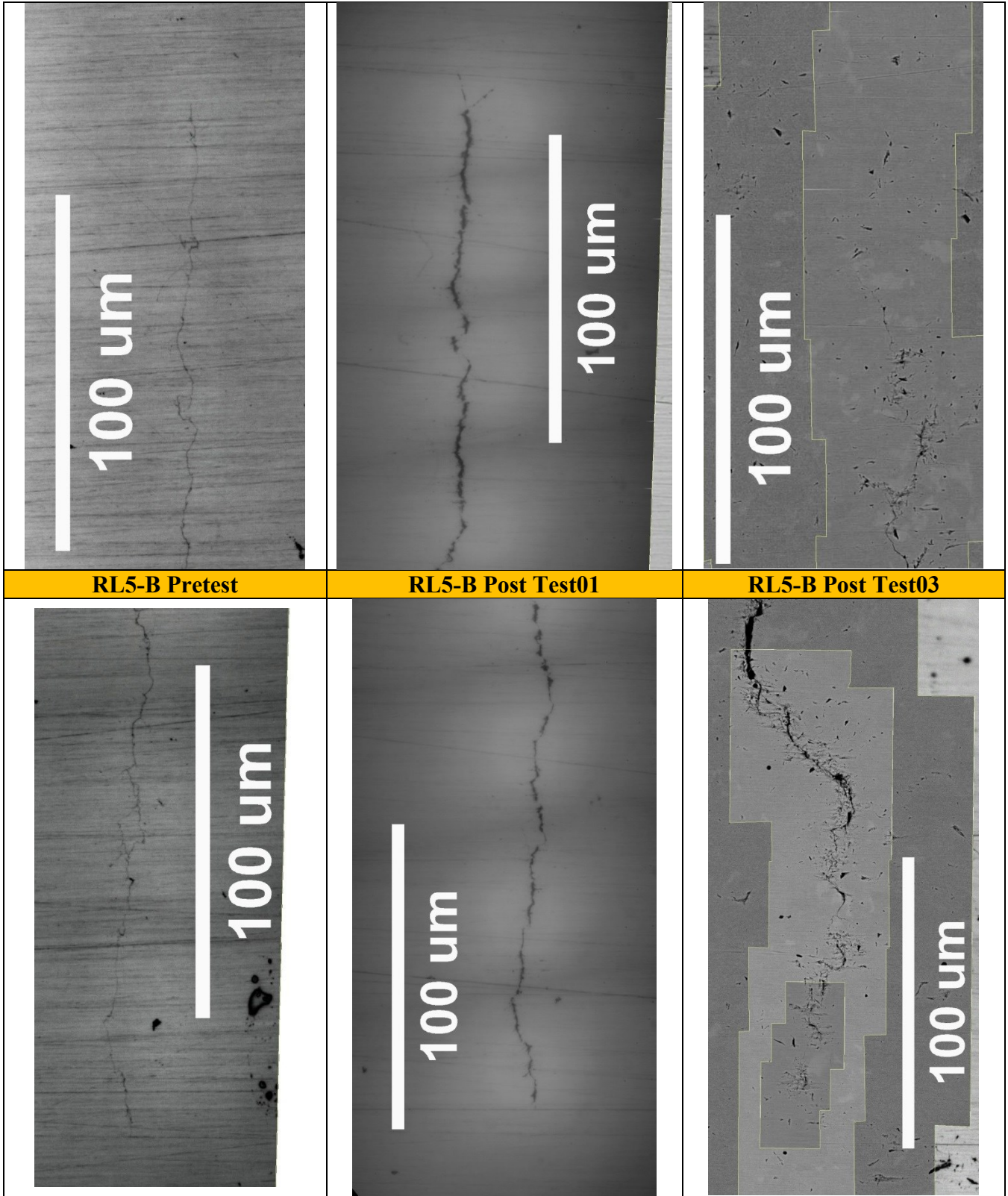
Figure B-2 High magnification images of the surface crack tips for RL5-B, taken prior to testing (pretest), after test01, and after test03. The images for post test03 were taken with SEM.
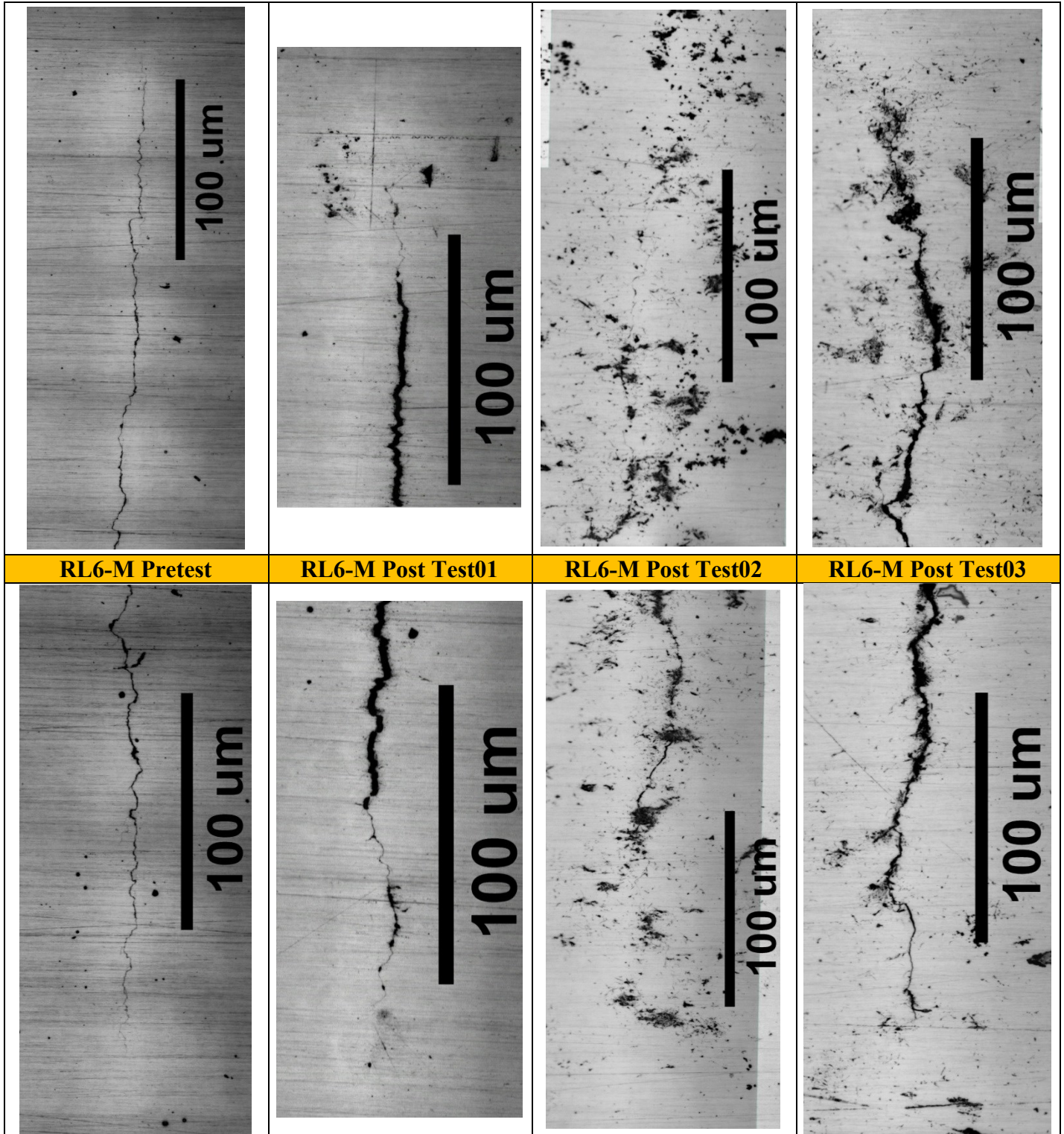
| RL5-M Pretest | RL5-M Post Test01 | RL5-M Post Test03 |
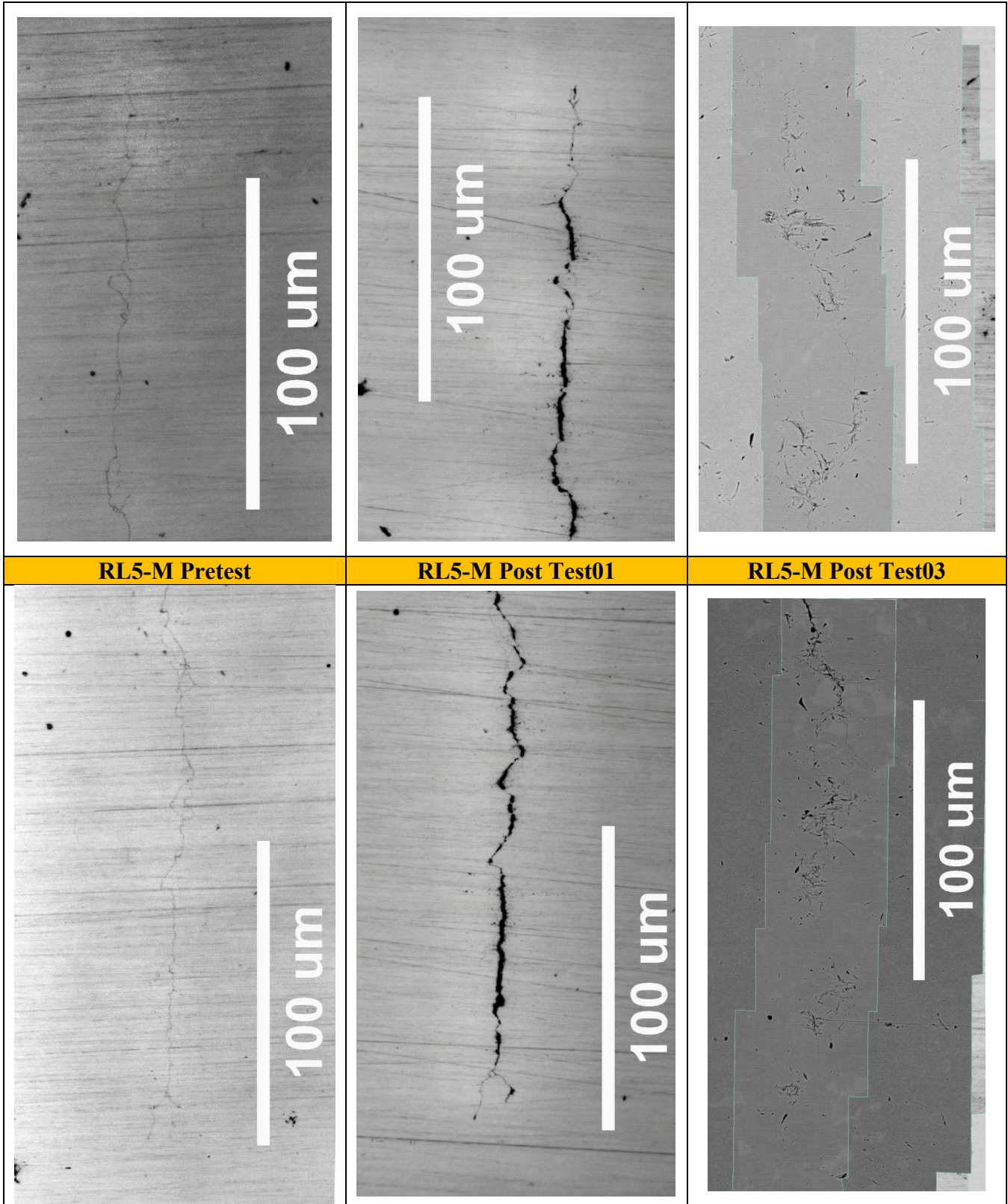
Figure B-3 High magnification images of the surface crack tips for RL5-M, taken prior to testing (pretest), after test01, and after test03. The images for post test03 were taken with SEM.
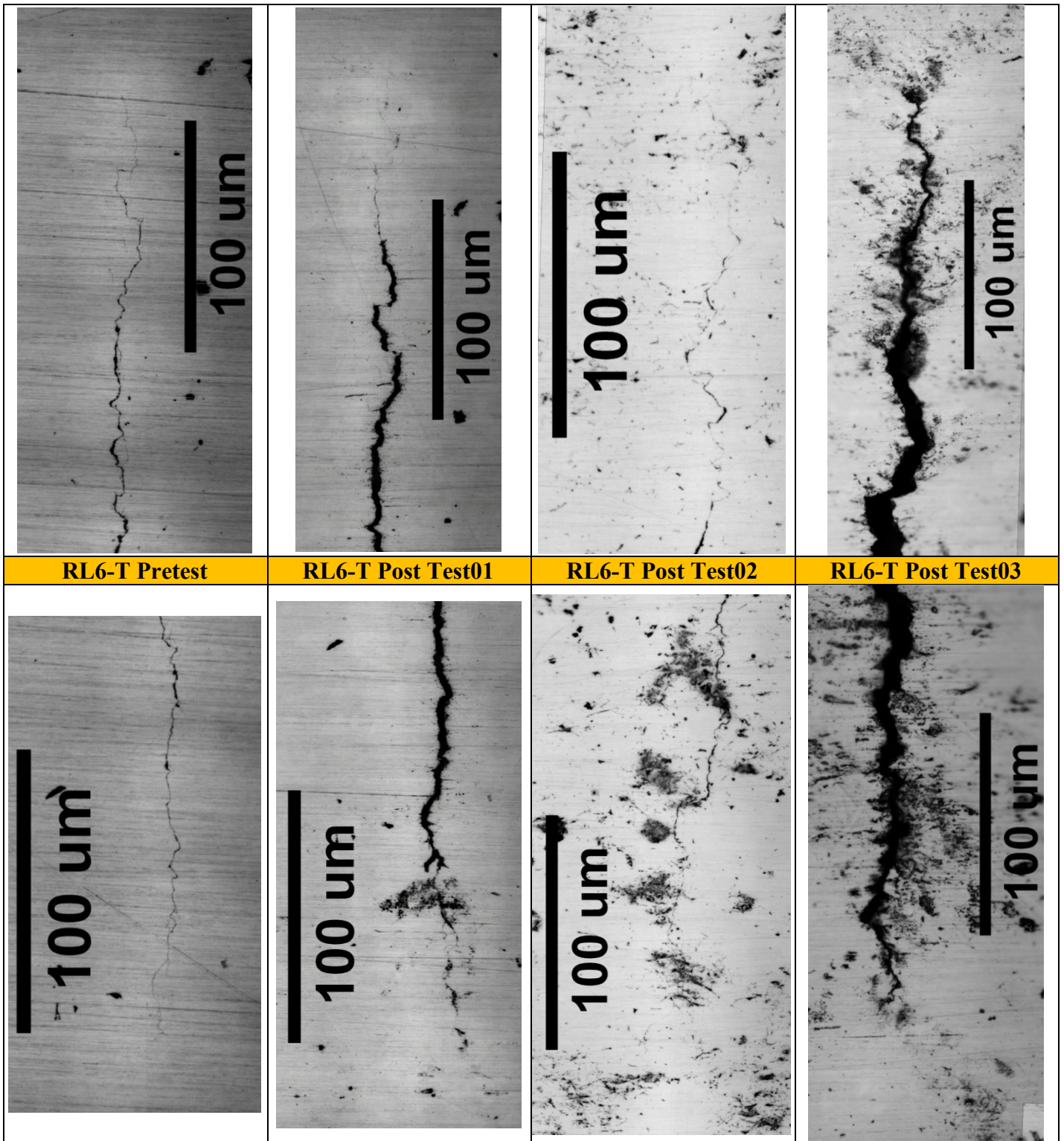
212

| RL5-T Pretest | RL5-T Post Test01 | RL5-T Post Test03 |
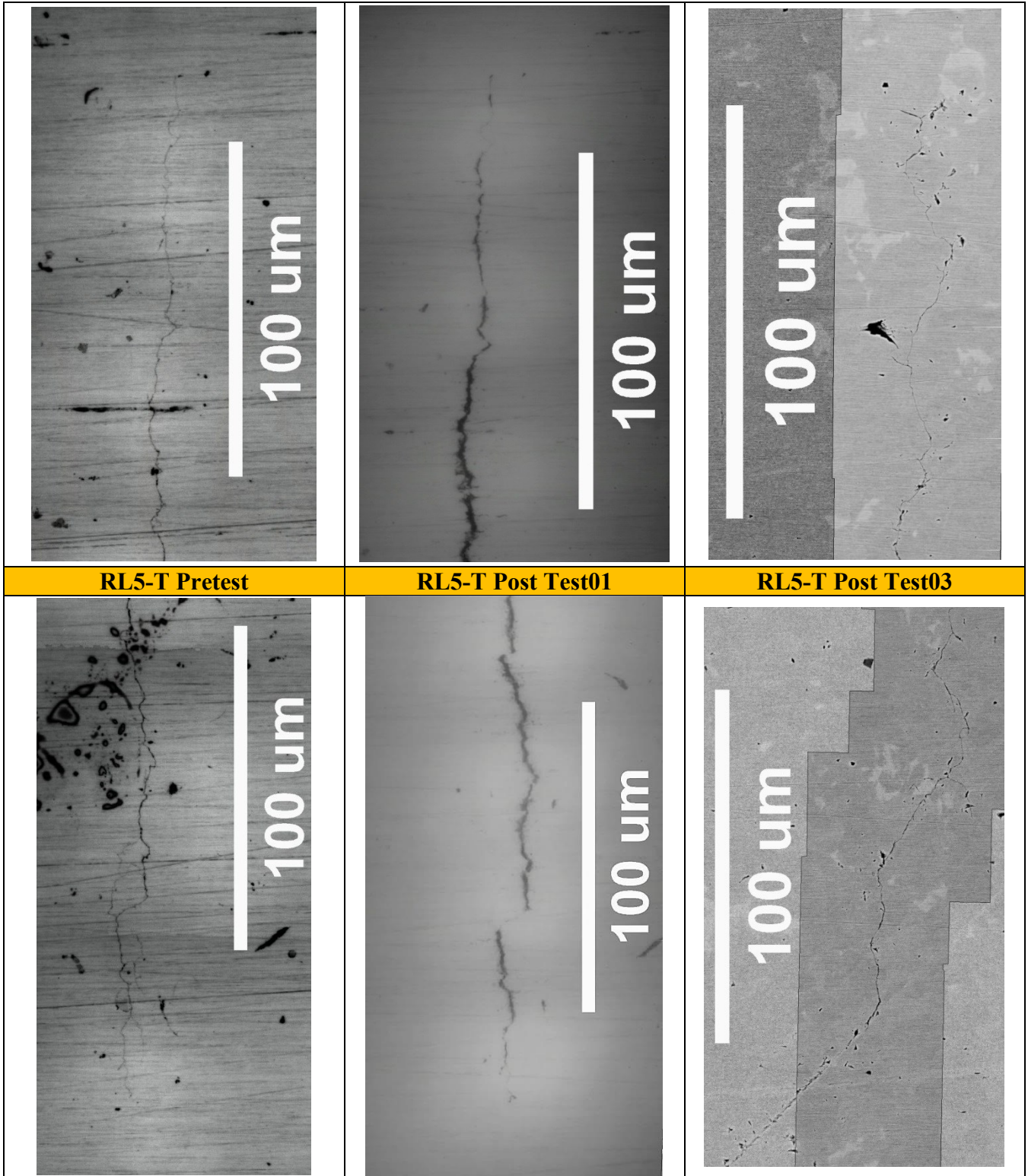
**Figure B-4 High magnification images of the surface crack tips for RL5-T, taken prior to testing (pretest), after test01, and after test03. The images for post test03 were taken with SEM.**
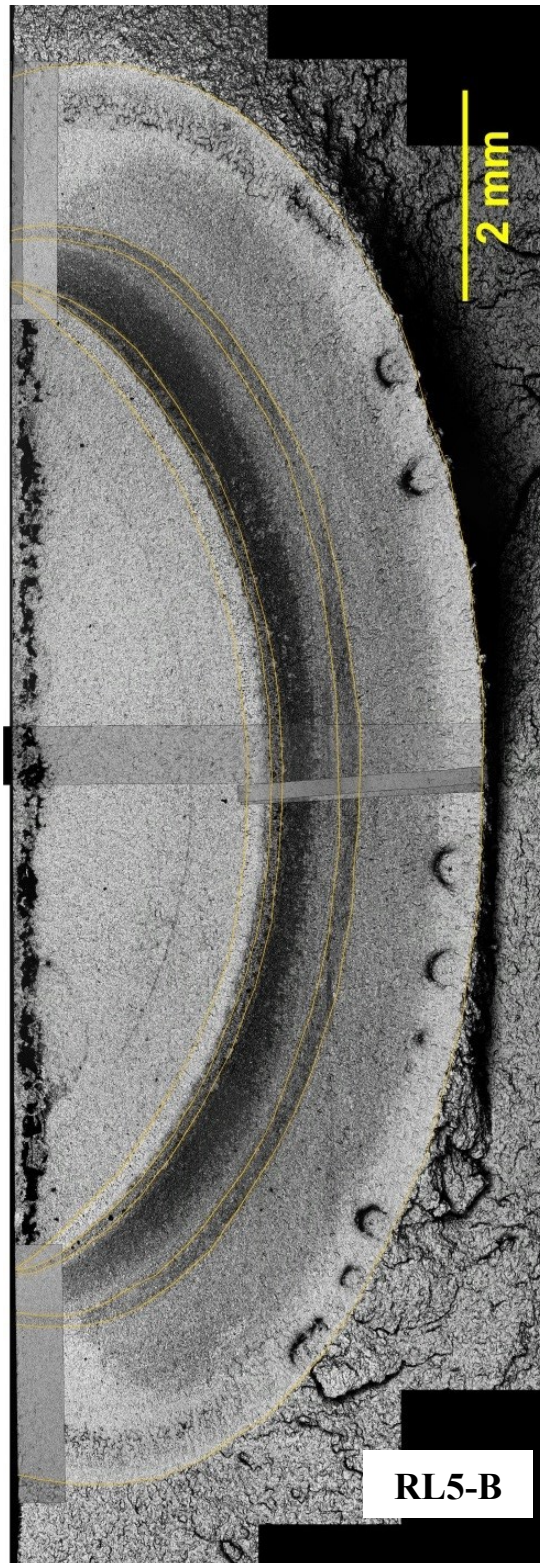
Figure B-5 Fractograph for RL5-B, taken with SEM. The orange lines demarcate the different test and beachmark regions. The beachmark and test regions can be distinguished under high magnification as shown in section 5.2.1 because of the differences in fracture surface morphology.
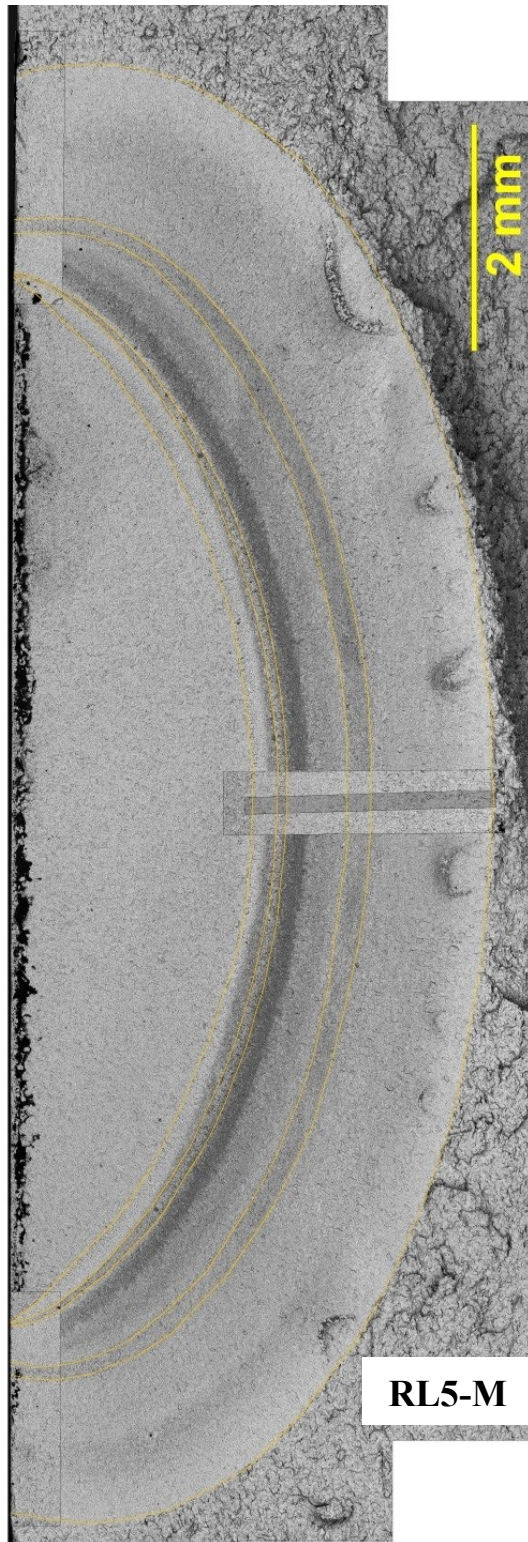
Figure B-6 Fractograph for RL5-M, taken with SEM. The orange lines demarcate the different test and beachmark regions. The beachmark and test regions can be distinguished under high magnification as shown in section 5.2.1 because of the differences in fracture surface morphology.
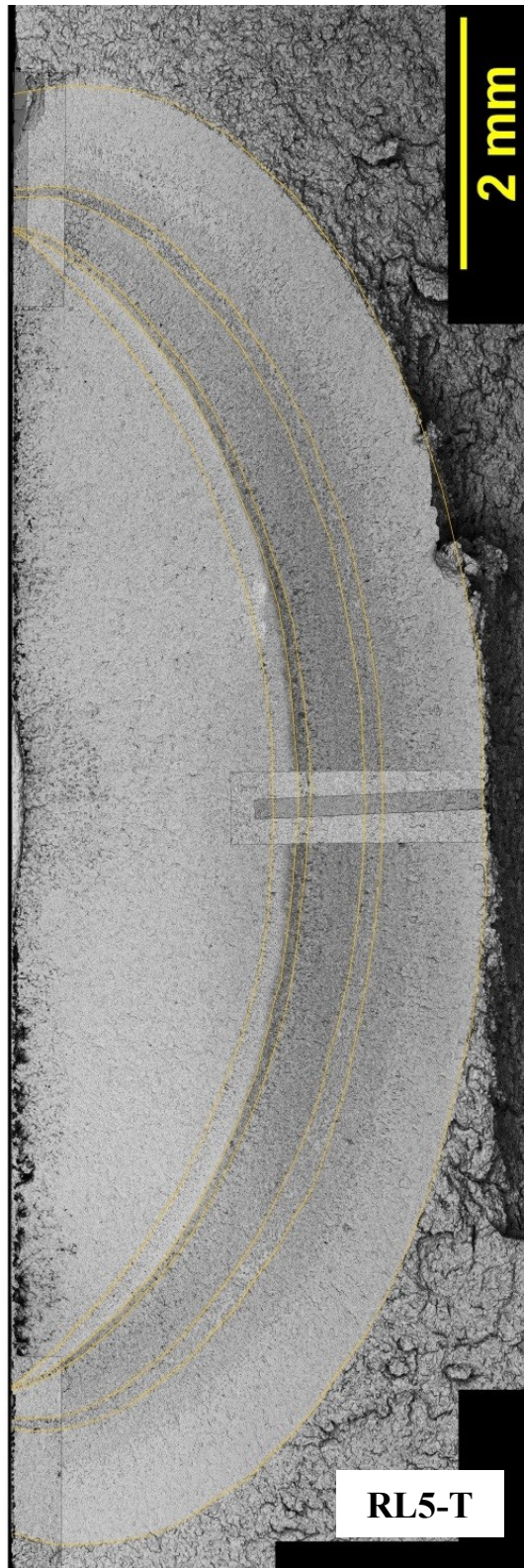
Figure B-7 Fractograph for RL5-T, taken with SEM. The orange lines demarcate the different test and beachmark regions. The beachmark and test regions can be distinguished under high magnification as shown in section 5.2.1 because of the differences in fracture surface morphology.

RL6-B	RL6-M	RL6-T
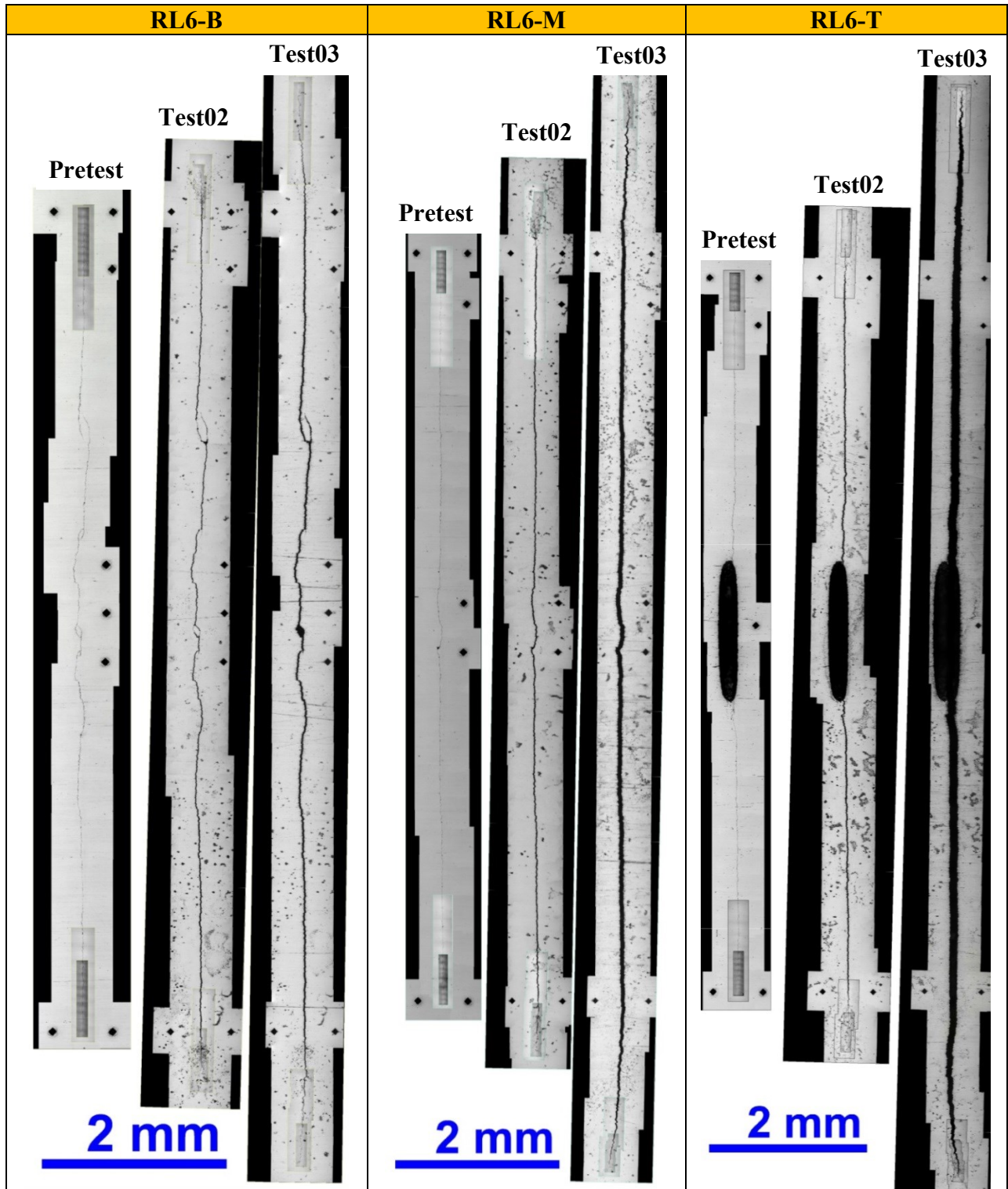
Figure B-8 Surface images taken prior to testing, after test02, and after test03 for RL6 cracks.

| RL6-B Pretest | RL6-B Post Test01 | RL6-B Post Test02 | RL6-B Post Test03 |

Figure B-9 High magnification images of the surface crack tips for RL6-B. The images were taken prior to testing (pretest) and after test01, test02, and test 03

| RL6-M Pretest | RL6-M Post Test01 | RL6-M Post Test02 | RL6-M Post Test03 |

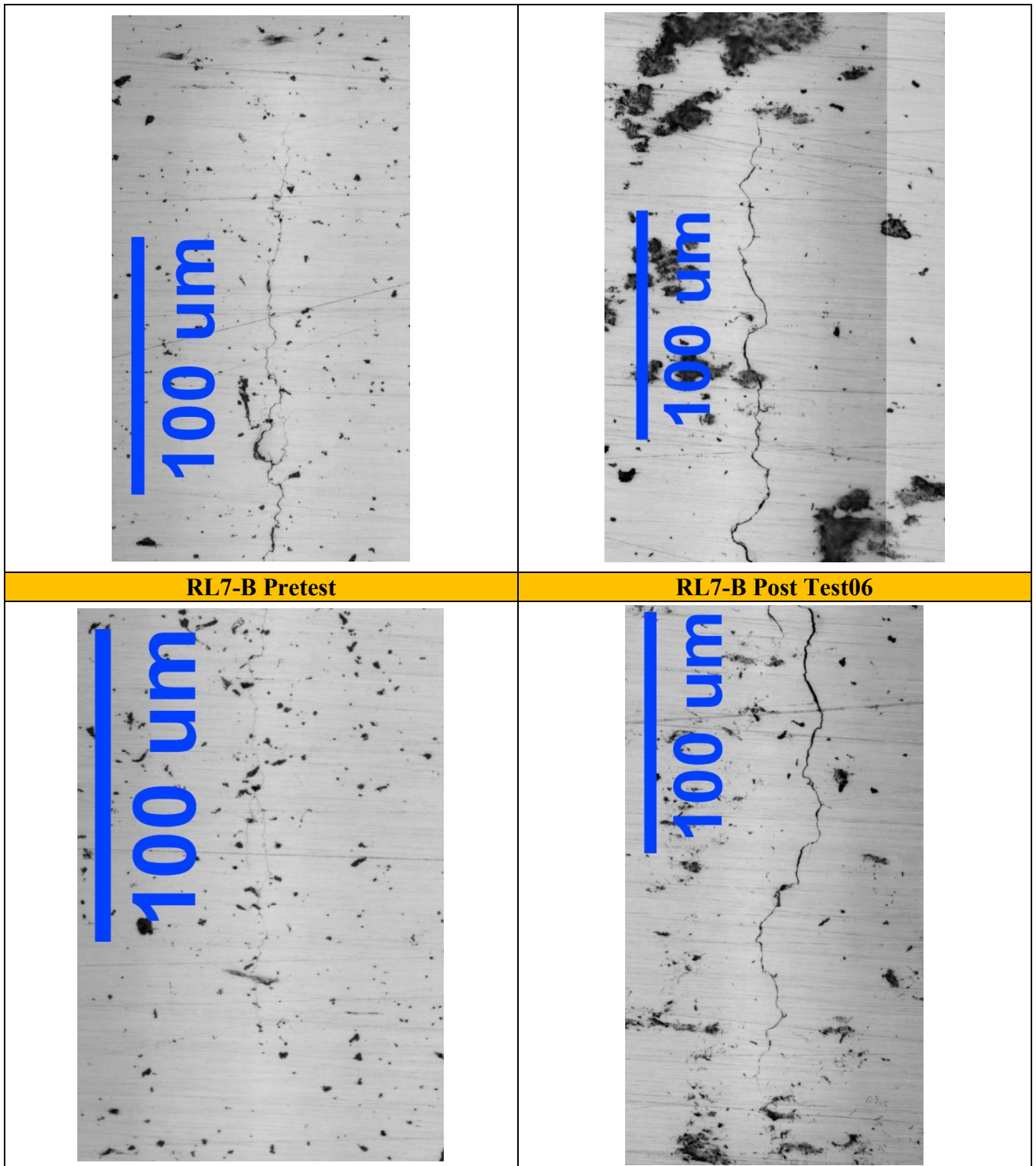**Figure B-10 High magnification images of the surface crack tips for RL6-M. The images were taken prior to testing (pretest) and after test01, test02, and test 03**
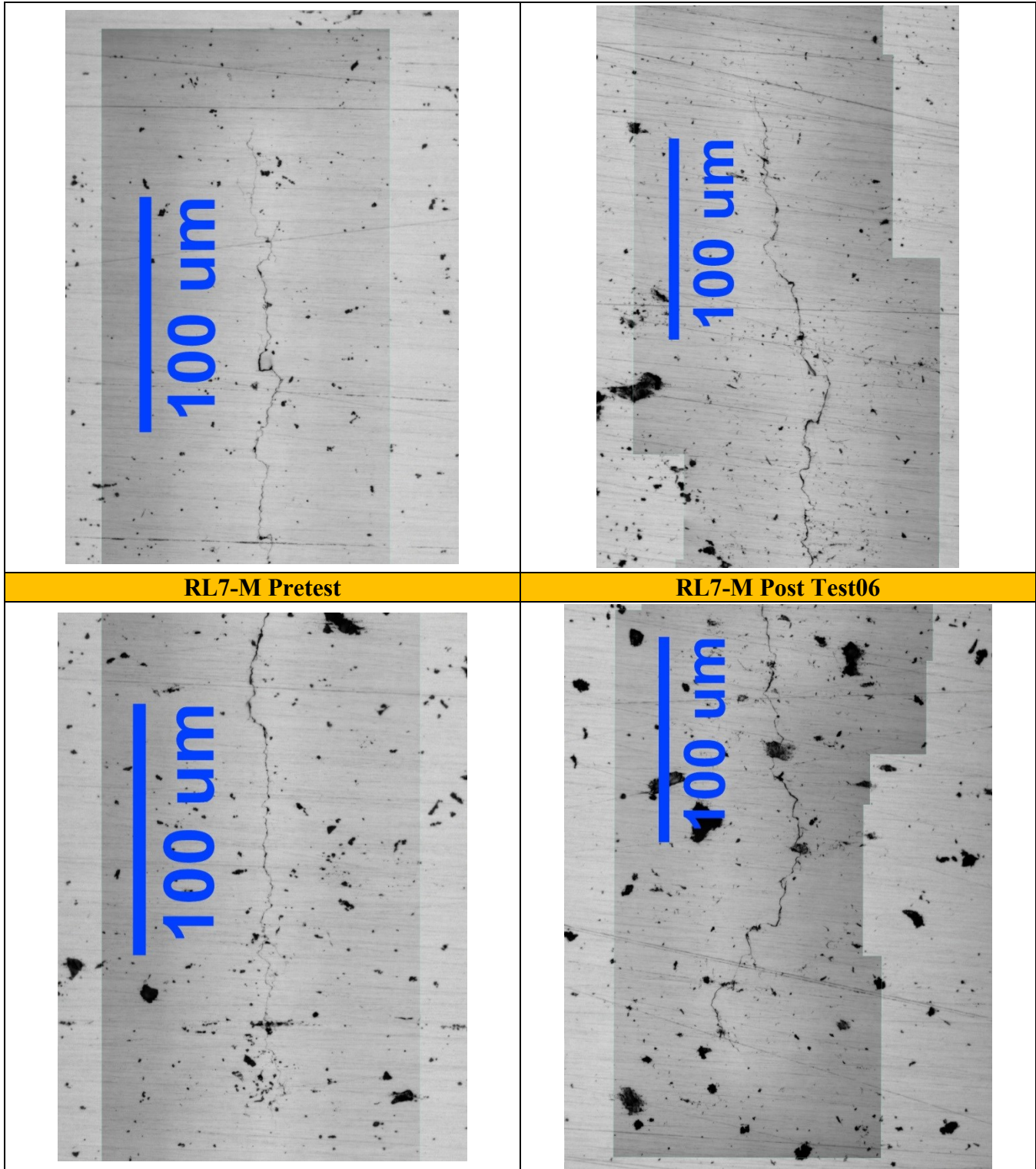
Figure B-11 High magnification images of the surface crack tips for RL6-T. The images were taken prior to testing (pretest) and after test01, test02, and test 03
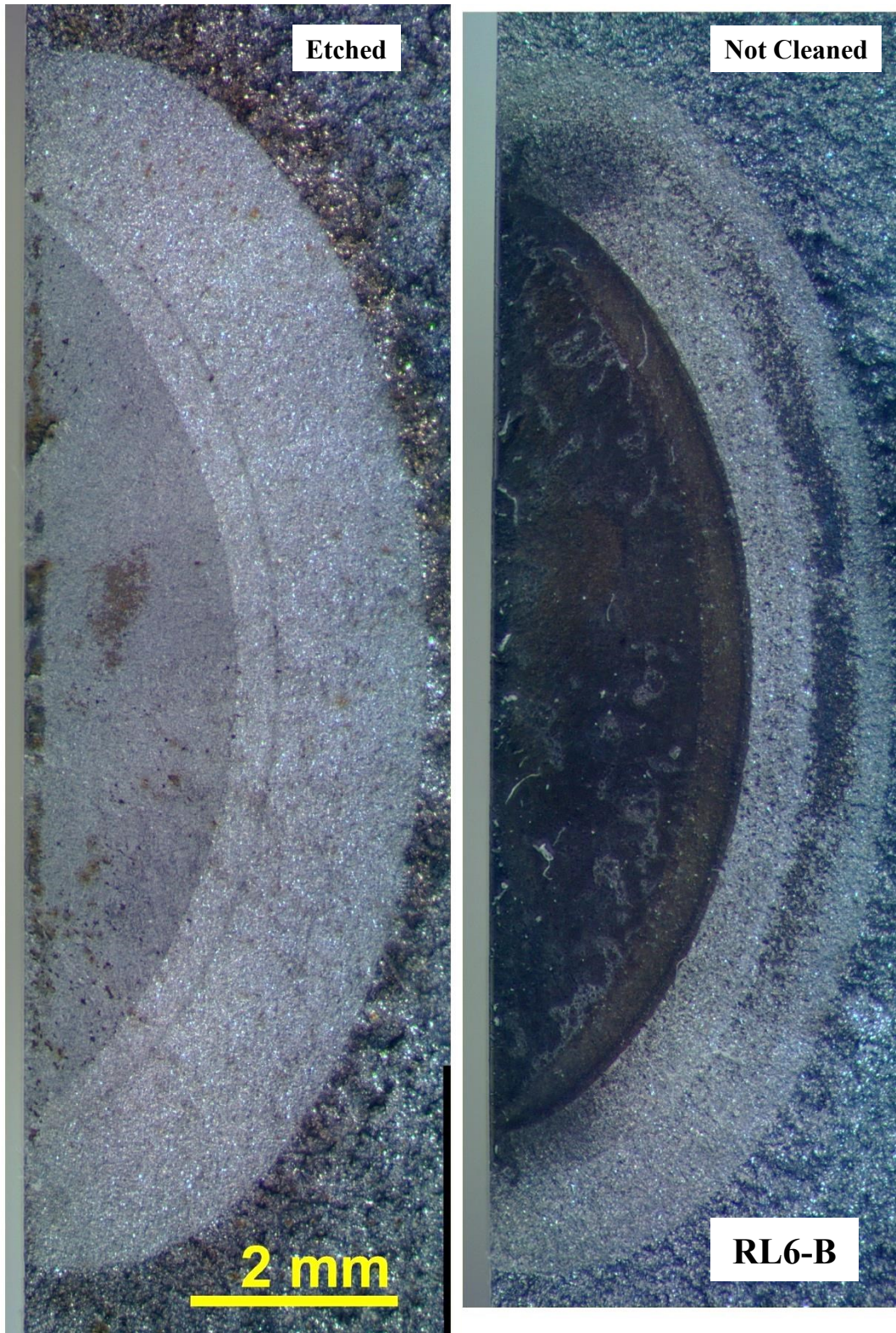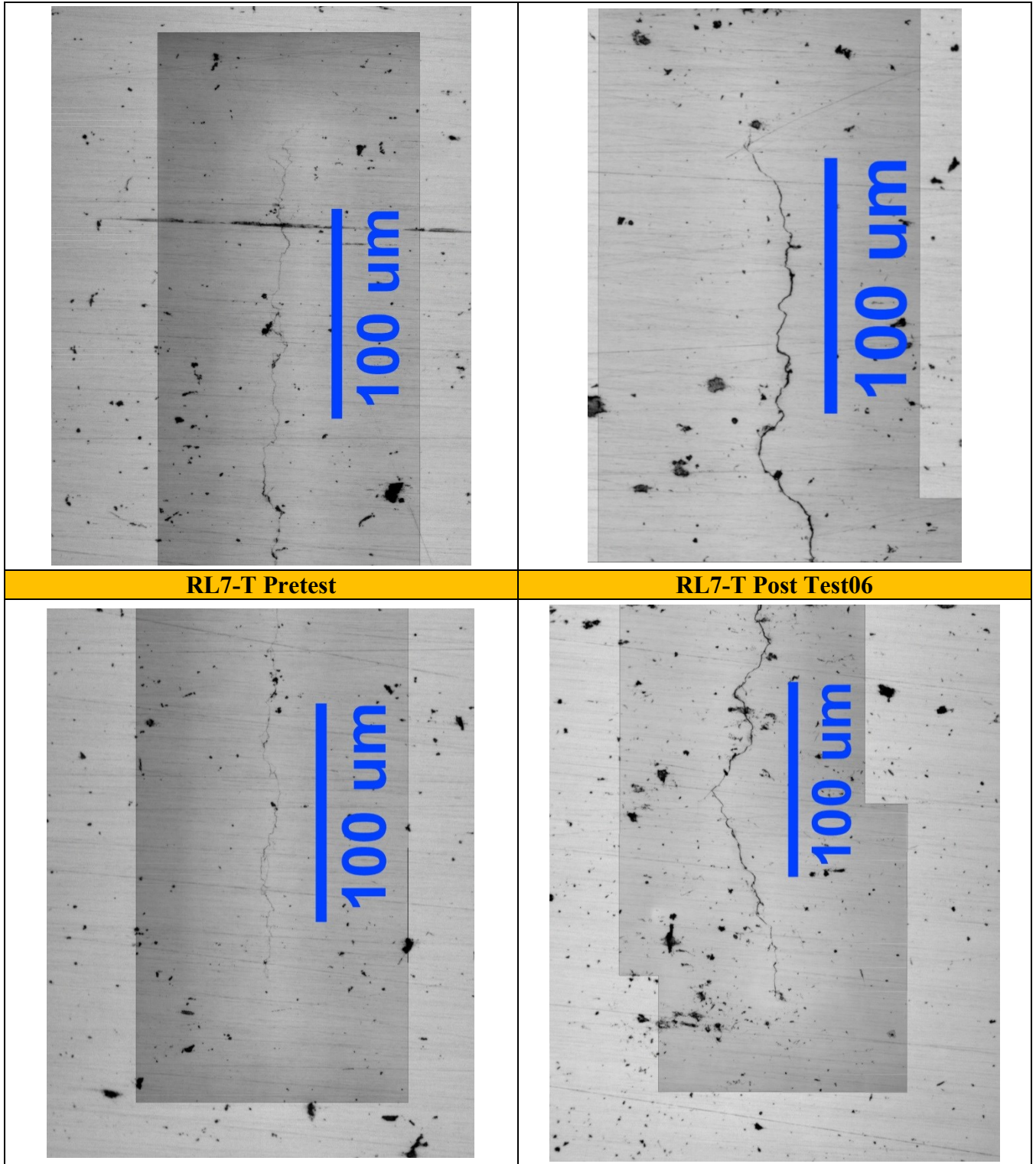
Figure B-12 Fractograph for RL6-B. Imaged with a stereomicroscope. On the left is an etched fracture surface. On the right is a fracture surface that has not undergone cleaning.
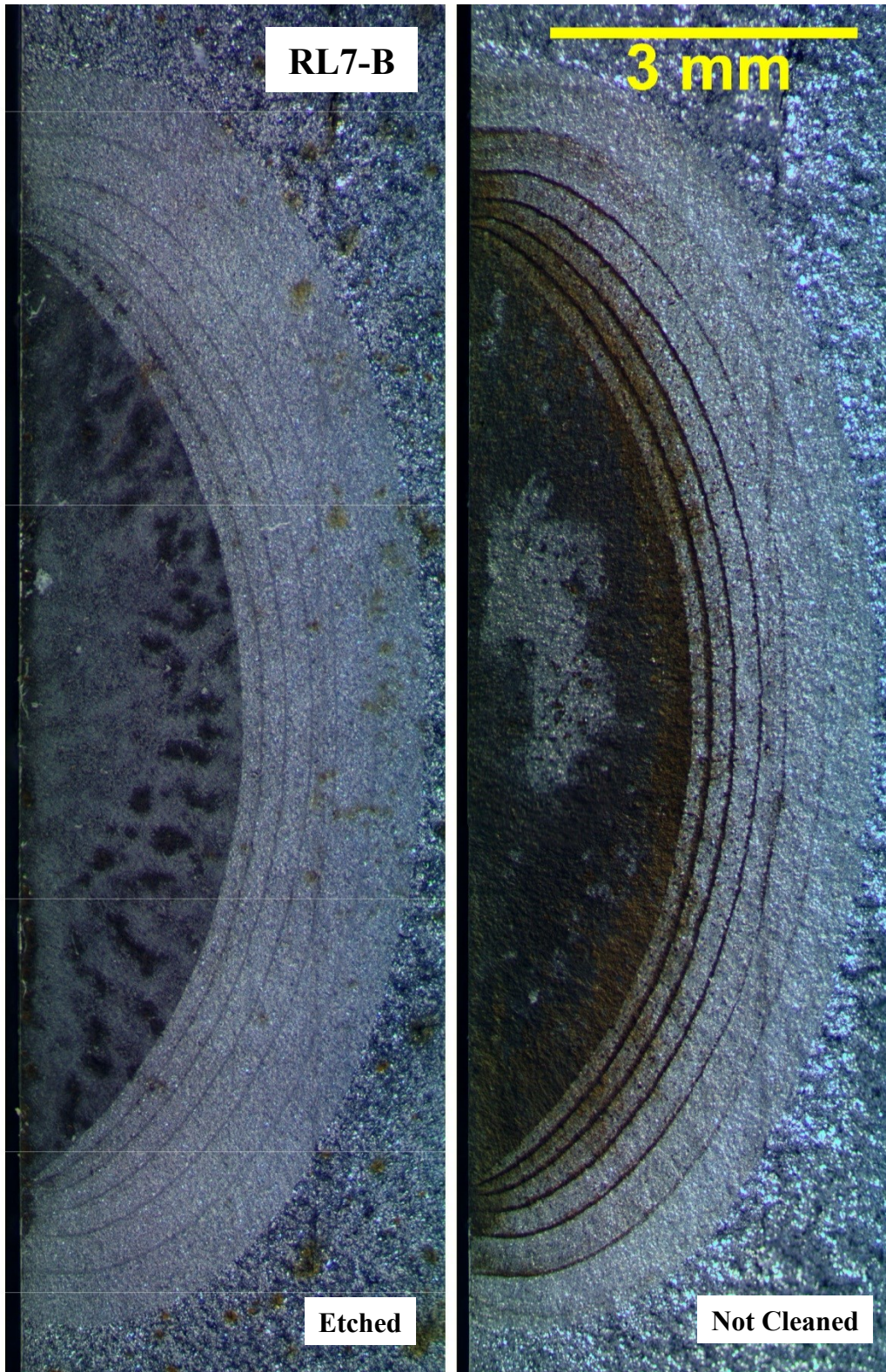
221
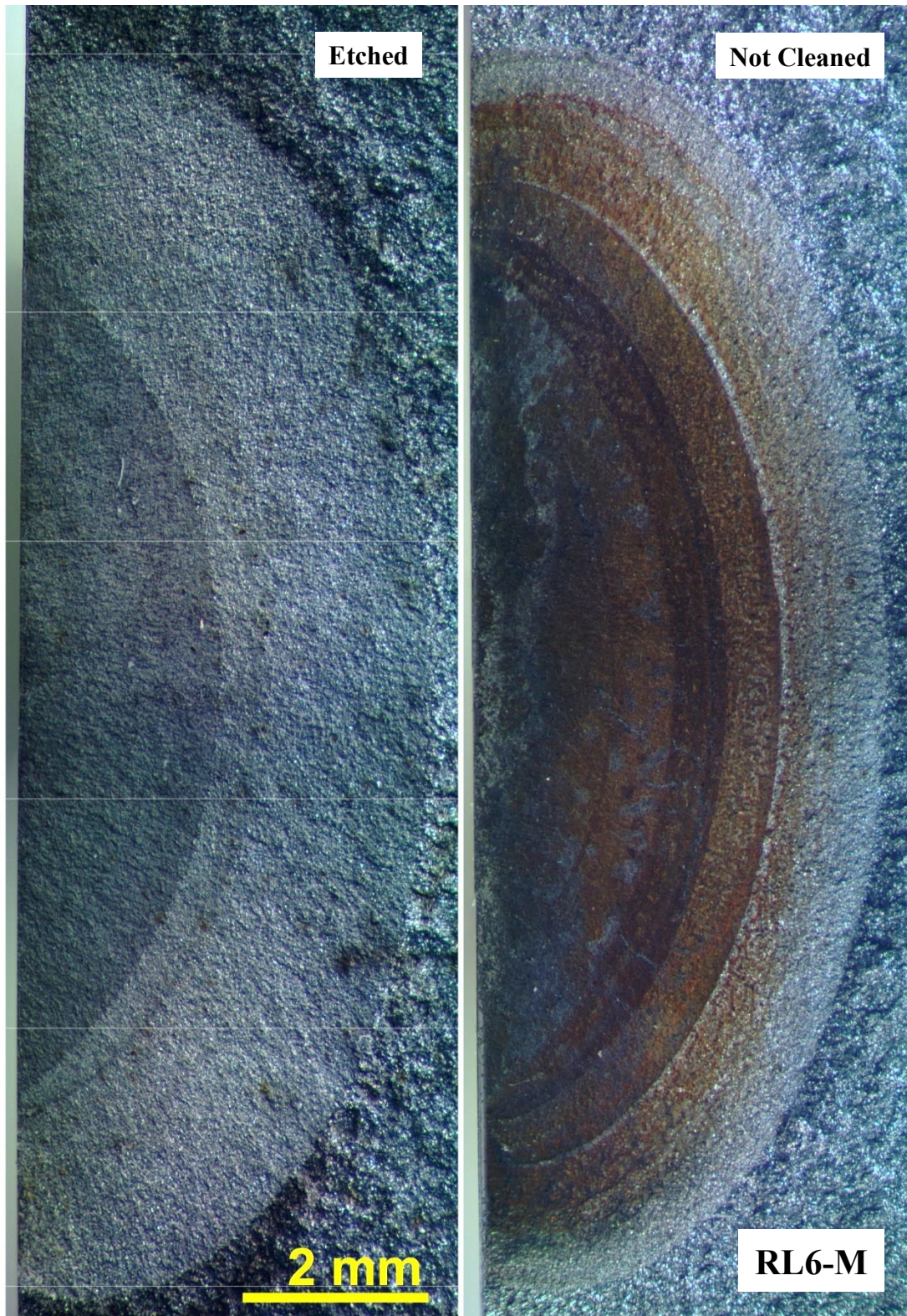
Figure B-13 Fractograph for RL6-M. Imaged with a stereomicroscope. On the left is an etched fracture surface. On the right is a fracture surface that has not undergone cleaning.
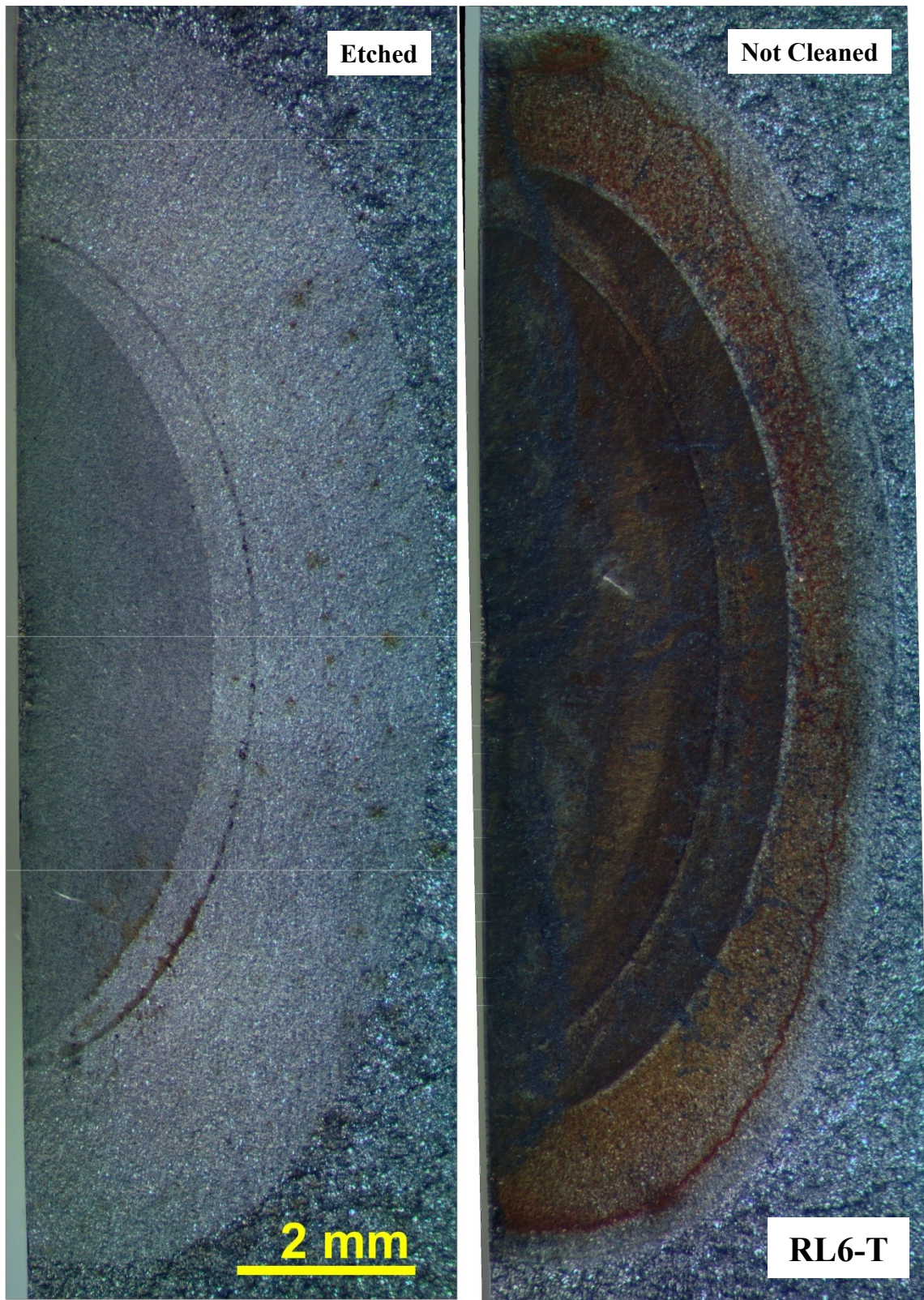
Figure B-14 Fractograph for RL6-T. Imaged with a stereomicroscope. On the left is an etched fracture surface. On the right is a fracture surface that has not undergone cleaning.

RL7-B	RL7-M	RL7-T
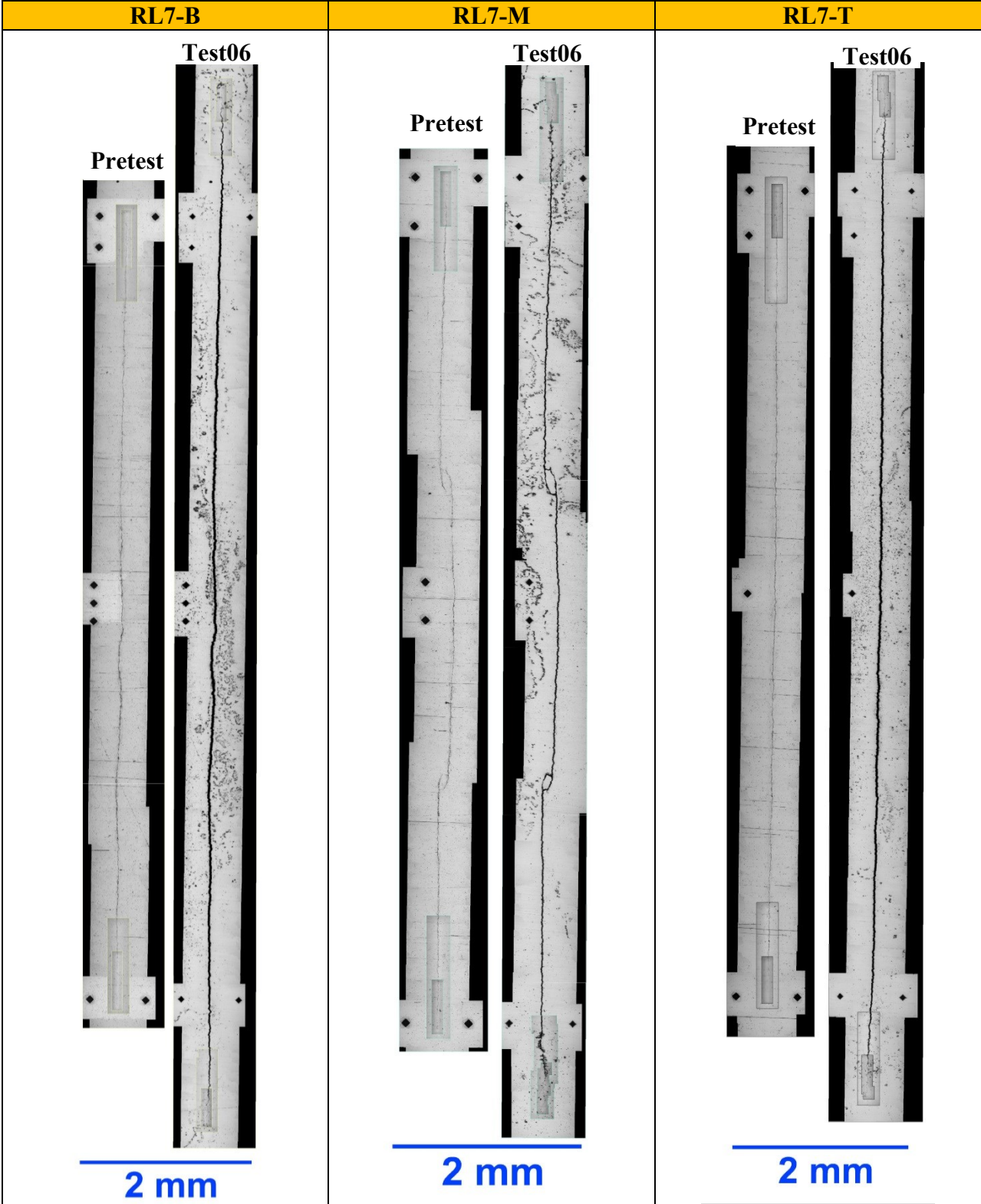
Figure B-15 Surface images taken prior to testing and after test06 for RL7 cracks

| RL7-B Pretest | RL7-B Post Test06 |

Figure B-16 **High magnification images of the surface crack tips for RL7-B. The images were taken prior to testing (pretest) and after test06.**

Figure B-17 High magnification images of the surface crack tips for RL7-M. The images were taken prior to testing (pretest) and after test06.

| RL7-T Pretest | RL7-T Post Test06 |

Figure B-18 High magnification images of the surface crack tips for RL7-T. The images were taken prior to testing (pretest) and after test06.

Figure B-19 Fractograph for RL7-B. Imaged with a stereomicroscope. On the left is an etched fracture surface. On the right is a fracture surface that has not undergone cleaning.
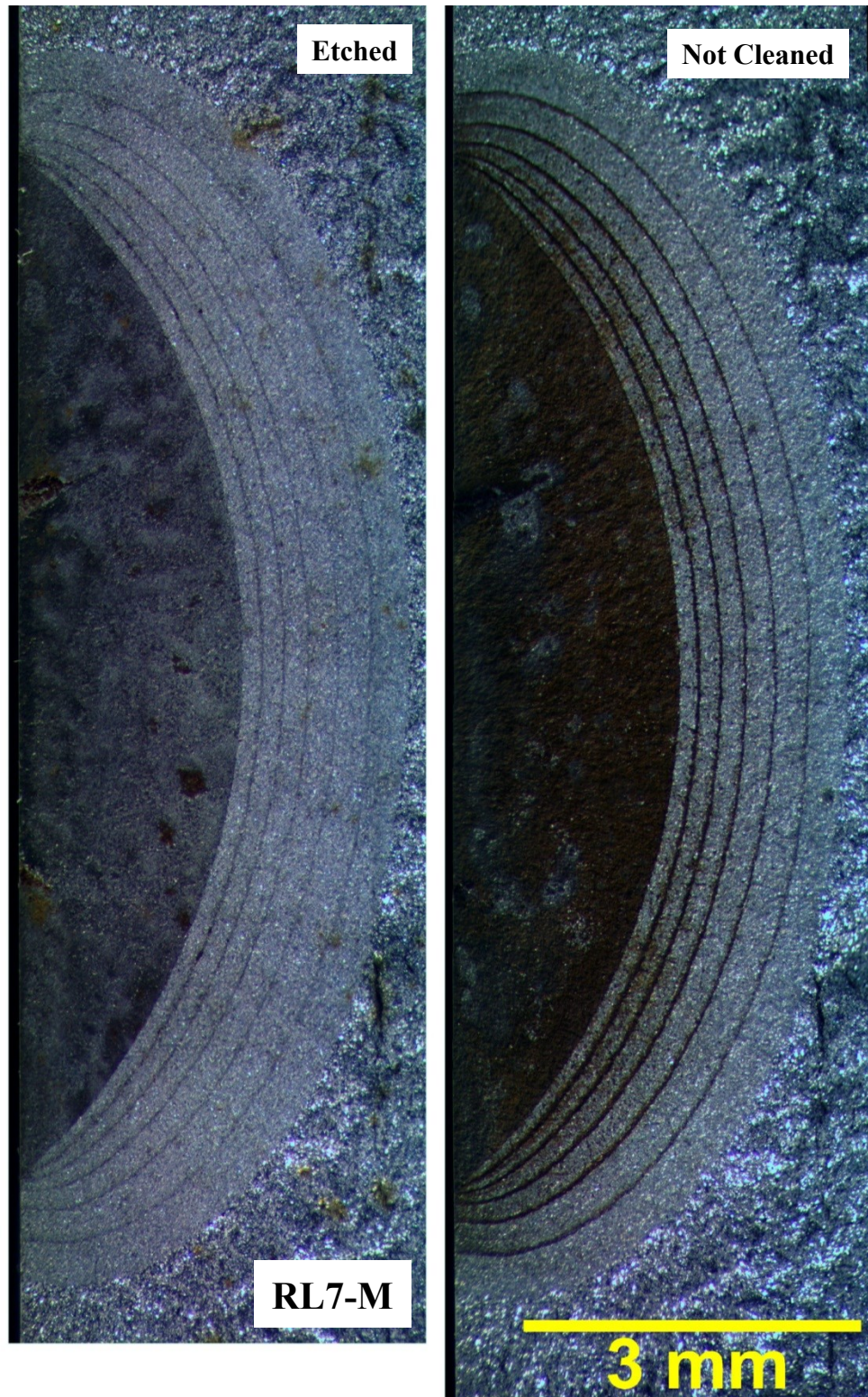
Figure B-20 Fractograph for RL7-M. Imaged with a stereomicroscope. On the left is an etched fracture surface. On the right is a fracture surface that has not undergone cleaning.
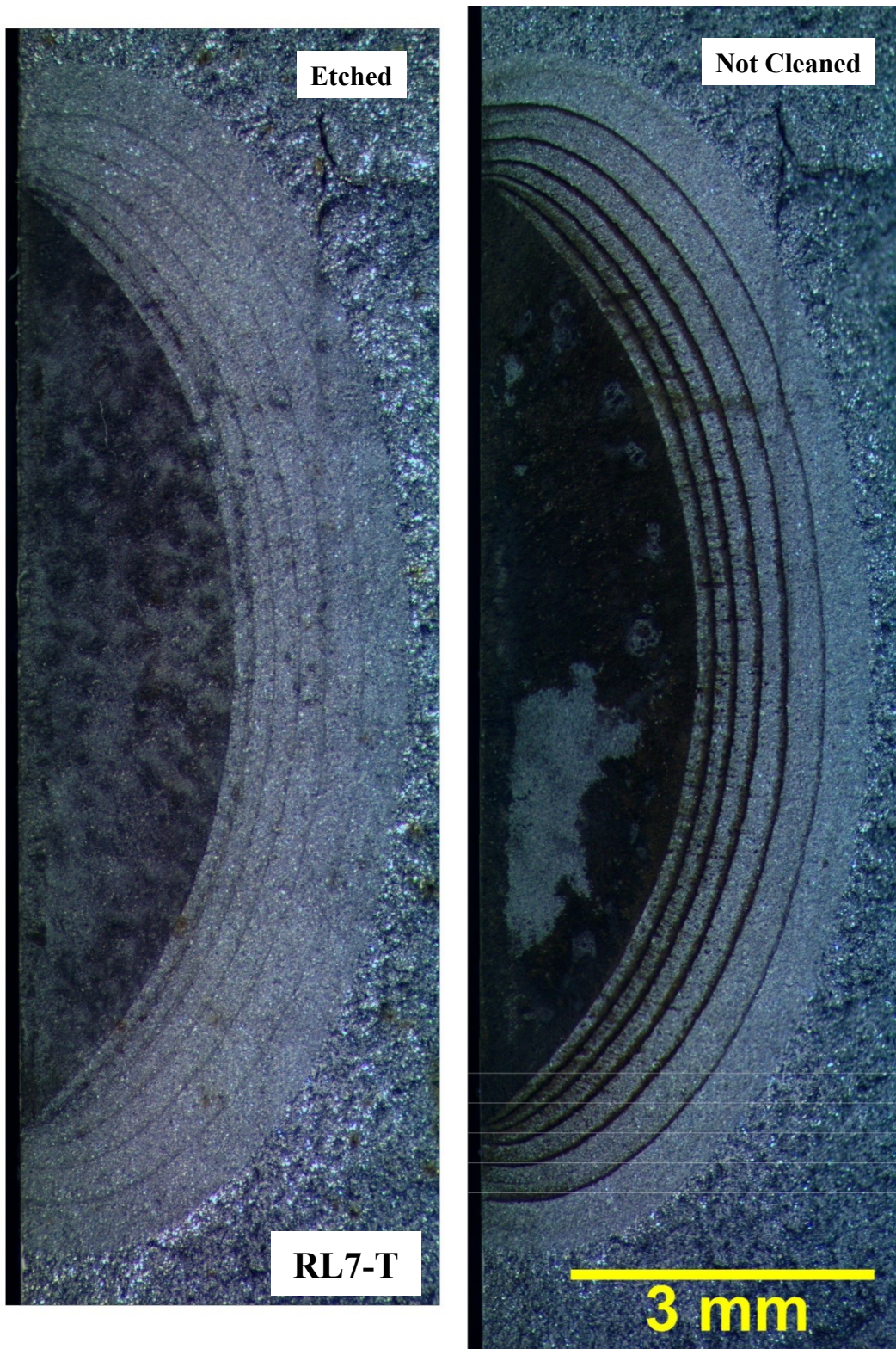
229

Figure B-21 Fractograph for RL7-T. Imaged with a stereomicroscope. On the left is an etched fracture surface. On the right is a fracture surface that has not undergone cleaning.
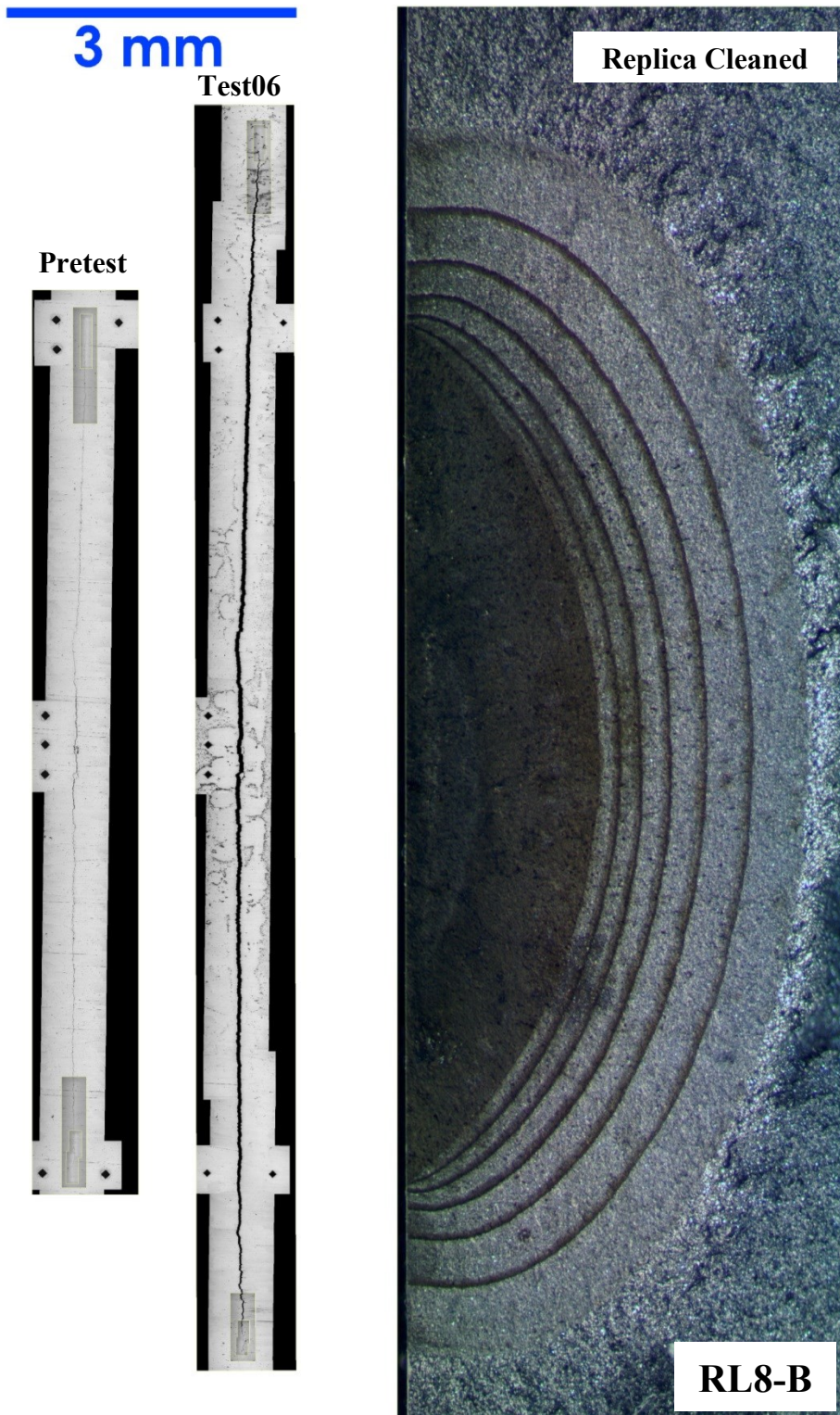
230

Figure B-22 Surface images and fractograph for RL8-B. The surface images were taken prior to testing and after test06. The fracture surface was cleaned with replicating tape.
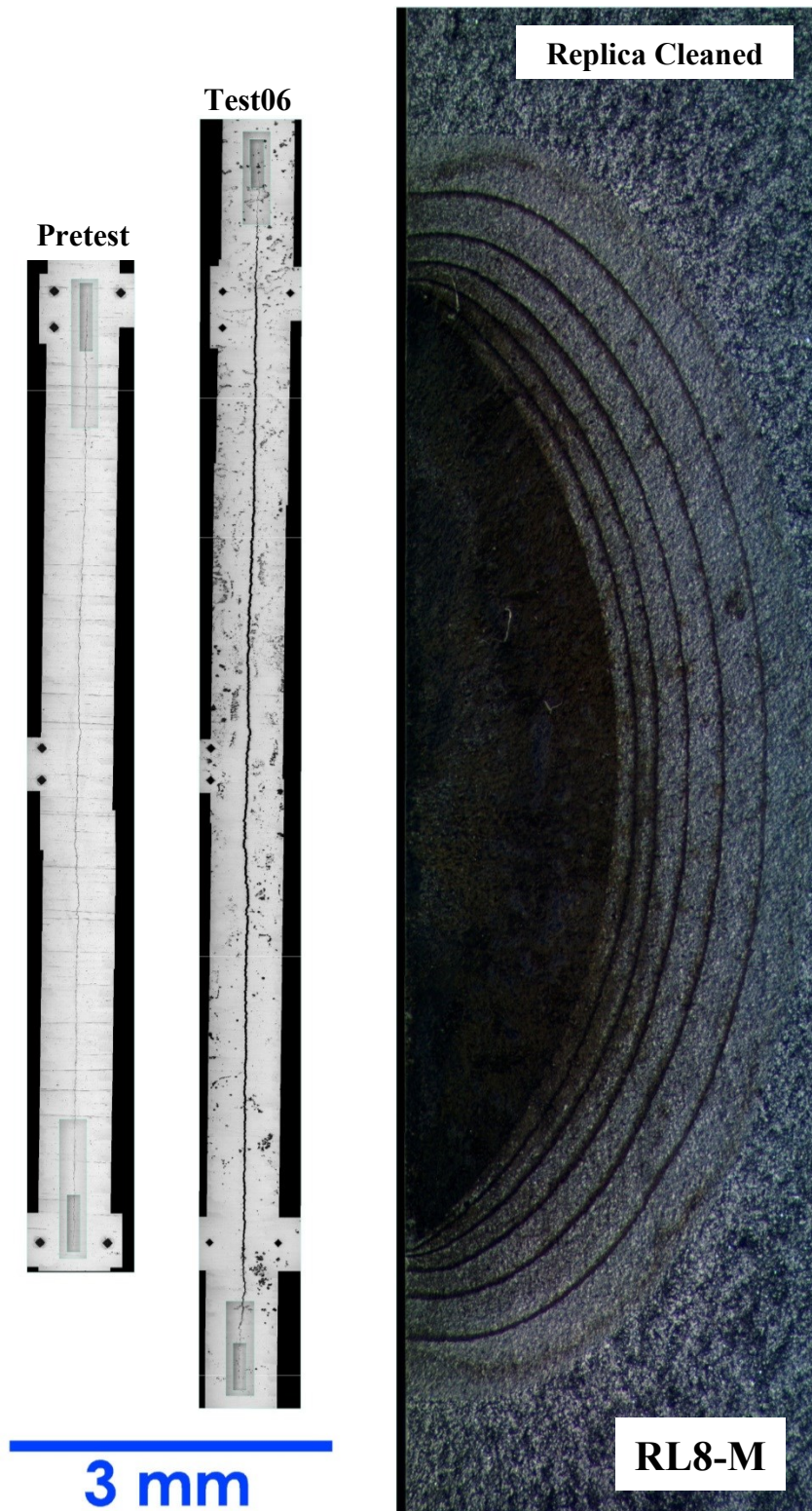
231

Figure B-23 Surface images and fractograph for RL8-M. The surface images were taken prior to testing and after test06. The fracture surface was cleaned with replicating tape.

Pretest

Test06
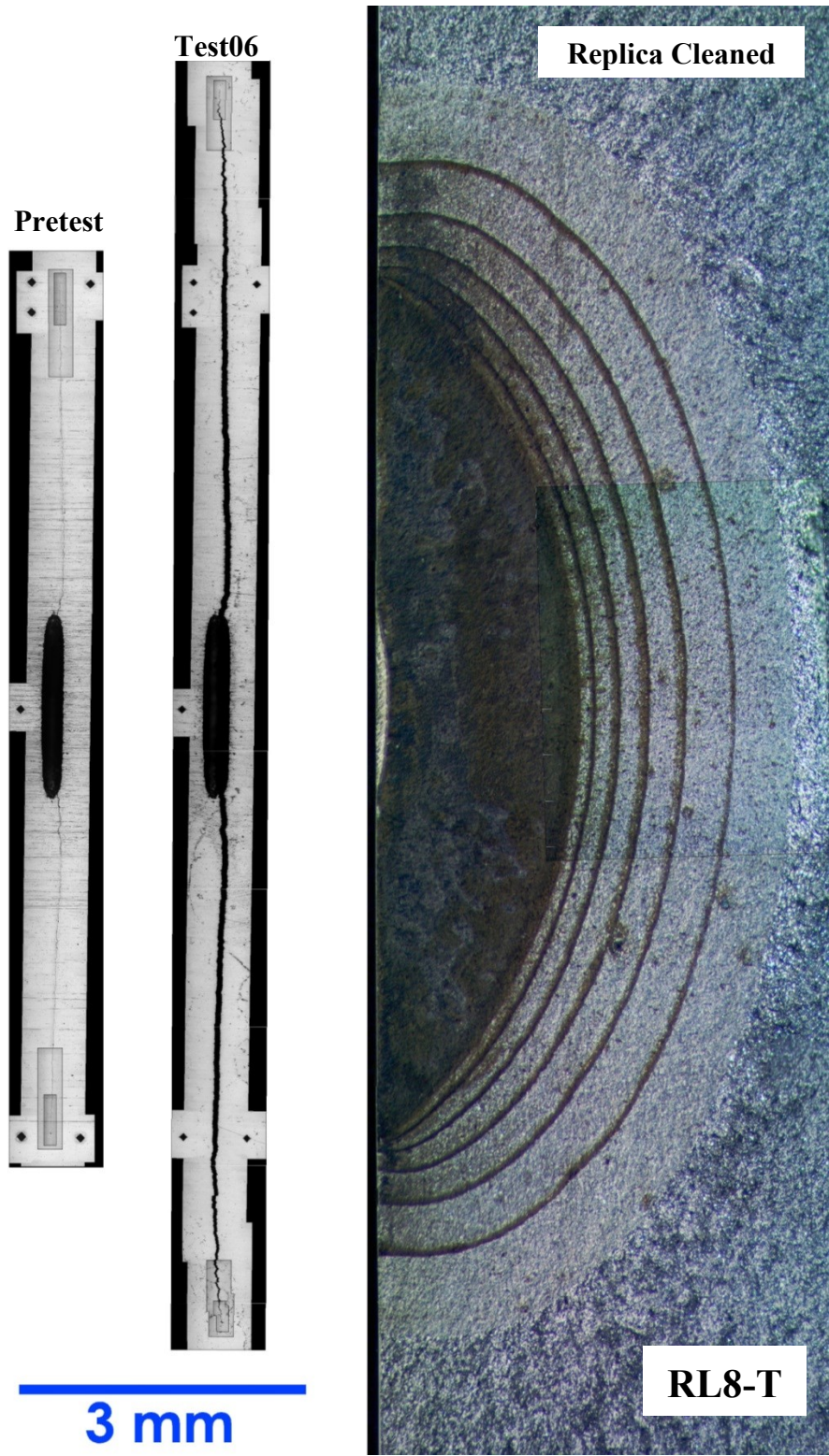
Replica Cleaned

3 mm

RL8-T

Figure B-24 Surface images and fractograph for RL8-T. The surface images were taken prior to testing and after test06. The fracture surface was cleaned with replicating tape.
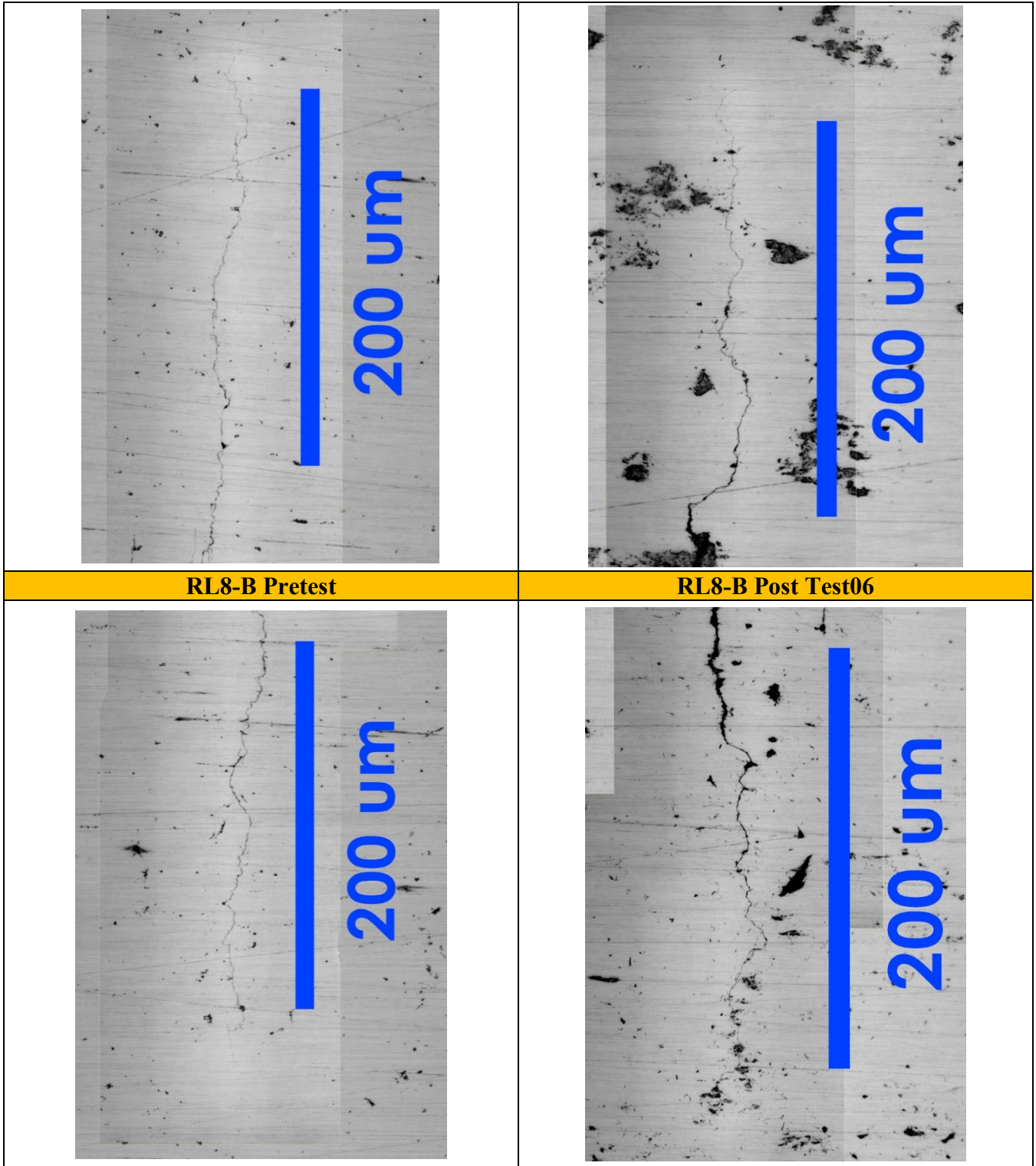
Figure B-25 High magnification images of the surface crack tips for RL8-B. The images were taken prior to testing (pretest) and after test06.
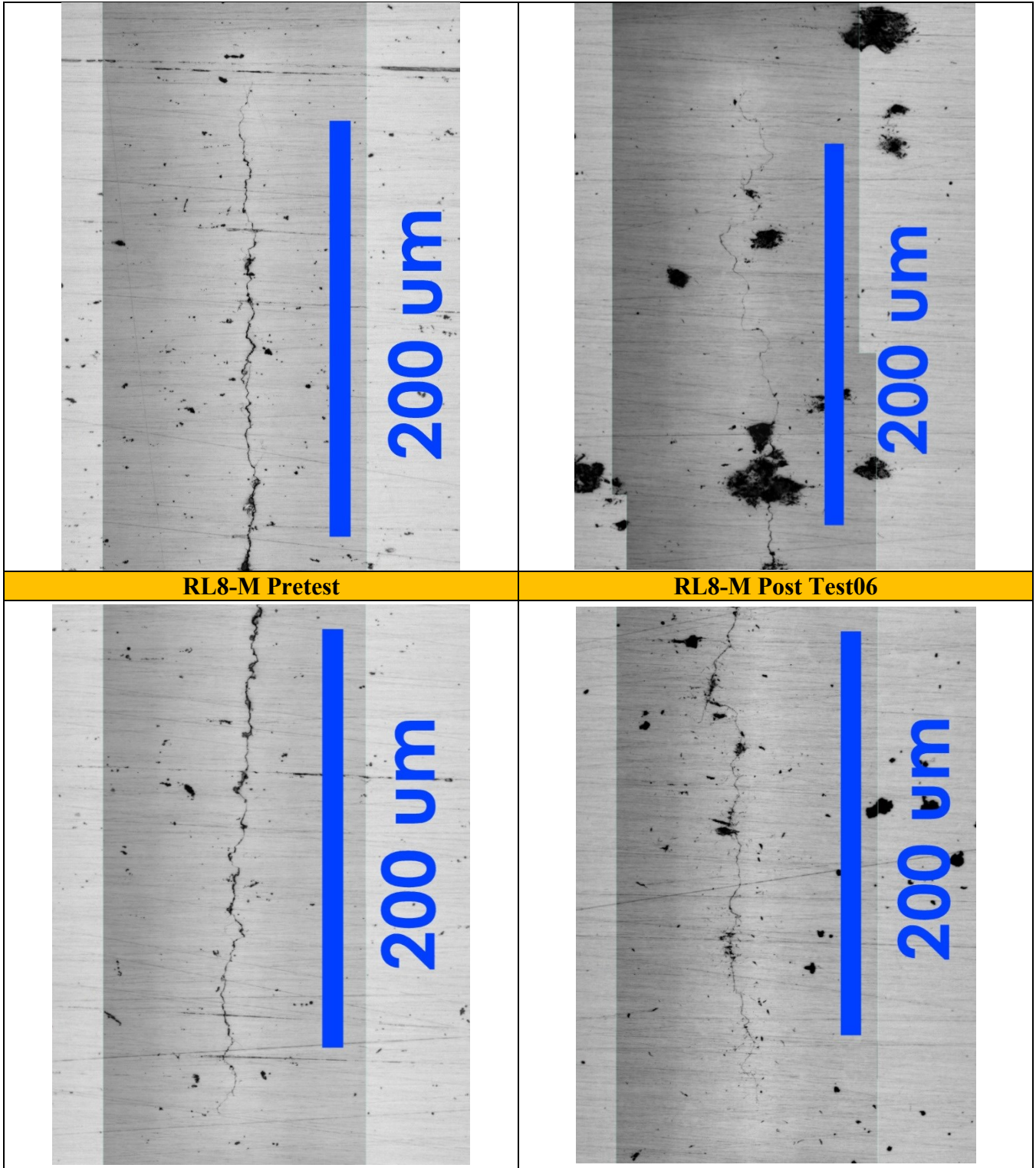
Figure B-26 High magnification images of the surface crack tips for RL8-M. The images were taken prior to testing (pretest) and after test06.
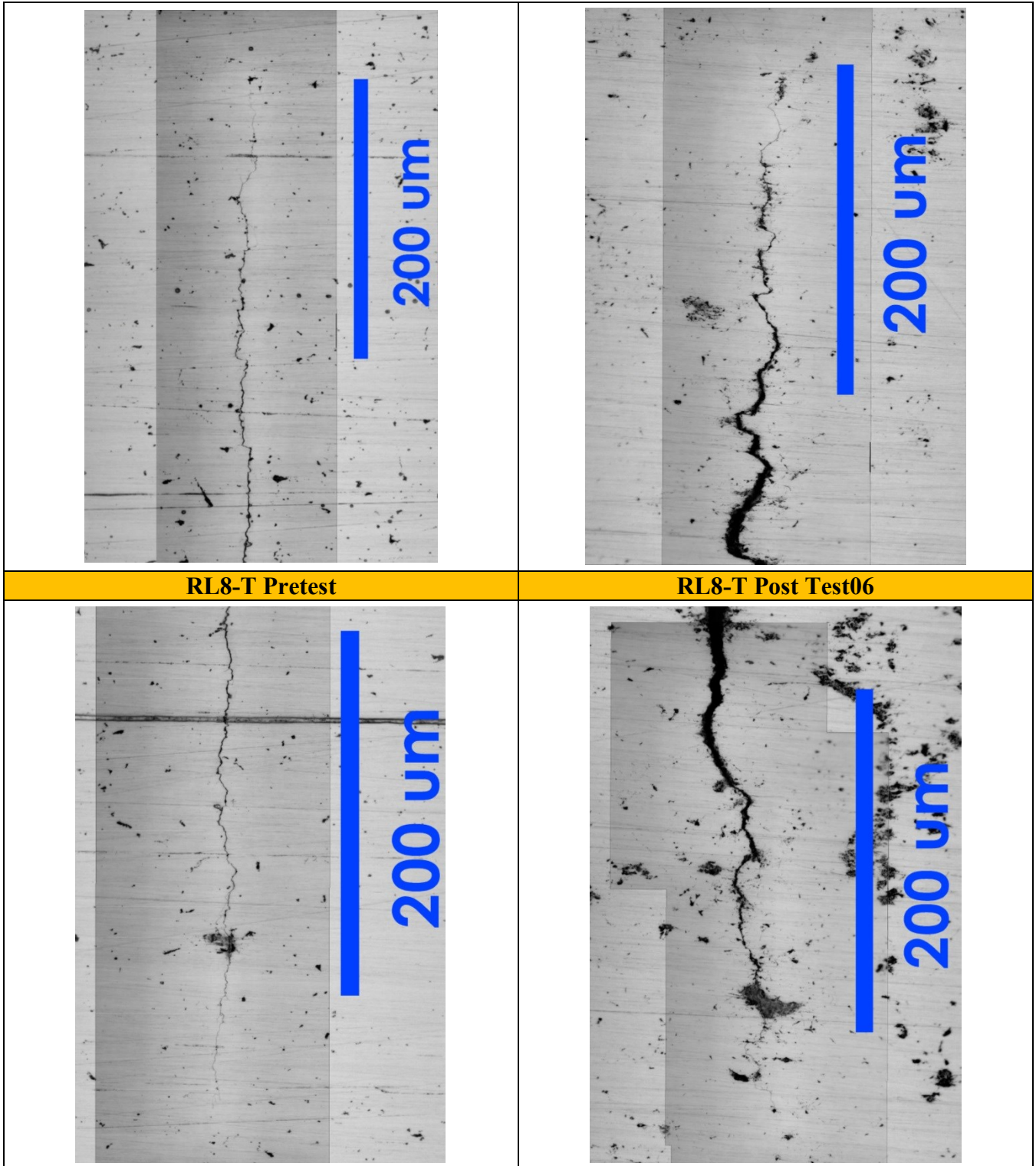
| RL8-T Pretest | RL8-T Post Test06 |

Figure B-27 High magnification images of the surface crack tips for RL8-T. The images were taken prior to testing (pretest) and after test06.

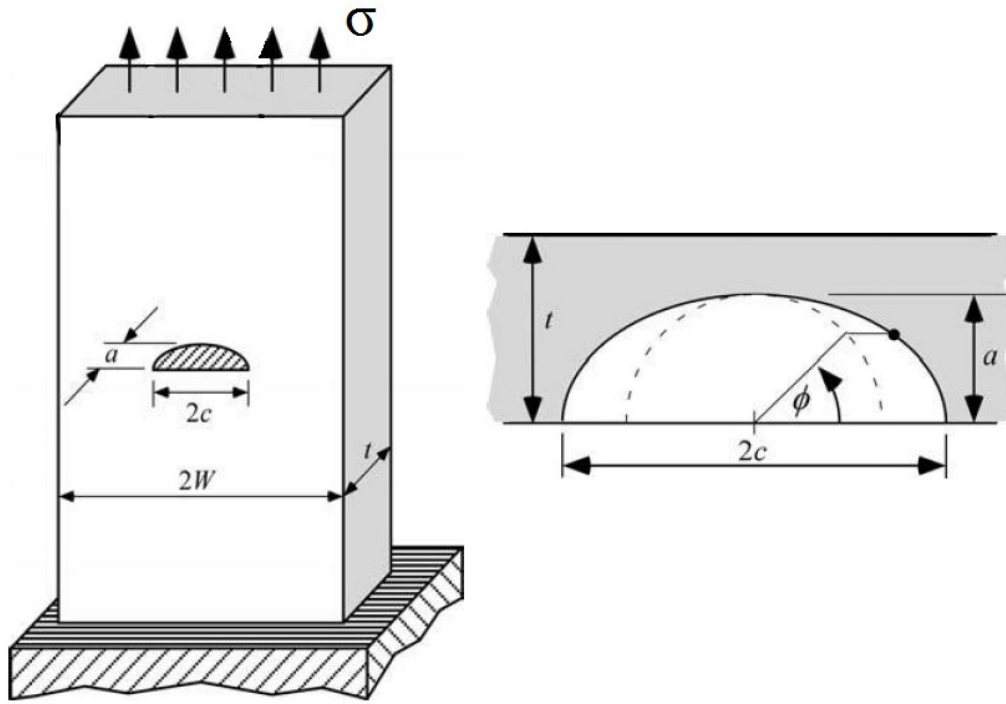# Appendix C - Stress Intensity Factor of Semi-Elliptical Surface Cracks

Figure C-1 Surface crack in a plate with uniform tensile loading. Variables defined for stress intensity solution for a semielliptical surface flaw in a flat plate with a ≤ c [120]. Adapted from [150], with permission from Taylor and Francis group.

Newman and Raju had developed a series of closed-form stress intensity factor (K_I) solutions for surface cracks [119–122] in a plate based on three-dimensional finite-element analysis of semi-elliptical surface cracks in a plate under tensile loading. These solutions have been validated by experimental data [119,121,124–129] and have been widely accepted in the industry. The stress intensity factor of surface cracks in this thesis was calculated using Newman and Raju's equations. The bulging effects observed on actual pipelines were not considered in this thesis. Therefore actual crack behavior may deviate from experimental values.

Figure C-1 shows the case of a semi-elliptical surface crack with the surface half-length less or equal to the depth (a ≤ c) undergoing remote uniform tensile stress (mode I loading). Newman and Raju have a developed a closed form SIF solution for this case using the variables shown in the figure. This case is a good representation of SCC found in the field that hasn't coalesced.

Most SCC has an elongated aspect ratio where the crack length is much larger than the crack depth (i.e. a ≤ c) [6,8,54]

The Newman and Raju SIF solution [119–122] for the surface crack shown in Figure C-1 can be expressed in the following form:

$$K(\phi) = \sigma \sqrt{\frac{\pi a}{Q}} F\left(\frac{a}{t}, \frac{a}{c}, \frac{c}{W}, \phi\right)$$

(C.1)

The shape factor of an elliptical (Q) is expressed as:

$$Q = 1 + 1.464 \left(\frac{a}{c}\right)^{1.65}$$

(C.2)

The boundary correction factor (F) can be expressed as:

$$F(\phi) = \left[M_1 + M_2 \left(\frac{a}{t}\right)^2 + M_3 \left(\frac{a}{t}\right)^4\right] f_\phi f_w g$$

(C.3)

$$M_1 = 1.13 - 0.09 \left(\frac{a}{c}\right)$$

(C.4)

$$M_2 = -0.54 + \frac{0.89}{0.2 + \frac{a}{c}}$$

(C.5)

$$M_3 = 0.5 - \frac{1.0}{0.65 + \frac{a}{c}} + 14 \left(1.0 - \frac{a}{c}\right)^{24}$$

(C.6)

$$f_\phi(\phi) = \left[\left(\frac{a}{c}\right)^2 \cos^2 \phi + \sin^2 \phi\right]^{1/4}$$

(C.7)

$$f_w = \left[\sec\left(\frac{\pi c}{2W} \sqrt{\frac{a}{t}}\right)\right]^{1/2}$$

(C.8)

$$g(\phi) = 1 + \left[0.1 + 0.35 \left(\frac{a}{t}\right)^2\right] (1 - \sin \phi)^2$$

(C.9)

The above equations calculate the stress intensity factor for any point on the crack front specified by the angle ϕ in Figure C-1. For a crack of a certain size (a and c), each point along the crack

front would have a different stress intensity factor. The angle ϕ range from 0 to 90°. The SIF at the surface tip is calculated as $K(0°)$, while the SIF at the depth tip is calculated as $K(90°)$.

Appendix D - Derivation of Shape Evolution Equations

The derivation of the shape evolution equations shown in section 3.3 is shown below.

For a crack with known dimensions a and c, the fatigue crack growth rates at the depth $\left(\frac{da}{dN}\right)$, and surface $\left(\frac{dc}{dN}\right)$ are described using the Paris law:

$$\frac{da}{dN} = C_a(\Delta K_a)^m \tag{D.1}$$

$$\frac{dc}{dN} = C_c(\Delta K_c)^m \tag{D.2}$$

Dividing eqn (D.1) by eqn (D.2), the following equation is obtained:

$$\frac{da}{dc} = \frac{C_a\,(F_a)^m}{C_c\,(F_c)^m} = \frac{C_a\,[g_a f_{\phi,a}]^m}{C_c\,[g_c\,f_{\phi,c}]^m} \tag{D.3}$$

For the above equation, eqns (C.1) to (C.9) have been plugged in. The terms $\Delta\sigma\sqrt{\pi a/Q}$, $\left[M_1 + M_2\left(\frac{a}{t}\right)^2 + M_3\left(\frac{a}{t}\right)^4\right]$, and f_w were all cancelled out. F_a is boundary correction factor at the depth tip ($\phi = 90°$), and F_c is the boundary correction factor at the surface tip ($\phi = 0°$). For the terms in the boundary factor that depend on ϕ and do not cancel out, they are defined below:

$$g_a = g(\pi/2) = 1 \tag{D.4}$$

$$f_{\phi,a} = f_\phi(\pi/2) = 1 \tag{D.5}$$

$$g_c = g(0) = 1.1 + 0.35\left(\frac{a}{t}\right)^2 \tag{D.6}$$

$$f_{\phi,c} = f_\phi(0) = \left(\frac{a}{c}\right)^{0.5} \tag{D.7}$$

Substituting eqns (D.4) to (D.7) into F_a/F_c result in:

$$\frac{F_a}{F_c} = \left(\frac{a}{c}\right)^{0.5} \left(1.1 + 0.35 \left(\frac{a}{t}\right)^2\right) \tag{D.8}$$

With eqn (D.8), *da/dc* in eqn (D.3) can be evaluated. For the two assumptions of the relationship between C_a and C_c shown in equation (3.3) and (3.4), the resulting shape evolutions equations are shown below:

- For the assumption $C_c = C_a$:

$$\frac{da}{dc} = \left[\left(\frac{a}{c}\right)^{0.5} \left(1.1 + 0.35 \left(\frac{a}{t}\right)^2\right)\right]^{-m} \tag{D.9}$$

- For the assumption $C_c = 0.9^m C_a$:

$$\frac{da}{dc} = \left[0.9 \left(\frac{a}{c}\right)^{0.5} \left(1.1 + 0.35 \left(\frac{a}{t}\right)^2\right)\right]^{-m} \tag{D.10}$$